NOTICE

The quality of this microform is heavily dependent upon the quality of the original thesis submitted for microfilming. Every effort has been made to ensure the highest quality of reproduction possible.

If pages are missing, contact the university which granted the degree.

Some pages may have indistinct print especially if the original pages were typed with a poor typewriter ribbon or if the university sent us an inferior photocopy.

Reproduction in full or in part of this microform is governed by the Canadian Copyright Act, R.S.C. 1970, c. C-30, and subsequent amendments.

AVIS

La qualité de cette microforme dépend grandement de la qualité de la thèse soumise au microfilmage. Nous avons tout fait pour assurer une qualité supérieure de reproduction.

S'il manque des pages, veuillez communiquer avec l'université qui a conféré le grade.

La qualité d'impression de certaines pages peut laisser à désirer, surtout si les pages originales ont été dactylographiées à l'aide d'un ruban usé ou si l'université nous a fait parvenir une photocopie de qualité inférieure.

La reproduction, même partielle, de cette microforme est soumise à la Loi canadienne sur le droit d'auteur, SRC 1970, c. C-30, et ses amendements subséquents.

Canada

University of Alberta

Instability and Transitions of Flow in a Curved Duct of Square Cross Section

by

Philip A. J. Mees ©

A thesis
submitted to the Faculty of Graduate Studies and Research
in partial fulfillment of the requirements for the degree of

Doctor of Philosophy

Department of Chemical Engineering

Edmonton, Alberta

Fall 1994

Name __Philip MEES__

Dissertation Abstracts International is arranged by broad, general subject categories. Please select the one subject which most nearly describes the content of your dissertation. Enter the corresponding four-digit code in the spaces provided.

__Chemical Engineering__
SUBJECT TERM

`0 5 4 2` **U·M·I**
SUBJECT CODE

Subject Categories

THE HUMANITIES AND SOCIAL SCIENCES

COMMUNICATIONS AND THE ARTS
Architecture	0729
Art History	0377
Cinema	0900
Dance	0378
Fine Arts	0357
Information Science	0723
Journalism	0391
Library Science	0399
Mass Communications	0708
Music	0413
Speech Communication	0459
Theater	0465

EDUCATION
General	0515
Administration	0514
Adult and Continuing	0516
Agricultural	0517
Art	0273
Bilingual and Multicultural	0282
Business	0688
Community College	0275
Curriculum and Instruction	0727
Early Childhood	0518
Elementary	0524
Finance	0277
Guidance and Counseling	0519
Health	0680
Higher	0745
History of	0520
Home Economics	0278
Industrial	0521
Language and Literature	0279
Mathematics	0280
Music	0522
Philosophy of	0998
Physical	0523

Psychology	0525
Reading	0535
Religious	0527
Sciences	0714
Secondary	0533
Social Sciences	0534
Sociology of	0340
Special	0529
Teacher Training	0530
Technology	0710
Tests and Measurements	0288
Vocational	0747

LANGUAGE, LITERATURE AND LINGUISTICS
Language
General	0679
Ancient	0289
Linguistics	0290
Modern	0291

Literature
General	0401
Classical	0294
Comparative	0295
Medieval	0297
Modern	0298
African	0316
American	0591
Asian	0305
Canadian (English)	0352
Canadian (French)	0355
English	0593
Germanic	0311
Latin American	0312
Middle Eastern	0315
Romance	0313
Slavic and East European	0314

PHILOSOPHY, RELIGION AND THEOLOGY
Philosophy	0422

Religion
General	0318
Biblical Studies	0321
Clergy	0319
History of	0320
Philosophy of	0322
Theology	0469

SOCIAL SCIENCES
American Studies	0323

Anthropology
Archaeology	0324
Cultural	0326
Physical	0327

Business Administration
General	0310
Accounting	0272
Banking	0770
Management	0454
Marketing	0338
Canadian Studies	0385

Economics
General	0501
Agricultural	0503
Commerce-Business	0505
Finance	0508
History	0509
Labor	0510
Theory	0511
Folklore	0358
Geography	0366
Gerontology	0351

History
General	0578

Ancient	0579
Medieval	0581
Modern	0582
Black	0328
African	0331
Asia, Australia and Oceania	0332
Canadian	0334
European	0335
Latin American	0336
Middle Eastern	0333
United States	0337
History of Science	0585
Law	0398

Political Science
General	0615
International Law and Relations	0616
Public Administration	0617
Recreation	0814
Social Work	0452

Sociology
General	0626
Criminology and Penology	0627
Demography	0938
Ethnic and Racial Studies	0631
Individual and Family Studies	0628
Industrial and Labor Relations	0629
Public and Social Welfare	0630
Social Structure and Development	0700
Theory and Methods	0344
Transportation	0709
Urban and Regional Planning	0999
Women's Studies	0453

THE SCIENCES AND ENGINEERING

BIOLOGICAL SCIENCES
Agriculture
General	0473
Agronomy	0285
Animal Culture and Nutrition	0475
Animal Pathology	0476
Food Science and Technology	0359
Forestry and Wildlife	0478
Plant Culture	0479
Plant Pathology	0480
Plant Physiology	0817
Range Management	0777
Wood Technology	0746

Biology
General	0306
Anatomy	0287
Biostatistics	0308
Botany	0309
Cell	0379
Ecology	0329
Entomology	0353
Genetics	0369
Limnology	0793
Microbiology	0410
Molecular	0307
Neuroscience	0317
Oceanography	0416
Physiology	0433
Radiation	0821
Veterinary Science	0778
Zoology	0472

Biophysics
General	0786
Medical	0760

EARTH SCIENCES
Biogeochemistry	0425
Geochemistry	0996

Geodesy	0370
Geology	0372
Geophysics	0373
Hydrology	0388
Mineralogy	0411
Paleobotany	0345
Paleoecology	0426
Paleontology	0418
Paleozoology	0985
Palynology	0427
Physical Geography	0368
Physical Oceanography	0415

HEALTH AND ENVIRONMENTAL SCIENCES
Environmental Sciences	0768

Health Sciences
General	0566
Audiology	0300
Chemotherapy	0992
Dentistry	0567
Education	0350
Hospital Management	0769
Human Development	0758
Immunology	0982
Medicine and Surgery	0564
Mental Health	0347
Nursing	0569
Nutrition	0570
Obstetrics and Gynecology	0380
Occupational Health and Therapy	0354
Ophthalmology	0381
Pathology	0571
Pharmacology	0419
Pharmacy	0572
Physical Therapy	0382
Public Health	0573
Radiology	0574
Recreation	0575

Speech Pathology	0460
Toxicology	0383
Home Economics	0386

PHYSICAL SCIENCES

Pure Sciences
Chemistry
General	0485
Agricultural	0749
Analytical	0486
Biochemistry	0487
Inorganic	0488
Nuclear	0738
Organic	0490
Pharmaceutical	0491
Physical	0494
Polymer	0495
Radiation	0754
Mathematics	0405

Physics
General	0605
Acoustics	0986
Astronomy and Astrophysics	0606
Atmospheric Science	0608
Atomic	0748
Electronics and Electricity	0607
Elementary Particles and High Energy	0798
Fluid and Plasma	0759
Molecular	0609
Nuclear	0610
Optics	0752
Radiation	0756
Solid State	0611
Statistics	0463

Applied Sciences
Applied Mechanics	0346
Computer Science	0984

Engineering
General	0537
Aerospace	0538
Agricultural	0539
Automotive	0540
Biomedical	0541
Chemical	0542
Civil	0543
Electronics and Electrical	0544
Heat and Thermodynamics	0348
Hydraulic	0545
Industrial	0546
Marine	0547
Materials Science	0794
Mechanical	0548
Metallurgy	0743
Mining	0551
Nuclear	0552
Packaging	0549
Petroleum	0765
Sanitary and Municipal	0554
System Science	0790
Geotechnology	0428
Operations Research	0796
Plastics Technology	0795
Textile Technology	0994

PSYCHOLOGY
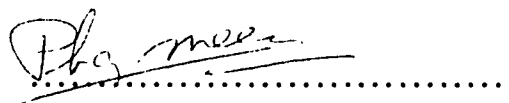|	
General	0621
Behavioral	0384
Clinical	0622
Developmental	0620
Experimental	0623
Industrial	0624
Personality	0625
Physiological	0989
Psychobiology	0349
Psychometrics	0632
Social	0451

✪

University of Alberta

Release Form

Name of Author: **Philip A. J. Mees**

Title of Thesis: **Instability and Transitions of Flow in a Curved Duct of Square Cross Section**

Degree: **Doctor of Philosophy**

Year this degree granted: **Fall 1994**

Permission is hereby granted to the **University of Alberta Library** to reproduce single copies of this thesis and to lend or sell such copies for private, scholarly or scientific research purposes only.

The author reserves all other publication and other rights in association with the copyright in the thesis, and except as hereinbefore provided neither the thesis nor any substantial portion thereof may be printed or otherwise reproduced in any material form whatever without the author's prior written permission.
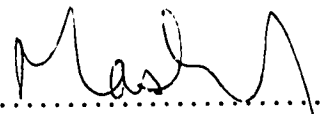
(Student's signature)
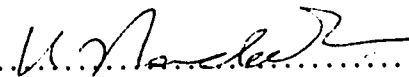
Philip A. J. Mees

c/o University of Alberta

Department of Chemical Engineering

Edmonton, Alberta
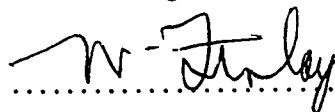
Canada T6G 2G6
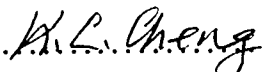
Date : September 27, 1994

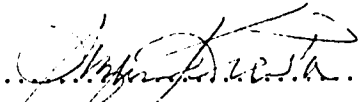University of Alberta

Faculty of Graduate Studies and Research

The undersigned certify that they have read, and recommend to the Faculty of Graduate Studies and Research for acceptance, a thesis entitled Instability and Transitions of Flow in a Curved Duct of Square Cross Section submitted by Philip A. J. Mees in partial fulfillment of the requirements for the degree of Doctor of Philosophy.
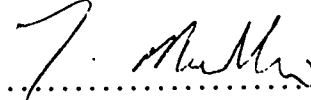
....
J. H. Masliyah (Supervisor)

....
K. Nandakumar (Supervisor)

....
K. C. Cheng

....
W. H. Finlay

....
S. M. Kresta

....
T. Mullin (External examiner)

Date : September 23, 1994

Abstract

Steady and time dependent flow in a curved duct of square cross-section (the Dean problem) is investigated both experimentally and numerically. The first part is a continuation of the work done on steady developing flow by Bara *et al.* (*J. Fluid Mech.* **244**, 339–376 (1992)). A 6-cell secondary flow state with two pairs of Dean vortices was observed above a Dean number of 350. In the second part, a new time dependent flow state, consisting of oscillating Dean vortices, is investigated.

In this study, steady flows for Dean numbers up to $Dn = 600$ are investigated ($Dn = Re/\sqrt{R_c}$ where Re is the Reynolds number, $\bar{v}_\theta a/\nu$. The curvature ratio, R_c is 15.1).The experimental methods used are visualization of secondary flow patterns using laser fluorescent dye and laser Doppler anemometry to measure streamwise or spanwise velocities. The development of two pairs of Dean vortices is observed at Dean numbers above 350. This 6-cell flow state breaks down spatially into a 2-cell flow. Numerical simulations, based on the parabolized Navier-Stokes equations, are in very good agreement with the experiments. Based on the similarity with boundary layer flow over a concave wall (the Görtler problem), it is suggested that the transition to 6-cell flow is the result of a decreasing spanwise wavelength of the Dean vortices with increasing flowrate. This is the first time that detailed experiments and simulations of the development of a 6-cell flow state are reported.

Another area that is investigated is a new traveling wave phenomenon that was

observed at Dean numbers between 170 and 260. This traveling wave state, which consists of two oscillating Dean vortices, was induced by a carefully positioned pin (diameter of 0.1-0.2 mm) at 5° from the inlet of the curved section along the symmetry line of the cross-section. The traveling wave was found to lock in to an imposed periodic disturbance at a selected frequency. The flow structure of the locked state was investigated in detail. Direct numerical simulations in FLOW3D are in very good agreement with the experiments and confirm the existence of a fully developed, streamwise periodic traveling wave state.

The inflow region between the two Dean vortices, which transports low-speed fluid away from the outer wall, creates strongly inflectional spanwise profiles of the streamwise velocity. Similarities with twisting vortices in a curved channel and sinuous oscillations of Görtler vortices suggest that the traveling waves observed here result from a secondary shear instability of these spanwise inflectional profiles.

Acknowledgments

I would like to thank Dr. J. H. Masliyah and Dr. K. Nandakumar for their encouragement and support. They were always available for advise, treating me as equal discussion partners, and leaving me the freedom to take this project into the direction that I preferred. This open work environment has greatly contributed to a very enjoyable four years of research.

Many other faculty members from various department have contributed through their advise and suggestions. I would also like to thank the staff from the instrument shop, the machine shop and the DACS computer centre for their excellent and important work.

This study was possible, thanks to the assistance from the Natural Sciences and Engineering Research Council (NSERC) in the form of operating and equipment grants to Dr. J. H. Masliyah and Dr. K. Nandakumar. Financial support from the Department of Chemical Engineering and the University of Alberta in the form of assistal tships, fellowships and scholarships is gratefully acknowledged.

Finally, I would like to thank my friends; it is because of them that Edmonton has been my home for the last five years.

Contents

Chapter 7
Conclusions and Recommendations   **253**

References   **257**

List of Tables

List of Figures

Nomenclature

a	width of rectangular duct	(m)
b	height of rectangular duct	(m)
c_f	LDA calibration factor, $\lambda/(2\sin(\phi/2))$	(m)
D_{pin}	diameter of the pin	(m)
Dn	Dean number, $Re/\sqrt{R_c}$	(-)
d_h	hydraulic diameter, $4*$ area/perimeter; for a square cross section $d_h = a$	(m)
f_d	measured Doppler frequency	(s^{-1})
g	gravitational acceleration	(m/s^2)
G	Görtler number, $v'_{\theta,\infty}\delta_m/\nu(\delta_m/R)^{1/2}$	(-)
L	flow development length	(m)
$\dot{m}$	mass flow rate	(kg/s)
n	number of velocity values per sample	
p',p	pressure, $p = p'/\rho\overline{v_\theta}^2$	$(kg/m\ s^2)$, (-)
r',r	radial coordinate, $r = r'/a = R_c + x$	(m), (-)
R	radius of curvataure of duct centre line	(m)
R_c	curvature ratio, R/d_h	(-)
Re	Reynolds number, $\overline{v_\theta}d_h/\nu$	(-)
Re_{pin}	Reynolds number of the pin, $v_\theta D_{pin}/\nu$	(-)

t	time	(s)
T	fundamental period of wave oscillations	(s)
v', v	velocity, $v = v'/\overline{v_\theta}$	(m/s), (–)
v'_{θ_i}	ith velocity value of a sample	(m/s)
v'_θ	mean sample velocity	(m/s)
$\overline{v_\theta}$	average streamwise velocity in duct cross section	(m/s)
$\overline{v'^2_{\theta,f}}, \overline{v'^2_{x,f}}$	amplitude of velocity fluctuations	(m^2/s^2)
$v'_{\theta,\infty}$	freestream velocity in Görtler flow	(m/s)
$v_{\theta,mn}$	measurement noise	(–)
$v_{\theta,sf}$	signal fluctuation	(–)
$v_{\theta,ti}$	turbulence intensity, $\sqrt{\overline{v'^2_\theta}}/v'_\theta$	(–)
x', x	radial coordinate with origin at duct centre, $x = x'/a$	(m), (–)
z', z	spanwise coordinate, $z = z'/a$	(m), (–)

Greek

γ	aspect ratio of a rectangular duct, b/a	(–)
δ	boundary layer thickness	(m)
η	refractive index	(–)
θ	streamwise coordinate	(–)
λ	laser light wave length	(m)
λ_G, Λ_G	spanwise wavelength of Görtler vortices	(m), (–)
μ	absolute viscosity of working fluid	(kg/m s)
ν	kinematic viscosity of working fluid	(m^2/s)
ρ	density of working fluid	(kg/m^3)
ρ_p	density of seeding particles	(kg/m^3)
ϕ	crossing angle between laser beams	(–)

Φ	Rayleigh's discriminant, $r^{-3}d(rv_\theta)^2/dr$	$(\mathrm{m^{-2}s^{-1}})$
ω	vorticity	$(\mathrm{s^{-1}})$

Subscripts

a	air
f	fluid
r	radial direction
s	solid (plexiglass)
z	spanwise direction
θ	streamwise direction

Superscripts

$'$	denotes dimensional quantity

Chapter 1

Introduction

Flow in curved pipes and ducts was initially studied for its engineering applications. Early work focussed on friction factor correlations (Adler, 1934) and heat transfer (Mori & Nakayama, 1965). The centrifugally induced secondary flow causes an increase of the friction factor and the Nusselt number, compared to a straight pipe. More recent applications include the flow of blood in the aorta (Hamakiotes & Berger, 1990), membrane filtration (Belfort *et al.*, 1993; Chung *et al.*, 1993) and the design of compact heat exchangers (Peerhossaini, 1993).

Along with the growing interest in dynamical systems and chaos theory of the past decade, an increasing number of studies on flow in curved geometries has focused on instabilities and the transition to turbulence. In closed fluid systems, the transition to turbulence often leads to chaotic behaviour (Eckmann, 1981). Examples of closed systems that exhibit chaotic behaviour are Rayleigh-Bénard convection in a horizontal fluid layer, heated from below (Gollub & Benson, 1980; Maurer & Libchaber, 1980); and Taylor-Couette flow between concentric rotating cylinders (Mullin, 1991; Pfister *et al.*, 1992). Due to a lack of feedback, dynamical systems and chaos theory does not apply to most open systems (Morkovin, 1988).

1

However, concepts of convective and global instability have proven to be very useful for explaining phenomena in open systems.

Roads to turbulence in open flow systems can be interpreted as sequences of often competing instabilities. This study focuses on the primary and secondary transitions of the flow of water in a curved duct of square cross section. In a curved square duct, the primary solution consists of two counter rotating Ekman vortices, which are the result of an imbalance between the centrifugal force and the pressure. This imbalance is created by the top and the bottom walls. The primary instability, which is of centrifugal nature, causes the development of two smaller vortices near the outer wall, called Dean vortices. These additional Dean vortices lead to a 4-cell flow state.

The 2-cell and the 4-cell flow states were studied experimentally and numerically by Bara (1991; 1992) up to a Dean number of 150. The purpose of the present study, which is a continuation of Bara's work, is to investigate developing and fully developed flow phenomena at Dean numbers higher than 150. Two new flow states were discovered experimentally, and later confirmed numerically. First, a 6-cell flow state, consisting of two Ekman vortices and two pairs of Dean vortices was observed during the steady flow development at Dean numbers between 350 and 550. Second, a traveling wave state, which is characterized by an oscillating motion of the two Dean vortices, was induced above a Dean number of 170 by inserting a horizontal pin along the symmetry line at the inlet of the curved duct. These two phenomena are the main focus of this thesis.

An overview of the literature on flow in open systems with curved geometries is presented in chapter 2. Work done on time dependent flows in curved channels and along a concave wall (Görtler flow) have been given special attention, because of the similarities with the observed traveling waves.

The experimental setup and error analysis are discussed in chapter 3. The apparatus, which was designed by Bara (1991), had a 270° long curved section with a square cross section of 1.27 cm (0.5″) and a curvature ratio, $R_c = R/d_h = 15.1$. Laser Doppler anemometry was used to measure streamwise and spanwise velocities and fluorescent dye was used for flow visualization.

In order to be able to compare the experiments with numerical simulations, velocity profiles at the inlet of the curved section were measured up to a Dean number of 600. Velocity fluctuations, which can have a large effect on the traveling wave state, were also measured. These results are presented in chapter 4.

In chapter 5, the steady flow development at Dean numbers of 272, 326, 375 and 453 is compared to numerical simulations, based on a parabolized version of the Navier-Stokes equations. Above a Dean number of 350, two pairs of Dean vortices develop near $\theta = 80°$, leading to a 6-cell flow state. The 6-cell flow breaks down symmetrically into a 2-cell state. An explanation for this transition is presented, based on the similarity with the Görtler problem.

At Dean numbers between 170 and 260, a traveling wave state was induced by inserting a pin at the inlet. In chapter 6, detailed experiments at $Dn = 220$ are compared to direct numerical simulations with the CFD package FLOW3D. The traveling wave state is very sensitive to upstream disturbances, which suggests that this state is convectively unstable. Individual modes were studied by periodically compressing one of the hoses of the flow system. This creates a periodic disturbance that the wave locks in to. The effects of the pin and the forcing were investigated in detail. Measured amplitude and phase distributions and the numerical simulations are used to analyse the structure of the traveling wave state. Symmetry arguments play an important role in this analysis. Based on the similarities with curved channel flow and Görtler flow, an instability mechanism is proposed for the transition to

wavy curved duct flow. The traveling wave state also shows similarities with sinuous oscillations in a two-dimensional wake.

The conclusions of this study are summarized in chapter 7. Also, some areas of future study are identified.

Chapter 2

Literature Review

Flow in curved ducts has been studied extensively since the early work by Williams *et al.* (1902), Eustice (1910; 1911; 1925) and Dean (1927; 1928b). Most studies were focused on engineering applications like friction factor correlations (Adler, 1934; Itō, 1959; Van Dyke, 1978; Manlapaz & Churchill, 1980; Ramshankar & Sreenivasan, 1988; Liu *et al.*, 1994) and heat transfer (Mori & Nakayama, 1965; Manlapaz & Churchill, 1981). In the last decade the emphasis has shifted towards more fundamental studies of flow development (Hille *et al.*, 1985; Yao & Berger, 1988; Bara *et al.*, 1992), transitions and bifurcation phenomena (Winters, 1987; Kao, 1992). Most recent work in this area deals with oscillatory and unsteady flows (Belaidi *et al.*, 1992; Ligrani *et al.*, 1992; Le Cunff & Bottaro, 1993). Excellent review articles on steady developing and fully developed flows in curved ducts are available by Berger *et al.* (1983), Nandakumar and Masliyah (1986), Itō (1987) and Bara *et al.* (1991; 1992).

The two main topics of this study are the development of two pairs of Dean vortices, leading to a 6-cell flow state, and the transition to a traveling wave state. Flow in a curved duct of square cross section shows similarities with a number of

5

other centrifugally unstable flow systems, in particular the flow in curved channels and flow along a concave wall (Görtler flow). These similarities have been very useful in explaining the phenomena observed in a curved square duct. This review therefore focuses on steady and time dependent developing flow in curved rectangular ducts and channels and the flow development along a concave wall.

A curved pipe has a circular cross section, while a curved duct has a square or rectangular cross section. Curved rectangular ducts with large aspect ratios (height divided by width) will be called curved channels.

2.1 Fully Developed Flow and Bifurcation Phenomena in Curved Pipes and Ducts

2.1.1 Bifurcation Phenomena in Pipes and Square Ducts

After the experiments by Eustice (1910; 1911; 1925), Dean (1927; 1928b) was the first to show theoretically the existence of one pair of counter-rotating vortices for fully developed viscous flow of a Newtonian fluid in a curved pipe. The terms fully developed, axially invariant and two-dimensional will be used interchangeably. Dean used a perturbation technique, with Poiseuille pipe flow as the leading term. He assumed a radius of curvature of the pipe that is much larger than the hydraulic diameter of the cross section. With this assumption, known as the loose coiling approximation, Dean showed that the flow is characterized by a single non-dimensional parameter, now known as the Dean number. The Dean number is defined as $Dn = Re\sqrt{(d_h/R)}$, where d_h is the hydraulic diameter of the pipe, R is the radius of curvature and Re is defined as $\overline{v_\theta} d_h/\nu$ where $\overline{v_\theta}$ is the average streamwise velocity. R/d_h is called the curvature ratio, R_c.

It wasn't until the 1950's that a perturbation analysis was done for flow in a curved duct with a square cross section. Itō (1951) and Cuming (1952) independently showed the existence of a 2-cell solution using perturbation analyses.

Series solutions obtained by perturbation analyses are only valid for relatively low flow rates. For higher Dean numbers a full numerical simulation of the Navier-Stokes equations is required. Collins and Dennis (1975) calculated a 2-cell flow in a curved pipe by solving the Navier-Stokes equations. Their results are in good agreement with the experiments by Adler (1934). Boundary layer analyses, valid for large Dean number, are discussed in detail by Berger *et al.* (1983).

Using a finite difference formulation, Cheng and Akiyama (1970) and Cheng *et al.* (1975) reproduced the 2-cell solution in a square duct. They also reported for the first time the existence of a new, 4-vortex solution. As the flowrate was increased a second counter rotating pair of vortices, smaller than the initial pair and located near the centre of the outer wall, was formed. Cheng *et al.* (1976) believed that the second pair of vortices is formed as the result of a centrifugal instability, similar to the vortices that are formed in flow between parallel curved plates (Dean, 1928a). Masliyah (1980) studied the flow in a curved duct of semicircular cross section with a flat outer wall. He showed numerically and experimentally the existence of a range of flow rates where both 2-cell and 4-cell flows are possible, a so called dual solution region. Both Nandakumar and Masliyah (1982) and Dennis and Ng (1982) discovered numerically the 4-cell flow states in a curved pipe, as well as a dual solution region.

It is well established by now that the initial pair of vortices is induced by the pressure gradients along the top and bottom walls and that the additional pair is indeed formed by a centrifugal instability. These processes will be discussed in detail in chapter 5. The large vortices induced by the lateral walls will be called Ekman

vortices and the vortices that are formed as a result of the centrifugal instability will be called either Dean, Görtler, or Taylor vortices, depending on the geometry.

Considering the non-linear nature of the Navier-Stokes equations, the existence of multiple solutions does not come as a surprise. The solution structure of fully developed or axially invariant flow is commonly represented in a bifurcation diagram, showing a characteristic quantity of the flow, e.g. friction factor, as a function of a control parameter, e.g. flow rate. A bifurcation, or state diagram can consist of a number of lines (branches) connecting different possible solutions. These branches can split (bifurcate) and show folds (multiple solutions) in limit points. The concepts and mathematical tools in this field of study have undergone significant development since the original work by Benjamin (1978). The terminology introduced by Benjamin (1978) will be followed here.

A number of studies focusing on the solution structure of curved duct flow showed that both in curved pipes and in curved square ducts dual solution regions exist (Yang & Keller, 1986; Winters, 1987; Daskopoulos & Lenhoff, 1989).

For curved pipe flow the bifurcation diagram consists of a primary branch of 2-cell flows, starting at flow rate zero and continuing up to very high flow rates. A branch of 4-cell flow solutions starts at a finite flow rate and appears to be connected to the primary branch through a pair of folds, although the upper limit point is sensitive to grid refinement and has not been determined accurately (Yang & Keller, 1986; Daskopoulos & Lenhoff, 1989). The critical Dean number above which the 4-cell solution exists increases with decreasing curvature ratio (Yanase *et al.*, 1994). Yang and Keller (1986) discovered a number of other branches with 6-cell and 8-cell flows, which are probably unstable. Yanase *et al.* (1988) calculated the linear stability of the 2-cell and 4-cell solutions. They found the 2-cell flow to be stable and the 4-cell flow to be unstable to asymmetric disturbances.

Dennis and Riley (1991) studied the 2-cell flow for the limit $Dn \to \infty$. Their results suggest the existence of an asymptotic solution consisting of an inviscid core and viscous boundary layers along the pipe wall.

Shantini and Nandakumar (1986) and Winters (1987) investigated the solution structure for the flow in a curved square duct. For a loosely coiled duct, the primary solution branch consists of 2-cell flows up to a limit point at $Dn = 131$ where the branch folds. After a second fold at $Dn = 113$ the primary branch consists of 4-cell flows. There is a dual solution region between $Dn = 113$ and $Dn = 131$. A separate, secondary, branch of 2-cell an 4-cell flows exists above a Dean number of 191. There is only a slight variation in the location of the limit points for curvature ratios above 10, but at smaller curvature ratios the limit points move to increasingly higher Dean numbers. Winters calculated the stability of the solutions and found that the 2-cell solutions on both branches are stable, while the 4-cell flow on the primary branch is unstable with respect to asymmetric perturbations. The solutions connecting the two limit points of the primary branch are unstable.

Daskopoulos and Lenhoff (1989) extended their study of fully developed flows in a loosely coiled curved square duct up to a Dean number of about 350. Starting with the 'perfect' problem of flow in an infinite curved channel, they added 'stickiness' at the cell boundaries to turn each pair of cells into a curved duct of rectangular cross section. Daskopoulos and Lenhoff imposed symmetry around the centre plane. They calculated four limit points on the secondary 2-cell branch, and found three different states with six vortices. The strength of the two additional vortices in each half of the domain is very different. One of these 6-cell states was predicted to be stable to symmetric disturbances.

Bara (1991; 1992) confirmed the solutions on the primary branch experimentally, including the dual solution region. In order to observe the 4-cell flows in

the dual solution region he inserted a pin in radial direction along the line of symmetry at the inlet of the curved section. The fact that the 4-cell flows can be observed experimentally, although they are unstable with respect to asymmetric perturbations, indicates that the growth rates of such asymmetric modes are small and that asymmetric disturbances in his apparatus were small.

Kao (1992) investigated the bifurcation structure of flow in curved ducts with 'super-circular' cross sections, in order to explain the transition of bifurcation structure with changing cross section. A super-circle is defined by $(x/a)^n + (y/a)^n = 1$ and by varying the exponent n, cross sections range between a circle ($n = 2$) and a square ($n = \infty$). The finite difference method used by Kao is not able to locate limit points accurately and because he defines the Dean number in terms of pressure gradient rather than mean velocity the results can not be compared directly. As the cross section changes from square to circular, the two limit points of the primary branch move to higher Dean number. The first limit point, above which no stable 2-cell solutions exist, moves to very high flow rates. For $n < 2.5$ this limit point is out of the range of flow rates investigated by Kao. The cross section with $n = 2.5$ is very close to circular with a ratio of large radius over small radius of 1.07. Kao (1992) also found that by inserting a splitter plate in the flow near the outer wall the 4-cell solution is stabilized with respect to asymmetric perturbations.

2.1.2   Fully Developed Flow in Rectangular Curved Ducts

Flow in curved ducts with aspect ratios (height divided by width) larger than one can be useful in interpreting flow in curved square ducts. Most numerical work was done for infinite aspect ratio curved channels (no end walls). This assumption simplifies the numerical approach by allowing spanwise periodic boundary conditions. Experimental work can not get around end wall effects, but

wall influence can be minimized by using a channel with a large aspect ratio and observing the flow away from the end walls. Some studies specifically look at the interaction between the Ekman vortices on the end walls and the internal vortices.

The Dean number for this geometry is defined as $Re\sqrt{2d/(R_i + R_o)}$, where d is the duct width and R_i and R_o are the radius of the inner and outer walls respectively. Re is defined as $\overline{v_\theta}d/\nu$ where $\overline{v_\theta}$ is the average streamwise velocity. At low flow rates the flow between curved plates is one-dimensional and strictly streamwise, similar to plane channel flow. The streamwise velocity profile is close to parabolic with the maximum shifted towards the inner wall. This flow is referred to as curved channel Poiseuille flow (CCPF).

At a critical Dean number curved channel Poiseuille flow becomes centrifugally unstable, which leads to the formation of streamwise oriented counter rotating Dean vortices. Dean (1928a) was the first to determine the onset of such two-dimensional vortices and calculated the critical Dean number. Dean's work was extended by Reid (1958), Hammerlin (1958), Sparrow (1964) and Walowit et al. (1964). Dean vortices were observed experimentally by Brewster et al. (1959) in a channel with aspect ratio 35 and curvature ratio 12.5.

More recently Finlay (1989) used a weakly nonlinear perturbation analysis to determine the nonlinear evolution of two-dimensional vortices in a curved channel with infinite aspect ratio. The vortex flow was expanded as a perturbation of one-dimensional curved channel Poiseuille flow. The results compared well with a full non-linear simulation obtained by a spectral method.

Thangam and Hur (1990) used a finite volume method to calculate the fully developed flow in rectangular ducts with aspect ratios, γ, of 1, 2, 4 and 8. They report 2-cell and 4-cell solutions for aspect ratios of 1, 2, and 4 and an 8-cell flow for a duct with an aspect ratio of 8, but did not investigate the range of possible

solutions in these geometries and their stability characteristics. Their main focus is a friction factor correlation defined in terms of a modified Dean number, Dn/γ, which is valid for $10 \leq Dn \leq 1000$ and $1 \leq \gamma \leq 8$.

Finlay and Nandakumar (1990) investigated the onset of Dean vortices in curved rectangular channels with aspect ratios ranging from 20 to 30. Using a two-dimensional finite difference method, they found that vortex pairs first appear in the centre of the channel. As the flow rate is increased, more vortices are formed towards the end walls. The large Ekman vortices near the top and bottom walls seem to have a dampening effect on the interior cells resulting in a decreasing vortex amplitude away from the centre of the channel. Amplitudes become more uniform as the flowrate is increased.

Finlay and Nandakumar attempted to model the vortex amplitude and spacing in the channel, using a Ginzburg-Landau model that was developed for Taylor-Couette flow. The model correctly describes the vortex amplitude as a function of the flow rate in the centre of the duct. However, the model fails to describe the decreasing vortex amplitude near the end walls, mainly due to the effects of the Ekman vortices. Finlay and Nandakumar point out that in Taylor-Couette flow the fluid is driven equally over the entire span by the inner cylinder and that the end vortices drive the interior Taylor vortices. In curved channel flow the streamwise pressure gradient does not drive the fluid near the end walls as effectively, resulting in much larger boundary layers. There is only a weak interaction between the Ekman vortices and the Dean vortices. The Ginzburg-Landau model did not take these wall effects into account.

2.2 Steady Developing Flow in Curved Ducts and Channels

2.2.1 Developing Flow in Pipes and Rectangular Ducts

Most of the work on developing flow has been focused on curved pipes. As was mentioned in section 2.1, the dual solution region in a curved pipe extends up to very high flow rates, so that 4-cell flows will not spontaneously develop in a curved pipe. Three different approaches have been taken in numerical investigations of developing flow in a curved pipe. Singh (1974) obtained a solution as a perturbation of developing flow in a straight tube, which is only valid very close to the inlet of a loosely coiled pipe. Boundary layer methods assume the flow to consist of an inviscid core surrounded by secondary flow boundary layers. As the flow rate increases the secondary boundary layers become thinner near the outer bend and thicker near the inner bend. The boundary layer near the inner bend eventually separates and interacts with the inviscid core. Boundary layer methods were used by Barua (1963), Yao and Berger (1975; 1988), Smith (1976), Stewartson *et al.* (1980; 1982) and Yeung (1980). Friction factor predictions based on boundary layer models agree reasonably well with experimental data.

Full numerical simulations were performed by Patankar *et al.* (1974), Humphrey *et al.* (1978; 1985), Soh and Berger (1984) and Snyder and Lovely (1990). Experimental work on curved pipes is presented by Adler (1934), Austin and Seader (1974), Agrawal *et al.* (1978), Talbot and Wong (1982), Olson and Snyder (1985) and Kluwick (1984; 1986). These studies were mainly concerned with the boundary layer development and collision near the inner bend. A detailed review of the literature on developing flow in curved pipes up to 1990 is given by Berger *et al.*

(1983) and Bara (1991).

Recently, Chung *et al.* (1993) used magnetic resonance imaging (MRI) to measure secondary flow in a curved pipe of 180°. MRI is a relatively new method to measure velocity fields non-intrusively (see the review by Caprihan and Fukushima (1990)). The measurements by Chung *et al.* compare well with the experimental results by Olson and Snyder (1985) and a numerical simulation based on Patankar's method (Patankar, 1980).

Ghia and Sokhey (1977) were the first to numerically investigate developing flow in a rectangular curved duct using an ADI finite-difference method. Aspect ratios of 0.5, 1.0 and 2.0 and curvature ratios of 3, 14 and 100 were used. In a square duct they observed a transition from 2-cell to 4-cell flow at $Dn = 143$.

Humphrey *et al.* (1977) investigated both experimentally and numerically the developing flow in a 90° bend with high curvature (curvature ratio of 2.3) at $Dn = 520$. The fully developed inlet flow was strongly influenced by elliptic effects of the downstream curved duct flow. As a result a 2-cell secondary flow was already present at the inlet plane. Secondary velocities at the inlet were up to 15% of the mean streamwise velocity, and about half the strength of secondary flow velocities at $\theta = 90°$. Both experimentally and numerically only a 2-vortex flow was observed.

Taylor *et al.* (1982) extended the work by Humphrey *et al.* (1977) experimentally. They studied both laminar and turbulent flow at Dean numbers of respectively 520 and 26,000. At $Dn = 520$ the highest secondary flow velocities were observed at $\theta = 60°$ with values of the order of 0.6 $\overline{v_\theta}$. They also observed only a 2-vortex flow.

Yee *et al.* (1980) also investigated the developing flow in a 90° bend with a curvature ratio of 2.3, using both a fully elliptic and a parabolic formulation. This study included heat transfer. They conclude that in this strongly curved channel a

fully elliptic formulation is necessary in order to describe the flow accurately.

The 4-cell flow pattern in a square duct was observed experimentally by Sugiyama et al. (1983). They studied the flow development in curved rectangular ducts with aspect ratios ranging from 0.5 to 2.5 and curvature ratios between 5 and 8. Photographs of smoke flow visualization in air were taken at the exit of the $180°$ ducts. In the square duct they observed a 2-cell state at $Dn = 93$, a developing 4-cell state at $Dn = 139$ and a fully developed 4-cell state at $Dn = 183$. At higher flow rates the smoke visualization pictures are very hard to interpret, but it looks like 2-cell states have developed for Dean numbers of 383 and 527. At aspect ratios of 2.0 and 2.5 Sugiyama et al. (1983) observe the development of two pairs of Dean vortices along the outer wall of the duct, leading to 6-cell flow states.

Hille et al. (1985) studied the flow in a $180°$ bend with a curvature ratio of 6.45 using laser-Doppler anemometry. They observed a 4-cell flow for Dean numbers between 150 and 300. The second pair of vortices was asymmetric and smaller than the ones observed by Sugiyama et al. (1983). The additional vortices formed between $\theta = 108°$ and $\theta = 171°$ with the flow still developing at the end of the $180°$ bend. Hille et al. observed a smooth transition between 2-cell and 4-cell flows without a dual solution region.

Soh (1988) simulated the flow development in the geometry used by Hille et al. (1985) using a fully elliptic formulation of the steady Navier-Stokes equations. They found that for $116.5 < Dn < 130.2$ the flow developed into one of two solutions, depending on the inlet condition. For a free vortex inlet the flow developed into a 4-cell state with a strong second vortex pair, much like the 4-cell state calculated by Winters (1987). With a fully developed one-dimensional inlet flow a 4-cell state with a much weaker second vortex pair developed. Both 4-cell flows appeared to be fully developed. The weak 4-cell state has not been observed by any other researchers,

and may have been an artifact of the coarse grid used by Soh (1988).

Sankar *et al.* (1988) solved a parabolized version of the steady three-dimensional Navier-Stokes equations to investigate the flow development in a curved square duct using Patankar's method (Patankar, 1980). For a curvature ratio of 100 and Dean numbers up to 128 the flow developed into the familiar 2-cell solution. For $128 < Dn < 200$ initially a 4-cell state was formed, but periodic spatial oscillations between 2-cell and 4-cell states developed farther downstream. During these spatial oscillations a pair of Dean vortices is periodically formed and destroyed. Sankar *et al.* related the development of the oscillations to asymmetries in the flow.

Sugiyama *et al.* (1988) performed another, more rigorous, study of developing flow in a 270° curved rectangular duct with an aspect ratio of 2.0 and a curvature ratio of 8. In this study they used smoke visualization in air and a one component laser-Doppler anemometer to measure all three velocity components. Both the flow visualization and the velocity measurements show the development of two pairs of Dean vortices. The onset of these vortex pairs takes place around $\theta = 135°$. Profiles of the s eamwise velocity in the spanwise centre plane show two regions of low streamwise velocity, corresponding to the two inflow regions of the vortex pairs. These inflow regions transport fluid with low streamwise velocity from the outer wall towards the centre of the channel. As the two additional vortex pairs grow in strength they also move apart towards the top and bottom corners along the outer wall. At $\theta = 270°$ the two Dean vortex pairs have folded up into the two large Ekman vortices, resulting in a 2-cell flow. There seems to be some discrepancy between the results from flow visualization and the LDA at $\theta = 225°$ and $\theta = 270°$, but this could be due to the inherent difficulties with the interpretation of smoke visualization.

In a related study, Miyake *et al.* (1988) and Kajishima *et al.* (1989) solved the

elliptic Navier-Stokes equations using a finite difference method. Their simulation of developing flow in a curved duct with an aspect ratio of 2 shows the development of two pairs of Dean vortices and is in qualitative agreement with the experiments by Sugiyama *et al.* (1988). Miyake *et al.* also simulated smoke or dye flow visualization patterns for this geometry, but the calculated patterns do not show the four Dean vortices.

Finlay *et al.* (1993) recently investigated the interpretation of flow visualization numerically. They compared numerically simulated smoke or dye patterns with calculated spatially developing secondary flow patterns in curved channel flow, Görtler flow and twisted square duct flow. Finlay *et al.* found that smoke or dye visualization can represent the secondary flow patterns correctly if the streamwise variation of the secondary flow is small. However, secondary flow that changes quickly with streamwise position can be misrepresented by smoke or dye.

The most complete study of developing flow in a curved square duct for Dean numbers up to 150 was performed by Bara (1991; 1992). He investigated both experimentally and numerically the flow in a 270° curved square duct with a curvature ratio of 15.1. Both laser-Doppler anemometry and dye flow visualization in water were used in the experimental investigation. At $Dn = 125$ the flow reaches a fully developed 2-cell state while at $Dn = 150$ a fully developed 4-cell state develops. At intermediate flow rate ($Dn = 137$) the flow develops towards a 4-cell state, but is still developing at the end of the 270° duct. An important characteristic of 4-cell flow is the inflow region in the centre of the outer wall where the streamwise velocity is relatively low. Bara shows both numerically and experimentally that the length to reach a fully developed 4-cell state (development length) decreases with increasing flow rate.

Bara (1991; 1992) observed for the first time the dual solution region predicted

by Winters (1987). By inserting a pin along the symmetry line at $\theta = 5°$ a 4-cell flow state was induced for Dean numbers between 114 and 131. Without the pin 2-cell flows were observed in this region. At higher flow rates the pin reduces the development length of the 4-cell flow. Although the 4-cell flow is unstable with respect to asymmetric perturbations, they can be observed if asymmetries in the apparatus are small. By disturbing the flow asymmetrically the 4-cell state was found to break down.

The experimental results were in good agreement with the numerical predictions calculated using the developing flow code by Sankar *et al.* (1988) and the fully developed flow code by Shantini and Nandakumar (1986). The results were also consistent with the predictions by Winters (1987). The experimental apparatus used by Bara (1991; 1992) did not extend far enough to confirm the spatial oscillations predicted by Sankar *et al.* (1988). Considering that no unconditionally stable solutions exist in a range above $Dn = 131$ and that the code by Sankar did not include time dependence, Bara speculates that time-dependent solutions may develop for higher flow rates, possibly even in the same apparatus.

Arnal *et al.* (1992) studied the developing flow in a 180° curved square duct with a curvature ratio of 3.36. They measure the development of the streamwise velocity at the symmetry line for a Dean number of 764. The measured profiles compare well with finite difference elliptic calculations. The model shows the development of two pairs of Dean vortices near the outer wall at $\theta = 135°$. The arrows in their figures 4 and 5, showing the secondary velocities at $\theta = 45°$ and $\theta = 135°$, are pointing in the opposite direction of the flow. Arnal *et al.* (1992) also observed low frequency oscillations, which will be discussed in section 2.3.1.

2.2.2 Developing Flow in Curved Channels

In the past decade a growing amount of work has been done on curved channel flow. Kelleher *et al.* (1980) studied experimentally the flow of air in a 180° curved channel with an aspect ratio of 40 and a curvature ratio of 47.5. They used both flow visualization with aerosol and a hot wire anemometer to measure streamwise velocities at $\theta = 135°$. At Dean numbers between 78.8 and 112.8 the flow develops a spanwise periodic series of counter-rotating vortices that cover the full width of the channel. These Dean vortices are the result of a centrifugal instability, very similar to the mechanism that creates the Dean vortex pair in a square duct.

Kelleher *et al.* (1980) measured streamwise velocity profiles at $\theta = 135°$ and different spanwise positions in the outer half of the channel. Close to the outer wall these profiles show periodic minima. Kelleher *et al.* interpreted these minima as corresponding to the cores of the Dean vortices. However, this interpretation is not consistent with the findings of Sugiyama *et al.* (1988) and Bara *et al.* (1992) who both find minima in the streamwise velocity to correspond to the inflow regions between two vortices.

Kelleher *et al.* mention that for higher flow rates ($Dn = 250$) time-dependent flows were observed consisting of streamwise periodic traveling waves superimposed on the Dean vortices. They do not explore this area further. Traveling wave phenomena will be discussed in more detail in section 2.3.

Developing flow of air in a curved channel was investigated both numerically and experimentally by Bottaro *et al.* (1991). The experimental setup consisted of a 270° curved channel with an aspect ratio of 29 and a straight inlet section to ensure fully developed inlet flow. They measured the streamwise velocity in cross sections using a hot wire anemometer and defined a perturbation velocity as the streamwise velocity of curved channel Poiseuille flow subtracted from the streamwise velocity

of vortex flow. Contour plots of the perturbation velocity clearly show the shape of the Dean vortices and compare well with results from a three-dimensional time-dependent simulation, although in the simulation the vortices develop 40° farther downstream. The computational domain had an aspect ratio of 9 in order to allow for a natural development of the spanwise wave number. The cross-sectional averaged streamwise perturbation velocity increases initially linearly and after reaching a maximum settles at a steady value; the vortices seem to reach a fully developed state. Vortex merging and splitting events were observed farther downstream, both experimentally and numerically.

Matsson and Alfredson (1992) present more experimental results on developing steady and unsteady curved channel flow, using the same apparatus used by Bottaro et al. (1991). They studied the flow development at Dean numbers of 73, 88 and 116 and show that the development length of the Dean vortices reduces with increasing flow rate. Spanwise profiles of the streamwise velocity show minima at the inflow regions between vortex pairs, which is consistent with results from Sugiyama et al. (1988) and Bara et al. (1992). Their unsteady results will be discussed in section 2.3.

A full three-dimensional time dependent elliptic simulation of developing vortices in a curved channel was performed by Bottaro (1993). The channel had a curvature ratio of 38 and an aspect ratio of 9, allowing for vortex splitting and merging events. He stresses the importance of inlet-outlet boundary conditions when simulating convectively unstable flows such as curved channel flow. In convectively unstable systems the flow phenomena are determined by disturbances that are convected through the system. By imposing periodic boundary conditions disturbances are continuously fed back to the inlet of the domain, that way destroying the convective nature of the flow. When specifying inlet-outlet boundary conditions, care should be taken in specifying the outlet flow condition in order to minimize numerical

reflections back into the computational domain.

Bottaro (1993) found that if a stationary disturbance is imposed at the inlet of the channel, steady Dean vortices develop, which may merge or split steadily farther downstream. Bottaro used steady Dean vortices in their early linear stage as inlet flow. When fluctuating disturbances are present at the inlet, the Dean vortices are not locked into place and unsteady interactions between neighbouring vortex pairs may take place. Bottaro observed fluctuating inlet conditions as a result of pressure waves that are transmitted from the computational domain to the inlet boundary. This situation is called self-excitation. Unsteady inlet fluctuations could also be imposed externally. Above a critical Dean number traveling waves could develop in the flow, but these were not observed by Bottaro because of a low amplification of initial disturbances.

Guo and Finlay (1991) studied the stability of two-dimensional Dean vortices in a curved channel with respect to spanwise perturbations using a temporal formulation. This spanwise secondary instability or Eckhaus instability leads to splitting and merging of vortex pairs. Guo and Finlay used linear stability theory to calculate the Eckhaus stability boundary, within which Dean vortices are stable to spanwise perturbations. If the spanwise wave number is larger than the stable region two vortex pairs will merge. A vortex pair will split in two vortex pairs if the wave number is smaller than the stable region. For $Re > 1.5Re_c$ all spanwise wavenumbers are unstable to spanwise perturbations. Their results were confirmed by nonlinear flow simulations. It is clear that the spanwise secondary instabilities are of fundamental importance in the wave number selection process.

In a later study Guo and Finlay (1994) used spatial stability theory and three-dimensional simulations to study the spanwise secondary instability of Dean and Görtler vortices. Results from a spatial formulation are easier to compare with

spatially developing experimental observations. They used a Legendre spectral-element method to solve the same version of the parabolized Navier-Stokes equations that was used by Bara *et al.* (1992). Spanwise periodicity was imposed over a few vortices, allowing vortex splitting and merging to occur naturally.

Linear stability results show that in the linear growth phase wavenumber selection is determined by growth rates of the primary instability. Several wavenumbers can grow independently. Once the dominant wavenumber reaches the nonlinear phase it becomes unstable to spanwise secondary instabilities. Farther downstream the energy from other wavenumbers is transferred to these spanwise secondary instabilities. Eventually those wavenumbers with the lowest growth rate of spanwise secondary instability will be observed. The three-dimensional nonlinear simulations show that spanwise secondary instabilities lead to vortex splitting and merging.

2.3 Time Dependent Flow in Curved Geometries

This thesis presents the first experimental and numerical evidence of a secondary transition in curved square duct flow leading to traveling waves. This time-dependent flow is characterized by periodically oscillating Dean vortices. Although some experimental work has been reported on oscillatory flow in curved pipes and square ducts, sustained oscillations of the Dean vortices have not been reported before. However, oscillating vortices have been observed both experimentally and numerically in curved channel flow, as well as in boundary layer flow along a concave wall (Görtler problem). The oscillations in a curved square duct show strong similarities with these other geometries.

2.3.1 Time Dependent Flow in Pipes and Rectangular Ducts

Taylor (1929) already observed non-turbulent oscillations of 2-cell flow in a helical pipe using dye visualization. The oscillations were observed at flowrates between steady laminar and turbulent flow. Sinusoidal oscillations near the inner wall of a helical pipe were also observed by Sreenivasan and Strykowski (1983).

Oscillations in a helical pipe were studied in more detail by Webster and Humphrey (1993). They observed low frequency oscillations near the inner wall of a helically coiled pipe with curvature ratio 9.1. Webster and Humphrey measured streamwise and spanwise velocities along the horizontal symmetry plane using a laser-Doppler anemometer. Oscillations with a frequency around 1 Hz were observed for Dean numbers between 1680 and 2100. At some positions along the symmetry plane a frequency doubling takes place which Webster and Humphrey could not explain. It is suggested here that the frequency doublings could be the result of an inaccurate positioning of the measuring volume. The oscillations presented in chapter 6 of this thesis show a frequency doubling very close to the symmetry line of the duct. It will be explained in section 6.5.2 that this frequency doubling is a direct result of the shift-and-reflect symmetry of the flow. Similar symmetry properties could explain the frequency doublings observed by Webster and Humphrey (1993). Webster and Humphrey suggest that the oscillations are the result of an instability of the secondary flow jet coming off the centre of the inner wall. This jet is formed when the boundary layers along the top and bottom walls collide in the centre of the inner wall.

A number of authors have recently reported on flow oscillations in curved square and rectangular ducts. Tsuda and Ohba (1984) and Ohba et al. (1986) studied the

developing flow in a 180° curved square duct with curvature ratio 9.5. Measuring the streamwise velocity with a laser-Doppler anemometer, they observed instantaneous velocity doublings and halvings at Dean numbers of 217 and 435. These irregular oscillations with a frequency of about 3 Hz occurred at the spanwise centre line, about halfway between the centre and the lateral walls. Tsuda and Ohba could not explain the observed phenomena and the physical impossibility of such instantaneous velocity doublings are a reason to question their experimental method.

Belaidi *et al.* (1992) studied the flow in a tightly coiled 90° bend with aspect ratios of 0.5 and 0.25 and a curvature ratio of one. They measure streamwise velocities along the line of symmetry at different streamwise positions and observe flow oscillations near the inner wall of the duct at a frequency of around 25 Hz. The oscillations seem to be associated with an instability of the secondary flow jet.

Arnal *et al.* (1992) report low frequency oscillations of developing flow in a 180° curved square duct with a curvature ratio of 3.36 at a Dean number of 764. As was reported in section 2.2.1, two pairs of Dean vortices develop at this flow rate. Irregular oscillations with a frequency around 0.1 Hz developed at $\theta = 135°$. Measurements were taken at the symmetry line near the outer wall. Arnal *et al.* attempted to simulate these oscillations using a time dependent elliptic calculation procedure. An antisymmetric perturbation of 2.5% of the fully developed steady flow was imposed at the inlet. This perturbation was convected downstream, but resulted in much lower fluctuation amplitudes than experimentally observed. This discrepancy is possibly due to the relatively coarse grid of 30x30 points that was used. Arnal *et al.* interpret the observed oscillations as random perturbations that are amplified by the flow.

2.3.2   Time Dependent Flow in Curved Channels

Flow oscillations in a curved channel were first observed experimentally by Kelleher et al. (1980), although their study was focused on steady, low Reynolds number flow. Their channel had an aspect ratio of 40 and a curvature ratio of 47.5. They report that "observations of the flow patterns at much higher Reynolds number (of the order of 1700) indicated that the flow took on a streamwise periodicity in the form of longitudinal waves superimposed on the secondary flow which would travel down the vortices in direction of flow". These traveling waves have been studied extensively since 1988 and some of the results have been helpful in explaining the traveling wave phenomena in a curved square duct.

Ligrani and Niver (1988) investigated flow oscillations in the geometry used by Kelleher et al. (1980) scaled by 200%. Due to the larger scale, these experiments may have been more sensitive to disturbances. Using smoke visualization, Ligrani and Niver observed mainly radial oscillations of the Dean vortices at Dean numbers between 73 and 100. During radial oscillations the heights of vortex pairs vary while the radial positions of the two vortices are in phase. Since Dean vortices are initiated by unsteady disturbances, the initial streamwise positions of the vortices vary with time. Therefore, vortex pairs will be at different and changing stages of their development at certain streamwise positions, creating an impression of radial oscillations.

Twisting vortices were observed for $100 < Dn < 200$ and streamwise positions of at least 95° from the inlet of the curved section. Twisting vortex pairs oscillate again mainly in the radial direction but this time the radial positions of the two vortices are out of phase. Ligrani and Niver (1988) identified a number of other oscillating modes as well as unsteady splitting and merging of Dean vortices.

The first numerical study of traveling waves in curved channel flow was conducted

by Finlay *et al.* (1987; 1988). They used a three-dimensional time dependent pseudospectral method with both streamwise and spanwise periodicity. Two types of traveling waves were discovered: long wavelength undulating waves and short wavelength twisting waves. Both modes are sinuous and have shift-and-reflect symmetry: the flow field is invariant over a reflection in the centre plane, combined with a spatial shift over half a streamwise wavelength.

Undulating waves show similarities with wavy Taylor vortices. At a curvature ratio of 39.5 and a spanwise wavenumber ($\alpha = \pi d / \lambda$) of 2.5 the onset of undulating vortices takes place at $Re = 1.2Re_c$ where Re_c is the Reynolds number where curved channel Poiseuille flow becomes unstable to Dean vortex flow. Onset of twisting vortices is at $Re = 1.96Re_c$ and their growth rate is higher than that of the undulating mode for $Re > 2.11Re_c$. Although these periodic flow oscillations are not axially invariant or two-dimensional, they are in a sense 'fully developed'. This periodic flow will be called the fully developed wave state.

Other differences between undulating and twisting vortices are their development lengths and spanwise amplitude of the oscillations. Undulating waves take more than one circumference to reach a fully developed state, making it difficult to observe them experimentally. Twisting waves develop in less than half this distance. In the undulating wave mode the spanwise locations of the vortex centres oscillate considerably, while in the twisting wave mode the spanwise amplitude is small. The spanwise oscillation of the undulating waves is also called sideslipping and it is one of the most characteristic features of undulating waves. In the twisting wave mode the directions of the inflow jets oscillate while the spanwise positions of the jets at the outer wall move little. By comparing the features of the wavy flow states, Finlay *et al.* suggest that Kelleher *et al.* (1980) observed twisting vortices.

Finlay *et al.* (1988) propose that twisting vortices are the result of a shear

instability that is caused by inflectional spanwise profiles of the streamwise velocity. These inflectional profiles are created by the inflow jets along the outer wall, which move fluid with low streamwise velocity away from the wall. Finlay *et al.* use an Orr-Sommerfeld analysis to calculate linear growth rates of the shear instability. The fastest growing modes have short wavelengths in the same range as twisting vortices, suggesting that the shear instability causes twisting vortices.

Bland and Finlay (1991) extended the numerical investigation of unsteady curved channel flow and discovered a three-frequency flow at $Re = 8.84Re_c$ for a curvature ratio of 7.5 and a spanwise wave number of 2.5. In this flow the traveling wave is modulated by two nonpropagating oscillations at incommensurate frequencies. These two frequencies became phase locked at $Re = 10.10Re_c$, leading to a two-frequency modulated wave similar to that observed in Taylor-Couette flow. Since these computations are based on spanwise periodicity, experimental verification of these flows will be difficult.

Matsson and Alfredsson (1990) studied the flow in a curved rotating channel. The flow phenomena in a rotating straight channel are very similar to those observed in a curved channel. In a rotating channel the transitions are induced by an imbalance between Coriolis forces and pressure, rather than centrifugal forces and pressure (see for example Finlay, 1989). Without channel rotation Matsson and Alfredsson observed experimentally that the development length for both steady and wavy Dean vortices decreases with increasing flowrate. Both a linear stability analysis and experiments showed that depending on the direction of rotation the Coriolis effects either counteract or enhance centrifugal effects. When centrifugal and Coriolis effects almost cancel the flow transitions to steady and wavy Dean vortices can be substantially delayed.

Matsson and Alfredsson (1992) used a hot wire anemometer to study twisting

vortices in a curved channel with an aspect ratio of 29 and a curvature ratio of 38.5. The streamwise wavelength of the observed twisting vortices is close to the spanwise wavelength and the wave speed is about 80% of the bulk velocity. The nondimendional frequencies of the streamwise velocity fluctuations at Dean numbers of 160 and 235 collapse close to $fd/\overline{v_\theta} = 1$. The first harmonic was clearly present. Matsson and Alfredsson show that the amplitude of the streamwise velocity fluctuations is highest near the inflow regions between two Dean vortices. Drawing an analogy with Görtler flow (Yu & Liu, 1991), they suggest that it is the spanwise inflectional profile of the streamwise velocity that drives the secondary instability.

Experimental evidence for undulating Dean vortices was first reported by Ligrani et al. (1992), using the same apparatus as Ligrani and Niver (1988) (aspect ratio 40, curvature ratio 47.5). Ligrani et al. measured the three mean velocity components using a five-hole pressure probe and used these data to calculate vorticity profiles. In addition smoke flow visualization was used. Experimental results for both undulating and twisting vortices were compared to the simulations by Finlay (1988) and showed generally good agreement.

Ligrani at al. (1992) observed undulating vortices for $1.1Re_c < Re < 3.4Re_c$. Onset of undulations is in good agreement with linear stability analysis. The two principal characteristics of simulated undulating waves, long spanwise wavelength and spanwise oscillation (sideslipping) were clearly observed. However, the frequency of the oscillations was lower than that predicted from the linear stability analysis. This discrepancy is possibly due to the fact that the linear stability analysis is only valid for fully developed vortices, while in the experiment the vortices are still developing when they become unstable to undulating waves. Frequency spectra of the streamwise velocity show a broadband peak around 1-2 Hz. The experimentally observed undulating waves are sometimes interrupted by

vortex splitting and merging or other convected disturbances.

Twisting vortices were observed by Ligrani $et\ al.$ for $3.5Re_c < Re < 5.0Re_c -$ $5.4Re_c$ although linear stability analysis predicts the onset of twisting vortices to take place at $Re = 2.11Re_c$ (Finlay $et\ al.$, 1988). This difference may again be due to the assumption of fully developed flow that was made in the simulations. Frequency spectra are again broadband with maxima in the 70-100 Hz range. Contour plots of time averaged streamwise velocity, streamwise vorticity, radial vorticity and spanwise vorticity are in good agreement with the simulations.

Ligrani $et\ al.$ (1992) propose the following scenario for the transition to turbulent flow in a curved channel: after the transitions to Dean vortex flow and twisting Dean vortices the regions with high velocity fluctuations (initially the inflow regions near the outer wall) merge together to form a fully turbulent flow.

Undulating Dean vortices in a curved channel were also observed experimentally by Matsson and Alfredsson (1993a) using a hot wire anemometer. The 270° duct had an aspect ratio of 29 and a curvature ratio of 38.5 (see Matsson and Alfredsson, 1992). At 4.5 times the critical Dean number for transition to steady Dean vortices the frequency spectrum of the streamwise velocity shows two broad peaks, one around 8 Hz that is associated with long undulating waves and one around 135 Hz associated with twisting waves.

Contour plots of the filtered streamwise velocity fluctuations for both modes show that velocity fluctuations of twisting waves are located near the minimum of the perturbation velocity (in the inflow region between two vortices, about a third channel width from the outer wall). However, because twisting waves are shift-and-reflect symmetric, a minimum in the velocity fluctuations is expected at the centre line. Two separate maxima have indeed been observed at positions further upstream (Alfredsson, private communication). The shift-and-reflect symmetry has also been

confirmed by velocity traces (Matsson & Alfredsson, 1993b). Streamwise velocity fluctuations of the undulating waves are highest near the two regions with spanwise infection of the streamwise velocity (to the sides of the inflow region, about a fifth channel width from the outer wall).

The time-averaged streamwise perturbation velocity is a measure of the amplitude of the steady component of the developing Dean vortices. It reaches a steady value after an initial linear growth phase, very similar to that observed for steady Dean vortices (Bottaro et al., 1991). Matsson and Alfredsson (1993a) found that the streamwise development of the amplitude of the oscillatory component associated with twisting Dean vortices shows a very similar trend, with the maximum at the same streamwise position as the steady component. This demonstrates that the wavy mode develops parallel to the development of steady Dean vortices and that it is not fully developed Dean vortices from which the wavy mode develops.

Le Cunff and Bottaro (1993) investigated the nature of the transitions to twisting and undulating waves in curved channel flow. They performed linear stability analyses of one-dimensional streamwise velocity profiles and extrapolated the results to three-dimensional flow situations. Le Cunff and Bottaro study the stability of streamwise and spanwise profiles obtained from a full numerical simulation of steady developing Dean vortices (Bottaro, 1993). Both these profiles have inflection points, although the inflection of the spanwise profiles is much more pronounced. Their results show that twisting waves are the result of a shear instability of spanwise profiles of the streamwise velocity. The predicted frequencies, wavelengths and wave velocities compare well with previous results (Finlay et al., 1988; Ligrani et al., 1992). For twisting waves it is always the sinuous mode that is more unstable than the varicose mode. These results are qualitatively similar to the stability analyses of a single wake profile by Sato and Kuriki (1961) and Mattingly and Criminale (1972).

They conclude that undulating waves are probably related to normal distributions of the streamwise velocity and that this instability is of centrifugal nature.

2.3.3 Developing Flow along a Concave Wall (Görtler flow)

Boundary layer flow over a concave wall was named after H. Görtler, who first studied this problem in the 1940s (Görtler, 1940; Görtler, 1941). The main difference between Görtler flow and Dean flow is that Görtler flow is a boundary layer phenomenon and therefore never reaches a fully developed state; the boundary layer keeps growing and eventually breaks down into turbulence. The dynamic parameter for this problem is the Görtler number, $G = v'_{\theta,\infty}\delta_m/\nu\sqrt{\delta_m/R}$, where $v'_{\theta,\infty}$ is the freestream velocity and δ_m is the momentum thickness of a Blasius boundary layer at a distance $R\theta$ from the leading edge. G increases with downstream position.

Görtler flow experiments are often performed in geometries that are very similar to those used for curved channel flow. Swearingen and Blackwelder (1987) for example used a channel with aspect ratio 8 and curvature ratio 21. The sidewall boundary layers are removed through a suction slot just before the leading edge of the curved section. The effect of the inner wall can be limited by ensuring that the boundary layer thickness is much smaller than the channel width, for example by using air at high flow velocities.

The phenomena observed in Görtler flow are very similar to what was discussed for curved channel flow, except that now the flow keeps developing until turbulent breakdown of the boundary layer. At very low Görtler number (close to the leading edge) a one-dimensional developing boundary layer flow is found, very similar to a developing Blasius boundary layer. At a critical G a transition to steady streamwise

counter-rotating Görtler vortices takes place as the result of a centrifugal instability. The dimensionless spanwise wavelength Λ_G is defined as $\Lambda_G = v'_{\theta,\infty}\lambda_G/\nu\sqrt{\lambda_G/R}$, where λ_G is the dimensional spanwise wavelength. Park and Huerre (1988) showed that this primary instability in the Görtler problem is convective, which means that Görtler vortices are likely to be very sensitive to upstream perturbations.

Farther downstream (higher G) time dependence appears in the form of traveling waves superimposed on the Görtler vortices. The amplitude of the traveling waves keeps growing until the boundary layer breaks down into turbulence. The literature on Görtler flow was recently reviewed by Floryan (1991). Only a short review of some of the more recent work will be given here.

Bippes and Görtler (1972) triggered the onset of Görtler vortices with a series of lengthwise heating elements in the wall, which induced secondary circulation. Spanwise oscillations of Görtler vortex pairs developed with the two vortices oscillating in phase (sinuous mode). Turbulent breakdown was observed farther downstream. Bippes (1972) imposed random disturbances at the inlet and found the dimensionless wavelengths of the naturally occurring Görtler vortices to be around $\Lambda_G = 210$. This is in very good agreement with the linear stability result by Floryan and Saric (1984). In Bippes' experiments curved plates are towed in a water tank.

Ito (1980; 1985) observed a different mode of oscillations: a varicose mode with two Görtler vortices oscillating out of phase. Because no external perturbation was imposed, the flow development is the result of amplified random disturbances in the flow. This caused the Görtler vortex pairs to develop time dependence at varying streamwise positions. Görtler vortex pairs seem to be connected periodically by horseshoe shaped vortices. Ito also measured spanwise and normal profiles of the streamwise velocity with a hot wire anemometer; both are inflectional. Spanwise profiles of the streamwise velocity show minima near the inflow region between two

counter-rotating vortices, very similar to observation by Sugiyama *et al.* (1988) and Bara *et al.* (1992) in a curved duct. The inflow regions move fluid with low streamwise velocity away from the outer wall.

Aihara and Koyama (1981) also observed the varicose mode of the traveling waves and horseshoe shaped vortices connecting two Görtler vortices periodically. They suggest that the inflectional normal profiles are subject to a Kelvin-Helmholtz instability, which generates periodic spanwise vortices. These vortices are bent into a horseshoe shape due to the rotating action of the original Görtler vortices.

Blackwelder (1983) compared the transitions in Görtler flow with phenomena observed in transitional and turbulent flat plate boundary layers. In these boundary layers streamwise vortices followed by oscillations have been observed that are very similar to Görtler vortices.

Swearingen and Blackwelder (1987) investigated the structure of Görtler vortices in more detail using multi-probe hot wire anemometers and a smoke-wire visualization technique. Their channel had an aspect ratio of 8 and a curvature ratio of 21. The boundary layers were removed by suction just before entering the curved section. Because naturally occurring disturbances were used to generate Görtler vortices, oscillations develop at different streamwise positions. Both sinuous and varicose modes were observed, although the sinuous oscillation mode was most often found.

The naturally occurring spanwise wavenumber Λ_G is near 670. Although this is higher than the result by Bippes (1972), who found $\Lambda_G = 210$, it is within the region where an amplified disturbance is predicted by Floryan and Saric (1982) and Hall (1983) based on linear theory. Guo and Finlay (1994) suggest that the larger wavelengths observed by Swearingen and Blackwelder (1987) may be the result of flow restrictions imposed by the inner wall and possibly a small misalignment of the

experiment. Bippes used a curved plate towed in a ·· ·ter tank rather than a curved channel.

Swearingen and Blackwelder measured streamwise velocity profiles in the spanwise and normal direction. In the normal direction the streamwise velocity becomes strongly inflectional with S-shaped velocity profiles. Spanwise velocity profiles are also inflectional and show minima near the inflow regions. Swearingen and Blackwelder note a similarity between the spanwise velocity profiles and a typical unstable plane-wake profile (see for example Sato and Kuriki, 1961). It was shown by Mattingly and Criminale (1972) that these profiles are unstable to transverse oscillations and that the sinuous mode is always more unstable than the varicose mode. The similarity suggests that a similar free-shear-layer-type instability mechanism might cause the sinuous oscillations of Görtler vortices.

Contour plots of streamwise velocity fluctuations show maxima on either side of the inflow regions. The locations of these maxima correspond very well to the regions with high spanwise shear, where spanwise velocity profiles are inflectional. These results show that the developing oscillations are indeed the result of inflectional spanwise profiles of the streamwise velocity. Similar results were obtained numerically by Le Cunff and Bottaro (1993) for the onset of twisting vortices in curved channel flow (section 2.3.2). It follows that Görtler vortices do not directly break down to turbulence. Instead, they set up a flow field that is unstable to secondary instabilities (oscillations) that ultimately lead to turbulence.

Swearingen and Blackwelder (1987) also introduced a periodic acoustic disturbance into the developing flow. The flow oscillations were found to lock in to the forcing frequency between 70 Hz and 200 Hz. At lower forcing frequencies the oscillations locked in to the first harmonic of the forcing. Streamwise velocity fluctuations were measured using a rake of 12 hot wire sensors. Results show a 180°

phase difference between velocity fluctuations on either side of a low-speed inflow region, which corresponds to the sinuous mode of oscillation. In the centre of a low-speed inflow region a frequency doubling was observed. This behaviour is very similar to that of a two-dimensional wake (Sato & Kuriki, 1961).

Peerhossaini and Wesfreid (1988) used a laser light sheet to visualize cross sections of developing flow in a curved duct with aspect ratio 2 and curvature ratio 1.5. Typically two to four pairs of Görtler vortices were observed. Peerhossaini and Wesfreid observe two different oscillating modes. Because of the small aspect ratio of the duct, the end walls could have significant effect on the flow. The study was continued by Petitjeans (1992; 1993)

Yu and Liu (1991) calculated the growth rates of sinuous and varicose oscillations of Görtler vortices using a three-dimensional analysis. They show that the sinuous mode grows faster than the varicose mode, which is in agreement with the observations by Swearingen and Blackwelder (1987). A contour plot of the calculated streamwise velocity fluctuations of the sinuous mode corresponds well with the measured fluctuations by Swearingen and Blackwelder. The calculated streamwise velocity fluctuations of the varicose mode correlate well with the shear in the normal direction, measured by Swearingen and Blackwelder. This might suggest that the varicose mode is a result of inflectional profiles in the normal direction, in agreement with the mechanism that was proposed by Aihara and Koyama (1981)

The spatial development of non-linear Görtler vortices was simulated by Lee and Liu (1992) They solved the three-dimensional parabolized Navier-Stokes equations with periodic boundary conditions in the spanwise direction using Patankar's method (1980). Their results are in good agreement with experiments by Swearingen and Blackwelder (1987).

Liu and Domaradski (1993) extended simulations of Görtler vortices to the

turbulent regime. They solved the three-dimensional Navier-Stokes equations with periodic boundary conditions in both spanwise and streamwise directions using a pseudospectral numerical method. Görtler vortices developed from imposed random noise. The time-evolving solutions were converted into spatially developing ones by means of a convection velocity. Although this method has been used successfully, the selection of a suitable convection velocity is often rather arbitrary, as was pointed out by Floryan (1991). The simulations agree well with the experiments by Swearingen and Blackwelder (1987).

Liu and Domaradski performed stability analyses of various one-dimensional streamwise velocity profiles in the spanwise and normal direction. They show that the sinuous mode is the result of inflectional spanwise velocity profiles and that the inflectional normal velocity profiles are responsible for the varicose mode of oscillations. Liu and Domaradski confirm numerically the observation by Swearingen and Blackwelder (1987) that the highest streamwise velocity fluctuations correspond to the regions with high spanwise shear. An analysis of the kinetic energy balance shows that turbulence production is also mainly associated with the spanwise shear.

2.4 Summary

Winters (1987) calculated the two-dimensional solution structure for flow in a curved square duct. For a loosely coiled duct, the main branch consists of 2-cell flows up to a first fold at $Dn = 131$. After a second fold at $Dn = 113$, the main branch consists of 4-cell flows, which are unstable to asymmetric perturbations. There is a dual solution region between $Dn = 113$ and $Dn = 131$. No stable solutions exist between Dean numbers of 131 and 191. Recently Bara (1991; 1992) confirmed the solutions on the main branch experimentally, including the dual solution region.

Sankar *et al.* (1988) predicted the development of spatial oscillations between 2-cell and 4-cell flows for a curvature ratio of 100 and $128 < Dn < 200$.

The development of a 6-cell flow state in a curved rectangular duct with aspect ratio 2, was reported experimentally by Sugiyama *et al.* (1983; 1988) and numerically by Miyake *et al.* (1988) and Kajishima *et al.* (1989). The 6-cell flow consists of two large Ekman vortices and two pairs of Dean vortices near the outer wall. This 6-cell flow state is unstable and breaks down spatially into a 2-cell state. Arnal *et al.* (1992) showed numerically the development of two pairs of Dean vortices in a curved square duct at $Dn = 764$.

The development of counter-rotating Dean vortices in a curved channel has been observed both experimentally (Kelleher *et al.*, 1980; Bottaro *et al.*, 1991; Matsson & Alfredsson, 1992) and numerically (Bottaro, 1991; 1993). Guo and Finlay (1991; 1994) showed that Dean vortices can be unstable to spanwise secondary instabilities that lead to vortex splitting and merging. Vortex splitting and merging has also been observed experimentally (Bottaro *et al.*, 1991) and is believed to play an important role in the wavelength selection process.

Several authors have reported oscillations in curved pipes and square ducts (Sreenivasan & Strykowski, 1983; Tsuda & Ohba, 1984; Ohba *et al.*, 1986; Belaidi *et al.*, 1992; Arnal *et al.*, 1992; Webster & Humphrey, 1993). These oscillations all seem to be related to an instability of the secondary inflow jet in the centre of the inner wall. There is little consistency between the observations, and no numerical evidence is available.

Flow oscillations in a curved channel were first observed by Kelleher *et al.* (1980) and later by Ligrani and Niver (1988). Similar oscillations were observed along a curved plate by Bippes (1972). Two distinctly different traveling wave modes have been observed experimentally and numerically in both curved channel flow and

Görtler flow. Because curved channel flow reaches a fully developed state it is easier to study numerically than Görtler flow.

Finlay (1988) predicted numerically the existence of short wavelength twisting waves and long wavelength undulating waves in a curved channel. Both modes are sinuous. Undulating waves show similarities with wavy Taylor vortices. Twisting waves have the highest growth rates and are most often observed experimentally (e.g. Ligrani & Niver, 1988; Matsson & Alfredsson, 1992). More recently undulating waves have been observed experimentally by Ligrani et al. (1992) and Matsson and Alfredsson (1993a).

Several authors have shown that twisting vortices are the result of a shear instability of inflectional spanwise profiles of the streamwise velocity (Finlay et al., 1988; Matsson & Alfredsson, 1992; Le Cunff & Bottaro, 1993). These profiles have minima near the inflow regions between two Dean vortices, where low velocity fluid is transported away from the outer wall. The strongly inflectional spanwise profiles are similar to profiles of two-dimensional wakes (Sato & Kuriki, 1961), which also have been shown to undergo a shear instability (Mattingly & Criminale, 1972). It has been suggested that undulating waves are related to normal distributions of the streamwise velocity and that this instability is of centrifugal nature (Finlat et al., 1988; Le Cunff & Bottaro, 1993).

The two oscillating modes observed in Görtler flow are a sinuous mode (e.g. Bippes & Görtler, 1972) and a varicose mode (e.g. Ito, 1980; 1985). Both kinds of waves have streamwise wavelengths that are close to their spanwise wavelength. The sinuous and varicose modes were observed simultaneously by Swearingen and Blackwelder (1987). The sinuous mode has been related to spanwise inflectional profiles of the streamwise velocity (Swearingen & Blackwelder, 1987; Yu & Liu, 1991; Liu & Domaradzki, 1993). The instability mechanism is very similar to that

proposed for twisting Dean vortices in a curved channel.

The varicose mode is characterized by horseshoe shaped vortices that periodically connect two Görtler vortices. It has been suggested that these horseshoe vortices are generated by a Kelvin-Helmhotz instability of inflectional normal profiles of the streamwise velocity (Aihara & Koyama, 1981). Other authors have also shown that the varicose mode is related to the normal profiles (Yu & Liu, 1991; Liu & Domaradzki, 1993).

In this chapter, the literature on flow in curved ducts and channels, and flow along a concave wall was reviewed. It is clear that there are still many unresolved issues related to curved square duct flow that are worth investigating. First there is that of fully developed flows at Dean numbers above 131. Since the 4-cell flow is unstable to asymmetric perturbations the question is what will happen farther downstream. Sankar *et al.* (1988) have predicted the development of steady spatial oscillations, but the observed traveling waves in curved channel flow and Görtler flow would suggest the existence of time dependent solutions. Another area that has not been studied systematically, is that of developing flow in curved square duct at Dean numbers above 150. This is the starting point of the present study.

Chapter 3

Experimental System

The experimental apparatus used in this study was designed by Bara (1991; 1992) for the experimental investigation of developing and fully developed flow in a curved duct of square cross section. Only minor modifications were made to this apparatus. The main experimental methods used in this study are fluid velocity measurements and flow visualization. Streamwise or spanwise velocities were measured with a one-dimensional laser-Doppler anemometer (LDA). Two methods of fluorescent dye flow visualization were used: the secondary flow was studied by illuminating a cross section of the duct with a laser light sheet; sideview pictures of streamwise flow patterns were taken by illuminating a 20° section of the duct. Both the LDA and the flow visualization methods were modified significantly after Bara's study. The description of the equipment and the experimental procedures focuses on these modifications. Detailed specifications of the experimental apparatus can be found in Bara (1991).

3.1 Experimental Apparatus

A schematic of the experimental setup is shown in figure 3.1. The apparatus has a curved section with a square cross section of 1.27 cm and a curvature ratio, $R_c = R/a$, of 15.1 (figure 3.2). The curved duct is 270° long and is aligned in a horizontal plane. The curved section was machined out of a 3.3 cm 'hick disk of plexiglass. A 1.27 cm square groove was cut into the curved wall of the disk and covered by a 1.5 mm thick sheet of plexiglass. A stilling chamber and a 1 m straight inlet section were designed to provide a fully developed flow field at the inlet of the curved section for flow rates up to $Dn = 225$. A detailed schematic of the stilling chamber is shown in figure 3.3. The stilling chamber, inlet section and curved section were made out of plexiglass, in order to make velocity measurements and flow visualization possible. The apparatus can be rotated in a horizontal plane around the centre of curvature. This allows velocity measurements at different streamwise positions in the duct. The LDA traversing system provides vertical and radial movement of the measuring volume.

A constant pressure drop over the apparatus is maintained by two constant head tanks, approximately 3.5 m above each other, and an overflow reservoir. From the lower overflow tank the water is either returned to the reservoir or to the drain, depending on whether the system is running in an open or a closed loop. Water is pumped from the reservoir to the upper overflow tank. The flow rate is controlled by two Brooks 600 mm model 6-1110-24 rotameters, each with a maximum flow rate of 0.7 l/min. The mass flow rate was determined by collecting the outlet of the lower overflow tank over a timed interval. A hand held digital stopwatch with a resolution of 0.01 s was used for the timing and a Mettler PC 8000 electronic balance with a resolution of 0.1 g was used to weigh the sample.
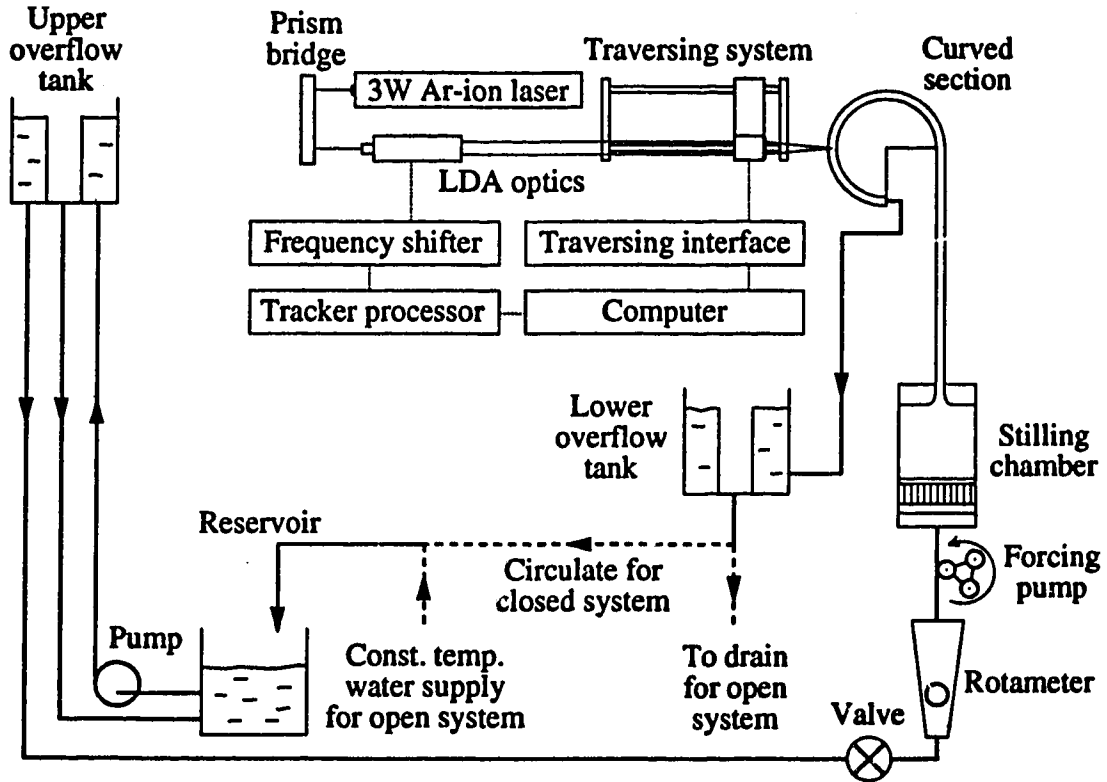
Figure 3.1: Schematic of the experimental setup.
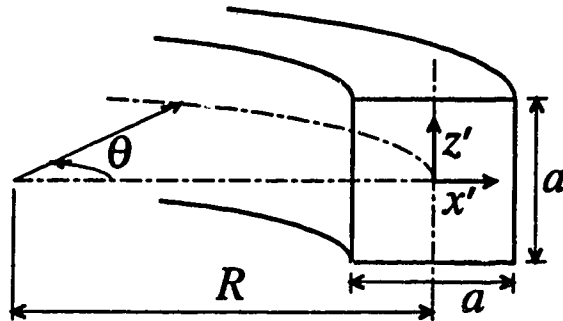
Figure 3.2: Detailed schematic of the curved duct section.

All dimensions in centimeters

| 4.0 |3.0| 7.5 | 2.0 | | 13.0 | 6.0 | 5.0 |

20.3

Inlet

1.9

Screen

Flow
straightener

Screen

Dye
injection
tube

2.5
1.27

Adjustable height

Dye reservoir

To syringe pump

Tygon tube
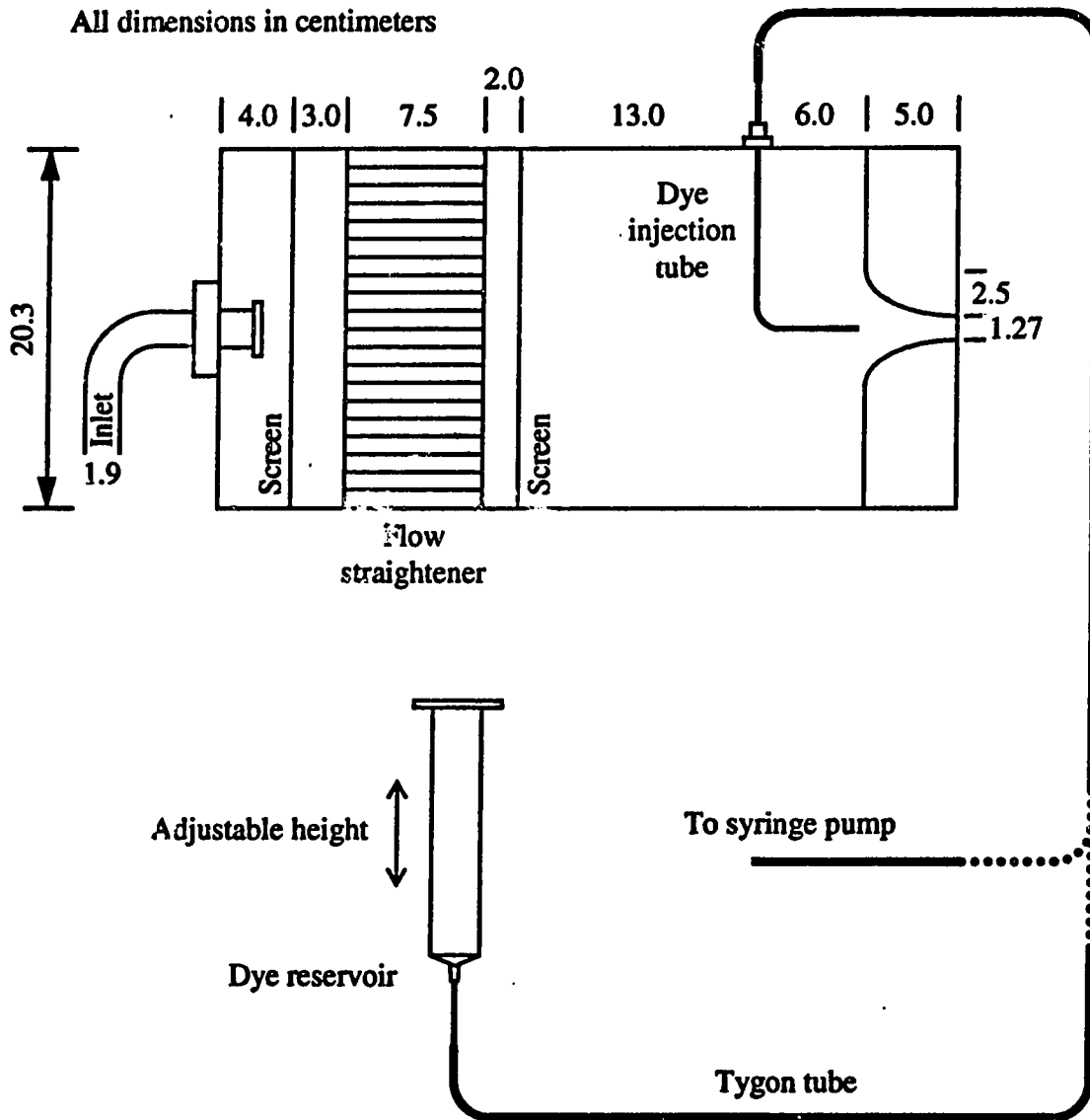
Figure 3.3: Detailed schematic of the stilling chamber with dye injection system.

In order to limit the buoyancy driven secondary flows and viscosity variations, the temperature of the water needs to be controlled. A combination of a cooling coil and a heating element connected to a setpoint control mechanism keeps the water temperature in the reservoir at 23.1°C ±0.1°C. Bara (1991) showed that temperature differences in the fluid should be kept below 0.25°C in order to maintain a level of buoyancy driven secondary flows below 1% of the mean flow velocity when the Reynolds number, $Re \geq 400$ $(Dn \geq 100)$. The room temperature, measured near the stilling chamber, is typically 23.1°C ±0.5°C. At a temperature difference of 0.5°C between the working fluid and the surroundings, the temperature increase of the water as it flows through the system from the reservoir to the outlet of the lower overflow tank is less than 0.1°C. This shows that heat transfer between the surroundings and the fluid is negligible and th∘t temperature differences are well below 0.25°C. The water temperature is verified in the stilling chamber by a Fisherbrand 15-000 A glass thermometer with a resolution of 0.1°C.

At 5° from the inlet of the curved section, a pin with a diameter of 0.2-0.5 mm can be inserted in radial direction through a hole in the outer wall at $z = 0$. Five different pins were used: 33, 29, 27, 26 and 25 gauge with diameters of 0.2, 0.33, 0.41, 0.46 and 0.5 mm respectively. The pins were bent slightly where they enter the flow. This results in a conical movement of the end of the pin that is in the flow when the other end is rotated and allows the introduction of symmetric and asymmetric perturbations. A Masterflex model 7020-70 peristaltic pump without its casing can be used to compress the 2 cm inside diameter tygon hose that is connected to the stilling chamber periodically. This creates a periodic flow disturbance. The distance over which the hose is compressed can be adjusted by moving the hose up and down. This is illustrated in figure 3.4. The forcing frequency is set on a scale from 0-15 Hz or 0-150 Hz.
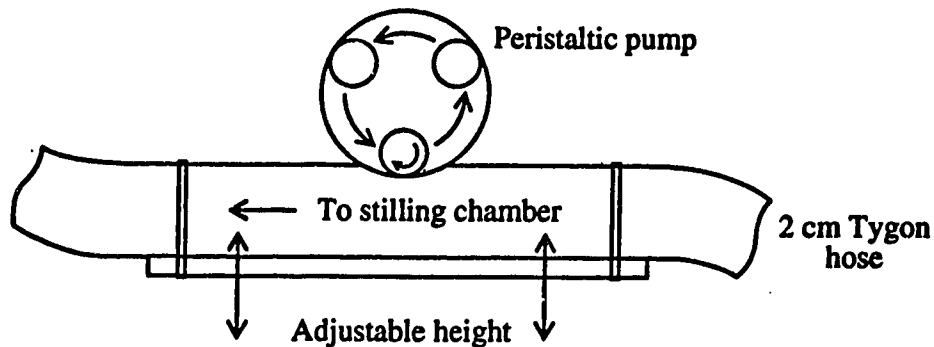
Figure 3.4: Detailed schematic of the forcing system.

3.2 Velocity Measurements

Fluid velocities were measured with a one-component laser-Doppler anemometer that can measure either horizontal (streamwise) or vertical (spanwise) velocities. The system uses a 3 W Argon-ion laser and is operated in backscatter mode. Dantec 55X modular optics are used in combination with a Dantec 55N10 frequency shifter and a Dantec 55N20 Doppler frequency tracker. Dantec 57H10/57H11 traversing mechanisms allow vertical and horizontal (parallel to the optical axis) movement of the measuring volume. The traversing system is controlled through a Dantec 57G15 traversing interface by a personal computer, using Dantec's atTRACKtion software. The traversing mechanisms have a backlash of less than 0.1 mm and a repeatability of 0.017 mm. The atTRACKtion software, in combination with a MetraByte DASH-16 analog to digital converter (ADC), is used to collect data. Only raw data files were collected; data analysis software was developed using Borland's Turbo Pascal, because this provides much greater flexibility than the atTRACKtion

software and allows for easy correction of curvature effects.

The MetraByte A/D converter has a resolution of 12 bits (count ranging from 0-4095). The ADC was calibrated by determining the output count as a function of the frequency of a sine wave, generated by a wave generator. This was done for two different tracker range settings. The calibration data are shown in figure 3.5. The calibration curve was approximated by the function

$$f/\text{Range} = 1.900 * 10^{-4} (\text{ADC Count})^{1.030} \tag{3.1}$$

where f is the measured frequency. Calibration equation 3.1 was used by the data analysis program.
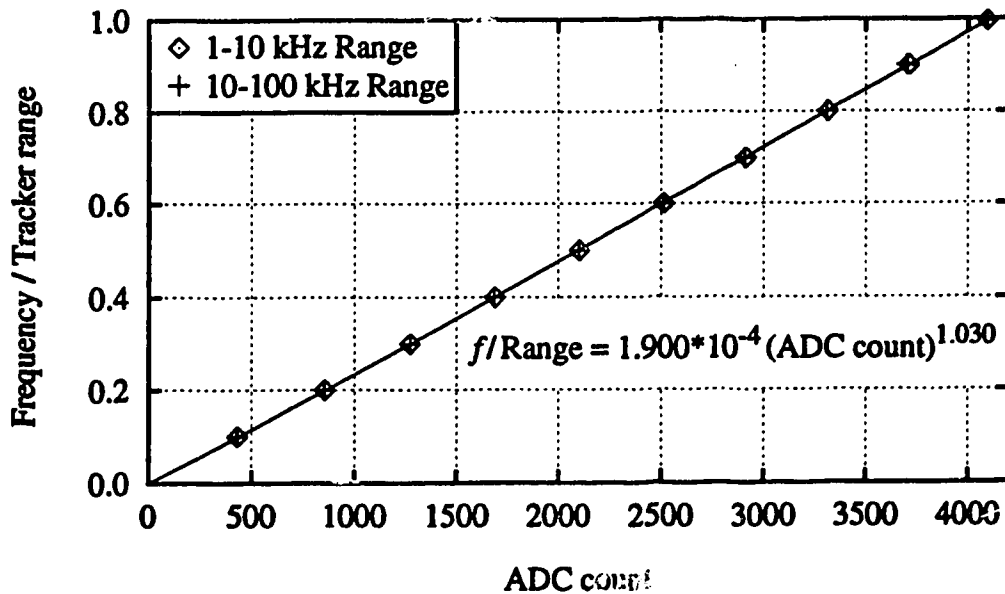
Figure 3.5: Tracker calibration curve: ADC count vs. measured frequency.

The blue line (488 nm in air) of a Coherent Innova 90-3 laser was used to take velocity measurements; the laser power was typically 600 mW. With a 80 mm focal length front lens the measuring volume has a diameter of 0.017 mm and a length of 0.12 mm. Silicon carbide particles with a mean diameter of 1.5×10^{-6} m and a density of 3.2×10^3 kg/m^3 were used to generate Doppler signals. Since the velocity that is measured is the velocity of the particles, the accuracy of the measurement depends on how closely the particles follow the flow. The settling velocity of the particles, based on Stoke's law and assuming that the particles behave like spheres, is 3×10^{-6} m/s and was neglected compared to fluid velocities.

The laser light that is scattered by the particles is Doppler shifted by an amount that is proportional to the particle's velocity in the plane of the crossing beams and perpendicular to the optical axis. The frequency tracker measures the Doppler frequency of this scattered light. The particle velocity can be calculated from the measured Doppler shift, using the relation

$$v'_p = \frac{\lambda}{2\sin(\phi/2)} f_d \qquad (3.2)$$

where: v'_p = velocity of particle
λ = wavelength of laser light
ϕ = crossing angle between beams
f_d = measured Doppler frequency

The calibration factor, $c_f = \lambda/(2\sin(\phi/2))$, depends on the wavelength of the laser light and the beam crossing angle. As the crossing point is traversed through water the laser light wavelength is constant, but because of the curved geometry, the beam crossing angle depends on the traversed distance. This effect of the curvature will be discussed in detail in section 3.4. Bara (1991) showed that the calibration factor can be determined accurately by using the fully developed inlet profile at low

flow rates as a velocity standard. This method was followed throughout this study.

When positioning the measuring volume, first the apparatus was rotated to the required streamwise position, θ. The radial direction of the apparatus was aligned with the optical axis so that traversing the measuring volume along the optical axis corresponds to traversing in the radial direction of the apparatus. The outer wall near $z = 0$ was located by finding the radial position where wall reflections are at a maximum. Next, the centre of the bottom wall ($x = 0$) was located, after which the outer wall at $z = 0$ was located again. The measuring volume was positioned with the outer and bottom walls as references.

3.3   Flow Visualization

Two types of flow visualization were used: secondary flow patterns were studied by visualizing cross sections of the duct and sideviews showed the streamwise development of the flow. Both methods make use of fluorescent dye; a 1×10^{-3} M solution of Rhodamine 6G was used for all experiments.

A schematic of the setup used for flow visualization of cross sections of the duct is shown in figure 3.6. After the laser beam is reflected by the prism bridge, the beam either enters the LDA optics, or enters an input coupler for a 250 μm multi-mode fiber optic cable. This fiber optic cable is connected to a portable laser light sheet, created by a combination of two spherical lenses and a 10 mm focal length cylindrical lens. At the beam waist, the laser sheet is 1 mm wide and 2.5 cm long. The laser power of the sheet was typically around 500 mW.

Pictures of cross sections were taken through a plexiglass viewing block that corrects for some of the curvature effects. The viewing block can be positioned
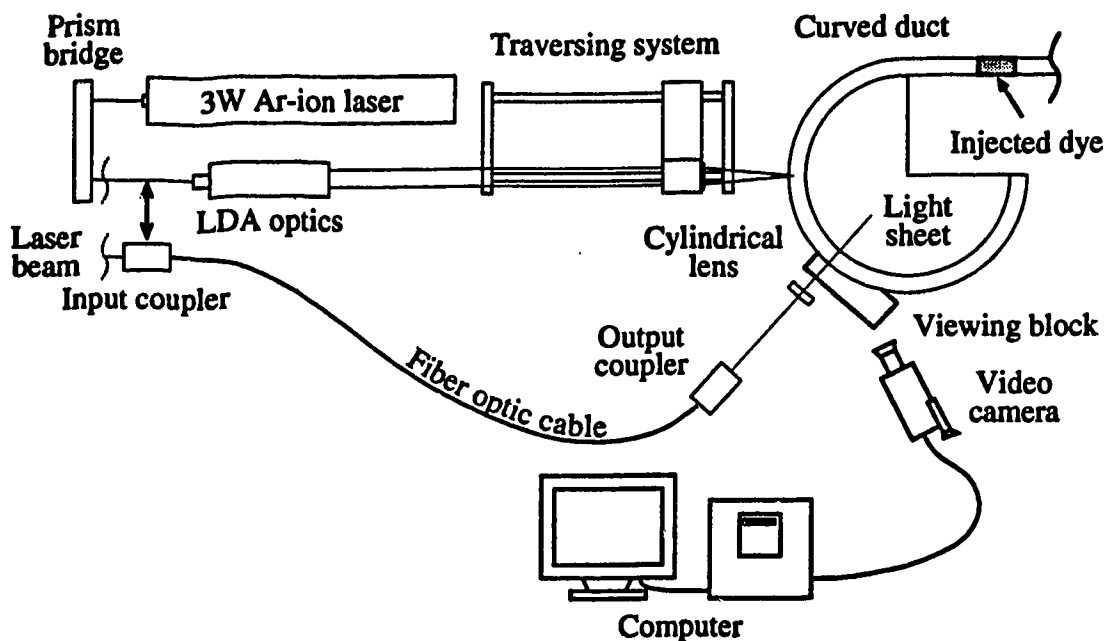
Figure 3.6: Schematic of the setup used for cross section pictures.

anywhere along the duct. The gap between the viewing block and the duct was filled with a thin water film.

For the sideview pictures, a 10-20° section of the duct was illuminated from above by shining a light beam from a slide projector on a mirror that reflects the light down. This setup is shown in figure 3.7.

The dye can either be injected continuously, creating a thin streak, or as a slug. In both cases the dye is injected just before the inlet contraction in the stilling chamber through a 1 mm piece of tubing, the end of which was bent in the flow direction. The piece of tubing can be moved up and down through a seal in the top
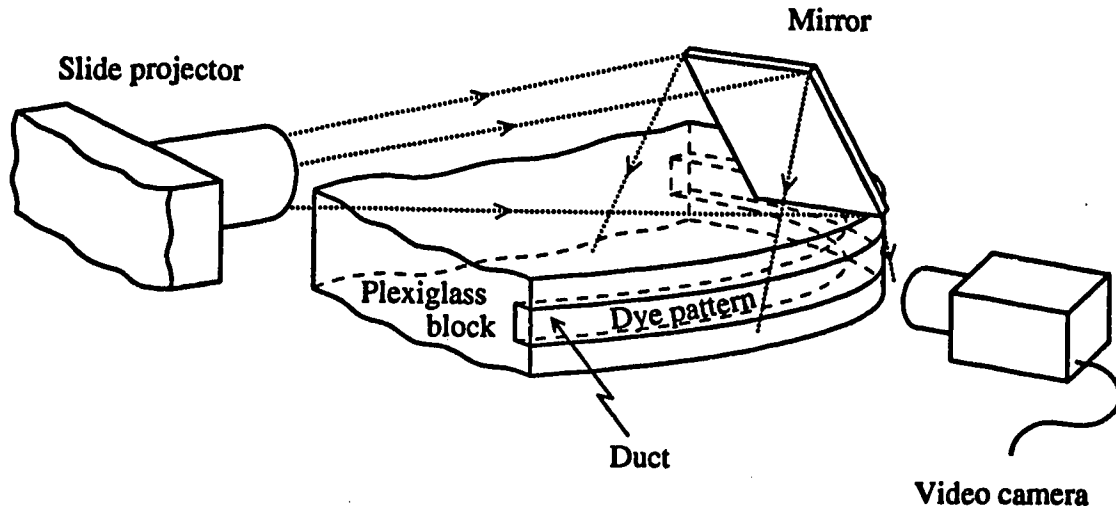
Figure 3.7: Schematic of the setup used for sideview pictures.

wall of the stilling chamber and also rotated to adjust the dye injection point.

When the dye is injected continuously, a reservoir with dye is connected through a 1 mm inside diameter tygon tube to the injection tubing in the stilling chamber. This is shown in figure 3.3. The dye flow is driven by the slightly less than atmospheric pressure in the stilling chamber. The flowrate can be adjusted by moving the dye reservoir up and down. The injection point was very carefully positioned such that the streak of dye was vertically centered. In those cases were a pin was inserted this meant that the streak of dye was split in half by the pin, creating an initially symmetric dye pattern.

The second method of dye injection uses a syringe pump that is switched on for a short period of time, causing 1-2 ml of dye to enter the flow. The slight increase in flow rate causes a small disturbance of the flow, which dies out quickly. As the slug of

dye moves through the observed area of the flow, the pattern changes continuously. The clearest structures were usually observed near the end of the dye slug.

Dye patterns are filmed with a Sony CCD-V801 video camera recorder and stored on 8 mm video tape. Frames can be selected from this movie by playing the tape back through the NeXTtv application on a NeXTdimension computer. A variety of image processing tools on the NeXT system was used to scale and enhance the pictures.

3.4 Curvature Effects

The curvature of the outer wall of the duct affects the distance traversed in water by the crossing point as well as the calibration factor in water. By passing a laser beam through a surface between materials with different refractive indices, the angle between the laser beam and the normal will change according to Snell's law of refraction:

$$\eta_1 sin\theta_1 = \eta_2 sin\theta_2 \tag{3.3}$$

where η is the refractive index and θ is the angle with the normal to the surface. Therefore, the angle between the two laser beams of the LDA is different in water than it is in air. If the surfaces that the laser beams pass through were flat, than the crossing angle in water, ϕ_f, would be constant:

$$\eta_f sin(\frac{\phi_f}{2}) = \eta_a sin(\frac{\phi_a}{2}) \tag{3.4}$$

where a and f stand for air and fluid. In that case the ratio of the distance traversed in air and the distance traversed in water is a constant, given by η_a/η_f.

The LDA calibration factor in a certain medium, $c_f = \lambda/(2sin(\phi/2))$, is a function of the crossing angle and the wave length in that medium. The wave length is given by:

$$\lambda = \eta_1 \lambda_1 \tag{3.5}$$

where λ is the wave length in vacuum and λ_1 is the wave length in a medium with refractive index η_1. Therefore, when the laser beams pass through a flat surface, the effects on the crossing angle and the wave length cancel each other out, leaving the calibration factor unchanged.

By traversing through a curved wall, this is no longer the case. When a laser beam passes through a curved wall, the beam is refracted twice, once at the outer surface, and once at the inner surface of the wall (see figure 3.8). The angle of refraction at the outer surface (θ_{s1}) is different than the angle of incidence at the inner surface (θ_{s2}). Therefore, if the laser beams are traversed through a curved surface, the crossing angle, θ_c, and the traversing ratio depend on the angle of incidence at the outer surface, θ_a; θ_a in turn depends on the traversed distance in air, l_a.

The distance traversed in air, l_a, can be divided into two components: the distance traversed to move the crossing point from the outer surface of the plexiglass to the inner surface of the plexiglass, l_{ai}, and the distance traversed in air while the crossing point is in the fluid, Δl_a. The distance traversed in the fluid, l_f, is given by

$$l_f = \frac{R_2 \sin \alpha_2}{\tan \dfrac{\theta_c}{2}} + R_2(1 - \cos \alpha_2) \tag{3.6}$$

Bara (1991) derived an expression for l_f as a function of l_a, that includes a number of iterative steps. The results of these calculations are shown in figure 3.9.
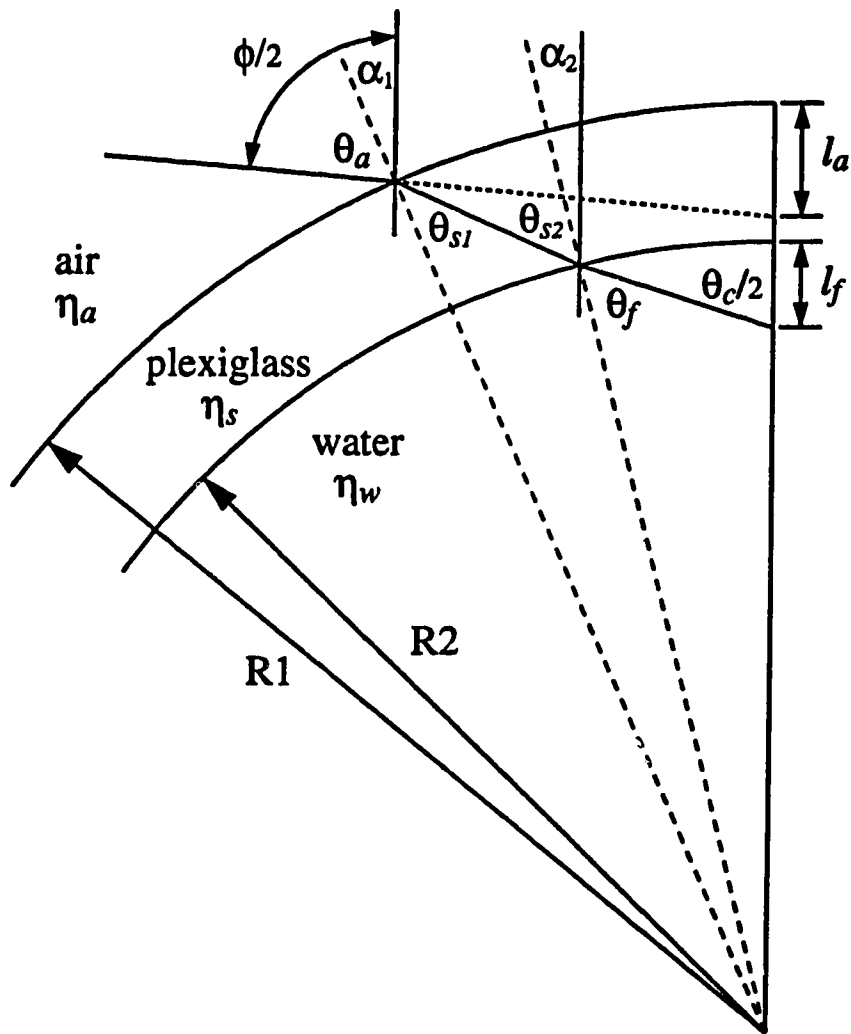
Figure 3.8: Schematic of laser beam passing through a curved surface.
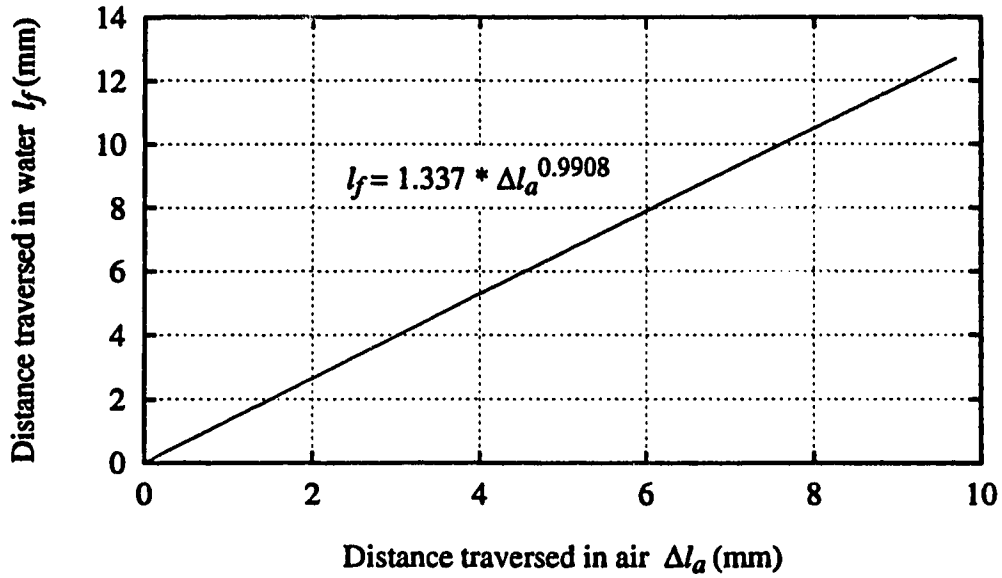
Figure 3.9: Traversing distance in water compared to traversing distance in air.
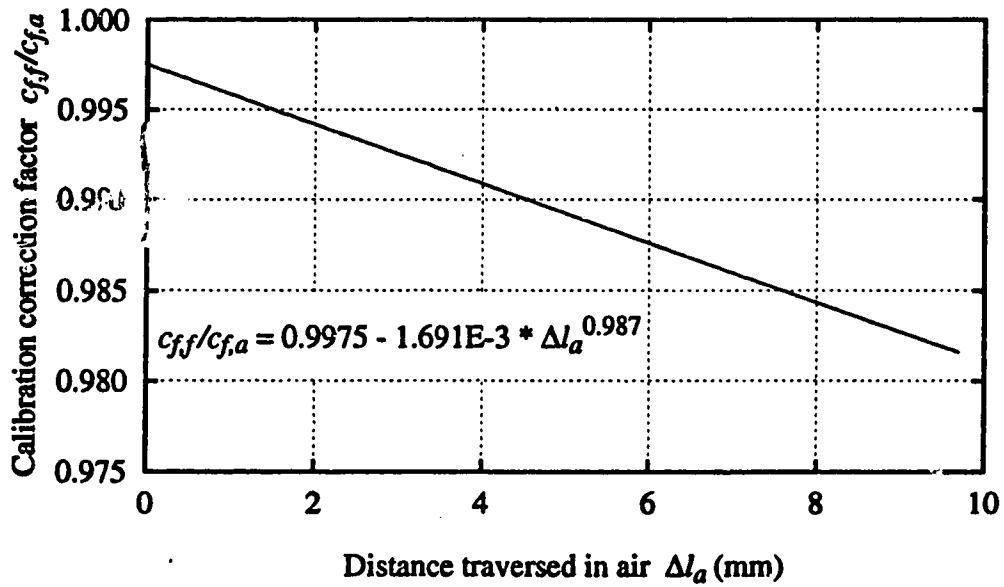
Figure 3.10: LDA calibration correction factor as a function of the distance traversed in air.

This relationship was approximated by the function $l_f = 1.337\,\Delta l_a{}^{0.9908}$, which has an average deviation of 0.2%.

The relationship between the LDA calibration factors in air and in water is given by

$$\frac{c_{f,f}}{c_{f,a}} = \frac{\eta_a}{\eta_f}\frac{\sin(\phi/2)}{\sin(\theta_c/2)} \qquad (3.7)$$

Bara (1991) also derived an expression for this calibration correction factor. The results are shown in figure 3.10. The approximate solution, $c_{f,f}/c_{f,a} = 0.9975 - 1.691*10^{-3}\,l_a{}^{0.987}$ is accurate to within 0.0004% on average. The approximate solution for both the traversing ratio and the calibration correction factor were used by the data analysis program.

3.5 Experimental Errors

An experimentally measured quantity usually deviates from it's true value by an amount called the experimental, or measurement error. Because the true value of a quantity is generally unknown, the magnitude of the measurement error can only be estimated. In order to get an idea of the magnitude of experimental errors and the importance of different sources of uncertainty, an error analysis was performed for the Dean number, the calibration factor, and for the streamwise velocity.

A distinction must be made between errors that are the same each time a quantity is measured (systematic errors) and errors with randomly distributed magnitudes (random errors). Random errors can be reduced by averaging the measured quantity over a number of measurements, while systematic errors can not be reduced, other than by eliminating the source of the error.

3.5.1 Dean Number

In this study, the Dean number, Dn, is defined as

$$Dn = \frac{Re}{\sqrt{R_c}} = \frac{\overline{v_\theta} d_h}{\nu \sqrt{R_c}} = \frac{\dot{m}}{\rho \nu \sqrt{R}} \frac{2\sqrt{a}}{(a+b)} = f(\dot{m}, \rho, \nu, R, a, b) \qquad (3.8)$$

where: Re = Reynolds number

         R_c = curvature ratio, R/a

         $\overline{v_\theta}$ = mean streamwise velocity, $\dot{m}/(\rho a b)$

         d_h = hydraulic diameter, $2ab/(a+b)$

         $\dot{m}$ = mass flow rate

         ρ, ν = density and kinematic viscosity

         a, b = duct dimensions

The error in Dn depends on the individual errors in $\dot{m}$, ρ, ν, R, a and b. The principle of propagation of variances can be used to derive an expression for the variance of Dn as a function of the variances of the different variables that Dn depends on:

$$\sigma_{Dn}^2 = \left(\frac{\partial f}{\partial \dot{m}}\right)^2 \sigma_{\dot{m}}^2 + \left(\frac{\partial f}{\partial \rho}\right)^2 \sigma_\rho^2 + \left(\frac{\partial f}{\partial \nu}\right)^2 \sigma_\nu^2 + \left(\frac{\partial f}{\partial R}\right)^2 \sigma_R^2 + \left(\frac{\partial f}{\partial a}\right)^2 \sigma_a^2 + \left(\frac{\partial f}{\partial b}\right)^2 \sigma_b^2$$

$$(3.9)$$

where σ_{Dn}^2 is the variance of the Dean number. I: i: assumed that the variables are symmetrically distributed random variables and statistically independent (Schenck, 1979). Substitution of equation 3.8 into equation 3.9 gives:

$$\frac{\sigma_{Dn}}{Dn} = \sqrt{\frac{\sigma_{\dot{m}}^2}{\dot{m}^2} + \frac{\sigma_\rho^2}{\rho^2} + \frac{\sigma_\nu^2}{\nu^2} + \frac{1}{4}\frac{\sigma_R^2}{R^2} + \frac{1}{4}\frac{\sigma_a^2}{a^2}} \qquad (3.10)$$

σ_{Dn}/Dn is the relative error of the Dean number. The variances of the different variables, required to evaluate equation 3.10, are not known. Therefore, an estimate of the variances, s^2, must be used.

Because in this study higher flow rates were used than in the work by Bara (1991), the error in the measured flow rate is slightly higher than the one used by Bara. With a typical error of 0.1 s in a time interval of on average 40 s for a flow rate of $Dn = 220$, the relative error of $\dot{m}$ is 0.25%. This error is directly proportional to the flow rate. The relative errors of ρ, ν, R, and a were estimated by Bara at 0.002%. 0.25%, 0.013% and 0.2% respectively, and are based on a temperature variation of 0.1°C and a machining tolerance of ± 0.0025 cm. This results in a relative error of 0.4% for the experimentally determined Dean number.

3.5.2 LDA Calibration Factor

The particle velocity is calculated from equation 3.2, where $\lambda/(2\sin(\phi/2))$ is the calibration factor, c_f. An error in the calibration factor introduces a systematic error in the calculated velocity. The calibration factor can be determined either by measuring the crossing angle, ϕ, directly, or by using a velocity standard. Bara (1991) used three different calibration methods: direct measurement of ϕ, a spinning wheel as velocity standard, and the inlet velocity profile as velocity standard. He demonstrated that at flow rates up to $Dn = 200$ the inlet velocity profile is fully developed, and that this inlet velocity profile provides an accurate velocity standard for calibration purposes.

Bara (1991) derived the following equation for the relative error of the calibration factor, determined from the inlet profile velocity standard:

$$\frac{\sigma_{c_f}}{c_f} = \sqrt{\frac{\sigma_{\dot{m}}^2}{\dot{m}^2} + \frac{\sigma_\rho^2}{\rho^2} + 2\frac{\sigma_a^2}{a^2} + \frac{\sigma_{f_d}^2}{f_d^2}} \qquad (3.11)$$

and estimated the error in the calibration factor at 0.3%. The error in the duct dimensions, a and b, adds up to more than 85% of the total error in the calibration

factor. Unfortunately, it is not easy to obtain a tolerance smaller than ± 0.0025 cm when machining plexiglass. This estimate does not include the output bias of the tracker processor, which will be discussed in the next section.

3.5.3   Velocity Measurement

The particle velocity is calculated from equation 3.2 ($v_\theta' = c_f * f_d$). Therefore, the error in the velocity depends on the errors in the calibration factor and the measured Doppler frequency:

$$\frac{\sigma_{v_\theta'}}{v_\theta'} = \sqrt{\frac{\sigma_{c_f}^2}{c_f^2} + \frac{\sigma_{f_d}^2}{f_d^2}} \tag{3.12}$$

An error in the calibration factor introduces a systematic error in the velocity. There are two independent sources of uncertainty in the measurement of the Doppler frequency: the random error associated with fluctuations in the measured Doppler signal and the systematic error introduced by the bias in the output of the tracker processor. Positioning errors, which are due to incorrectly locating the duct walls, also contribute to the error in the measured velocity. The measurement of the spanwise velocity component is very sensitive to the alignment of the LDA optics. Each of these errors was investigated.

It was demonstrated in the previous section that the uncertainty in the calibration factor introduces a systematic error in the velocity of 0.3%.

The Doppler frequency, determined by the tracker processor, varies randomly as a result of random fluctuations in the flow and measurement noise. Part of the measurement noise is the result of the random phase differences between consecutive particles in the measuring volume (Drain, 1980). This is called phase noise. Another source of measurement noise is introduced if the laser beams do not intersect in the

beam waists, in which case the interference planes are not parallel (Hanson, 1973). It will be shown in the next chapter that the relative error of the Doppler frequency, also called the signal fluctuation, is around 1%.

Several factors have to be taken into account when deciding on the number of velocity values per sample. When measuring steady flow phenomena, the random signal fluctuations can be reduced by averaging over a number of velocity measurements. When a randomly varying quantity is averaged over a large number of sample values, n, the relative error of the means is lower by a factor of $\sqrt{n}$ compared to the original relative error (Harnett, 1982). Therefore, averaging the Doppler frequency over 512 values reduces the relative error of the Doppler frequency from a typical 1% to 0.04%, well below other sources of uncertainties. This is only true if the average velocity does not change between different samples.

Some of the steady and time dependent flow phenomena that will be discussed later were very sensitive to unwanted and uncontrollable disturbances. This made it necessary to keep the total measuring time of a velocity profile or amplitude distribution to a minimum. Steady velocity profiles were therefore measured at 42 to 63 positions with 512 values per position, sampled at 100 Hz. With a time delay of 1 second between consecutive positions, the measurement time for a profile is between 4.3 and 6.4 minutes. If much more time is used for the measurement, the chance that the flow is disturbed during the measurement becomes significant.

The time dependent flow phenomena were characterized by determining the frequency content of velocity samples. The resolution of a frequency spectrum is equal to the inverse of the total measuring time of a sample. The observed periodic phenomena were typically in the 1-10 Hz range and required a frequency resolution of at most 0.5 Hz, and preferably smaller. By sampling 512 times at a frequency of 100 Hz, the frequency resolution of the spectra is 0.2 sec. By measuring velocity

traces at 61 positions, the total measuring time was limited to 6.2 minutes.

The output of the tracker processor is sensitive to wall reflections and to the tracker range and gain settings. When measuring near the wall, reflections from the wall at the shift frequency start to dominate the Doppler signal. Bara (1991) showed that in this region the tracker processor measures low. This indicates that the tracker processor locks on to a frequency between the Doppler frequency of the particles and the lower shift frequency of the wall reflections. The wall reflections are significant only within 1 mm from the wall.

The measured Doppler frequency shows a slight dependence on the tracker range and gain settings. These systematic errors can not easily be reduced. However, with proper seeding the error introduced is less than 0.5%. This is the main contribution to the error in the measured Doppler frequency. Combining the errors due to the signal fluctuation (0.04%) and the tracker settings (0.5%), gives a total error in the Doppler frequency of 0.5%.

Substitution of relative errors in the calibration factor and Doppler frequency of 0.3% and 0.5% respectively, gives an estimated error in the streamwise velocity of 0.6%.

Some of the measured velocities are non-dimensionalized by dividing the velocity by the average streamwise velocity in a cross section of the duct:

$$v_\theta = \frac{v'_\theta}{\overline{v'_\theta}} = \frac{c_f f_d \rho a b}{\dot{m}} \tag{3.13}$$

where: v_θ = non-dimensional streamwise velocity
v'_θ = dimensional streamwise velocity
$\overline{v'_\theta}$ = average streamwise velocity
c_f = calibration factor
f_d = measured Doppler frequency

ρ = density

a, b = duct dimensions

$\dot{m}$ = mass flow rate

In that case, also the errors in $\dot{m}$, ρ, a and b must be taken into account when evaluating the error in the streamwise velocity. Using the method of propagation of variances, the uncertainty in a calculated value of v_θ is:

$$\frac{\sigma_{v_\theta}}{v_\theta} = \sqrt{\frac{\sigma_{c_f}^2}{c_f^2} + \frac{\sigma_{f_d}^2}{f_d^2} + \frac{\sigma_\rho^2}{\rho^2} + 2\frac{\sigma_a^2}{a^2} + \frac{\sigma_{\dot{m}}^2}{\dot{m}^2}} \qquad (3.14)$$

As shown previously, the relative errors in c_f, f_d, ρ, a and $\dot{m}$ are 0.3%, 0.5%, 0.002%, 0.2% and 0.1% respectively. Substitution of these values into equation 3.14 gives an estimated error of the non-dimensionalized velocity of 0.7%.

An error in the location of the outer or bottom wall introduces a systematic error in the positioning of the crossing point. When locating the outer wall, the crossing volume is moved to the position with maximum wall reflections. There is an uncertainty of about 0.2 mm in locating the outer wall. To eliminate any effects of the backlash of the traversing mechanism, the outer wall was always located while moving inwards. Because of the more defined reflections at the bottom wall, this wall can be located to within 0.1 mm.

Systematic errors in the positioning have the largest effect on the measured velocity in regions with high velocity gradients, which is generally near the walls. The error in the inlet velocity caused by a positioning error of 0.2 mm in the radial position is 0% in the centre, 3% at $x = 0.25$ and about 10% at $x = 0.4$. Although the relative error near the wall becomes significant, the absolute error remains reasonably small because of the lower velocities in this region. When measuring a profile in radial direction, a systematic error in the radial positioning can sometimes be detected by comparing the measured profile with a numerical simulation. The

positioning error could then be corrected for by shifting the profile in radial direction. The same is true for a vertical positioning error when measuring a spanwise profile.

The laser Doppler anemometer measures the velocity component in the plane of the crossing laser beams and perpendicular to the optical axis. Because the streamwise velocity is generally more than an order of magnitude larger than the spanwise velocity, the alignment of the LDA optics is critical when measuring spanwise velocities. A small error in the alignment of the optics can result in a large contribution of the streamwise velocity to the measured signal. The accuracy of the alignment is difficult to estimate, but is at least 1°. An alignment error of 1° can cause an error in the spanwise velocity of 5%.

3.5.4   Summary of Experimental Errors

The error in the experimentally determined Dean number is estimated at 0.4%. When the calibration factor is determined with the inlet velocity profile as a velocity standard, the estimated error in the calibration factor is 0.3%. The error in the streamwise velocity, not including positioning errors, is estimated to be around 0.6%. When the streamwise velocity is non-dimensionalized, the error increases to 0.7%. Velocity errors of more than 0.7% are the result of the wall location uncertainty, which results in incorrect positioning of the measuring volume. These velocity errors depend on the velocity gradients; the error is generally less than 1% near the centre of the duct and can be as high 10% near the walls. Errors in the spanwise velocity that are the result of the misalignment of the LDA optics are estimated at at least 5%.

Chapter 4

Inlet Flow

Flow phenomena in open systems such as a curved duct can be very sensitive to upstream flow disturbances. Velocity fluctuations at the inlet of the curved section should therefore be kept to a minimum. Also, numerical simulations are most accurate when the experimental inlet velocity profile is used as inlet condition for the simulations. For these reasons, the stilling chamber and 1 m inlet section were designed to provide a steady and fully developed, one-dimensional, velocity field at the inlet of the curved section.

Based on the measurements by Goldstein and Kreid (1967), the flow would reach a fully developed inlet profile for flowrates up to a Dean number of 225 ($Re = 875$). Bara (1991) showed that for Dn up to 200 the inlet flow is indeed fully developed. In this study however, flow rates as high as $Dn = 600$ ($Re = 2335$) were used. This made it necessary to have a close look at the inlet flow conditions at these higher flow rates. First, the turbulence intensity of the inlet flow is investigated. Second, measured radial and spanwise inlet profiles are compared to the analytical solution for fully developed laminar flow in a rectangular duct. Last, slow fluctuations of the velocity, which are a measure of the steadiness of the flow, are examined.

4.1 Turbulence Intensity

Flow disturbances, whether these are induced or inherent to the experimental system, play an important role in this study. It is therefore essential to quantify the inherent fluctuations of the flow entering the curved section. Measured signal fluctuations are a combination of velocity fluctuations and measurement noise. The magnitudes of both these contributions to the total fluctuations were determined. Frequency spectra were calculated in order to determine whether there are any dominant frequencies present in either the velocity fluctuations or measurement noise.

The root mean square of the streamwise velocity provides a measure of the magnitude of the velocity fluctuations. This is defined by:

$$\sqrt{v_\theta'^2} = \sqrt{\frac{1}{n}\sum_{i=1}^{n}(v_{\theta_i}' - v_\theta')^2} \tag{4.1}$$

where: $\sqrt{v_\theta'^2}$ = root mean square velocity

n = number of velocity values

v_{θ_i}' = the ith velocity value of a sample

v_θ' = mean sample velocity

The turbulence intensity $v_{\theta,ti}$ is defined as $\sqrt{v_\theta'^2}/v_\theta'$, or the root mean square of the streamwise velocity fluctuations, divided by the mean flow velocity. The signal fluctuation $v_{\theta,sf}$ is the root mean square of the measured signal fluctuations divided by the measured mean velocity. Fluctuations of the measured signal are a combination of velocity fluctuations and measurement noise, $v_{\theta,mn}$. For independent measurement noise one can show that

$$v_{\theta,sf}^2 = v_{\theta,ti}^2 + v_{\theta,mn}^2 \tag{4.2}$$

It is not possible to separate these two effects completely.

Streamwise velocity signal fluctuations were measured for a number of flow rates by sampling 1024 velocity values at 100 Hz in the centre of the duct. The measured signal fluctuations vary between 2 and 17% and are very sensitive to the tracker range and shift settings (see table 4.1). Changing the range or the frequency shift settings does not affect the turbulence intensity, which is an inherent property of the flow, but may affect the measurement noise. Therefore, any variation in the measured signal fluctuation can be attributed to the measurement noise.

Re	Dn	Signal fluct. (%)	Range (kHz)	Shift (kHz)
383	98.4	7.50	3-33	-20
		16.55	10-100	+10
772	198.5	2.78	3-33	-40
		6.60	10-100	+10
1159	298.2	4.01	10-100	-10
		10.44	33-333	+35
1548	398.2	3.05	10-100	-50
		8.11	33-333	+35
1951	501.9	3.40	10-100	-100
		5.71	33-333	+35
2346	603.3	2.99	10-100	-150
		5.70	33-333	+35

Table 4.1: Measured unfiltered signal fluctuations for different flow rates and range and shift settings at $x = 0$, $z = 0$.

Because the measured signal fluctuation is a combination of the turbulence intensity and the measurement noise, the turbulence intensity at each flowrate is lower than the lowest measured signal fluctuation. At a Reynolds number of 383, corresponding to a Dean number of 98.4, the flow is expected to be truly laminar. This is supported by the excellent agreement between the measured inlet profiles and the theoretical profile for laminar flow, to be discussed in the next section. For laminar flow the velocity fluctuations would be zero, indicating that all the measured signal fluctuations are the result of measurement noise. It is shown in table 4.1 that the minimum signal fluctuation does not increase with increasing flow rate, suggesting that also at the higher flow rates all, or most of the signal fluctuations are caused by measurement noise.

Frequency spectra for flow rates of $Re = 395$ and $Re = 1951$ are shown in figures 4.1 and 4.2. The highest sampling frequency that can be obtained with the atTRACKtion software is 9500 Hz. This frequency is close to the sampling limit of the tracker, as well as the rate of particles crossing the measuring volume. In order to reduce the signal fluctuation, a first order low pass filter was used (BW1 setting on Dantec 55N20 frequency tracker). The effect of this filter is shown in figures 4.3 and 4.4. Measured fluctuations of the filtered velocity signal at different flow rates and range and shift settings are given in table 4.2.

When a velocity profile is measured, the range and frequency shift settings must be chosen such that the Doppler frequencies corresponding to all the velocities in the profile are within the set frequency range. The appropriate frequency range for a certain profile is determined by the maximum velocity difference within that profile. When very low velocities near the walls are measured, the Doppler frequency is close to the frequency shift itself. In that case a positive frec⋯⋯ shift within the processor's frequency range must be used. However, when ⋯⋯ velocity is
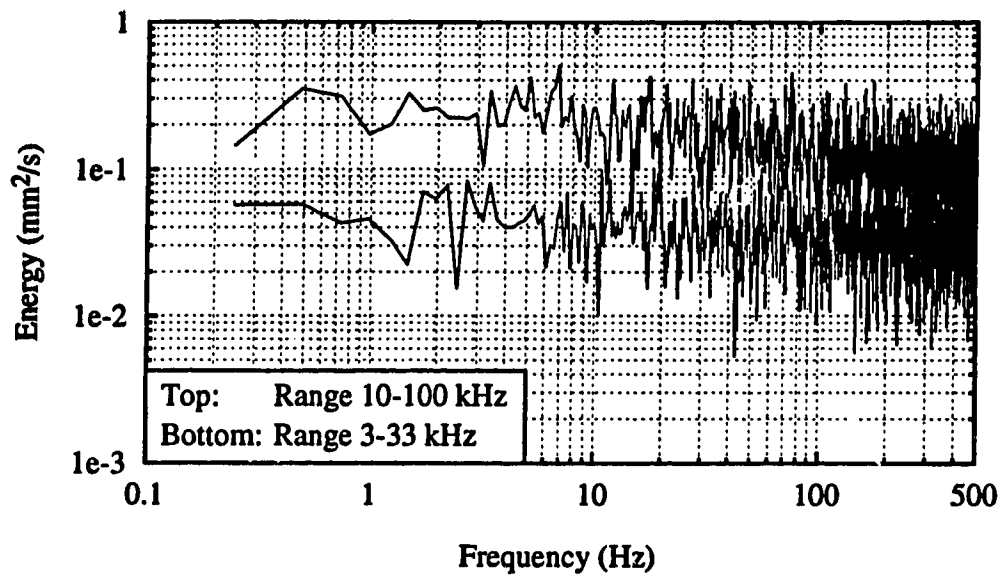
Figure 4.1: Inlet velocity spectra for Re=395 (Dn=101.6). Spectra were averaged over 7 blocks of 4096 values each, sampled at 1000 Hz.
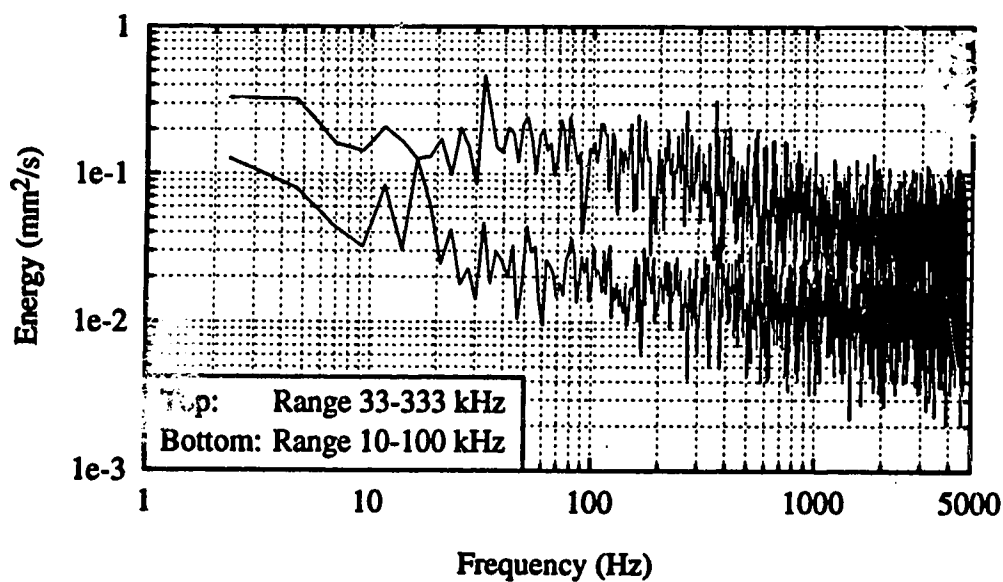
Figure 4.2: Inlet velocity spectra for Re=1951 (Dn=501.9). Spectra were averaged over 7 blocks of 4096 values each, sampled at 9500 Hz.
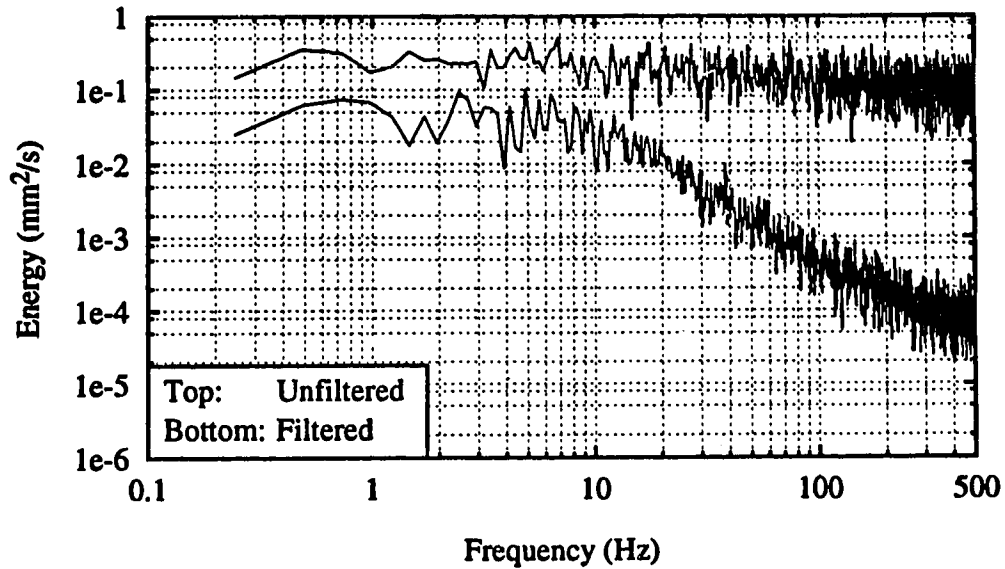
Figure 4.3: Filtered and unfiltered inlet velocity spectra for $Re=395$ ($Dn=101.6$). Range 10-100 kHz.
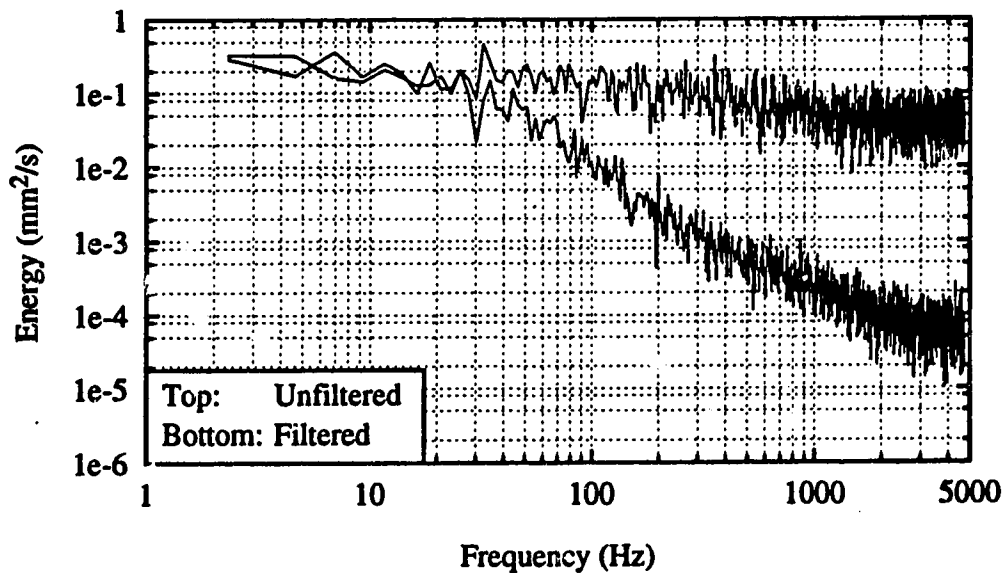
Figure 4.4: Filtered and unfiltered inlet velocity spectrum for $Re=1951$ ($Dn=501.9$). Range 33-333 kHz.

		Minimum in duct centre			Centre region of profiles		
Re	*Dn*	Signal fluct. (%)	Range (kHz)	Shift (kHz)	Signal fluct. (%)	Range (kHz)	Shift (kHz)
397	102.1	0.52	3-33	-20	0.8	10-100	+10
774	199.1	0.39	3-33	-40	0.6	··	+10
1162	298.9	0.51	10-100	-10	1.2	...	+35
1558	400.8	0.37	10-100	-50	0.9	...	+35
1945	500.2	0.39	10-100	-100	0.9	33-333	+35
2329	599.1	0.42	10-100	-150	0.9	33-333	+35

Table 4.2:   Minimum measured fluctuations of the filtered velocity signal in the centre of the duct and average filtered signal fluctuations in the centre region of measured profiles.

measured, only the Do   r frequency corresponding to this velocity has to be within the frequency range   ower range settings and negative frequency shifts can be used.

The measured signal fluctuation tends to be lower when a low frequency range is used. It is not clear why this is, although it is not caused by the resolution of the A/D converter that converts the analog voltage signal from the tracker processor into a 12 bit digital signal (range 0-4095). At a range setting of 10-100 kHz, the velocity resolution is 0.04 mm/s and at a range setting of 33-333 kHz the velocity resolution is 0.14 mm/s. In both cases the velocity resolution is well below 0.1% of the streamwise velocity in most of the flow field.

The minimum filtered signal fluctuations when measuring only the velocity in the centre of the duct are around 0.4-0.5%. For these measurements low range settings and negative frequency shifts were used. The average signal fluctuations in

the centre region of the radial and spanwise velocity profiles that will be discussed in the next section are around 1%, or twice as high as the minimum signal fluctuation in the duct centre. These profiles required higher range settings and positive frequency shifts.

Because the flow in the curved section is very sensitive to small inlet perturbations, it is important to know whether there are any dominant frequencies present in the velocity fluctuations. The difference between the two spectra in each of the figures 4.1 and 4.2 is due to measurement noise. This contribution to the measurement noise is clearly broad band and does not have any dominant frequencies.

Turbulence intensity spectra can be obtained by subtracting the measurement noise from the total signal fluctuations. The spectra of those runs that produc d the lowest signal fluctuations set an upper limit to the turbulence intensity spectra. It seems likely that the contribution of the measurement noise to these spectra is also broad band, although it is not known how much of the total fluctuations is due to measurement noise. With this assumption the turbulence intensity spectra will also be broad band and without dominant frequencies.

4.2 Inlet Profiles

In order to compare experimental results with flow development simulations, it is important to know the flow conditions at the inlet of the curved section. The stilling chamber and inlet section of the apparatus were designed to provide a fully developed velocity profile at the inlet of the curved section for Dn up to 225 ($Re = 875$). The analytical solution for the streamwise velocity distribution of fully developed laminar flow in a rectangular straight duct is given by Shah and London (1978):

$$v'_\theta(x', z') = -\frac{4a^2 c_2}{\mu\pi^3} \sum_{n=1,3,5,\ldots}^{\infty} \frac{1}{n^3}(-1)^{(n-1)/2}\left[1 - \frac{\cosh(n\pi z'/a)}{\cosh(n\pi b/2a)}\right]\cos\left(\frac{n\pi x'}{a}\right) \quad (4.3)$$

$$\overline{v'_\theta} = -\frac{a^2 c_2}{12\mu}\left[1 - \frac{192}{\pi^5}(\frac{a}{b})\sum_{n=1,3,5,\ldots}^{\infty} \frac{1}{n^5}\tanh\left(\frac{n\pi b}{2a}\right)\right] \quad (4.4)$$

$$-a/2 \le x' \le a/2 \qquad -b/2 \le z' \le b/2$$

where: $v'_\theta(x', z')$ = streamwise velocity

$\overline{v'_\theta}$ = average streamwise velocity in the duct

a, b = duct width and height respectively

μ = absolute viscosity

c_2 = pressure gradient in streamwise direction

Shah and London also give a simple approximation to this series solution. The non-dimensional streamwise velocity according to this approximation is given by:

$$v_\theta = \left(\frac{m+1}{m}\right)\left(\frac{n+1}{n}\right)\left[1 - \left(\frac{2z'}{b}\right)^n\right]\left[1 - \left(\frac{2x'}{a}\right)^m\right] \quad (4.5)$$

For a square cross section, where $a = b$, the values of the exponents are $m = n = 2.2$. The maximum difference between the analytical solution and the approximation is in the centre of the duct, where the streamwise velocity calculated with the approximate solution is 1% higher than the analytical solution. The simple approximation is used as inlet condition for the numerical simulation of developing flows that uses the code by Sankar *et al.* (1988).

Due to elliptic effects of the downstream curved duct flow, the velocity profile at the inlet of the curved section could deviate from fully developed straight duct flow. Humphrey *et al.* (1977) observed strong elliptic effects in a tightly curved square duct with curvature ratio 2.3. He showed numerically the presence of a 2-cell

secondary flow at the inlet plane. Inlet secondary flows were about half the strength of the secondary flows at $\theta = 90°$. Bara (1991) did not expect significant elliptic effects in the large curvature duct used in this study ($R_c = 15.1$).

This assumption was verified by simulations of the inlet section with the simulation package FLOW3D, which solves the fully elliptic Navier-Stokes equations using a control volume approach. The SIMPLEC algorithm (Patankar, 1980) was used for the velocity-pressure coupling and hybrid differencing was used to model the convective terms of the transport equations. A 10 cm long straight inlet section was followed by a 6.7 cm curved section. Fully developed straight duct flow was specified at the inlet of the straight section. A mass flow boundary condition was selected for the outlet of the curved section. A 21x21 volume grid was used in the cross section and a total of 167 cells were used in the streamwise direction. Simulations were performed for Dean numbers ranging from 100 to 600 ($Re = 390 - 2335$).

Results of the simulations showed small secondary velocities in the inlet plane at all studied flow rates. In all cases, the secondary velocities are around 1% of the mean streamwise velocity and point towards the inner wall. No circulation flow has been formed yet. The streamwise velocity distribution is very similar to fully developed straight duct flow, but with the maximum velocity shifted slightly towards the inner wall. This type of secondary flow is similar to simulation results by Humphrey et al. (1977) at 0.3 and 0.9 hydraulic diameters before the inlet plane. Overall the elliptic effects at the inlet are minimal. Only the direction of the velocity vectors is changed by about 1°, while the streamwise velocity distribution is hardly affected. Two hydraulic diameters upstream of the inlet, the secondary flow velocities are less than 0.05% of the mean streamwise velocity and at 5 hydraulic diameters no secondary flows can be observed.

Radial and spanwise profiles of the streamwise velocity were measured 5 hydraulic diameters upstream of the curved section. For radial profiles, velocity samples of 512 values were taken at 48 positions along the radial centre line, $z = 0$, with a traverse step size of 0.2 mm. Spanwise profiles were measured by sampling 512 values at 42 positions along the spanwise centre line, $x = 0$, and a step size of 0.3 mm. The streamwise velocity at each position was calculated by averaging the 512 velocity values. Signal fluctuations were calculated by taking the root mean square of the measured fluctuations, divided by the mean velocity.

Streamwise velocity and signal fluctuation profiles for flow rates up to $Re = 2329$ are shown in figures 4.5-4.16. The measured velocity profiles are compared to the analytical solution. Although much more computationally involved than the simple approximation, an accurate analytical solution can be calculated fairly quickly. Calculation of the radial or spanwise velocity profile through the centre of the duct, using 50 positions and 20 terms of the series expansion in equation 4.3 takes only 0.11 s on a personal computer with 80486 processor running at 33 MHz. The solution with 20 terms is within 0.01% of the exact solution.

Velocity profiles clearly start to deviate from the analytical solution at flow rates higher than $Re = 1162$ ($Dn = 300$). This deviation is most significant in the centre of the duct, where the profiles show a distinct flat velocity region at increasing flow rates. The theory of boundary layer development predicts that, starting from a flat velocity profile at the inlet of the duct, the boundary layers start to grow at the walls. The growing boundary layers will at some distance from the inlet meet, at which point the flow is fully developed. Goldstein and Kreid (1967) determined experimentally the development length in a square duct. They found that $L/d_h = 0.09 Re$, where L is the development length. Based on this correlation, the flow in the 1 m long inlet section reaches fully developed flow up to $Re = 875$
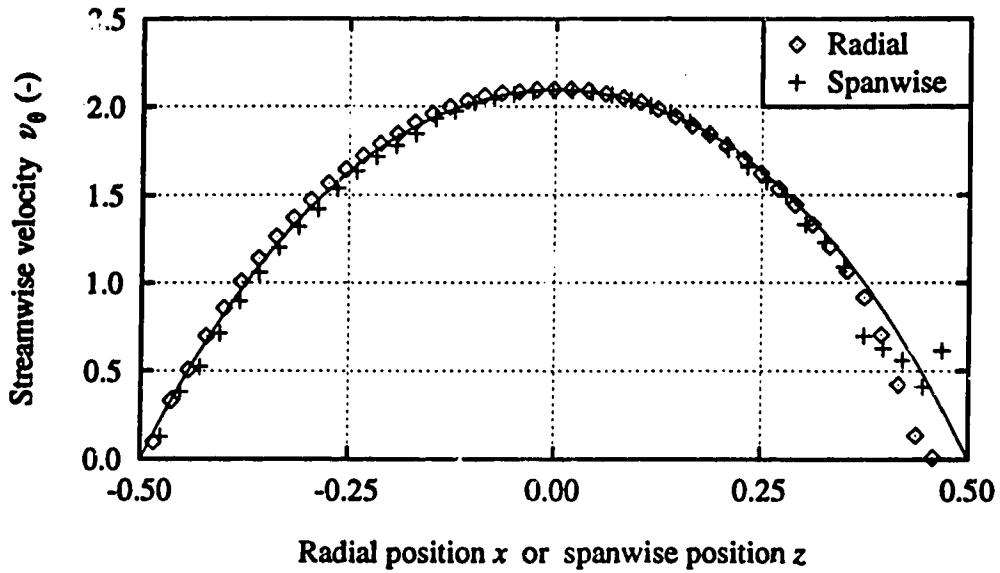
Figure 4.5: Comparison of measured inlet velocity profiles to the analytical solution for $Re=397$ ($Dn=102.1$).
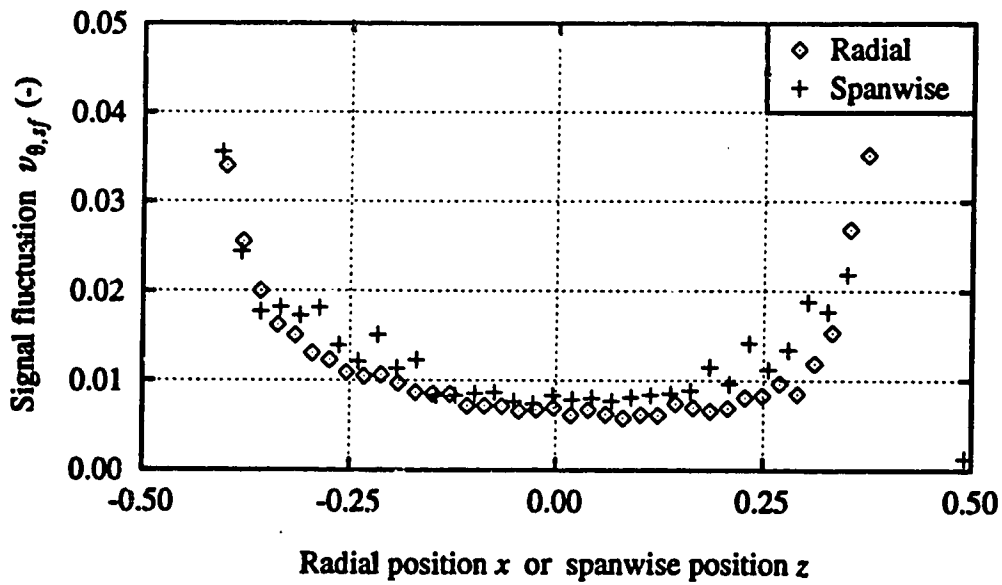
Figure 4.6: Inlet signal fluctuation profiles for $Re=397$ ($Dn=102.1$).
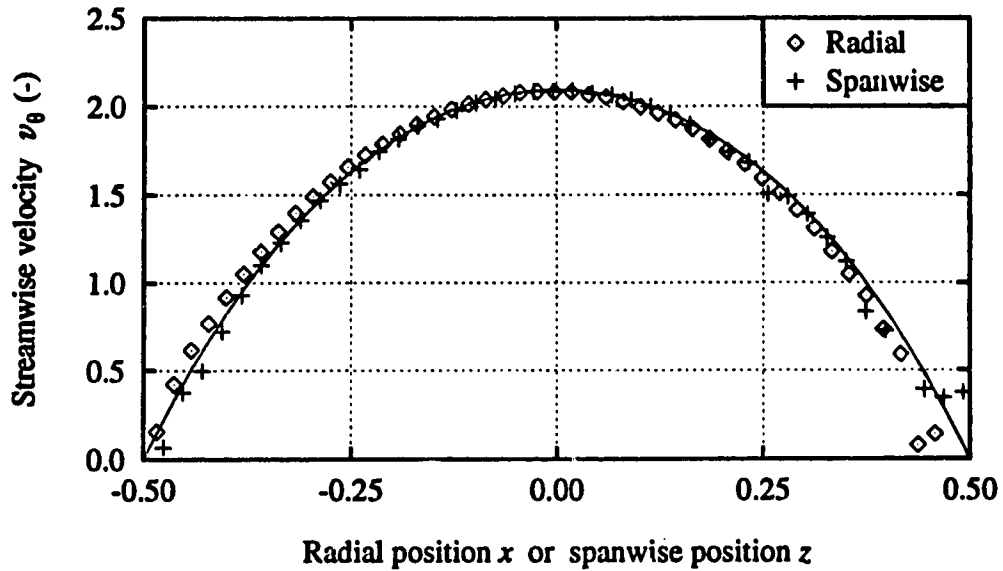
Figure 4.7: Comparison of measured inlet velocity profiles to the analytical solution for Re=774 (Dn=199.1).
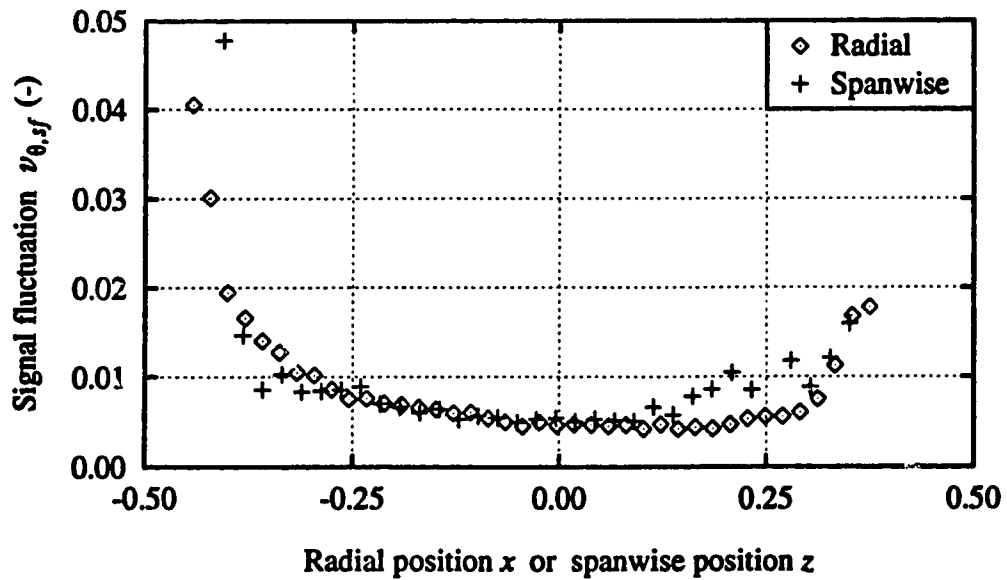
Figure 4.8: Inlet signal fluctuation profiles for Re=774 (Dn=199.1).
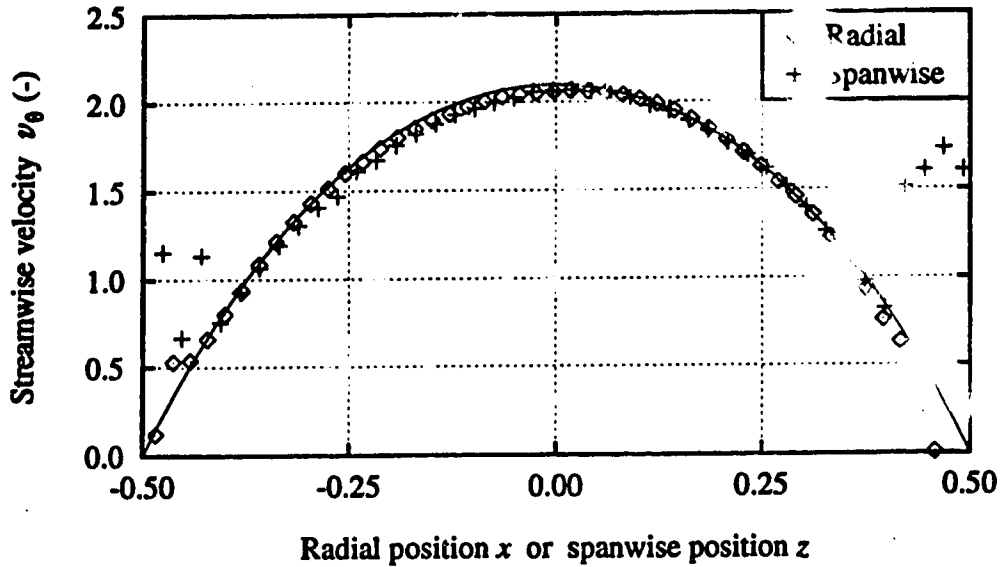
Figure 4.9: Comparison of measured inlet velocity profiles to the analytical solution for $Re=1162$ ($Dn=298.9$).
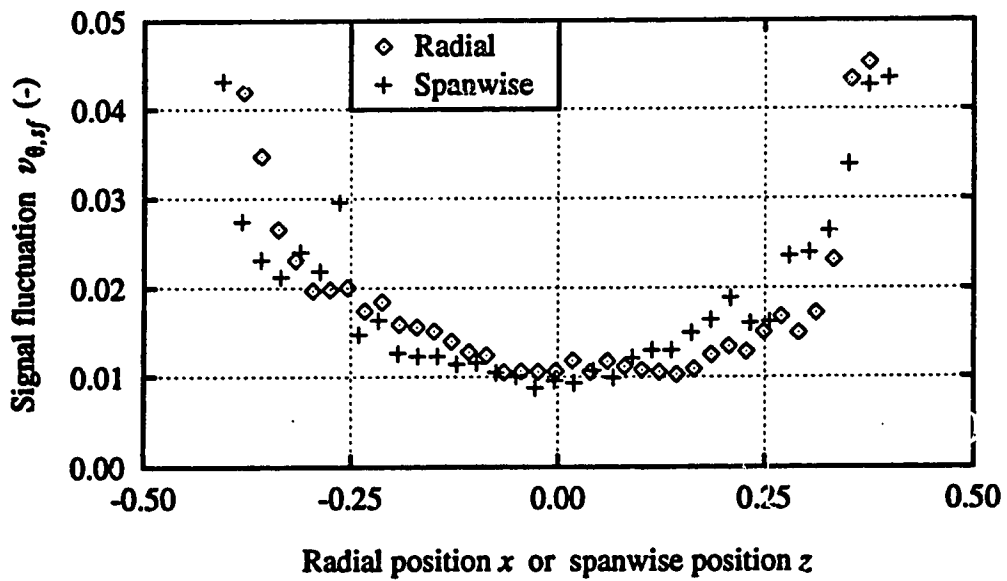
Figure 4.10: Inlet signal fluctuation profiles for $Re=1162$ ($Dn=298.9$).
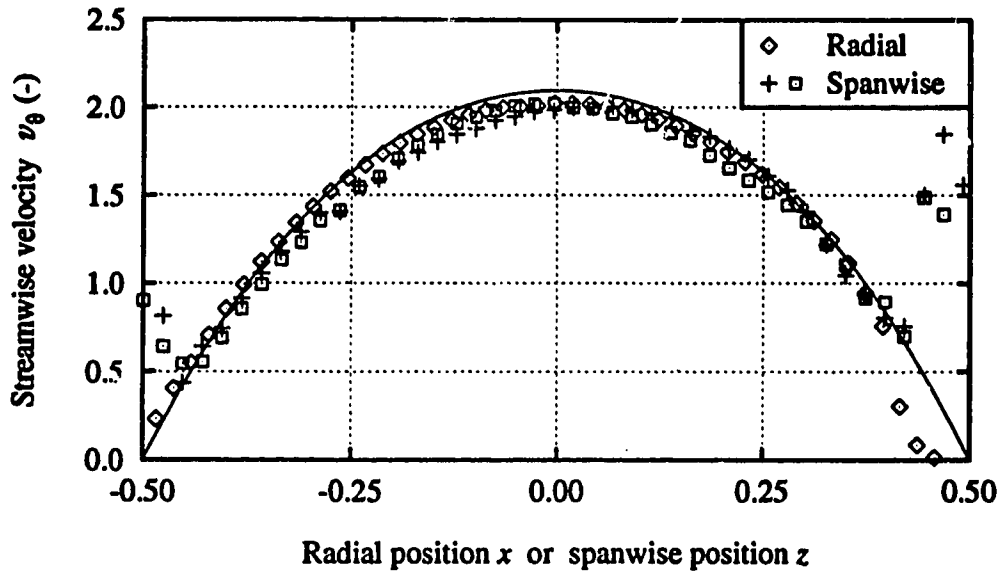
Figure 4.11: Comparison of measured inlet velocity profiles to the analytical solution for $Re=1558$ ($Dn=400.8$).
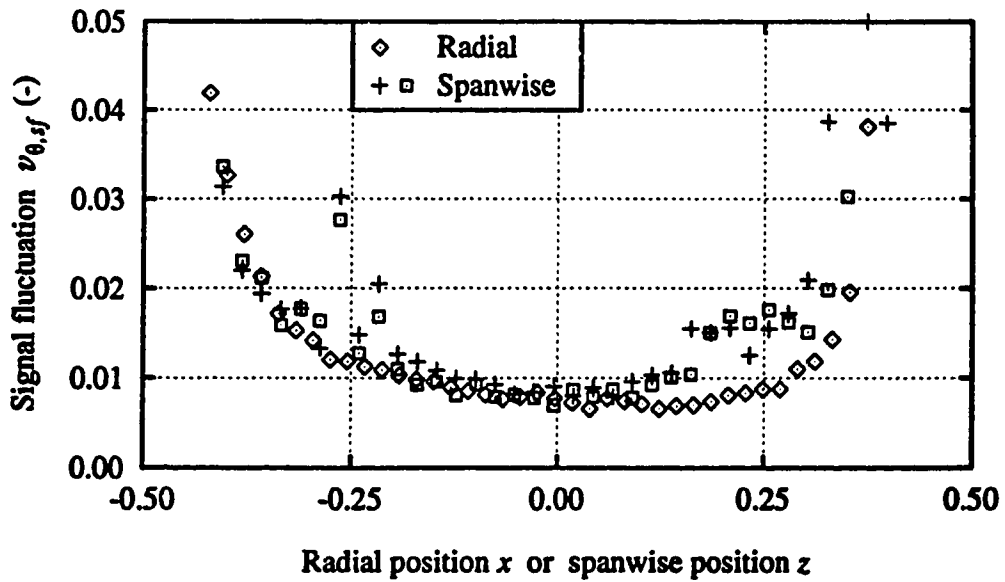
Figure 4.12: Inlet signal fluctuation profiles for $Re=1558$ ($Dn=400.8$).
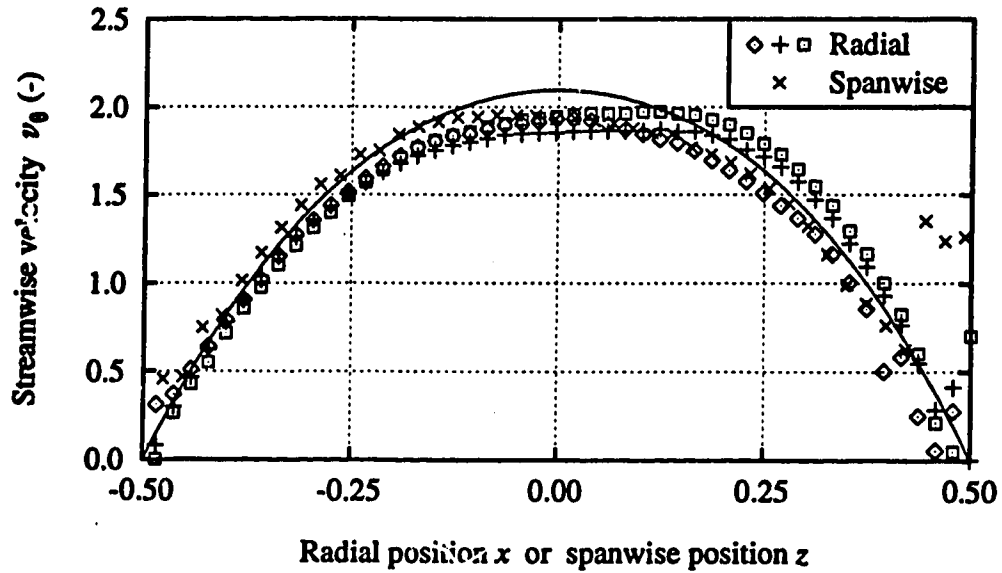
Figure 4.13: Comparison of measured inlet velocity profiles to the analytical
solution for Re=1945 (Dn=500.2).
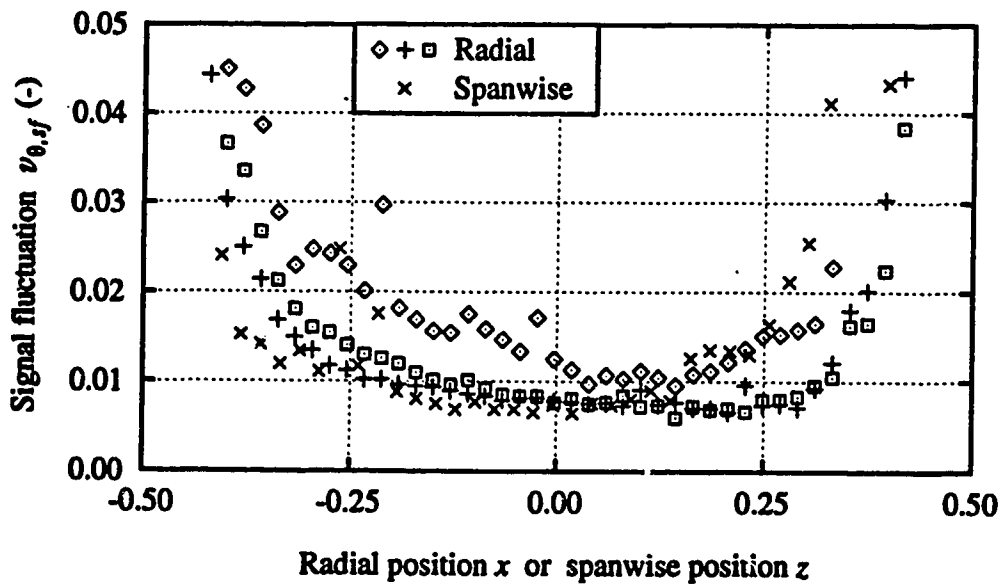
Figure 4.14: Inlet signal fluctuation profiles for Re=1945 (Dn=500.2).
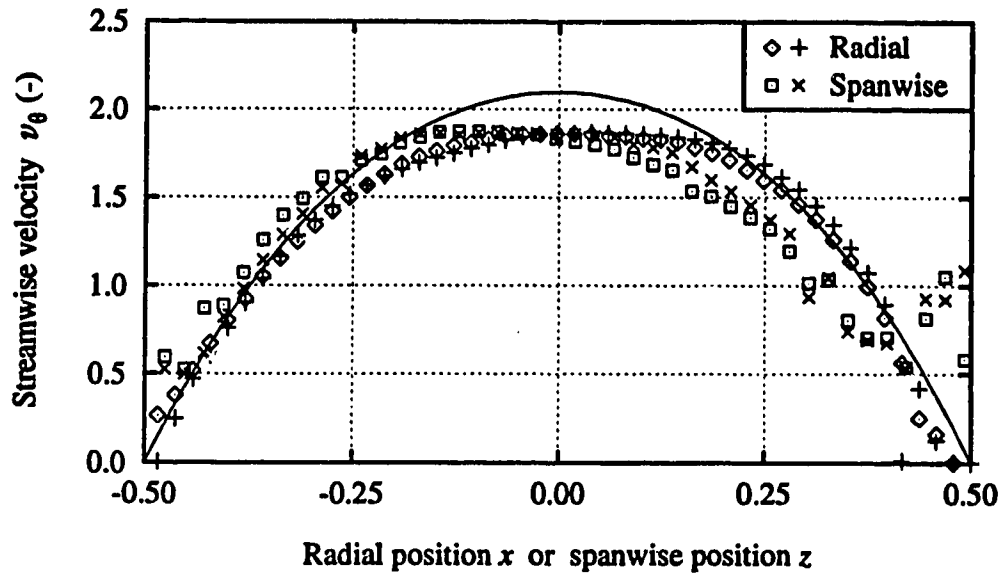
Figure 4.15: Comparison of measured inlet velocity profiles to the analytical solution for $Re=2329$ ($Dn=599.1$).
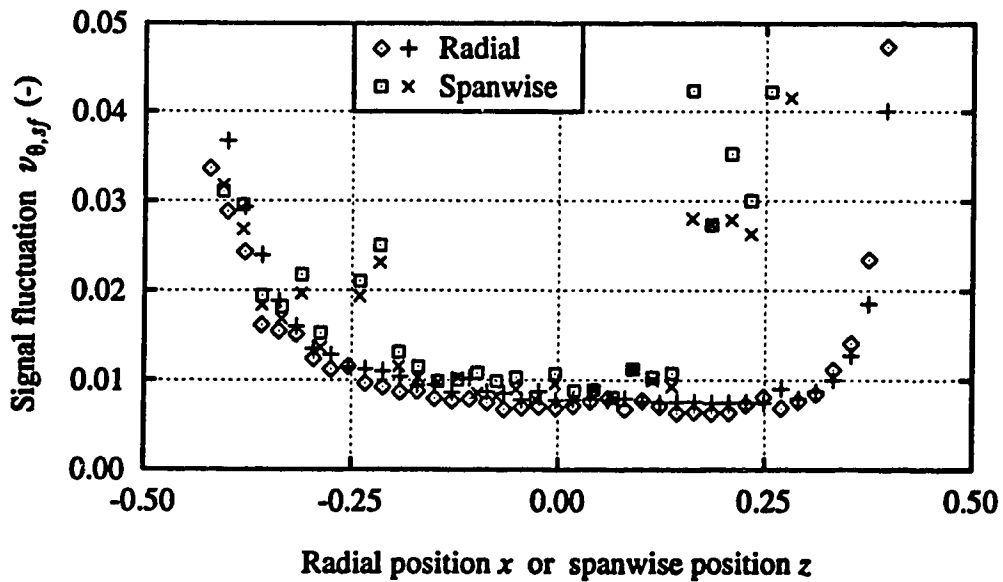
Figure 4.16: Inlet signal fluctuation profiles for $Re=2329$ ($Dn=599.1$).
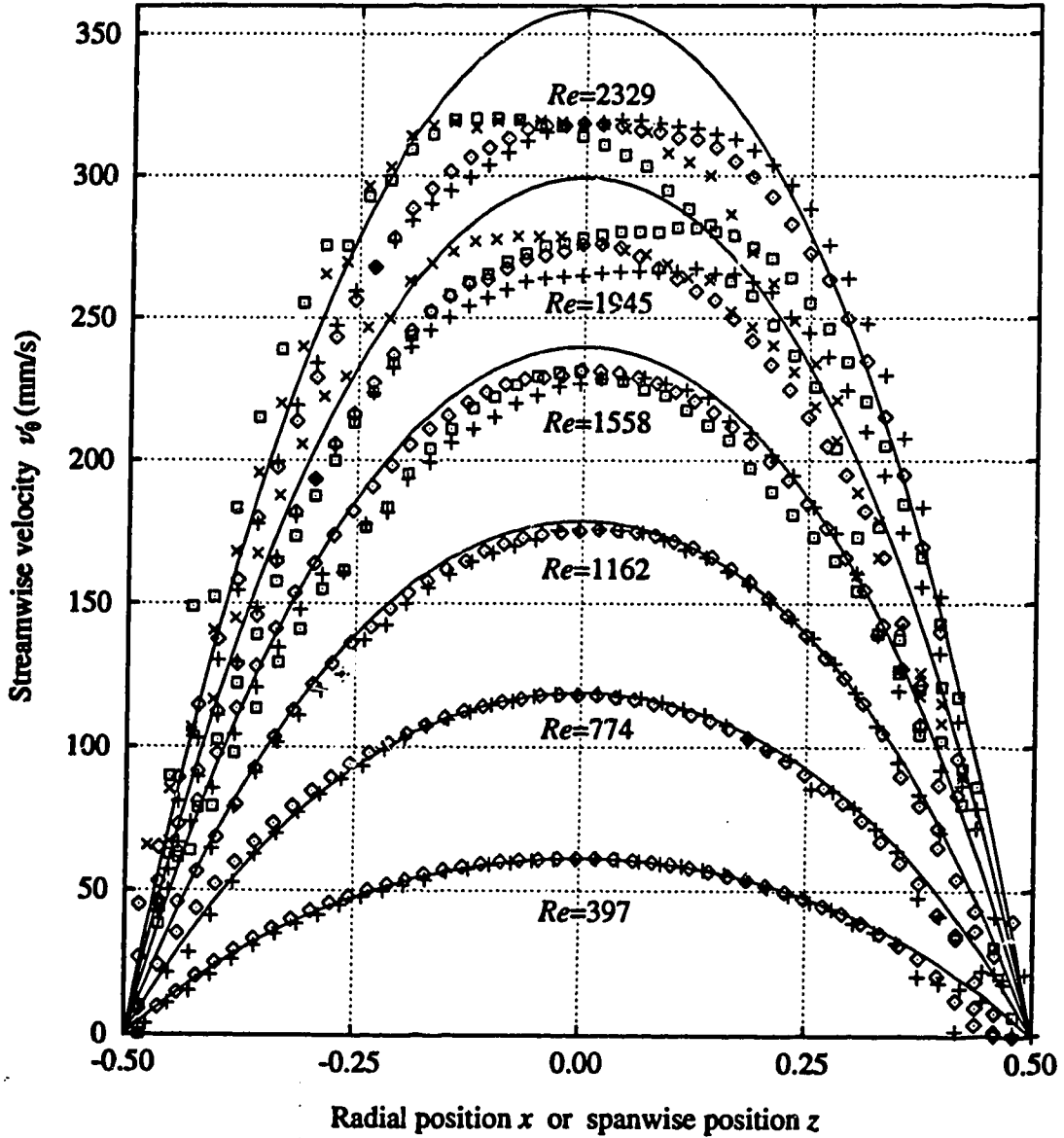
Figure 4.17: Inlet velocity profiles for Re=397-2329 (Dn=102.1-599.1).

($Dn = 225$). The flat regions of the velocity profiles at $Re = 1945$ ($Dn = 500.2$) and $Re = 2329$ ($Dn = 599.1$) indicate that the boundary layers have not merged yet. The streamwise velocity profiles are summarized in figure 4.17.

The deviation of the experimental profiles from the analytical solution is quantified by the difference between the maximum velocities of both profiles. These results are summarized in table 4.3. A velocity profile can be considered fully developed if the velocity is within 99% of the fully developed profile. The results show that for flow rates up to $Re = 774$ ($Dn = 200$) the centre velocity is within 99% of the fully developed value. At higher flow rates the flow is no longer fully developed. These results are in good agreement with the development length correlation by Goldstein and Kreid (1967).

The average signal fluctuation in the centre region of the profiles, summarized in table 4.2, was around 1%. The signal fluctuation increases significantly near the walls. This is caused mainly by the decreasing streamwise velocity and not so much by an increase in the signal fluctuations.

The velocity profiles at $Re = 1945$ and 2329 (figures 4.13 and 4.15) show that at these high flow rates the flow is not steady. The three radial profiles at $Re = 1945$ were taken shortly after each other, but show significant differences. This observation led to an investigation of the flow steadiness.

Re	Dn	Profile	Maximum v_θ	Deviation (%)	Average
397	102.1	Radial	2.098	-0.10	0.10
		Spanwise	2.090	0.29	
774	199.1	Radial	2.085	0.53	0.41
		Spanwise	2.090	0.29	
1162	298.9	Radial	2.063	1.60	1.60
		Spanwise	2.064	1.60	
1558	400.8	Radial	2.025	3.51	3.96
		Spanwise-1	2.002	4.70	
		Spanwise-2	2.022	3.66	
1945	500.2	Radial-1	1.933	8.43	8.61
		Radial-2	1.866	12.33	
		Radial-3	1.973	6.23	
		Spanwise	1.951	7.43	
2329	599.1	Radial-1	1.861	12.63	12.24
		Radial-2	1.869	12.15	
		Spanwise-1	1.872	11.97	
		Spanwise-2	1.868	12.21	

Table 4.3: Summary of radial and spanwise inlet profiles of the streamwise velocity with maximum streamwise velocity and deviation from a fully developed profile.

4.3 Flow Steadiness

It is clear from figure 4.13 that at higher flow rates the flow is not only not fully developed, but also not steady. The velocity fluctuations associated with this flow unsteadiness occur at a much larger time scale than the random fluctuations and measurement noise discussed in section 4.1. In order to quantify the flow steadiness, the fluctuation of the mean flow over a longer period of time was investigated. 60 samples of 512 streamwise velocity values, taken at 100 Hz, were collected at 1 minute intervals. These samples were taken at $x = 0.24$ and $z = 0$, where figure 4.13 shows a significant variation of the streamwise velocity. The mean velocities of these 60 samples are shown in figure 4.18 for different flow rates. The fluctuation of the means of these 60 samples, defined as the root mean square of the mean velocity divided by the average of the mean velocities, is a measure of the slow fluctuations in the flow.

As mentioned in section 3.5, the signal fluctuation of a quantity with constant mean is reduced by a factor of $\sqrt{n}$ when averaged over a large number of sample values, n. The measured fluctuations of the mean are listed in table 4.4. At $Re = 1545$, 1940 and 2330, two sets of data were collected on two different days. At none of the flow rates was the signal fluctuation reduced by a factor of $\sqrt{512} = 22.6$, indicating that there is a slow fluctuation of the mean velocity at all flow rates.

However, the flow was still considered steady if 95% of the measured mean velocities are within $\pm$ 1% of the mean flow, or when the fluctuation of the mean is less than 0.5%. Although the fluctuation of the mean at a certain flow rate can vary significantly, depending on when the data were collected, the flow is generally only steady for flow rates up to $Re = 770$ ($Dn = 200$).

At $Re = 1940$ ($Dn = 500$) and $Re = 2330$ ($Dn = 600$) the slow velocity
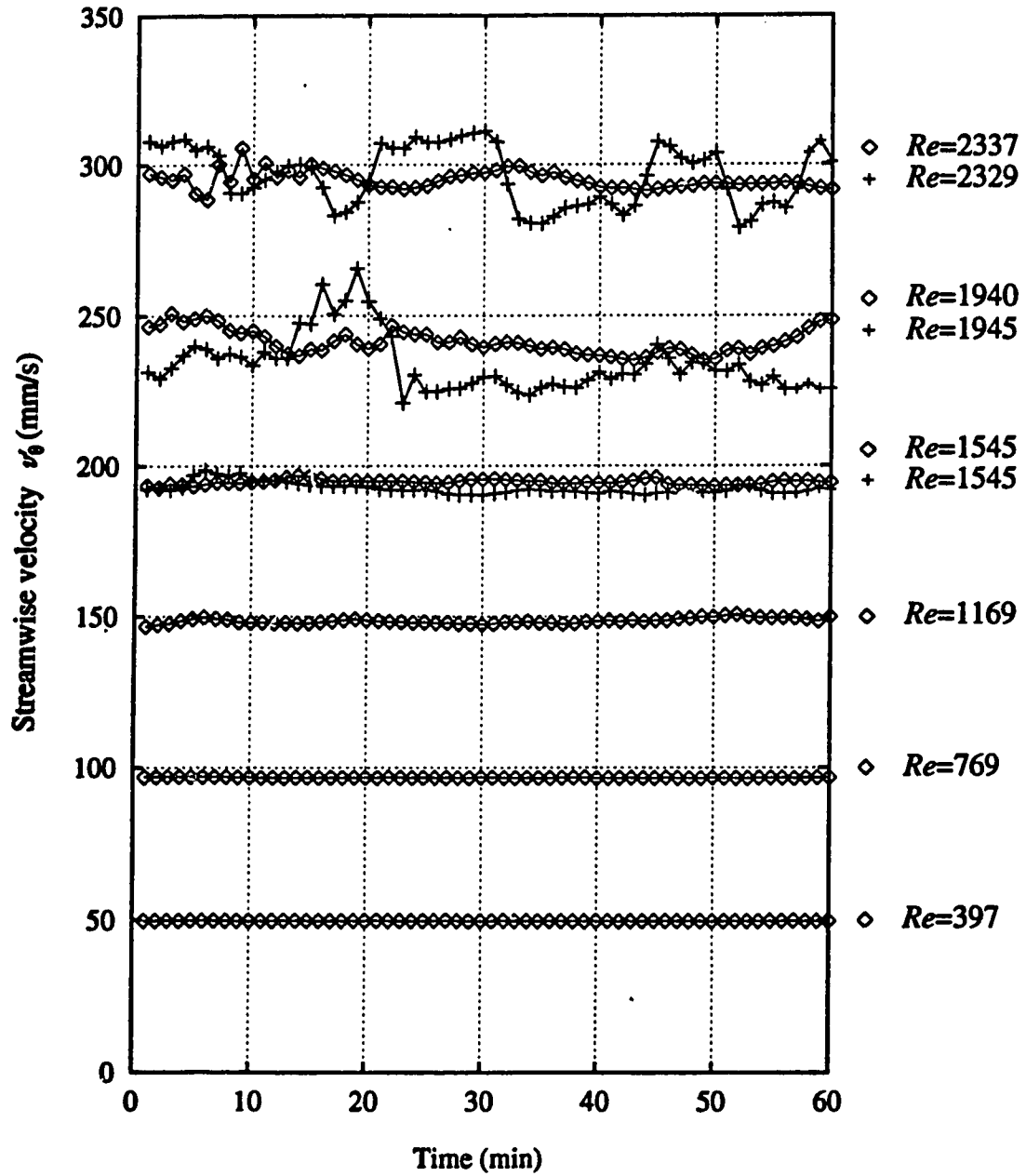
Figure 4.18:   Flow steadiness measurements.   Shown are mean velocities of 60
            samples at 1 minute intervals with 512 velocity values each.

Re	Dn	Average signal fluctuation (%)	Fluctuation of the mean (%)	Ratio
397	102.1	0.95	0.12	7.71
769	197.7	0.60	0.12	4.85
1169	300.6	1.48	0.56	2.63
1545	397.4	1.05	0.43	2.47
1545	397.5	0.94	1.02	0.92
1940	498.9	0.95	1.70	0.56
1945	500.2	0.81	4.01	0.20
2337	601.0	0.71	1.01	0.70
2329	599.1	0.75	3.33	0.23

Table 4.4: Average signal fluctuation of 60 velocity samples, with 512 velocity values each, and the fluctuation of the means of these 60 samples.

fluctuations related to the flow unsteadiness are much larger than the fast fluctuations and measurement noise. This is reflected by an increase of the signal fluctuation. At these high flow rates the flow field can change significantly during the 6 minutes it takes to measure a velocity profile.

4.4 Summary

The flow at the inlet of the curved section was investigated for flow rates up to $Dn = 600$ ($Re = 2335$). Measured fluctuations of the filtered velocity signal are typically between 0.5% and 2% of the mean streamwise velocity, and are a combination of velocity fluctuations and measurement noise. Most of the signal

fluctuation is caused by measurement noise; the turbulence intensity is very low at all flow rates, and does not contain any dominant frequencies.

Inlet profiles along the radial and spanwise centre lines were measured for Dean numbers up to 600 ($Re = 2335$), and compared to the analytical solution. Above $Dn = 200$ ($Re = 774$), the difference between the measured velocity and the analytical solution in the centre of the duct is more than 1%. At these high flow rates the inlet profiles are not fully developed, as is indicated by a flat centre region.

Slow velocity fluctuations were a sign of unsteadiness of the flow. The unsteadiness was quantified by measuring the streamwise velocity at $x = 0.24$ and $z = 0$ every minute, for one hour. The fluctuations of the mean velocities showed that above $Dn = 200$ ($Re = 774$) the flow is generally unsteady, but results vary from day to day.

Chapter 5

Steady Developing Flows

The development of steady flows up to a Dean number of 600 was investigated both experimentally and numerically. The experimental flow development was studied using visualization of secondary flow patterns and LDA measurements of profiles of the streamwise and spanwise velocity. The experiments are compared to results of a numerical simulation of the three-dimensional parabolized Navier-Stokes equations. A 6-cell flow state with two pairs of Dean vortices was observed both in the experiment and in the numerical simulation. The numerical code was also used to predict flow behaviour up to $\theta = 2000°$, and to study flow stability. This is the first time that detailed experiments and simulations of a 6-cell flow state in a curved duct of square cross section are reported.

First the governing equations and numerical code will be discussed. Then the different transitions that take place, in particular the transition to a 6-cell flow state will be introduced, followed by a detailed investigation of the flow development at $Dn = 272, 326, 375$ and 453. The transition to 6-cell flow will be explained by using the analogy with the Görtler problem. Stability considerations conclude this chapter.

5.1 Governing Equations

The curved square duct geometry used in this study is most conveniently described by a cylindrical coordinate system, shown in figure 5.1. r, θ and z are the radial, streamwise and spanwise coordinates respectively. The streamwise direction is sometimes called the axial direction. This terminology is inconsistent with a cylindrical coordinate system, but avoids confusion with existing literature. Early work in this field on curved circular pipes used a toroidal coordinate system in which case the streamwise velocity is along the axis of the pipe. In the cylindrical coordinate system the main flow is actually in the tangential direction and the spanwise velocity is actually in the axial direction. The duct walls are located at $z' = \pm a/2$ and $x' = \pm a/2$, where $x' = r' - R$. The flow perpendicular to the streamwise direction, in a plane containing the radial and spanwise components, is called the secondary flow.

The computer code used to track the flow development solves a parabolized version of the three-dimensional, stationary Navier-Stokes equations and does not adopt the loose coiling approximation. This code was developed by Sankar *et al.* (1988) and was modified to include the possibility to impose symmetry along $z = 0$. The streamwise momentum diffusion terms in the full three-dimensional steady state Navier-Stokes equations were neglected, allowing for a simple marching-step method, rather than a global, elliptic solution method. Although not part of the parabolization, the gradient of v_r in the θ direction was also neglected. The terms that were neglected are:

$$\frac{1}{Re\,r^2}\frac{\partial^2 v_r}{\partial \theta^2}, \qquad \frac{1}{Re\,r^2}\frac{\partial^2 v_\theta}{\partial \theta^2}, \qquad \frac{2}{Re\,r^2}\frac{\partial v_r}{\partial \theta}, \qquad \text{and} \qquad \frac{1}{Re\,r^2}\frac{\partial^2 v_z}{\partial \theta^2}.$$

Because these terms are proportional to $1/Re\,r^2$, the effect of neglecting them
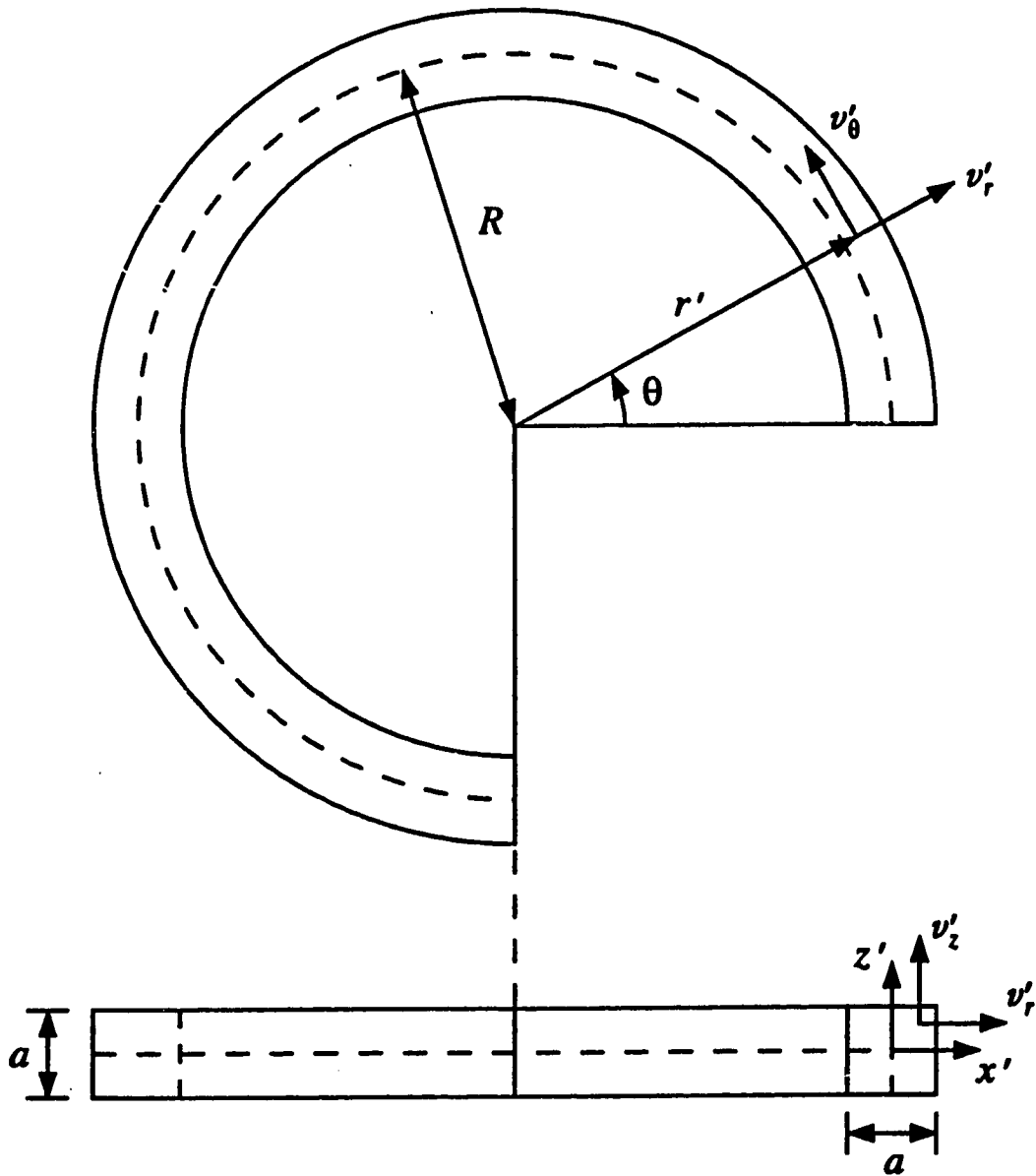
Figure 5.1: Cylindrical coordinate system.

will be smaller when the flow rate and the radius of curvature increase.

The non-dimensional parabolized Navier-Stokes equations for steady incompressible Newtonian flow are:

continuity

$$\frac{1}{r}\frac{\partial}{\partial r}(rv_r) + \frac{1}{r}\frac{\partial v_\theta}{\partial \theta} + \frac{\partial v_z}{\partial z} = 0 \tag{5.1}$$

momentum in r direction

$$v_r\frac{\partial v_r}{\partial r} + \frac{v_\theta}{r}\frac{\partial v_r}{\partial \theta} - \frac{v_\theta^2}{r} + v_z\frac{\partial v_r}{\partial z} = -\frac{\partial p}{\partial r} + \frac{1}{Re}\left[\frac{\partial}{\partial r}\left(\frac{1}{r}\frac{\partial}{\partial r}(rv_r)\right) - \frac{2}{r^2}\frac{\partial v_\theta}{\partial \theta} + \frac{\partial^2 v_r}{\partial z^2}\right] \tag{5.2}$$

momentum in θ direction

$$v_r\frac{\partial v_\theta}{\partial r} + \frac{v_\theta}{r}\frac{\partial v_\theta}{\partial \theta} + \frac{v_r v_\theta}{r} + v_z\frac{\partial v_\theta}{\partial z} = -\frac{1}{r}\frac{\partial p}{\partial \theta} + \frac{1}{Re}\left[\frac{\partial}{\partial r}\left(\frac{1}{r}\frac{\partial}{\partial r}(rv_\theta)\right) + \frac{\partial^2 v_\theta}{\partial z^2}\right] \tag{5.3}$$

momentum in z direction

$$v_r\frac{\partial v_z}{\partial r} + \frac{v_\theta}{r}\frac{\partial v_z}{\partial \theta} + v_z\frac{\partial v_z}{\partial z} = -\frac{\partial p}{\partial z} + \frac{1}{Re}\left[\frac{1}{r}\frac{\partial}{\partial r}\left(r\frac{\partial v_z}{\partial r}\right) + \frac{\partial^2 v_z}{\partial z^2}\right] \tag{5.4}$$

Global continuity requires that

$$\int_{z=-0.5}^{z=0.5}\int_{r=R_c-0.5}^{r=R_c+0.5} v_\theta\, dr\, dz = 1.0 \tag{5.5}$$

The variables have been non-dimensionalized as follows

$$r = \frac{r'}{a} = R_c + x \qquad x = \frac{x'}{a} \qquad z = \frac{z'}{a} \qquad R_c = \frac{R}{a}$$

$$v_r = \frac{v_r'}{\overline{v_\theta'}} \qquad v_\theta = \frac{v_\theta'}{\overline{v_\theta'}} \qquad v_z = \frac{v_z'}{\overline{v_\theta'}} \qquad p = \frac{p'}{\rho \overline{v_\theta'}^2} \qquad Re = \frac{\rho a \overline{v_\theta'}}{\mu}$$

where the prime denotes dimensional quantities. Note that all velocity components were non-dimensionalized by dividing by the mean streamwise velocity.

The code by Sankar et al. (1988) discretizes the equations by integrating them over a control volume and solves the equations using the SIMPLE algorithm as

outlined by Patankar (1980). Equally spaced grids were used, ranging in size from 51x51 to 151x151 points. Axial step sizes ranged from $1/4°$ for a coarse grid to $1/256°$ for the finest grid. The calculations were performed in double precision on IBM RS/6000 375 and 560 machines.

5.2 Transition to 6-Cell Flow

Bara (1991; 1992) investigated experimentally the flow development up to $\theta = 240°$ at Dean numbers of 125, 137 and 150. His results are in quantitative agreement with Winters' numerical study of fully developed flows in a curved duct of square cross section (Winters, 1987). Winters' results are represented in the state diagram of figure 5.2. In this diagram, χ_s, which is a measure for the symmetric component of the solution, is shown as a function of the control parameter, Dn.

For a loosely coiled duct, the state diagram consists of a stable 2-cell branch, S_1, starting at the origin and connected to a 4-cell branch, S_3, which is unstable with respect to asymmetric disturbances. The connecting branch S_2 is unstable. There is a stable 2-cell solution and a conditionally stable 4-cell solution in the region between limit points L_1 and L_2 for $113 < Dn < 131$. The 2-cell and 4-cell branches, up to a Dean number of 150, were confirmed experimentally by Bara (1991; 1992). The state diagram also shows an isolated branch of 2-cell flows and unstable 4-cell flows, connected by limit point L_3 at $Dn = 191$. Winters reported that the isolated 2-cell flow is stable, but found later only parts of this branch to be stable (Winters, private communication). The dashed line represents a pair of unstable asymmetric solution branches. No unconditionally stable fully developed flows exist for Dean numbers between 131 and 191. The results of the flow development study presented here as well as the unsteady flow phenomena of the next chapter will be interpreted
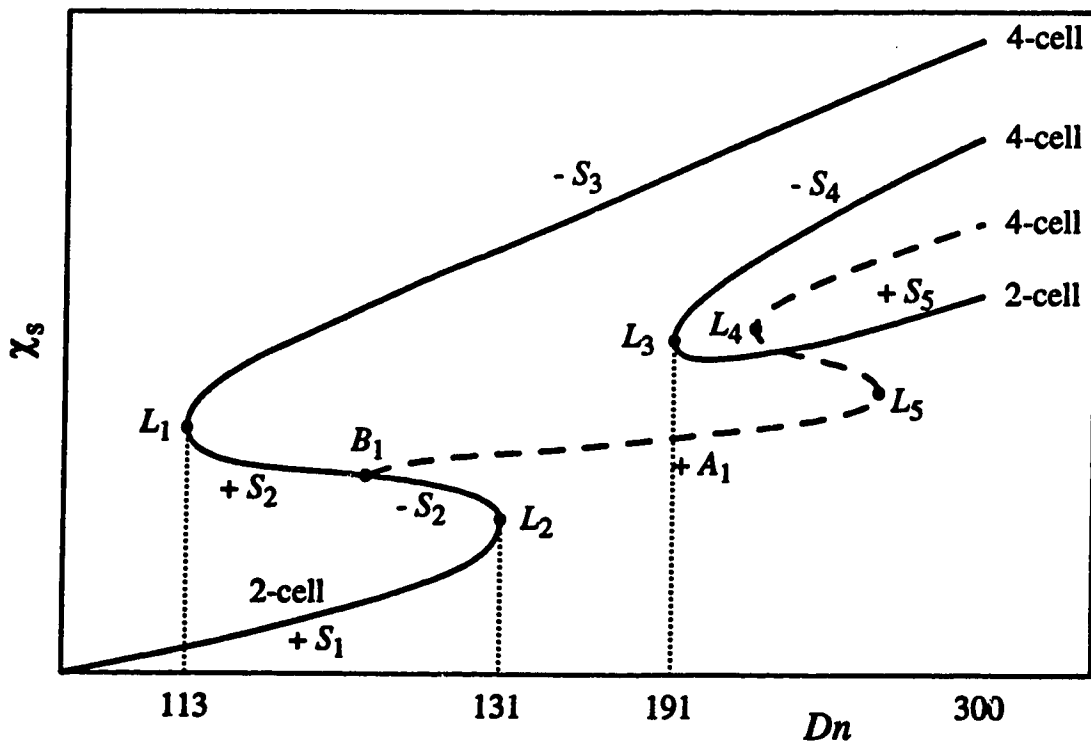
Figure 5.2: State diagram of fully developed solutions for a loosely coiled curved duct of square cross section. The sign of each branch is $(-1)^n$, where n is the number of negative eigenvalues of the Jacobian matrix. After Winters (1987).

in the context of this state diagram.

The location of the limit points varies very little for curvature ratios above 10, but at smaller curvature ratios the limit points move to increasingly higher Dean numbers. For a curvature ratio of 15.1, Bara (1991; 1992) located limit points L_1 and L_2 at Dean numbers of 114 and 131.

A convenient method of representing the streamwise flow development is to plot one of the velocity components at some point in the cross section as a function of the streamwise position, θ, in a flow development diagram. All flow development diagrams presented here show the radial velocity at $x = 0.4$ and $z = 0.0$, vertically centered and close to the outer wall. The additional Dean vortices cause this velocity component to change direction during the transition from 2-cell to 4-cell flow, allowing for an easy identification of these flow states.

A series of flow development diagrams, showing the development to $\theta = 2000°$ for Dean numbers up to 600 are presented in figure 5.3. All flow development diagrams were calculated on a 71x71 grid and an axial step size of $1/16°$. Between Dean numbers of 300 and 400 the solution is very sensitive to grid refinement and the development diagrams for these flow rates may not be very accurate. However, the trends discussed in this section are represented accurately by figure 5.3. More detailed results of the flow development up to 240° will be given in the following sections.

At a Dean number of 100 the flow develops into an axially invariant 2-cell state, the primary solution for this geometry. The streamwise length needed to reach a fully developed state is called the development length. An arrow plot of the 2-cell state is shown in figure 5.4a. The 2-cell flow state is induced by the pressure gradients along the top and the bottom (lateral) walls. This can most easily be understood as follows. In pressure driven flow between two curved walls, and no top
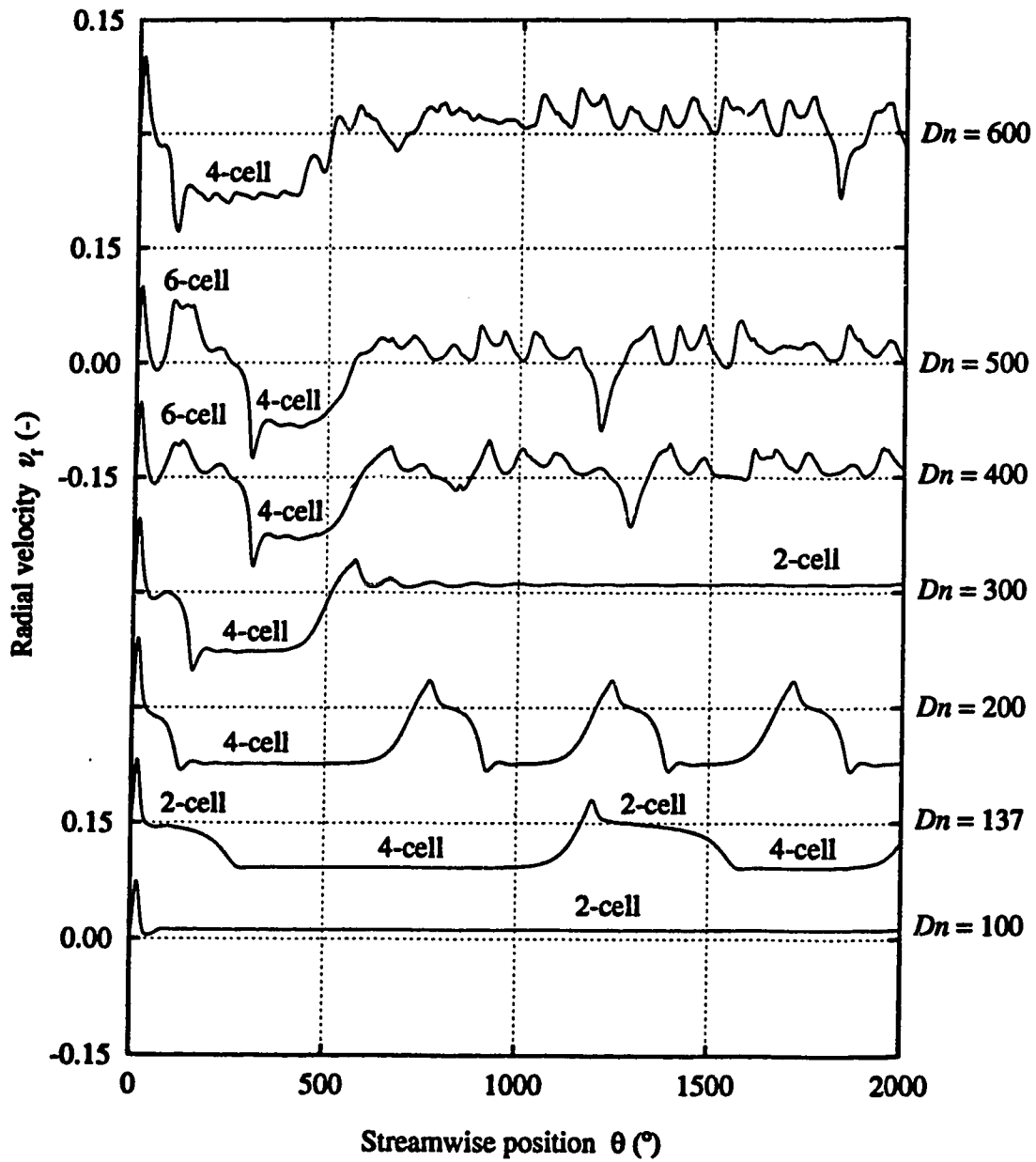
Figure 5.3: Calculated flow development diagrams of the radial velocity at $x = 0.4$, $z = 0.0$, showing the development to $\theta = 2000°$ at various Dean numbers.

Dn=100, θ=500° : 2-cell

Dn=137, θ=500° : 4-cell

Dn=453, θ=90° : 6-cell
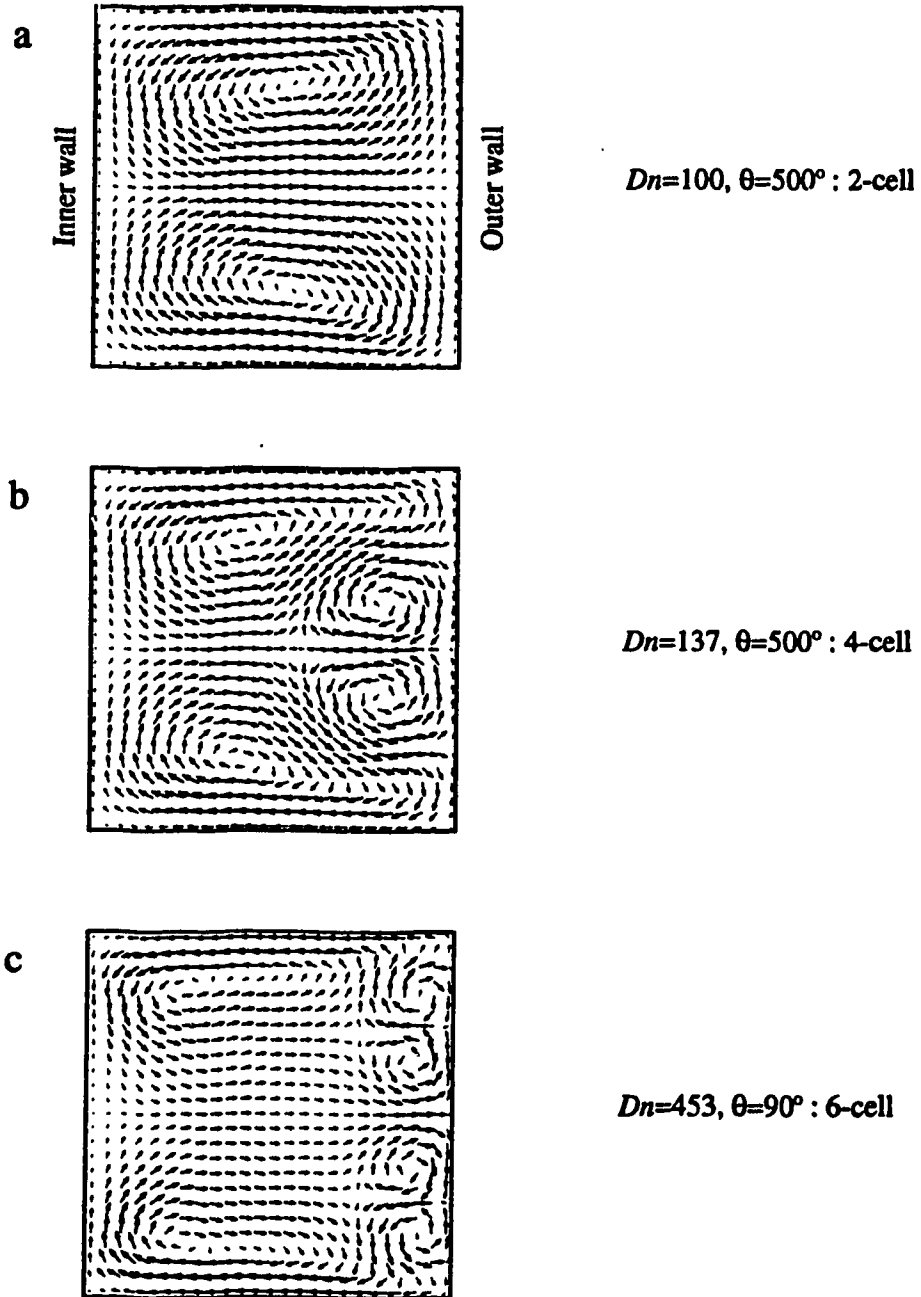
Figure 5.4:   Calculated arrow plots showing 2-cell, 4-cell and 6-cell secondary flow patterns.

and bottom walls, a radially inward pressure gradient develops to counter balance the centrifugal force acting on the fluid. In a duct with top and bottom walls, the centrifugal force near these walls is smaller than toward the centre of the duct because of the lower streamwise velocity in the boundary layers. Therefore, along the lateral walls the pressure gradient is larger than the centrifugal force, forcing the fluid to flow inwards near the lateral walls. For reasons of continuity the secondary flow in the central region of the duct must be towards the outer wall. This shows that the 2-cell flow state will be present starting from zero flow rate and is not the result of a flow instability. Thus, the 2-cell flow is the primary solution, which is connected to the origin of the state diagram.

The described phenomenon is called Ekman pumping and the end vortices are called Ekman vortices. Ekman vortices have also been observed in large aspect ratio ducts. Finlay and Nandakumar (1990) calculated two-dimensional flows in curved channels with aspect ratios between 20 and 30. At low flow rates their study showed the development of two elongated vortices near the top and bottom walls with nearly curved channel Poiseuille flow in the centre of the duct. In a square duct the space for each of the Ekman vortices is limited to half of the cross section, leading to the 2-cell flow state of figure 5.4a.

At a Dean number of 137 the flow initially develops into a 2-cell flow state. Around $\theta = 100°$ a pair of Dean vortices starts to develop near the centre of the outer wall until a fully developed 4-cell flow is reached at $\theta = 300°$. An arrow plot is shown in figure 5.4b. The inflow region between the two Dean vortices creates a negative radial velocity at the monitoring point (figure 5.3). This 4-cell flow remains axially invariant for about 700 degrees before it breaks down into a 2-cell state that again develops into a 4-cell flow pattern. The breakdown of the 4-cell flow is an asymmetric process, during which the Dean vortex pair moves up or down along the

outer wall and folds up into one of the Ekman vortices.

The numerical simulation predicts these spatial oscillations to continue up to a streamwise position of at least 3000°. The Dean vortices alternately fold up in the top and bottom Ekman vortex, although this is not reflected in the flow development diagram due to the choice of the monitoring velocity. Sankar *et al.* (1988) show by varying grid resolution and axial step size that these spatial oscillations are not a numerical artifact of the computer code. Although these results show that the 4-cell flow is unstable, the nature of this instability is uncertain because the numerical code does not include time dependence. The real flow may develop temporal or spatio-temporal oscillations rather than just spatial oscillations. These results are in agreement with Winters' calculations that for $131 < Dn < 191$ no stable fully developed flows exist.

At $Dn = 200$ the flow development is very similar to that at $Dn = 137$. The main difference is that the period of the spatial oscillations is much shorter at this higher flow rate. Although a Dean number of 200 is above the limit point L_3, at $Dn = 191$, the flow does not develop into a stable 2-cell flow. The development of a stable 2-cell flow has only been observed above a Dean number of 230. It could be that at Dean numbers between 191 and 230 the development length of a stable 2-cell is more than 2000°. However, it is more likely that this part of the isolated 2-cell branch, S_5, corresponds to unstable solutions.

At $Dn = 300$ the flow development is initially similar to the development for $Dn = 200$, but once the 4-cell flow breaks down at about $\theta = 500°$, a new 2-cell state forms that remains axially invariant over a long streamwise distance. Is seems likely that in this case the flow has been attracted to a stable 2-cell solution on the isolated branch in the state diagram.

Dean vortices, as observed in the 4-cell flow state, are the result of a centrifugal

instability, which is the primary instability of this system. This kind of instability is most easily explained by looking at three other centrifugally unstable flow systems: Taylor-Couette flow, Görtler flow and curved channel Dean flow.

Most extensively studied is the flow between concentric rotating cylinders, or Taylor-Couette flow. Rayleigh (1916) derived a criterion for the centrifugal instability of inviscid flow, now called the Rayleigh discriminant:

$$\Phi = r^{-3}\frac{d(rv_\theta)^2}{dr} \tag{5.6}$$

The flow is centrifugally unstable if the Rayleigh discriminant is negative. In most early studies of Taylor-Couette flow, the outer cylinder was kept stationary while the inner cylinder was rotating. In this case Rayleigh's discriminant is negative everywhere in the system, and therefore the flow is centrifugally unstable. This instability causes the formation of toroidal vortices with opposite sense of rotation, called Taylor vortices (figure 5.5). Rayleigh's criterion predicts the flow to be centrifugally unstable at any flow rate. However, in a viscous fluid small disturbances are dissipated by viscosity. This dissipation prevents the onset of Taylor vortices at low flow rates. Only at higher flow rates, where disturbances overcome the viscous forces, does a transition to Taylor vortices take place.

A second centrifugally unstable system is flow over a concave wall, or Görtler problem (see figure 5.5). In this case the flow in the boundary layer is centrifugally unstable. This causes a transition to streamwise, counter rotating Görtler vortices in the boundary layer.

The third centrifugally unstable system considered here is the pressure driven flow between two curved walls. Pressure driven flow through curved ducts and channels is commonly called the Dean problem (figure 5.5). The primary flow

Taylor-Couette flow   Görtler problem   Dean problem
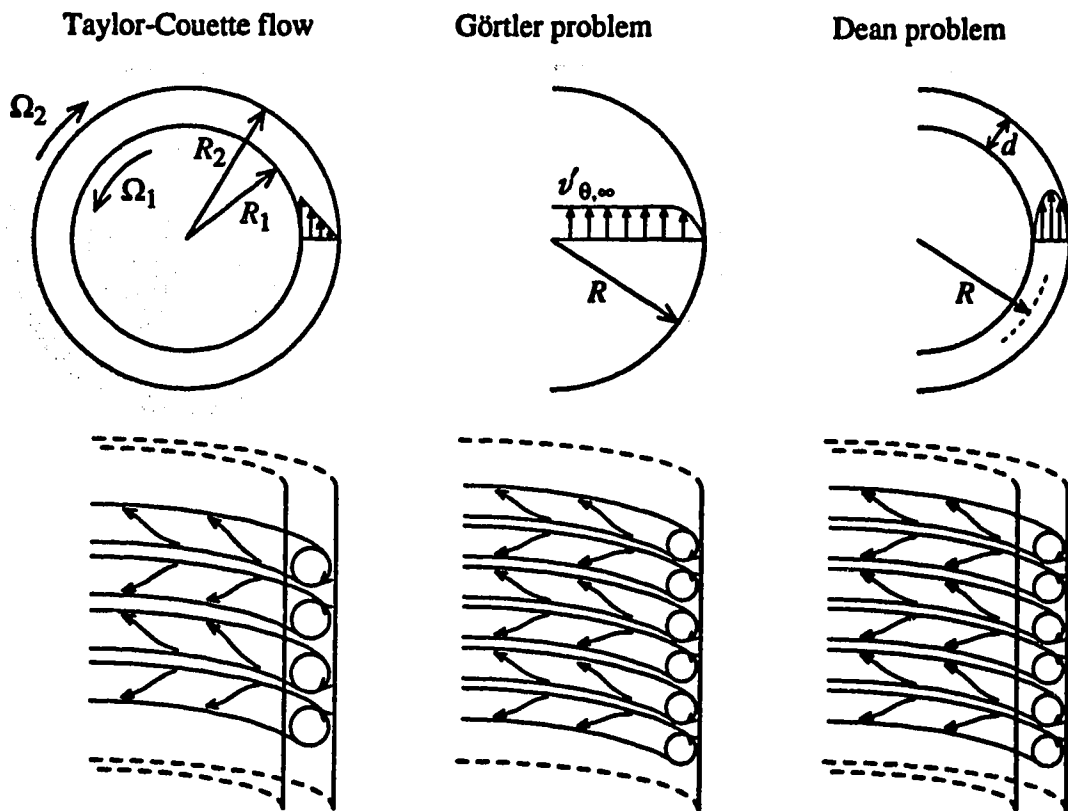
Figure 5.5: Three commonly studied centrifugally unstable flows.

state for pressure driven flow between two curved walls is similar to plane channel flow. The streamwise velocity profile is nearly parabolic with the maximum shifted towards the inner wall, and is referred to as curved channel Poiseuille flow (CCPF). Applying Rayleigh's discriminant to this velocity profile shows that the flow is centrifugally unstable in the outer region of the duct, which results in a transition to streamwise, counter rotating Dean vortices near the outer wall.

The three centrifugally unstable flow systems discussed above have one-dimensional primary flow states to which Rayleigh's criterion is easily applied. In all three cases spanwise periodic counter rotating vortices are created as the result of a centrifugal instability. In a curved duct of square cross section the primary flow state is two-dimensional 2-cell flow, which is also centrifugally unstable. At Dean numbers above 131 (limit point L_2) this instability induces a single pair of Dean vortices near the centre of the outer wall.

The flow development diagrams for Dean numbers of 400 and 500 in figure 5.3 show the development of a 6-cell flow state, which is the main subject of interest in this chapter. The 6-cell flow is characterized by two large Ekman vortices and two pairs of small Dean vortices near the outer wall. These Dean vortices are again the result of the centrifugal instability of the flow. The arrow plot for $Dn = 453$ and $\theta = 90°$ in figure 5.4c shows a 6-cell flow pattern. In the flow development diagrams of figure 5.3, the 6-cell state can be recognized by a high radial velocity that is the result of the outflow region between the two vortex pairs. The simulations predict the development of 6-cell flow in the first 100° of the curved duct. The 6-cell pattern does not reach a fully developed state, but immediately breaks down into a 2-cell state, from which then a 4-cell state develops.

The 6-cell flow state with two pairs of Dean vortices was not predicted by the bifurcation studies of two-dimensional fully developed flows by Winters (1987)

and Daskopoulos and Lenhoff (1989). The additional cells of the 6-cell flow states calculated by Daskopoulos and Lenhoff do not seem to form pairs of counter rotating vortices. However, two-dimensional flows with more than one Dean vortex pair have been observed in curved rectangular ducts with aspect ratios between 8 and 30 (Finlay & Nandakumar, 1990; Thangam & Hur, 1990). It seems therefore likely that the 6-cell flow state with two pairs of Dean vortices is a two-dimensional solution of curved square duct flow. An extensive bifurcation study for higher flow rates would have to be conducted to determine whether this 6-cell flow corresponds to a fully developed state or not. It will be shown in section 5.7 that if this two-dimensional 6-cell flow exists, it is unstable to arbitrary perturbations.

The development of two pairs of Dean vortices at high flow rates can be explained by looking at studies of the Görtler problem. The spanwise wavelength of streamwise Görtler vortices formed in the boundary layer over a concave wall is measured by the dimensionless parameter

$$\Lambda_G = \frac{v'_{\theta,\infty}\lambda_G}{\nu}\sqrt{\frac{\lambda_G}{R}} \tag{5.7}$$

where: $v'_{\theta,\infty}$ = freestream velocity

λ_G = dimensional wavelength in the spanwise direction

It has been shown both experimentally and numerically that wavelengths with $\Lambda_G = 210$ generally have the largest primary growth rates (e.g. Bippes, 1972; Floryan and Saric, 1984 and Guo and Finlay, 1994). This means that the preferred dimensional wavelength is proportional to $(v'_{\theta,\infty})^{-\frac{2}{3}}$ so that the size of the Görtler vortices decreases with increasing flow rate. Because of the centrifugal nature of both Dean vortices and Görtler vortices, Dean vortices can also be expected to decrease in size with increasing flow rate.

In a curved square duct the number of Dean vortices is restricted by the top and bottom walls. With increasing flow rate a point will be reached where two pairs of Dean vortices of the preferred wavelength can develop along the outer wall. This is when the transition to 6-cell flow takes place. The presence of the inner wall and especially the lateral walls of a square duct complicates the comparison between the Dean problem and the Görtler problem. It is believed however that since the mechanism that causes Dean and Görtler vortices is the same, comparison with the Görtler problem provides a qualitative explanation for the observed phenomenon.

At the highest flow rate, $Dn = 600$, another new phenomenon is predicted by the numerical code. The flow does not develop a 6-cell pattern. Instead, a 4-cell flow is formed from the initial 2-cell, but no fully developed 4-cell state develops. The size and radial position of the Dean vortices keeps changing. Especially just before the 4-cell flow breaks down (around $\theta = 400°$), the Dean vortices oscillate strongly in radial direction. This behaviour is also predicted by a simulation with a 101x101 grid, but has not been investigated any further.

In summary: the initial Ekman vortices are induced by the top and bottom walls, while the smaller Dean vortices near the outer wall are the result of the primary centrifugal instability and develop only above a critical flow rate. The size of the Dean vortices decreases with increasing flow rate, leading to a transition from a single pair of Dean vortices to two pairs of Dean vortices around $Dn = 350$. Another new transition is predicted between $Dn = 500$ and $Dn = 600$.

The evolution towards a 6-cell flow has also been observed experimentally. Secondary flow patterns at $\theta = 90°$ and various flow rates are shown in figure 5.6. At a flow rate of $Dn = 100$ the flow develops towards an axially invariant 2-cell state. At $Dn = 200$ the flow develops initially into a fully developed 4-cell state, but at $\theta = 90°$ this fully developed state has not been reached yet. At $Dn = 300$
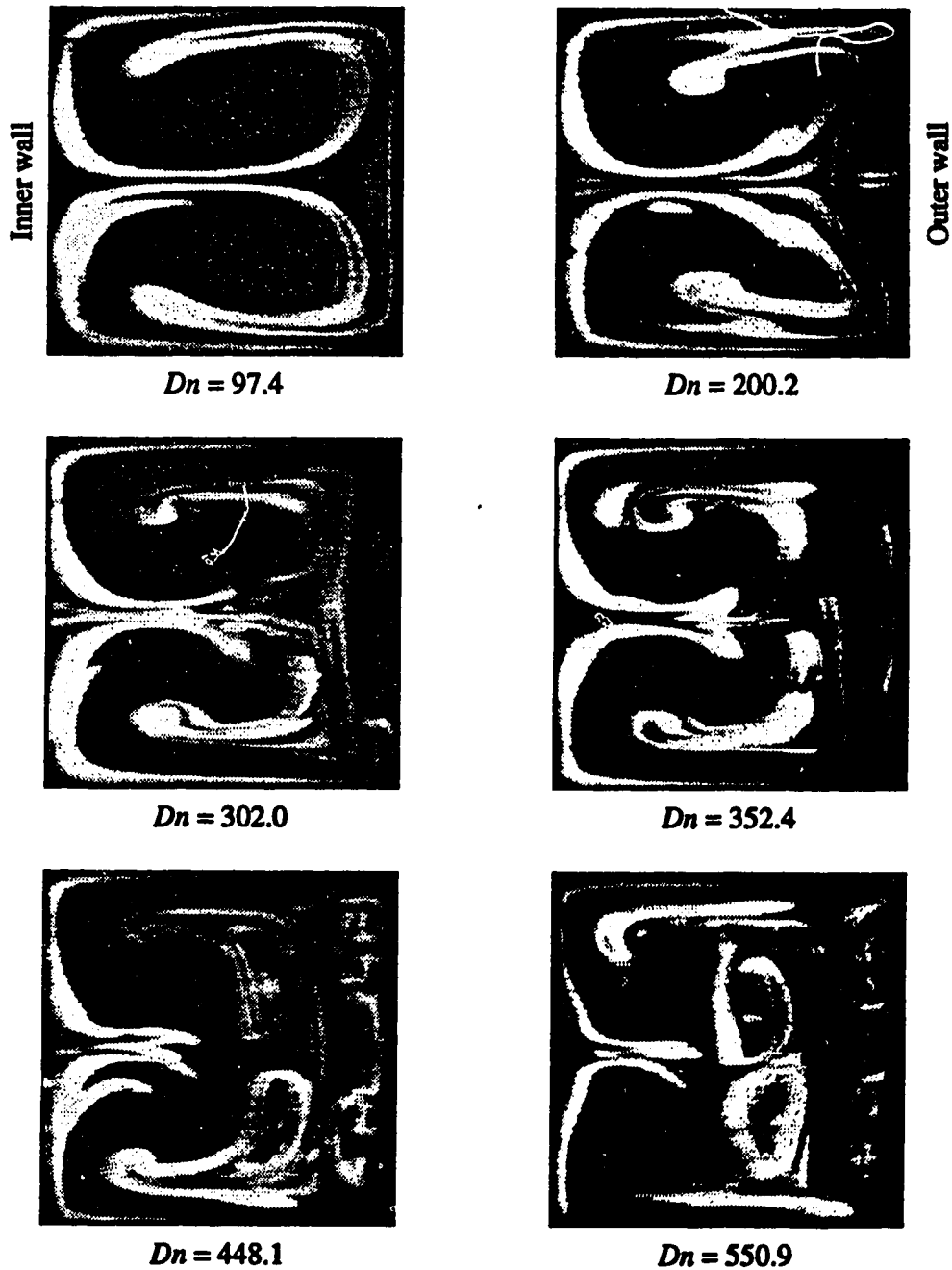
Figure 5.6:   Cross section flow visualization showing secondary flow at $\theta = 90°$ for increasing flow rate.

the single pair of Dean vortices that develops initially is very small and has moved down. The photograph in figure 5.6 for $Dn = 302.0$ shows a streak of dye at the stagnation point of this vortex pair at about $z = -0.3$ and close to the outer wall. The 6-cell secondary flow is first observed at $Dn = 350$, but the two pairs of Dean vortices are very small and break down before they can be distinguished clearly. At Dean numbers of 450 and 550 the two pairs of Dean vortices are very distinct around $\theta = 90°$, before the flow breaks down into a 2-cell state, farther downstream.

Detailed experimental observations of two pairs of Dean vortices in a curved duct of square cross section have not been reported previously. Arnal et al. (1992) studied developing flow in a curved square duct with a curvature ratio of 3.36 at a Dean number of 764. Their numerical simulations show two pairs of Dean vortices at $\theta = 135°$, although the arrows in their figure 5 are pointing in the opposite direction. It is not clear whether they observed this 6-cell flow experimentally.

6-cell flows have also been observed in a curved rectangular duct with an aspect ratio of 2. Sugiyama et al. (1983; 1988) reported detailed LDA measurements and flow visualization of the development and breakdown of 6-cell flow at a Dean number of 220 in a rectangular duct with curvature ratio 8. Numerical simulations for this geometry were performed by Miyake et al. (1988) and Kajishima et al. (1989) and are in qualitative agreement with the experiments. A study by Thangam and Hur (1990) reported fully developed 2-cell and 4-cell flows in a curved rectangular duct with aspect ratio 2.

In the following sections the observed transition will be investigated in more detail. Experimental and numerical results will be compared for Dean numbers of 272, 326, 375 and 453.

5.3 Flow Development at $Dn = 272$

According to the numerical simulations, a Dean number of 272 is in the region where a 4-cell state develops that breaks down into a stable 2-cell flow, and well below the transition to a 6-cell flow at $Dn = 350$. Flow visualization of the experimentally observed secondary flow development is shown in figure 5.7. The flow is not time dependent. The photographs were taken at different moments in time, each of them by injecting a slug of laser fluorescent dye into the flow. This method was described in section 3.3. In each of the photographs, the outer wall is on the right hand side.

The flow development up to $\theta = 120°$ is very similar to the development for $Dn = 150$, observed by Bara (1992). At $Dn = 150$ the flow develops into a fully developed 4-cell state at $\theta = 240°$. At a Dean number of 272 however, the flow does not remain symmetric; the 4-cell state starts to fold up even before a fully developed state has been reached. This is illustrated by the photographs at $\theta = 160° - 240°$.

It is important to realize that the cross section visualization photographs do not show the secondary flow pattern. The dye pattern that is seen in the photographs is not the result of the secondary flow at the observed position only. The pattern is the result of a combination of the dye injection method and the flow field, starting at the dye injection point up to the observed streamwise position. The secondary flow upstream from the observed position can have a significant effect on this dye pattern. A numerical study by Finlay et al. (1993) showed that especially when the flow field changes quickly in the streamwise direction, the dye pattern does not represent the secondary flow accurately.

Simulated development diagrams are shown in figure 5.8. Three different grid sizes were used, with very similar results. The main difference is that the 101x101
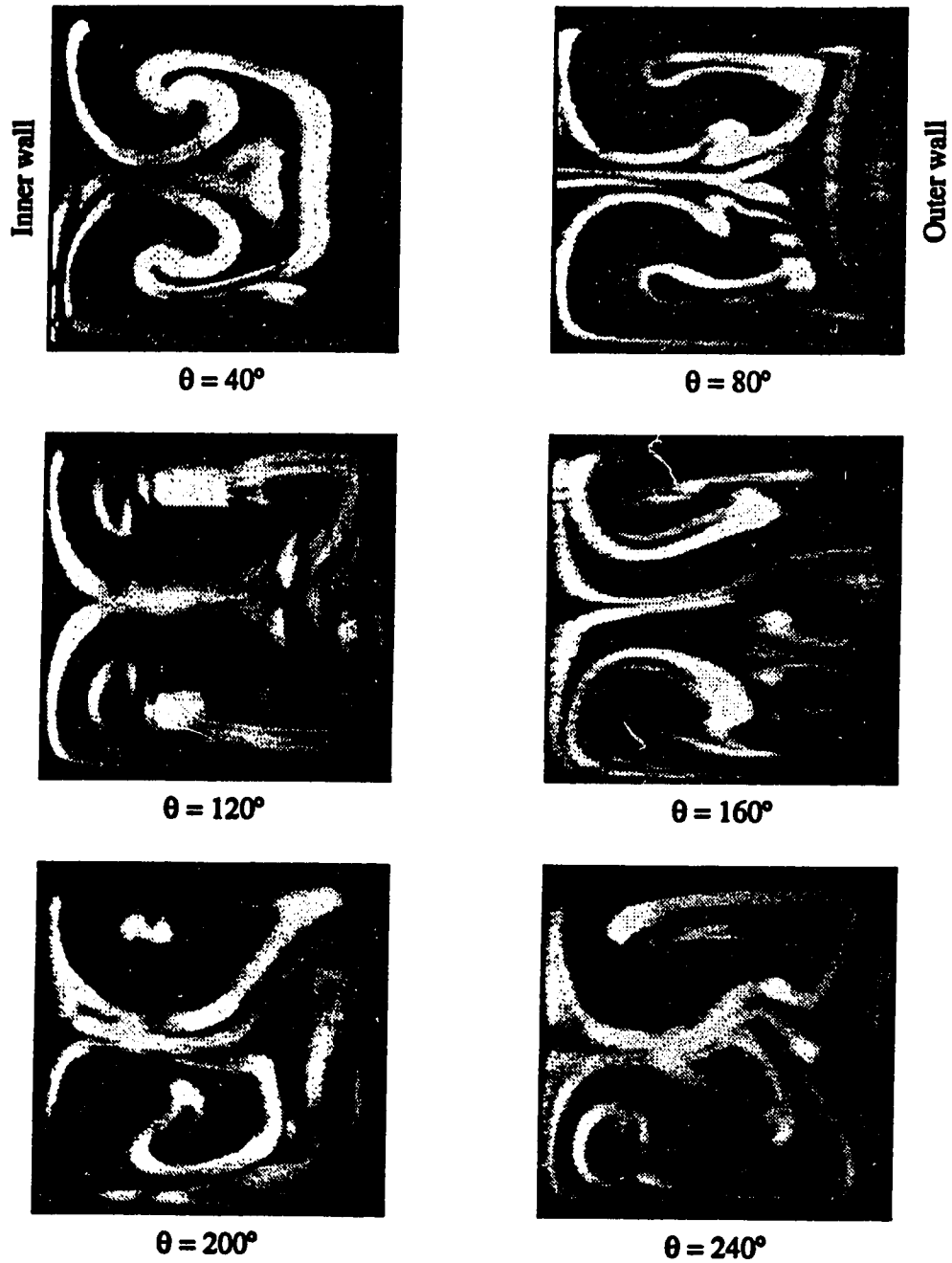
Figure 5.7: Cross section flow visualization showing secondary flow development at $Dn = 272$.
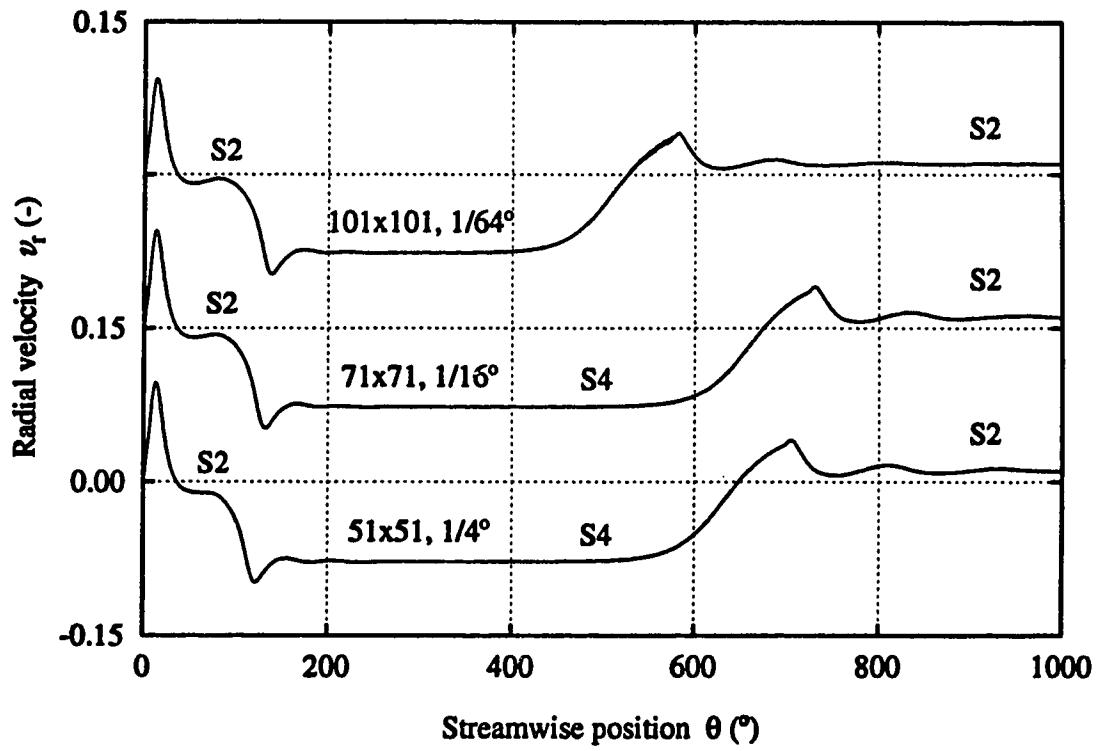
Figure 5.8: Calculated flow development diagrams of the radial velocity at
$x = 0.4$, $z = 0.0$, showing the flow development to $\theta = 1000°$ at
$Dn = 272$; $R_c = 15.1$. Labels indicate number of cells; S: symmetric
pattern. Grid size and axial step size as indicated.

grid simulation predicts a development length of the 4-cell flow that is about 18°
longer than with the 51x51 grid simulation. The 4-cell state breaks down into a
2-cell state around $\theta = 600°$. The streamwise position where this breakdown takes
place is sensitive to grid refinement, but the process itself is nearly identical for all
three grids. The 2-cell state is predicted to be stable up to at least $\theta = 3000°$. At
a Dean number of 272, above limit point L_3 in the state diagram, Winters (1987)
calculated a 2-cell branch, S_5, which is partially stable (figure 5.2). It seems likely
that the observed 2-cell state corresponds to this 2-cell branch. Because of the
limited length of the apparatus, the stability of the 2-cell flow could not be verified
experimentally.

The main difference between the simulation and the experiment is that it takes
much longer in the simulation for the 4-cell flow to break down into a 2-cell state.
This difference can be explained by looking at the asymmetric disturbances that
cause the 4-cell flow to break down.

The source of the asymmetric perturbations in the experimental setup and the
numerical simulation is very different. In the experiment, it is asymmetries in the
apparatus that cause small initial asymmetric disturbances that grow and cause the
4-cell flow to break down. In the numerical simulation however, the asymmetries
originate from round-off errors. Although the growth rate of asymmetries is
determined by the physics and therefore is the same in both cases, the initial
asymmetric disturbances are not of the same magnitude. The observed difference
in the streamwise position where the 4-cell breaks down indicates that the initial
asymmetric round-off errors are much smaller than initial asymmetric disturbances
in the experiment. However, once the 4-cell breaks down in the numerical simulation,
this process is very similar to the experimentally observed foldup process.

With this in mind, the calculated arrow plots in figure 5.9 are in excellent
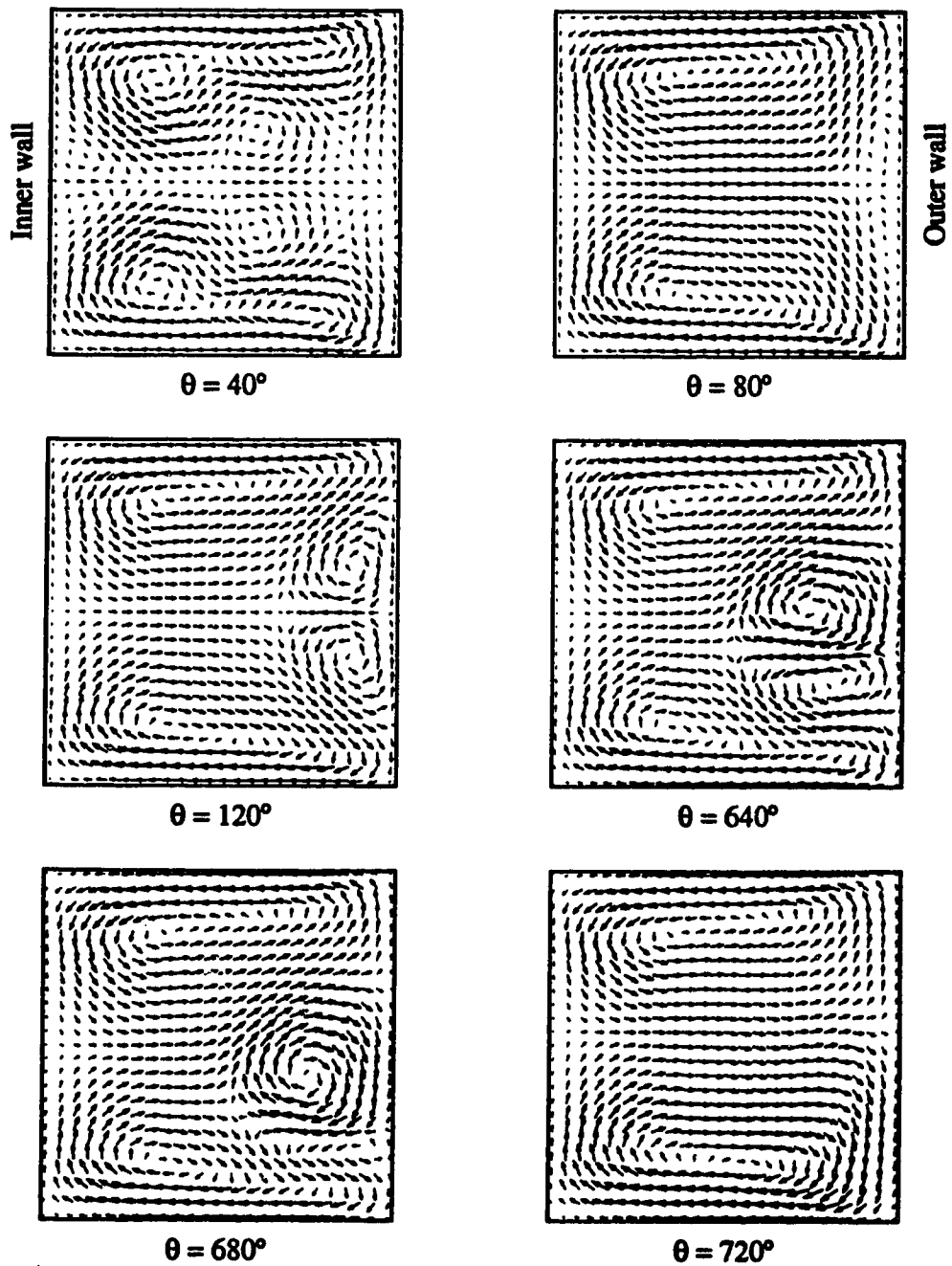
Figure 5.9:   Calculated arrow plots showing secondary flow development at
$Dn = 272$; $R_c = 15.1$.

agreement with the experiment. The arrow lengths in these and all other arrow plots in this chapter are proportional to the square root of the secondary velocity. This makes secondary flow patterns with low velocities more distinguishable. For example, the onset of the Dean vortices at $\theta = 80°$ would not be visible if the arrow length was proportional to the secondary velocity. The arrow plots at $\theta = 40°$, $80°$ and $120°$ were calculated with a 101x101 grid. Not all arrows are shown. The other three arrow plots show the secondary flow at $\theta = 640°$, $680°$ and $720°$ on a 51x51 grid. These last three arrow plots are in good agreement with the experiment at $\theta = 160°$, $200°$ and $240°$.

The photograph at $\theta = 240°$ in figure 5.7 is a good example of the upstream effect on the dye pattern. The asymmetric breakup of the 4-cell flow causes the flow field upstream from $\theta = 240°$ to be asymmetric, which in turn results in an asymmetric dye pattern. Thus, the secondary flow at 240° could in fact be a nearly symmetric 2-cell state, as predicted by the model at $\theta = 720°$. There is also some discrepancy between the flow visualization at $\theta = 200°$ and the model at $\theta = 680°$. The visualization gives the impression that the Dean vortices have rotated clockwise over close to 90°. However, this dye pattern could be the result of the large upper Dean vortex that has moved down, as shown in the model at $\theta = 680°$. Only detailed velocity measurements could reveal the true nature of the secondary flow. In this study velocity profiles were only measured at a Dean number of 453. These results will be presented in section 5.6.

5.4 Flow Development at $Dn = 326$

A Dean number of 326 is slightly below the onset of 6-cell flow, which was observed experimentally around $Dn = 350$. The secondary flow development is shown in figure 5.10. The flow becomes asymmetric very early in the development. The photograph at $\theta = 40°$ shows a blob of dye near the outer wall, just below the centre line. This seems to be the stagnation point of a pair of small Dean vortices that has moved down into the bottom corner of the duct at $\theta = 80°$. At $\theta = 120°$ this pair of vortices has folded up into the lower Ekman cell. The asymmetries in the photographs at $\theta = 40°, 80°$ and $120°$ are difficult to interpret from flow visualization alone. A new pair of Dean vortices starts to develop at $\theta = 180°$. This pair develops asymmetrically and starts to fold up before a fully developed state has been reached. At $\theta = 240°$ this new pair is in the process of folding up.

The development of asymmetric flow phenomena is determined by the relative growth rates of symmetric and asymmetric modes, and by the magnitude of asymmetric flow disturbances. The early development of asymmetries could be due to larger asymmetric disturbances at this higher flow rate. However, since at a Dean number of 453 the flow develops again symmetrically (section 5.6), the asymmetries that develop at $Dn = 326$ must be the result of relatively high growth rates of asymmetric modes. The asymmetric modes and their linear growth rate are only a function of the Dean number and can, in principle, be determined from the equations of motion. The experimental realization of these modes depends on the amplitude at which these modes are excited. Hence, a different experimental apparatus, with different asymmetric disturbances, will probably produce different results.

A mechanism for the high growth rates of asymmetries is proposed, based on
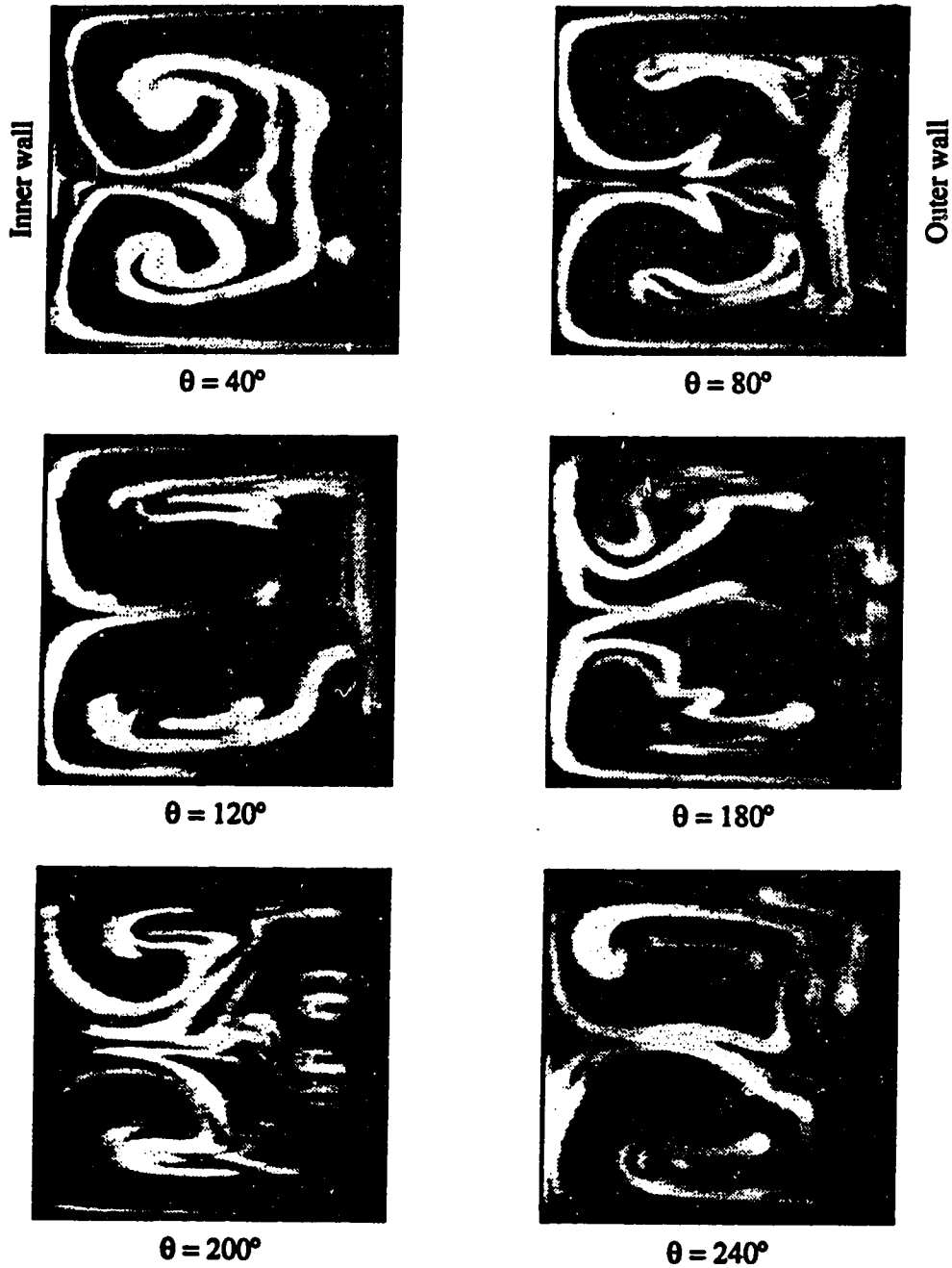
Figure 5.10:   Cross section flow visualization showing secondary flow development
at $Dn = 326$.

the analogy with the Görtler problem. It was mentioned in section 5.2 that the size of the fastest growing Görtler mode, λ_G, is proportional to $(v'_{\theta,\infty})^{-\frac{1}{2}}$ (equation 5.7). A difficulty with the analogy between the Görtler problem and the Dean problem is that in the Dean problem the freestream velocity is not well defined. If however the freestream velocity is estimated by the mean streamwise velocity in the duct, $\overline{v_\theta}$, the fastest growing mode is given by:

$$\lambda_G = 0.4536\, Dn^{-2/3} \tag{5.8}$$

At a Dean number of 326 the fastest growing wavelength is 0.96 cm. Although there is no exact analogy with the Görtler problem, this result suggests that the spanwise wavelength of the fastest growing mode is significantly smaller than the height of the duct, while two spanwise wavelengths is larger than the duct height. The flow can develop symmetrically in two different ways: either with a single pair of Dean vortices (4-cell), or with two pairs of Dean vortices (6-cell). Both these states have low growth rates because the wavelengths of the corresponding Dean vortices are significantly different than the preferred mode. There are many possible asymmetric flow states, and because of the relatively low growth rates of symmetric modes, some of these asymmetric modes will dominate the flow development.

Simulated development diagrams are shown in figure 5.11. The solution is very sensitive to grid refinement. In the numerical simulations, the development of asymmetries depends on the physics of the flow, the presence of asymmetric disturbances, and the grid size that is used in the calculations. Often, the challenge in computational fluid dynamics is to discriminate between spurious phenomena caused by discretization and real phenomena caused by complex physics of the flow.

It will be shown in section 5.6 that a 101x101 grid is able to predict the flow development accurately at a Dean number of 453. The same grid resolution can be

Figure 5.11: Calculated flow development diagrams of the radial velocity at $x = 0.4$, $z = 0.0$, showing the flow development to $\theta = 250°$ at $Dn = 326$; $R_c = 15.1$. Labels indicate number of cells; S: symmetric pattern; A: asymmetric pattern. Grid size and axial step size as indicated.
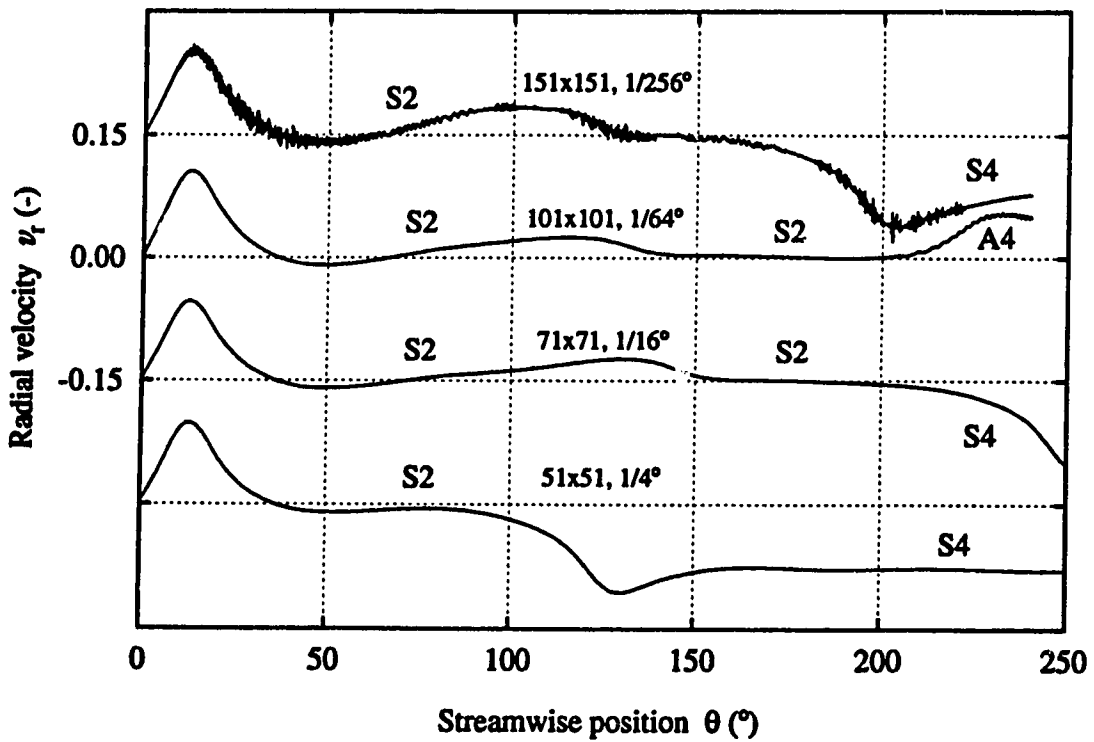
argued to be adequate at lower flow rates. Thus, the grid sensitivity observed here for $Dn = 326$ is not an artifact of a coarse grid.

We know from the experiment that at a Dean number of 326 the physical response is characterized by several closely spaced, competing unstable modes. Different grids excite each of these modes in a different manner. It is therefore believed that the observed grid sensitivity is the result of the complex physics in this region of the Dean number and the inherent properties of each discretization.

At a 51x51 grid the flow develops symmetrically towards a 4-cell state, without signs of a 6-cell flow state. Asymmetries only become prominent around $\theta = 500°$, where the 4-cell flow breaks down into a 2-cell state. The 71x71 simulation predicts the onset of two pairs of Dean vortices near $\theta = 100°$. These vortex pairs are very small and don't develop further. This stage of the flow development is characterized by a high radial velocity in the monitoring point, resulting in a peak in the flow development diagram between $\theta = 100°$ and $\theta = 150°$. At $\theta = 200°$ a single pair of Dean vortices develops symmetrically and a fully developed 4-cell state is reached around $\theta = 270°$. The flow is symmetric up to $\theta = 500°$, where the 4-cell breaks down into a 2-cell state.

The simulation with a 101x101 grid develops asymmetries much earlier than the other simulations. Arrow plots calculated with this grid are shown in figure 5.12. The onset of two Dean vortex pairs at $\theta = 80°$ is similar to that predicted by the 71x71 simulation. These Dean vortices have disappeared at $\theta = 120°$. At $\theta = 180°$ the flow has developed strong asymmetries in the form of a developing Dean vortex pair along the upper part of the outer wall. This vortex pair moves up while it develops and eventually folds up into the upper Ekman vortex. Many more simulations were done at this flow rate than are shown in figure 5.11. The 101x101 simulation shows the best agreement with the experiments. In the simulation the
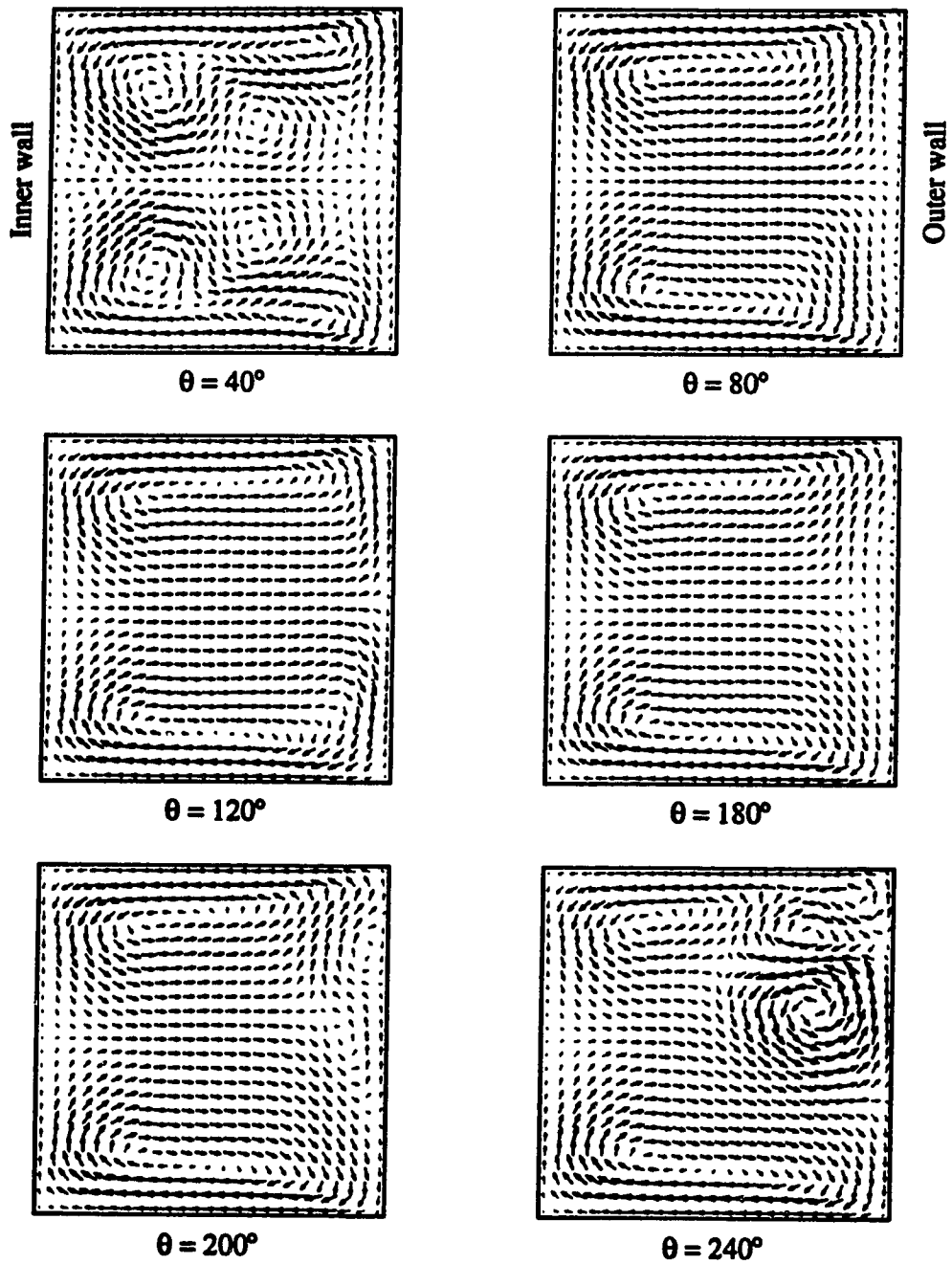
Figure 5.12: Calculated arrow plots showing secondary flow development at $Dn = 326$; $R_c = 15.1$.

Dean vortex pair at $\theta = 180°$ develops slightly later and is more asymmetric than was observed in the experiment.

The finest grid that was used had 151x151 points in the cross section. A very small axial step size of $1/256°$ was necessary in order to obtain a converged solution. The flow development diagram in figure 5.11 shows signs of some high frequency numerical scale oscillations. The flow develops symmetrically, and in a very similar way to the 71x71 simulation. Again the onset of two Dean vortex pairs develops around $\theta = 70°$ and has disappeared at $\theta = 100°$. Then a single pair of vortices develops, producing a symmetric 4-cell flow state.

5.5   Flow Development at $Dn = 375$

The flow development changes gradually when the Dean number is increased from 326 to 375. At the higher flow rate the growth rate of the 6-cell state has increased, changing the balance of the competition between the symmetric 4-cell and 6-cell states. The growth rates of the symmetric modes are still low compared to growth rates of asymmetric modes, causing asymmetries to develop early.

Flow visualization of the secondary flow development at a Dean number of 375 is shown in figure 5.13. This is the lowest flow rate at which a distinct 6-cell flow pattern can be observed experimentally. At $\theta = 80°$, the first sign of two stagnation points near the outer wall is evident. At $\theta = 100°$ the two pairs of Dean vortices are very distinct and have already started to fold up. As the 6-cell flow breaks down, one pair of cells moves down and folds up into the lower Ekman vortex, while the other pair folds up into the upper Ekman vortex. This break down process of the 6-cell looks symmetric. Asymmetries become dominant near $\theta = 180°$ with the development of an asymmetric pair of Dean vortices. This pair breaks up before a
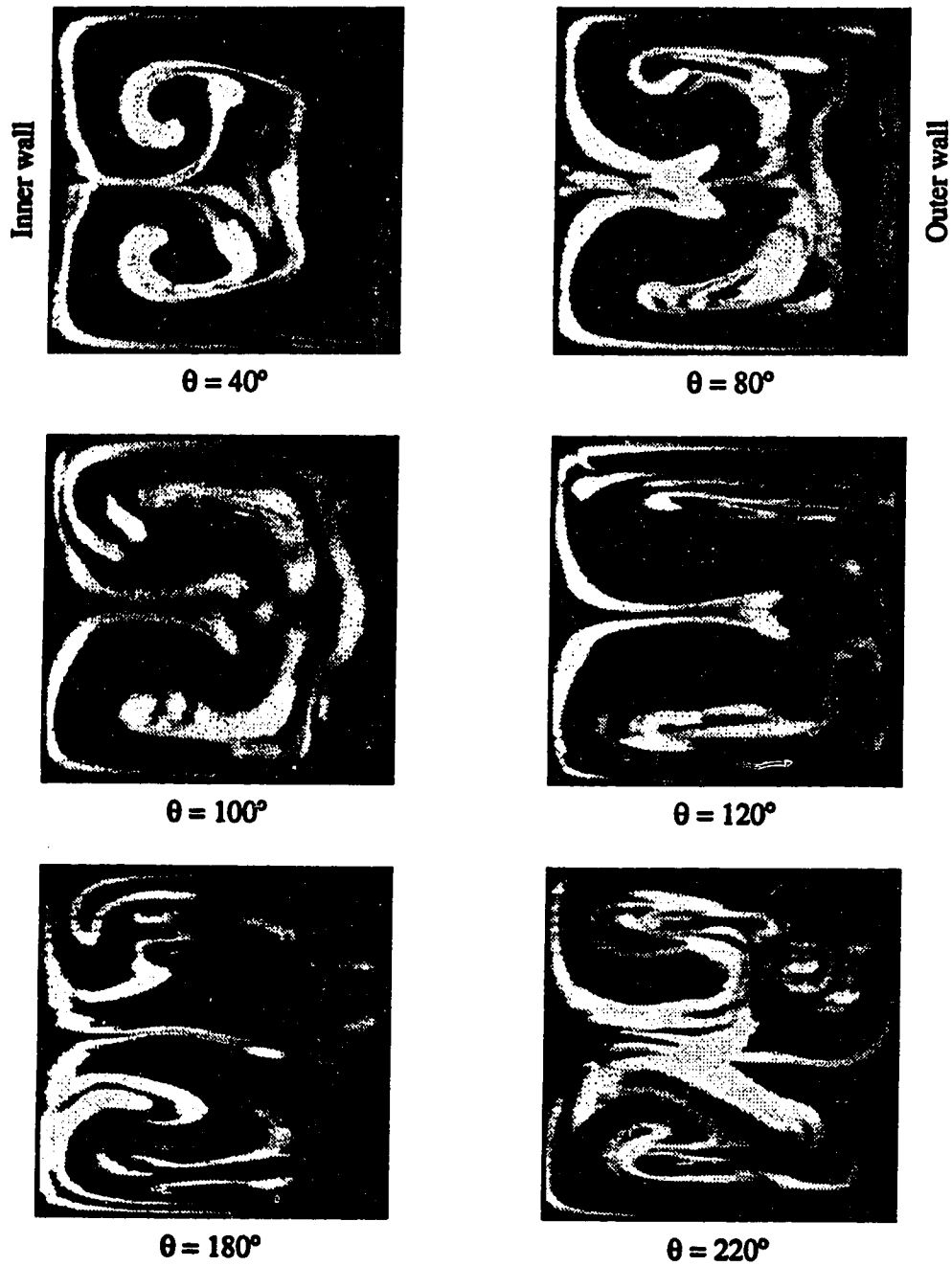
Figure 5.13: Cross section flow visualization showing secondary flow development at $Dn = 375$.

fully developed state has been reached.

Calculated flow development diagrams are shown in figure 5.14. Similar to the simulations at a Dean number of 326, the solution is very grid sensitive. The calculated flow development at a 51x51 grid shows the development of a distinct 6-cell flow that breaks down into a 2-cell flow from which a 4-cell state develops. This is very different from the flow development at $Dn = 326$ with a 51x51 grid, where no sign of a 6-cell flow was observed. At this coarse grid a very sudden transition takes place at a Dean number between 356 and 357. At finer grids, the solutions for Dean numbers of 326 and 375 are more similar, which is in agreement with the gradual transition that is observed in the experiment.

At a 71x71 grid the solution is very similar to that at $Dn = 326$ with the initial development of two Dean vortex pairs and later a symmetric 4-cell state. The grid sensitivity for a 101x101 grid is particularly interesting. With an axial step size of $1/32°$ the flow develops into a symmetric 4-cell flow, while the simulation with a step size of $1/64°$ develops an asymmetric vortex pair near $\theta = 180°$. The 151x151 simulation initially develops two Dean vortex pairs that have broken down at $\theta = 150°$. A 2-cell secondary flow pattern remains until $\theta = 240°$.

The simulation with a 101x101 grid and an axial step size of $1/64°$ is again the only simulation shown here that develops early asymmetries. This simulation is closest to the experimentally observed development. Arrow plots of the secondary flow development are shown in figure 5.15. At $\theta = 80°$, the arrow plot shows the onset of two Dean vortex pairs, corresponding to the two stagnation points in the flow visualization. These vortex pairs have grown and started to break down at $\theta = 100°$. At $\theta = 180°$ the onset of a new, asymmetric, vortex pair is visible, which was also observed in the experiment. This pair has started to break down at $\theta = 220°$. The simulation is in very good agreement with the flow visualization.

Figure 5.14: Calculated flow development diagrams of the radial velocity at $x = 0.4$, $z = 0.0$, showing the flow development to $\theta = 250°$ at $Dn = 375$; $R_c = 15.1$. Labels indicate number of cells; S: symmetric pattern; A: asymmetric pattern. Grid size and axial step size as indicated.
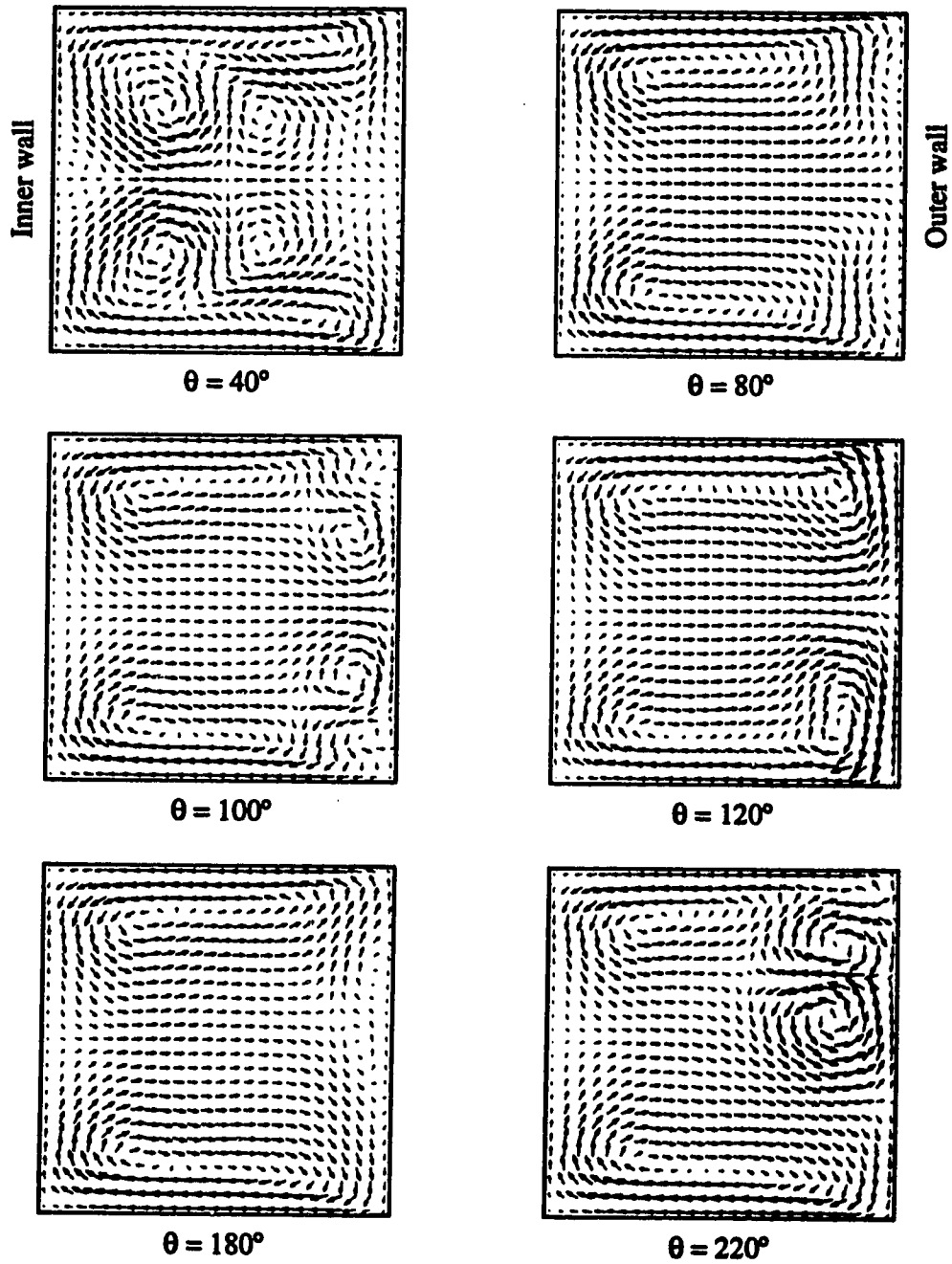
Figure 5.15: Calculated arrow plots showing secondary flow development at $Dn = 375$; $R_c = 15.1$.

5.6 Flow Development at $Dn = 453$

A Dean number of 453 is well above the transition to a 6-cell flow state. At this Dean number the growth rate of the 6-cell flow is significantly higher than the 4-cell flow state. As a result, the flow development in both experiments and simulations is dominated by symmetric modes.

Flow visualization photographs in figure 5.16 show the flow development. A distinct 6-cell secondary flow pattern has developed at $\theta = 100°$. The 6-cell flow breaks down symmetrically into a 2-cell state with one pair of Dean vortices folding up in each of the Ekman vortices. The 2-cell state that forms after the 6-cell breaks up remains almost invariant until $\theta = 240°$, although this is not obvious from the photographs of figure 5.16b. The 2-cell state between $\theta = 140°$ and $\theta = 240°$ was confirmed by LDA measurements, which will be discussed later.

The simulated flow development diagrams of figure 5.17 do not show a very high grid sensitivity. It is believed that this is due to the relatively low growth rates of asymmetric modes. The simulation predicts the development of a 6-cell secondary flow around $\theta = 100°$, that breaks down into a 2-cell state. From the 2-cell state a symmetric 4-cell pattern develops around $\theta = 300°$ which subsequently breaks down at $\theta = 500°$.

Arrow plots calculated with a 101x101 grid are shown in figure 5.18 and agree very well with the experiment up to $\theta = 120°$. After that the flow visualization becomes hard to interpret.

The flow development and 6-cell flow were also analysed by comparing measured velocity profiles with the simulation. First the 6-cell flow at $Dn = 453$ and $\theta = 90°$ was investigated. Next, streamwise velocity profiles were measured to show the flow development.
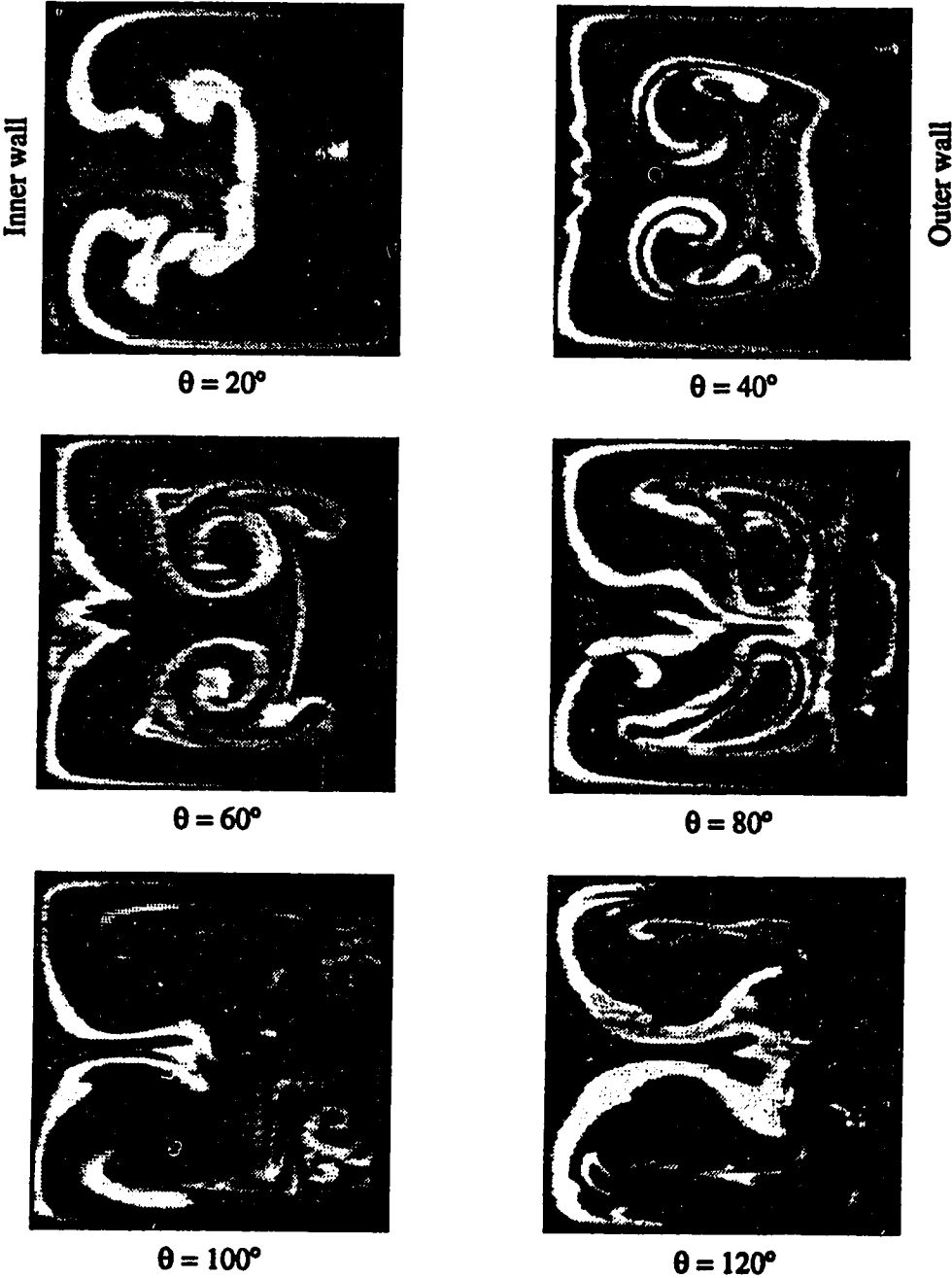
Figure 5.16a: Cross section flow visualization showing secondary flow development at $Dn = 453$.
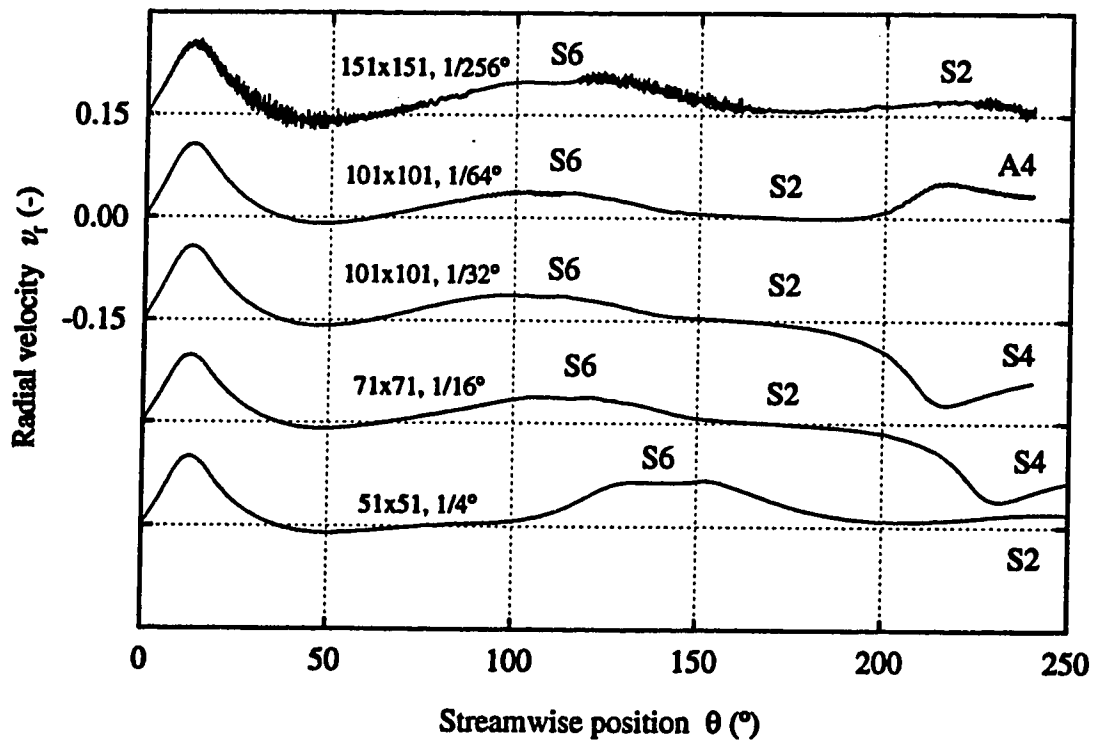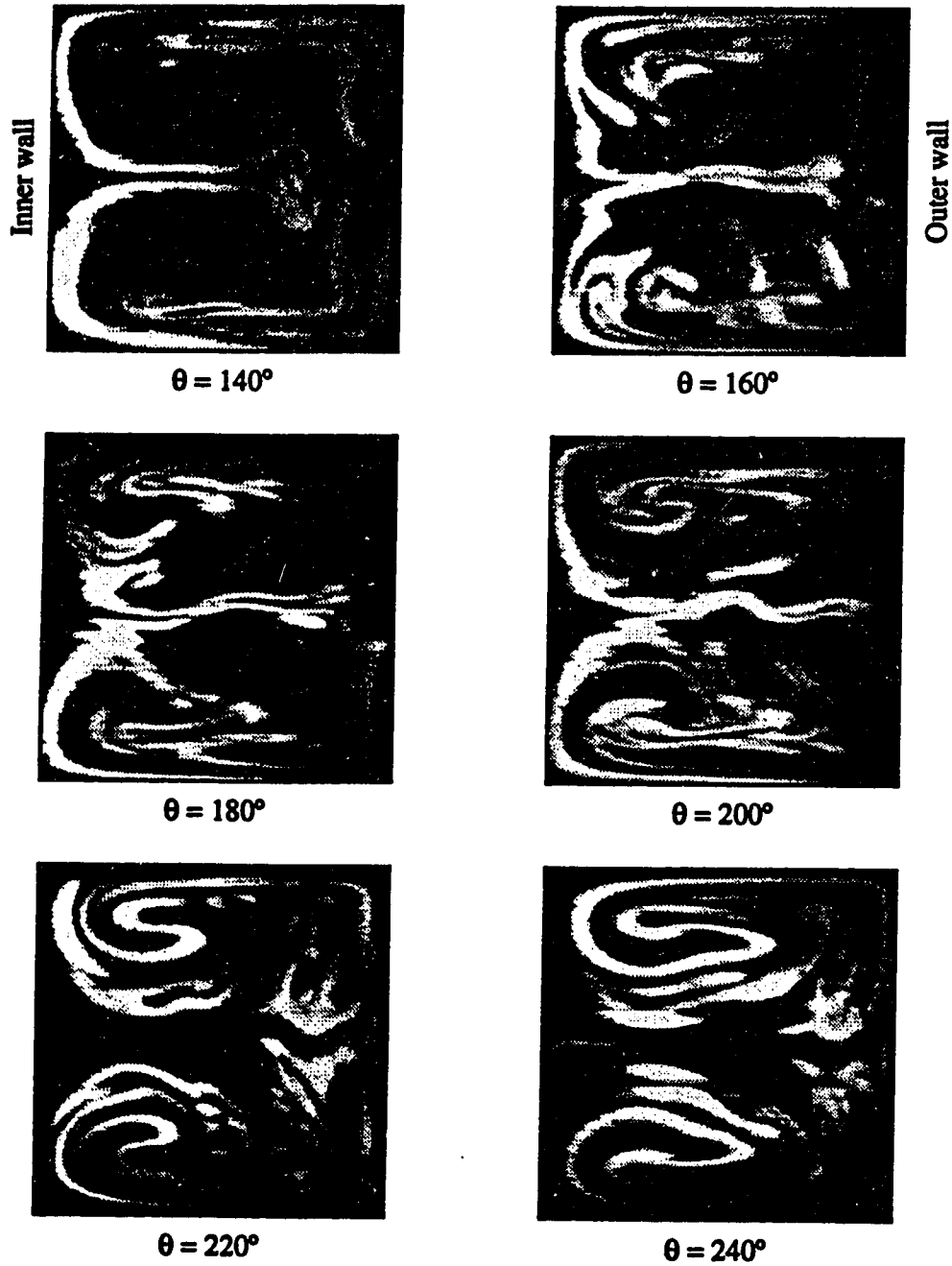
Figure 5.16b: See previous page for caption.
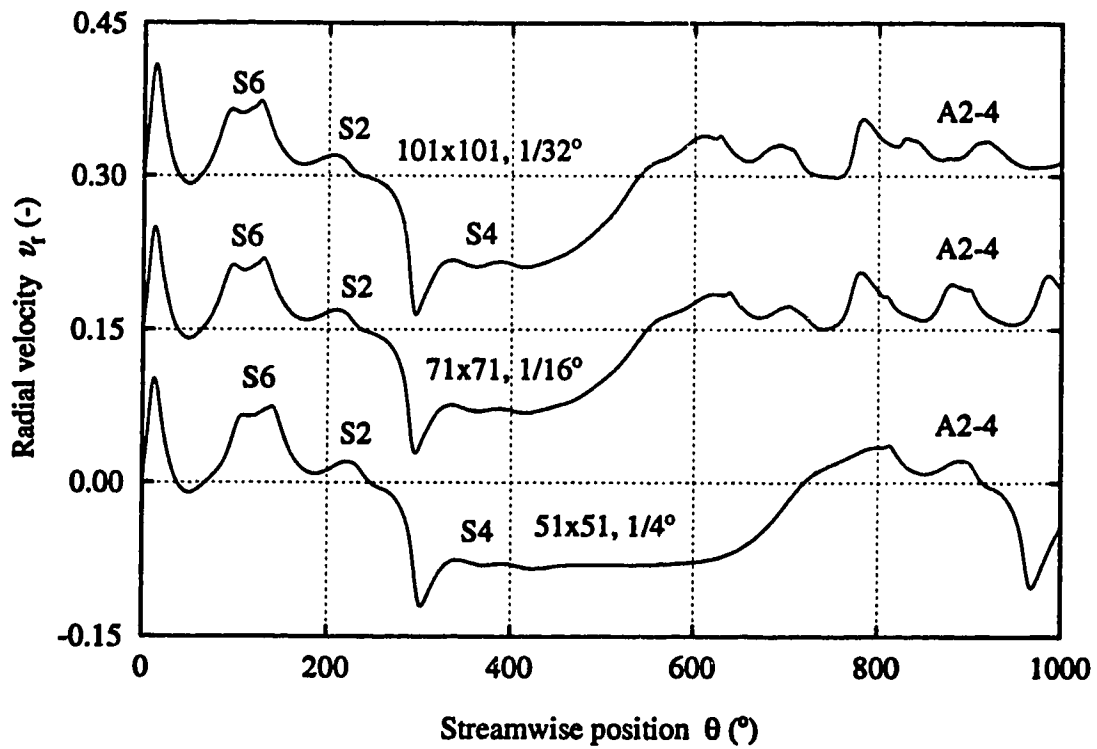
Figure 5.17:   Calculated flow development diagrams of the radial velocity at
$x = 0.4$, $z = 0.0$, showing the flow development to $\theta = 1000°$ at
$Dn = 453$; $R_c = 15.1$. Labels indicate number of cells; S: symmetric
pattern; A: asymmetric pattern. Grid size and axial step size as
indicated.
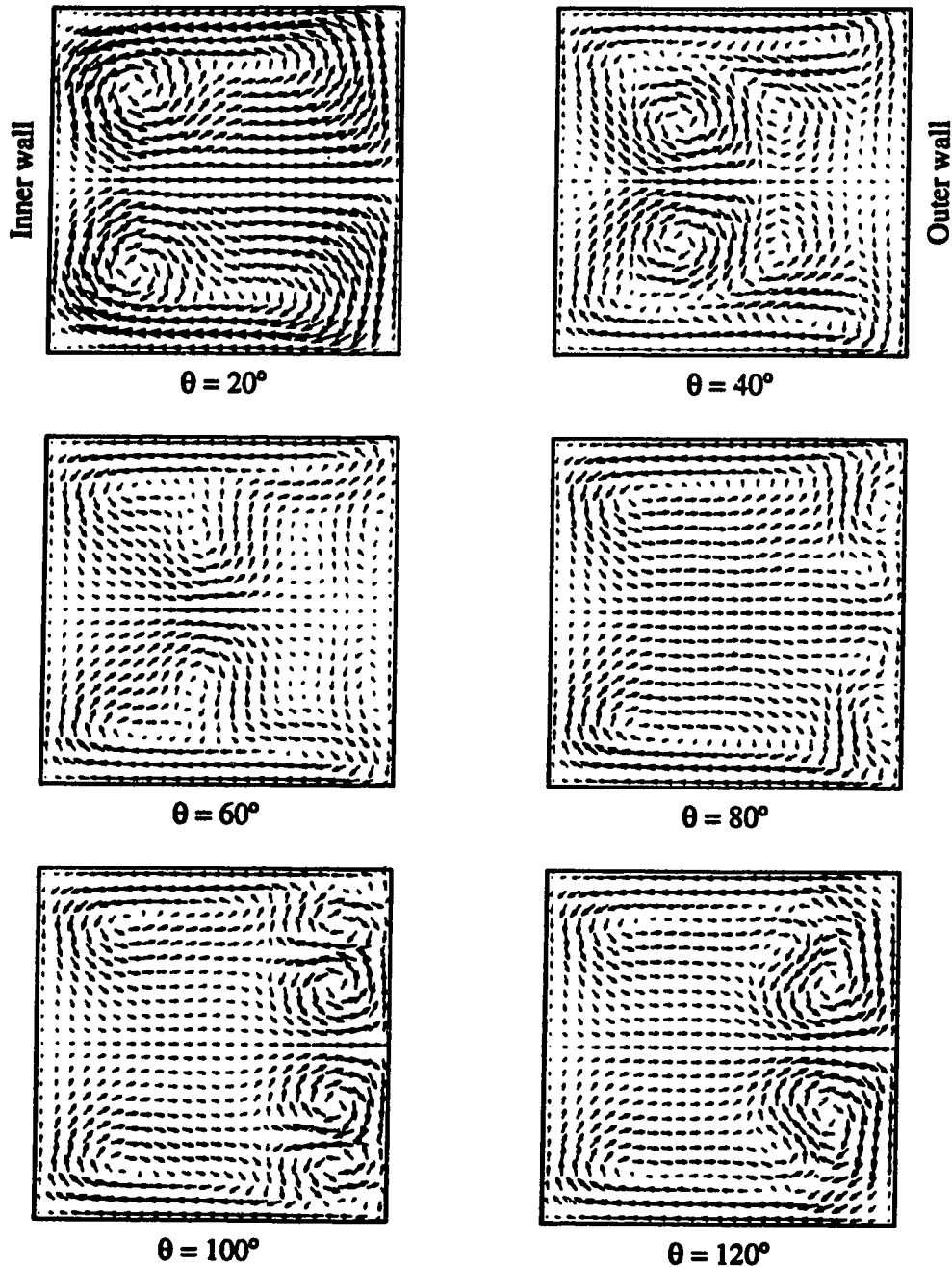
Figure 5.18a: Calculated arrow plots showing secondary flow development at $Dn = 453$; $R_c = 15.1$.
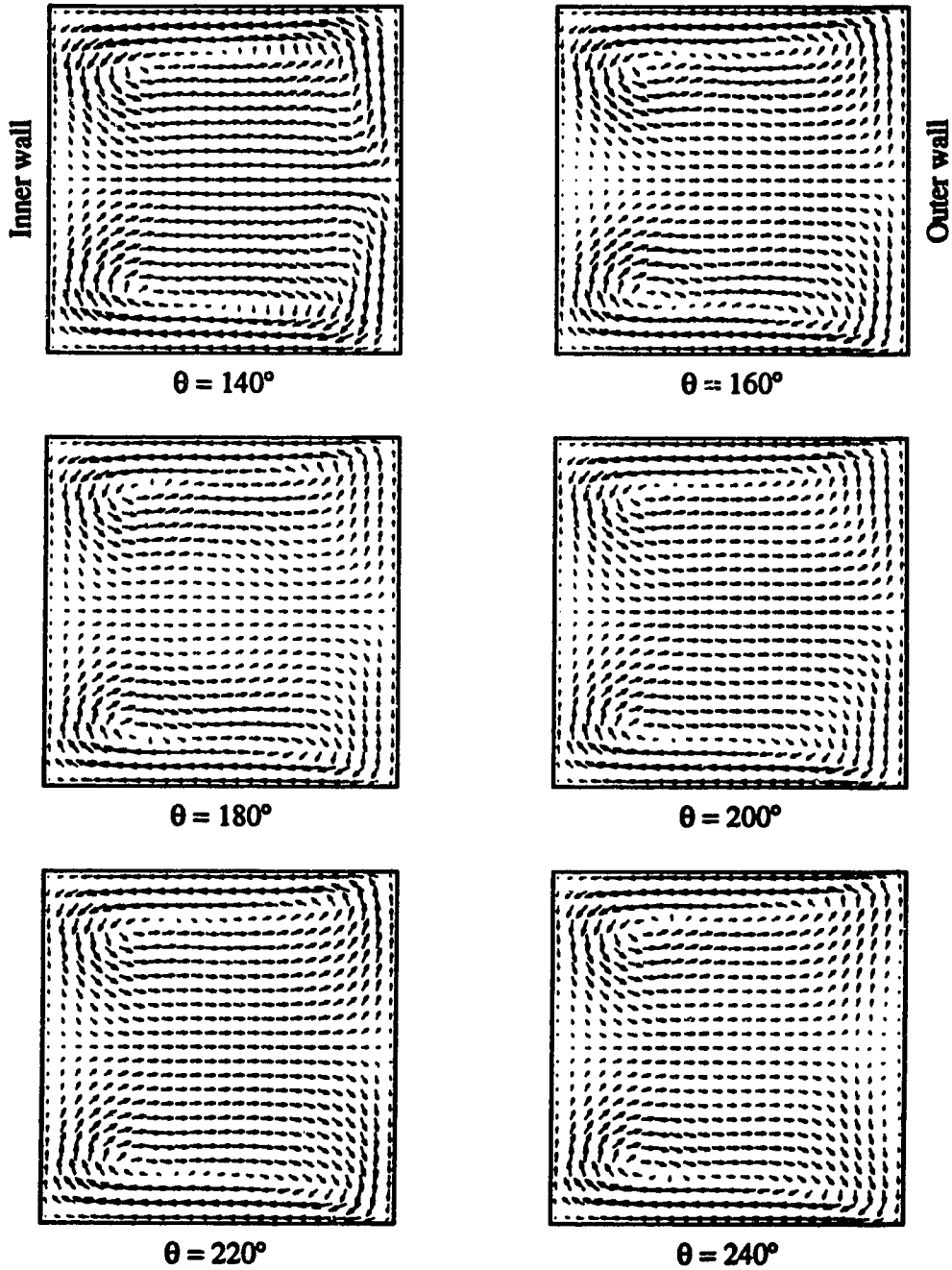
Figure 5.18b: See previous page for caption.

An important difference between the experiment and the simulation is the inlet flow condition. In the simulation a fully developed inlet flow profile is assumed, but it was shown in sections 4.2 and 4.3 that at flow rates higher than $Dn = 300$ the flow is no longer fully developed and slightly unsteady. Unsteadiness was also observed in the curved section at $Dn = 453$. Profiles that were measured shortly after each other show differences that can not be explained by experimental errors and must be due to unsteady flow.

A surface plot of the streamwise velocity for $Dn = 453$ and $\theta = 90°$, combined with an arrow plot of the secondary flow is shown in figure 5.19. The two inflow regions with low streamwise velocity near the outer wall are characteristic for the 6-cell flow pattern. The inflow jets of each of the two Dean vortex pairs transfer fluid with low streamwise momentum away from the wall. This leads to two regions with low streamwise velocity, represented by the dents in the surface plot.

The streamwise velocity profile measured in spanwise direction through the Dean vortices at $x = 0.38$ is shown in figure 5.20 together with the simulation result. The two minima in the profile correspond to the inflow regions near the outer wall. Although there is no perfect agreement between the experiment and the simulation, the experimental result clearly shows the presence of two Dean vortex pairs. Streamwise velocity profiles measured at $x = 0.0$ and $z = 0.0$ are shown in figures 5.21 and 5.22 and show very good agreement with the simulation results. Spanwise and radial profiles were measured at respectively 63 and 48 position, each with a traverse step size of 0.2 mm.

Careful observation of the arrow plot in figure 5.19 shows that the spanwise velocity along the outer wall changes direction a number of times. The experimental spanwise velocity profile at $x = 0.47$ and the simulation result are shown in figure 5.23. An experimental difficulty with measuring spanwise velocities is the
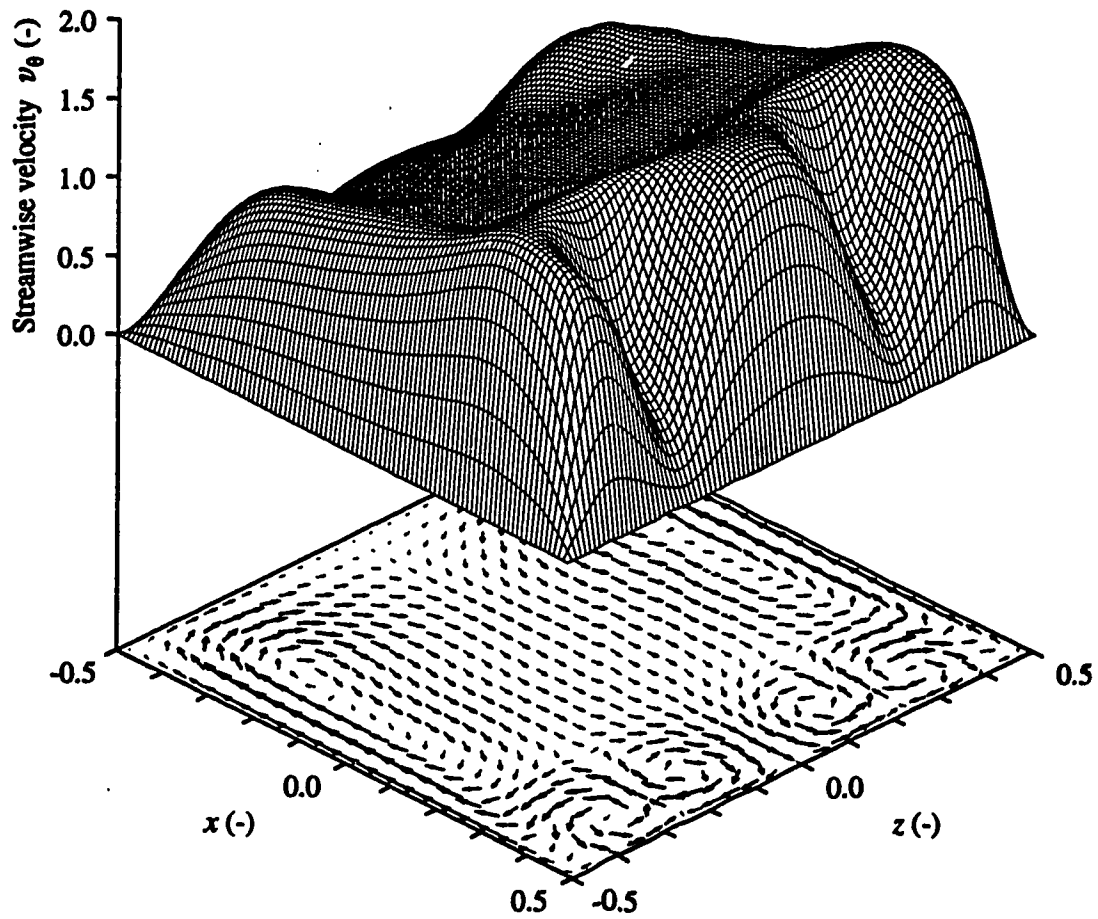
Figure 5.19: Calculated surface plot of the streamwise velocity and arrow plot showing the secondary flow at $Dn = 453$ and $\theta = 90°$; $R_c = 15.1$.

Figure 5.20: Measured spanwise profile of the streamwise velocity compared to the simulation at $Dn = 453$, $\theta = 90°$ and $x = 0.38$; $R_c = 15.1$.

Figure 5.21: Measured spanwise profile of the streamwise velocity compared to the simulation at $Dn = 453$, $\theta = 90°$ and $x = 0.0$; $R_c = 15.1$.

Figure 5.22: Measured radial profile of the streamwise velocity compared to the simulation at $Dn = 453$, $\theta = 90°$ and $z = 0.0$; $R_c = 15.1$.

Figure 5.23: Measured spanwise profile of the spanwise velocity compared to the simulation at $Dn = 453$, $\theta = 90°$ and $x = 0.47$; $R_c = 15.1$.

alignment of the LDA optics. In the measured region, the streamwise velocity is more than an order of magnitude larger than the spanwise velocity. Therefore, if the alignment of the optics is off by only 1°, the contribution of the streamwise velocity to the measured signal is about 5% of the magnitude of the spanwise velocity. The error in the alignment of the LDA optics was estimated at at least 1°. Although the margin of error is quite high, the experimental spanwise velocity profile shows the same direction changes as the simulation.

In the simulation the most significant changes in the streamwise velocity of the developing flow take place along the outer wall. Therefore, the experimental flow development was compared to the simulation by comparing spanwise profiles of the streamwise velocity at $x = 0.38$. These profiles, taken each 20°, are shown in figures 5.24 to 5.35. The overall agreement between the experiment and the simulation is good and shows that the model captures the physics of the flow very well.

The velocity profiles at $\theta = 60°$ (figure 5.26) show the development of a wide inflow region around $z = 0.0$. In the arrow plot for $\theta = 60°$ in figure 5.18 two counter rotating vortices have been formed along the outer wall. At lower flow rates, e.g. $Dn = 272$, this one pair of vortices reaches full development in a 4-cell secondary flow pattern. At $Dn = 453$ however, the two vortices move out towards the top and the bottom walls, while two more vortices form in the centre. As the two initial Dean vortices move out, the single inflow region splits up into two inflow regions as shown at $\theta = 80°$ (figure 5.27). These two inflow regions keep moving out as the 6-cell flow breaks up symmetrically.

The flow reaches a very distinct 6-cell flow state at $\theta = 100°$. The experimental profile is slightly asymmetric, but is in good agreement with the simulation (figure 5.28). In the experiment the 6-cell flow has broken up into a 2-cell flow state at $\theta = 120°$. The 2-cell flow is characterized by a nearly flat velocity profile.
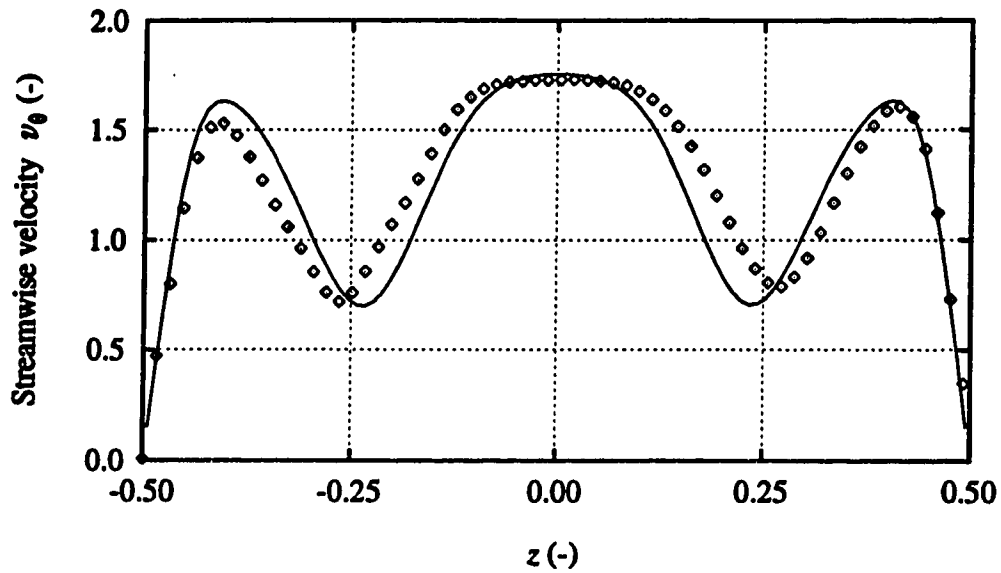
Figure 5.24: Measured spanwise profile of the streamwise velocity compared to the simulation at $Dn = 453$, $\theta = 20°$ and $x = 0.38$; $R_c = 15.1$.

Figure 5.25: Measured spanwise profile of the streamwise velocity compared to the simulation at $Dn = 453$, $\theta = 40°$ and $x = 0.38$; $R_c = 15.1$.
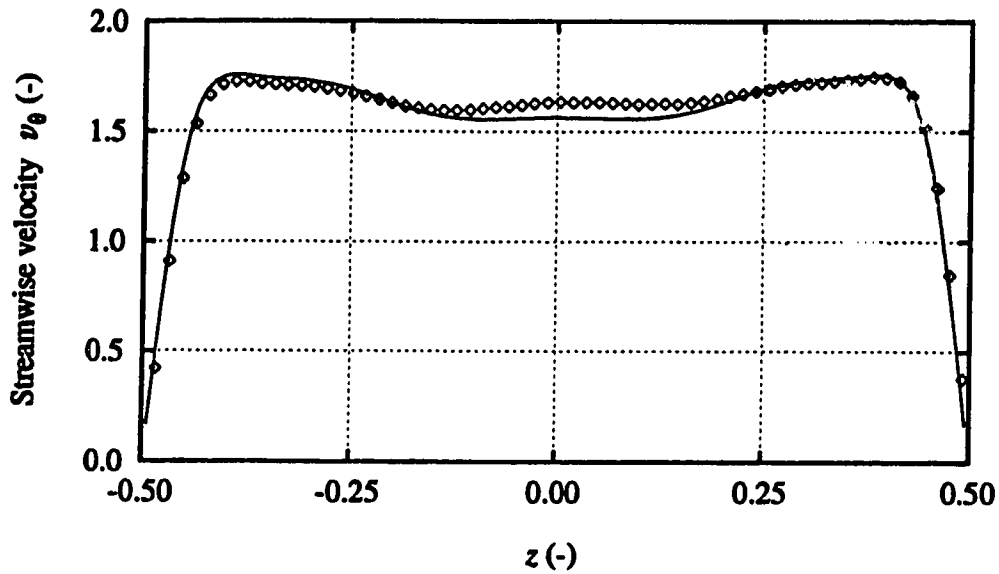
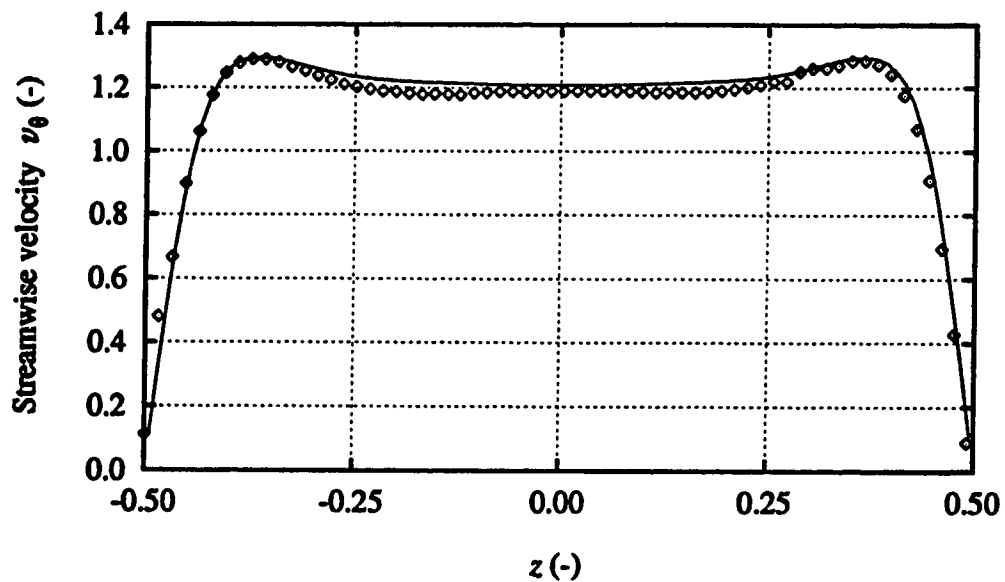Figure 5.26: Measured spanwise profile of the streamwise velocity compared to
the simulation at $Dn = 453$, $\theta = 60°$ and $x = 0.38$; $R_c = 15.1$.
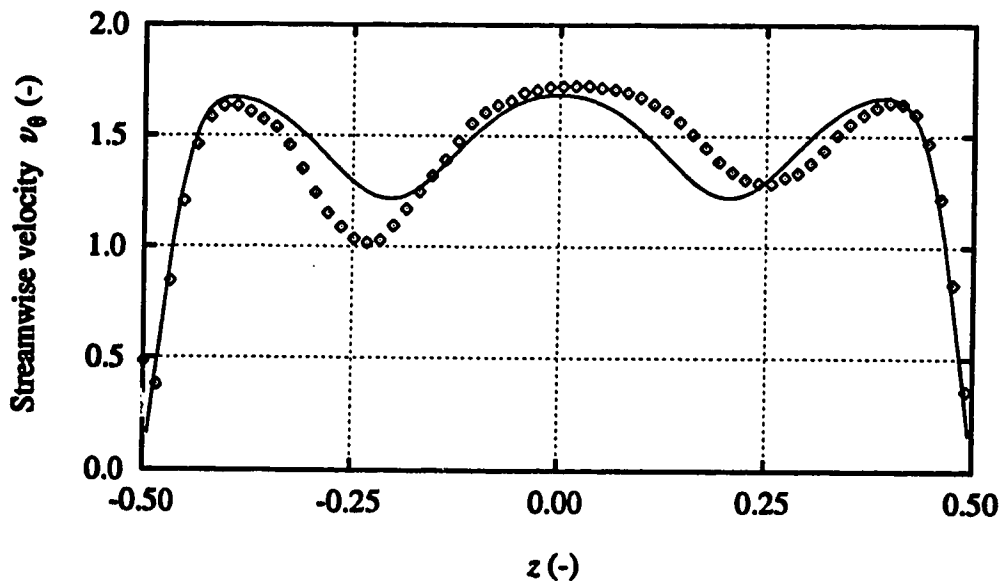
Figure 5.27: Measured spanwise profile of the streamwise velocity compared to
the simulation at $Dn = 453$, $\theta = 80°$ and $x = 0.38$; $R_c = 15.1$.
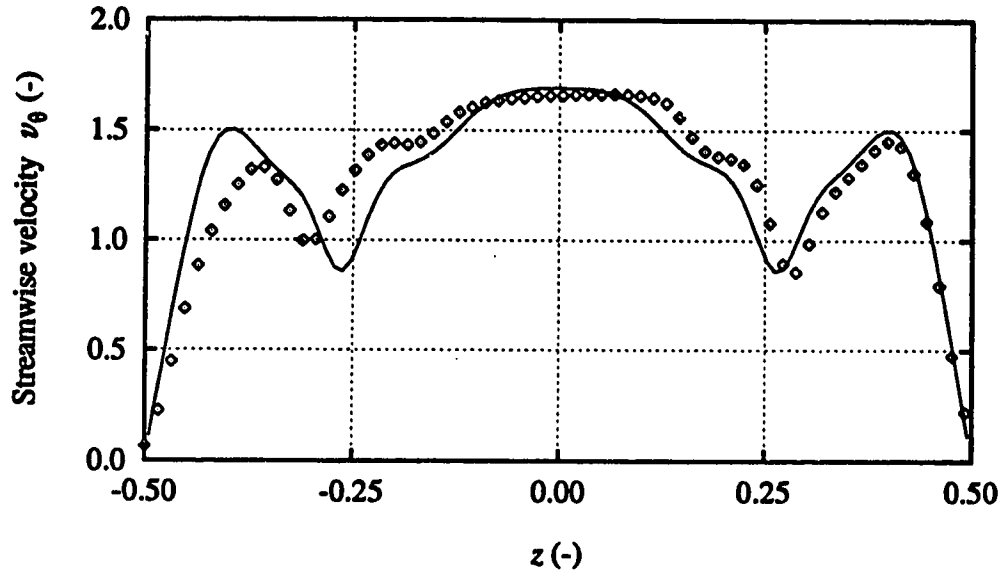
Figure 5.28: Measured spanwise profile of the streamwise velocity compared to the simulation at $Dn = 453$, $\theta = 100°$ and $x = 0.38$; $R_c = 15.1$.
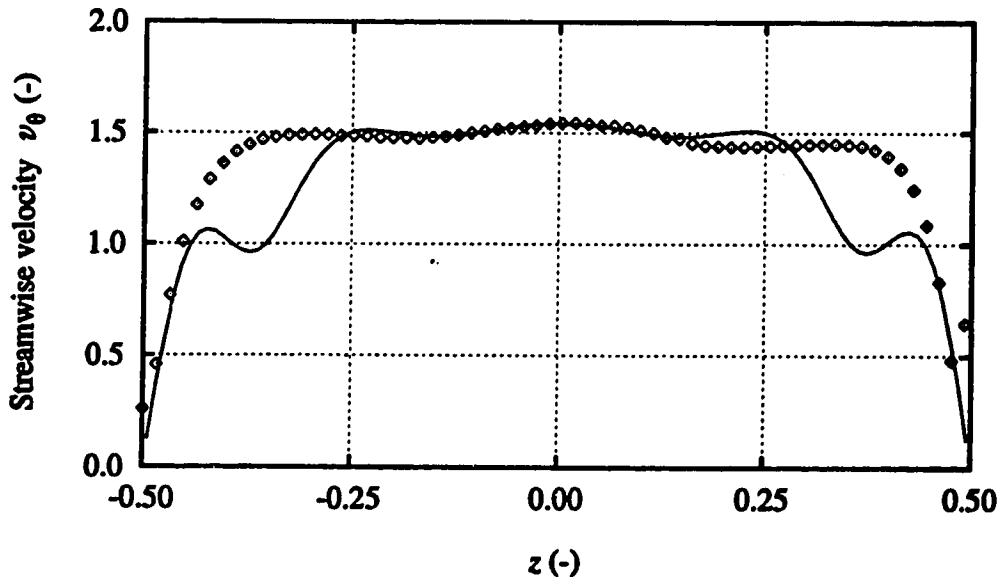
Figure 5.29: Measured spanwise profile of the streamwise velocity compared to the simulation at $Dn = 453$, $\theta = 120°$ and $x = 0.38$; $R_c = 15.1$.
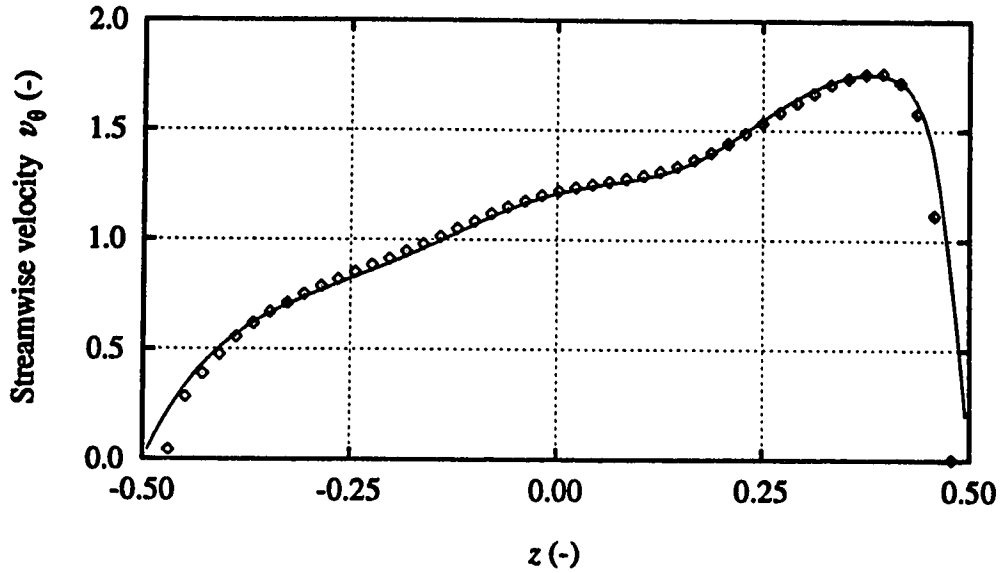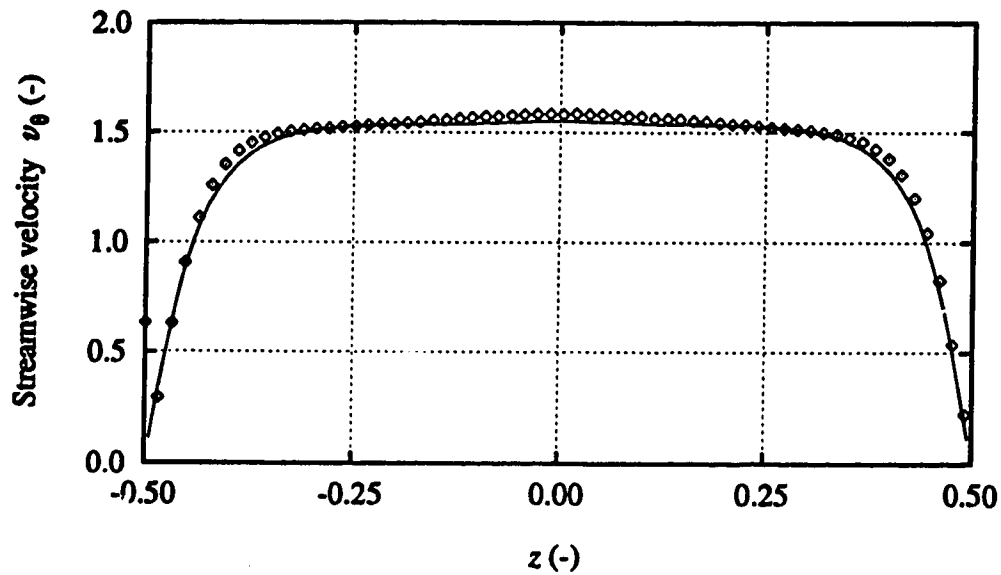
Figure 5.30: Measured spanwise profile of the streamwise velocity compared to the simulation at $Dn = 453$, $\theta = 140°$ and $x = 0.38$; $R_c = 15.1$.
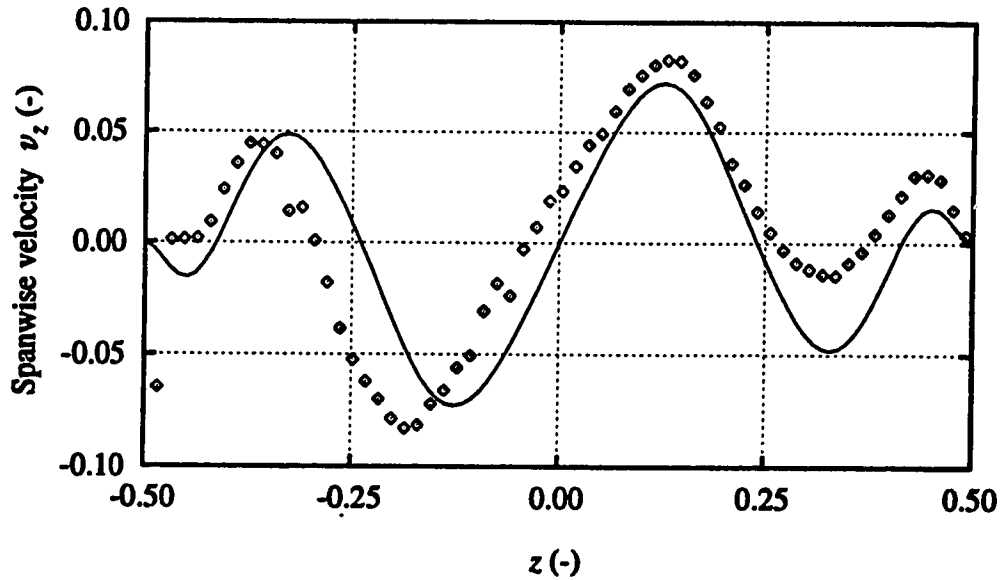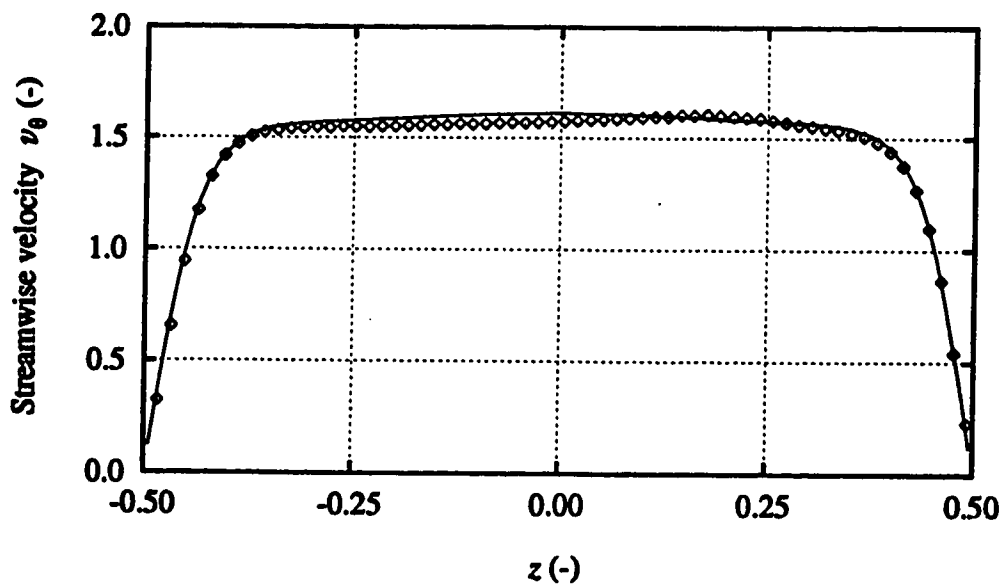

Figure 5.31: Measured spanwise profile of the streamwise velocity compared to the simulation at $Dn = 453$, $\theta = 160°$ and $x = 0.38$; $R_c = 15.1$.
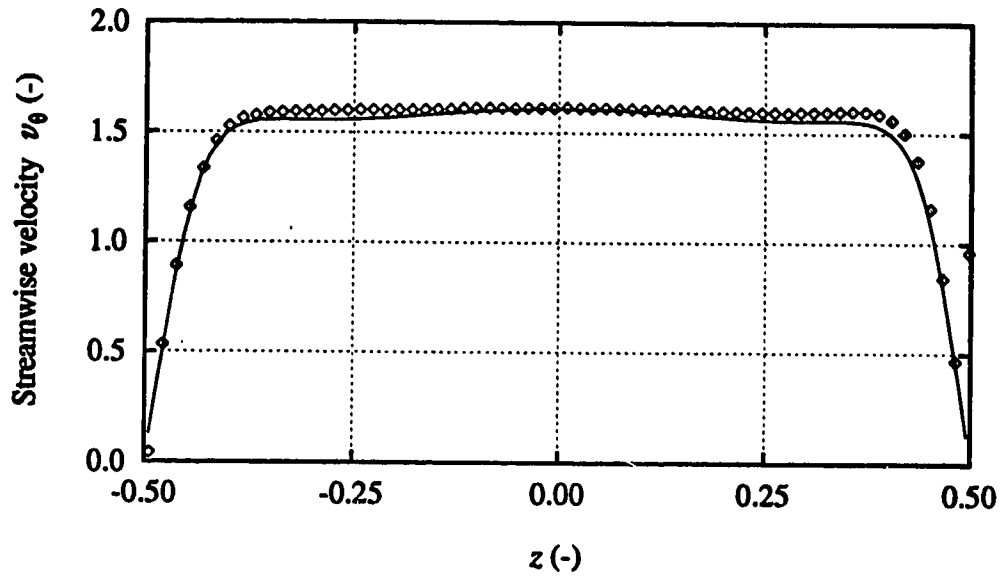
Figure 5.32: Measured spanwise profile of the streamwise velocity compared to the simulation at $Dn = 453$, $\theta = 180°$ and $x = 0.38$; $R_c = 15.1$.
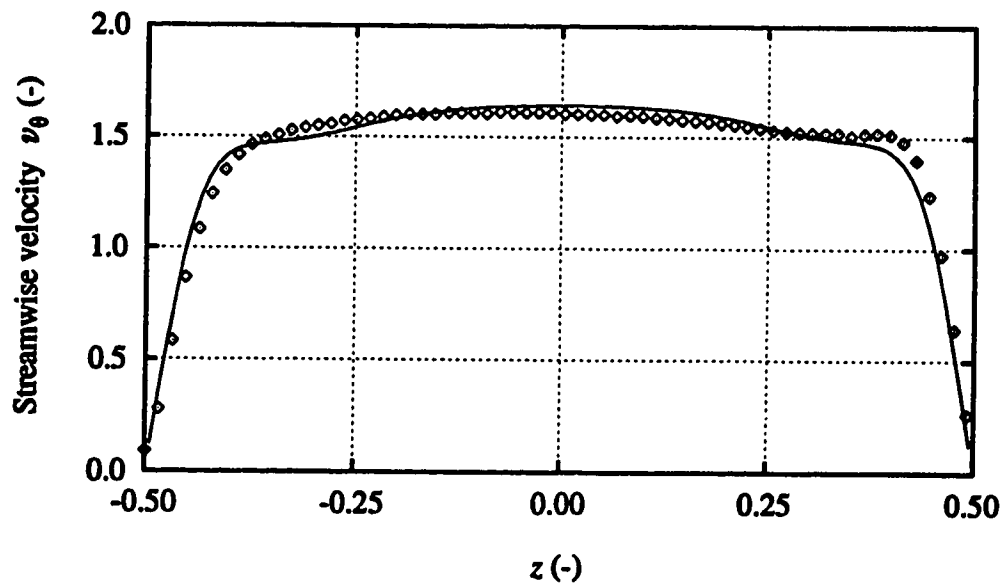
Figure 5.33: Measured spanwise profile of the streamwise velocity compared to the simulation at $Dn = 453$, $\theta = 200°$ and $x = 0.38$; $R_c = 15.1$.
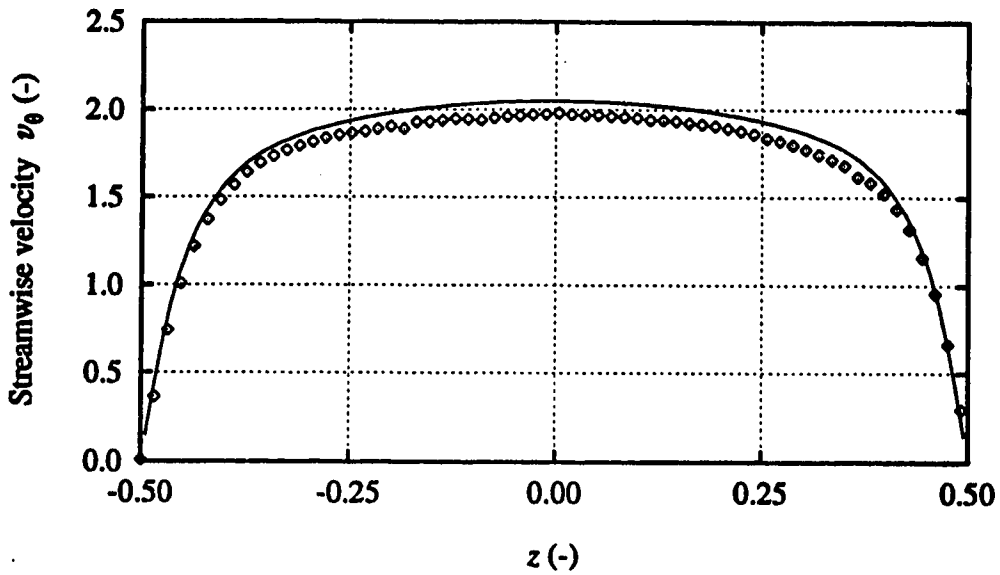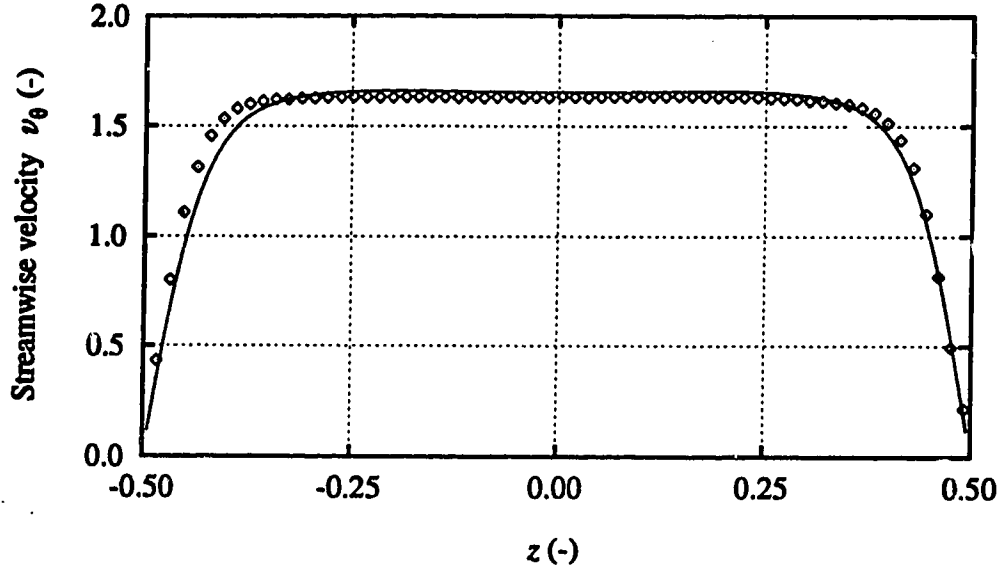
Figure 5.34: Measured spanwise profile of the streamwise velocity compared to the simulation at $Dn = 453$, $\theta = 220°$ and $x = 0.38$; $R_c = 15.1$.
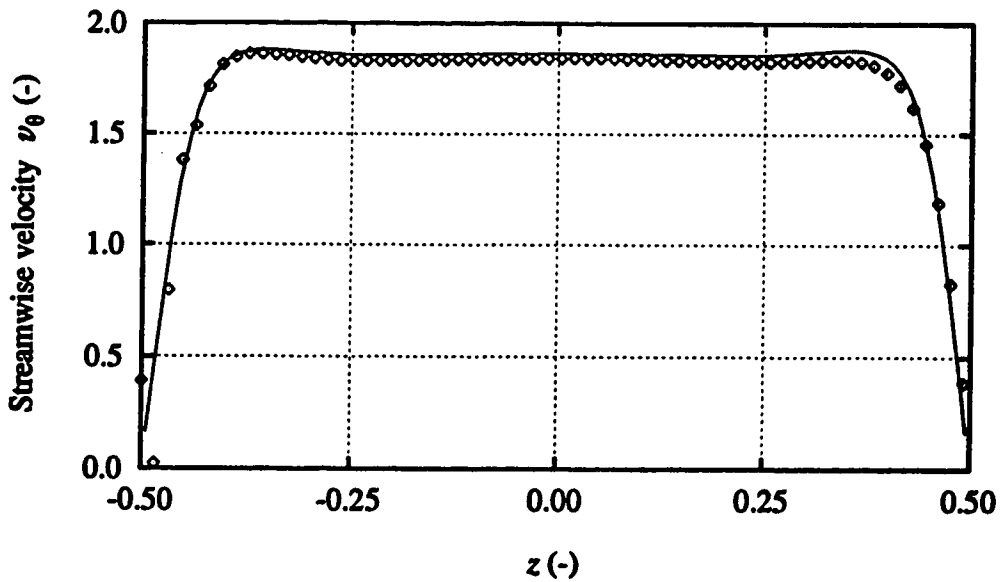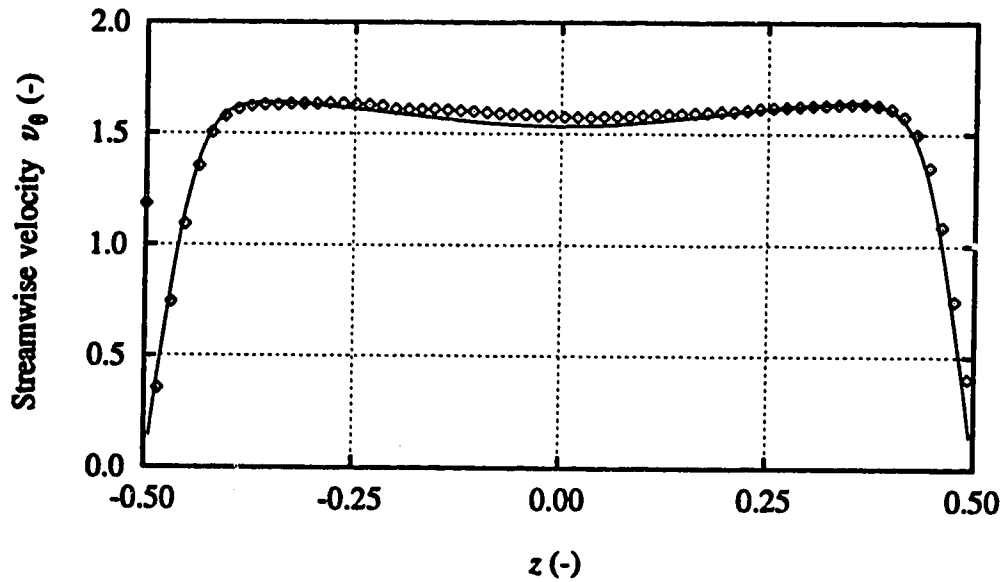

Figure 5.35: Measured spanwise profile of the streamwise velocity compared to the simulation at $Dn = 453$, $\theta = 240°$ and $x = 0.38$; $R_c = 15.1$.

The simulated velocity profile shows signs of Dean vortices in the form of velocity minima near the top and bottom walls. This is the only significant discrepancy between the experiment and the model.

Downstream from $\theta = 140°$ the secondary flow is basically a 2-cell state that changes very little with the streamwise position. The velocity profiles at $x = 0.38$ in figures 5.30 to 5.35 show a gradual change from being convex at $\theta = 140°$ to flat at $\theta = 220°$ and concave at $\theta = 240°$. All these profiles are in excellent agreement with the simulation results. The secondary flow at $\theta = 140° - 240°$ could not be determined from the flow visualization, but the measured velocity profiles confirm the development of a 2-cell secondary flow pattern. At $\theta = 240°$ a new inflow region develops along the centre of the outer wall from which a new 4-cell state is predicted to develop (see the flow development diagram in figure 5.17). The simulation predicts that this 4-cell state will break down asymmetrically into a 2-cell state near $\theta = 500°$. This is the first time in the flow development that the symmetry has been broken significantly.

Once the symmetric 4-cell flow has broken down at $\theta = 500°$, the simulation predicts an unstructured kind of flow behaviour that can best be characterized as a seemingly random sequence of Dean vortex forming and breakup processes. A number of arrow plots that demonstrate this flow behaviour are shown in figure 5.36. Simulations at a 71x71 grid show that this random behaviour continues up to at least $\theta = 2000°$. These random spatial oscillations indicate that at a Dean number of 453 all fully developed solutions are unstable. In reality these oscillations could very well have a temporal or spatio-temporal character.

The development and breakup of the 6-cell flow observed here is very similar to that observed by Sugiyama et al. (1988) in a curved rectangular duct with an aspect ratio of 2 and a curvature ratio of 8. They measured the secondary flow in
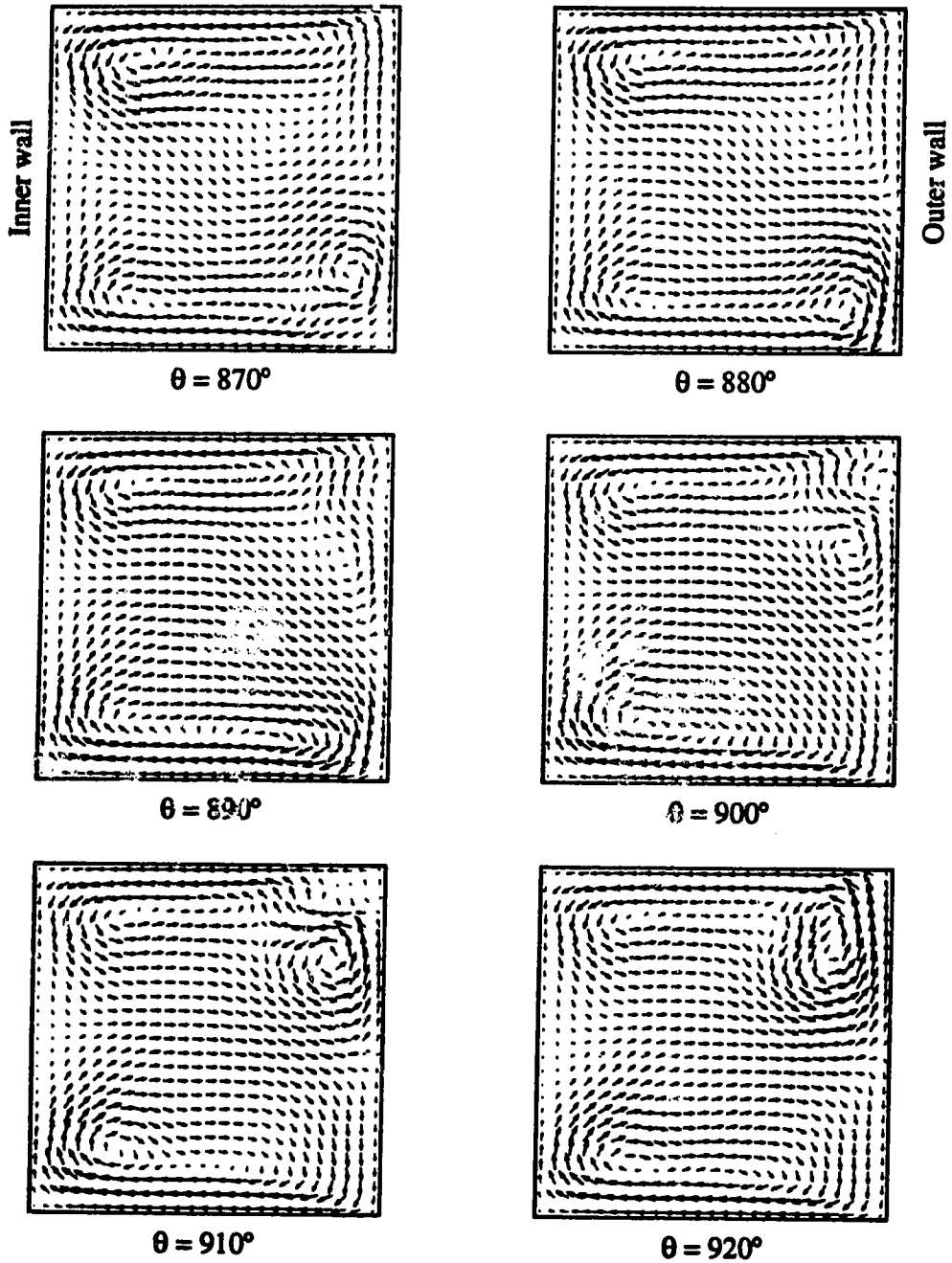
Figure 5.36: Calculated arrow plots showing randomly forming disappearing Dean vortices at $Dn = 453$; $R_c = 15.1$.

the full cross section and used dye visualization. At a Dean number of 220 the first sign of two pairs of Dean vortices is observed at $\theta = 135°$. The 6-cell pattern is most pronounced at $\theta = 180°$ and has broken down symmetrically at $\theta = 270°$.

5.7 Flow Stability

In this section the stability of 4-cell and 6-cell flows will be examined. Winters (1987) showed numerically that the fully developed 4-cell flows on the S_3 branch are unstable with respect to asymmetric perturbations. Two methods can be used to test the stability of 2-dimensional solutions, using the 3-dimensional flow development code: imposing symmetry around the horizontal centre line ($z = 0$) and perturbing the flow asymmetrically.

By imposing symmetry around $z = 0$, asymmetries are unable to develop. Therefore, a flow state that is only unstable with respect to asymmetric perturbations, is stable when symmetry is imposed. This is demonstrated in figure 5.37b for a Dean number of 300. As shown before, without symmetry the flow at $Dn = 300$ develops into a 4-cell state that breaks down asymmetrically into a 2-cell state (figure 5.37a). Imposing symmetry makes this asymmetric fold up process impossible, and thus stabilizes the 4-cell flow.

By perturbing the flow asymmetrically at the inlet of the curved section, the initial asymmetries in the flow are increased and dominate the flow behaviour in the first stage of its development. The flow is perturbed by setting the streamwise velocity along $z = 0.06$ (3 grid points above the centre line for a 51x51 grid) to zero. Because of these strong asymmetries a symmetric 4-cell state never develops (see figure 5.37c). Instead, the flow develops towards a stable 2-cell state that most likely corresponds to branch S_5 in the state diagram.
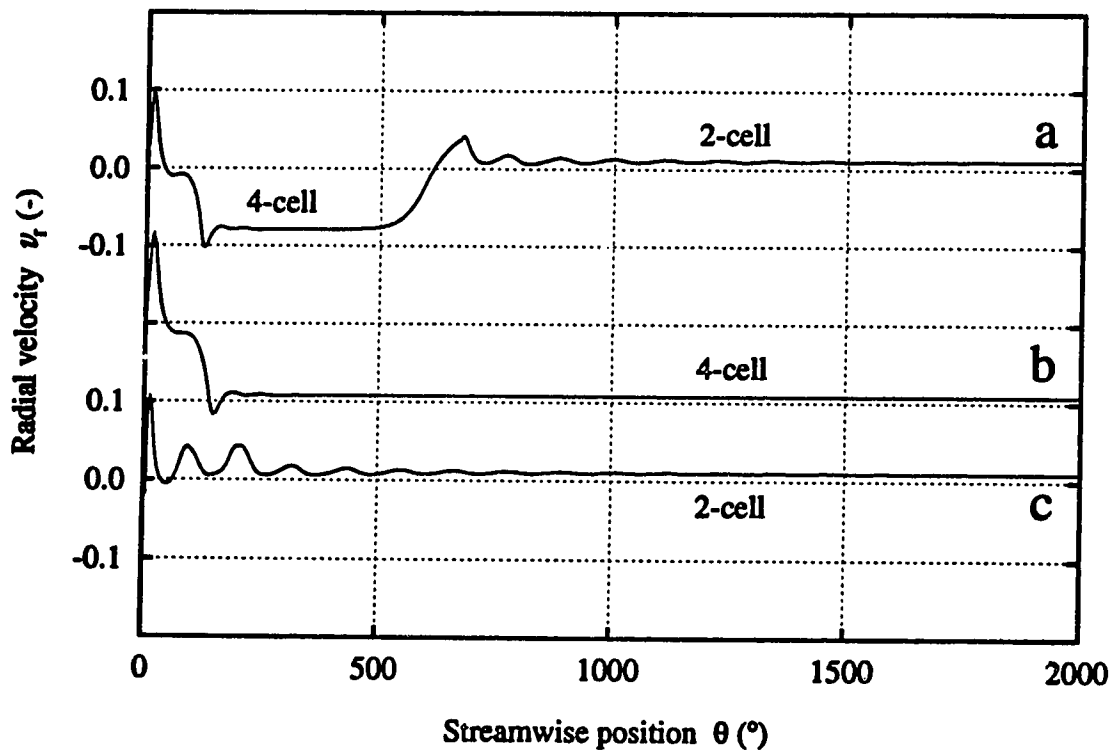
Figure 5.37: Calculated flow development diagrams of the radial velocity at
$x = 0.4$, $z = 0.0$, showing the flow development to $\theta = 2000°$
at $Dn = 300$; $R_c = 15.1$. a: no disturbances, full domain; b:
no disturbances, reflectional symmetry imposed at $z = 0$; c: flow
disturbed at $\theta = 5°$, $z = 0.06$, full domain.

A similar stability analysis was performed for a Dean number of 500. The results are shown in figure 5.38. Without symmetry the flow follows the familiar development of a 6-cell flow that breaks down into a 2-cell flow state from which a symmetric 4-cell develops that breaks down asymmetrically. Only when the 4-cell breaks down do asymmetries start to dominate the flow.

When symmetry is imposed the flow development is very similar up to the symmetric 4-cell state (see figure 5.38b). This 4-cell state is again stabilized by the symmetry. The 6-cell flow that develops around $\theta = 90°$ remains unstable. This was expected because the break up of the 6-cell flow into a 2-cell state seems to be a symmetric process that is not hindered by imposing symmetry. This result indicates that if the 6-cell state corresponds to a fully developed solution, this 6-cell flow is unconditionally unstable.

By perturbing the flow asymmetrically, none of the symmetric flow states develop. The flow develops generally directly towards a state of randomly forming and disappearing Dean vortices, sometimes preceded by periodic spatial oscillations (figure 5.38c).

In summary, the numerical simulations support Winters' result that the symmetric 4-cell is unstable with respect to asymmetric perturbations only, and show that the 6-cell flow is unconditionally unstable and therefore does not reach a fully developed state.
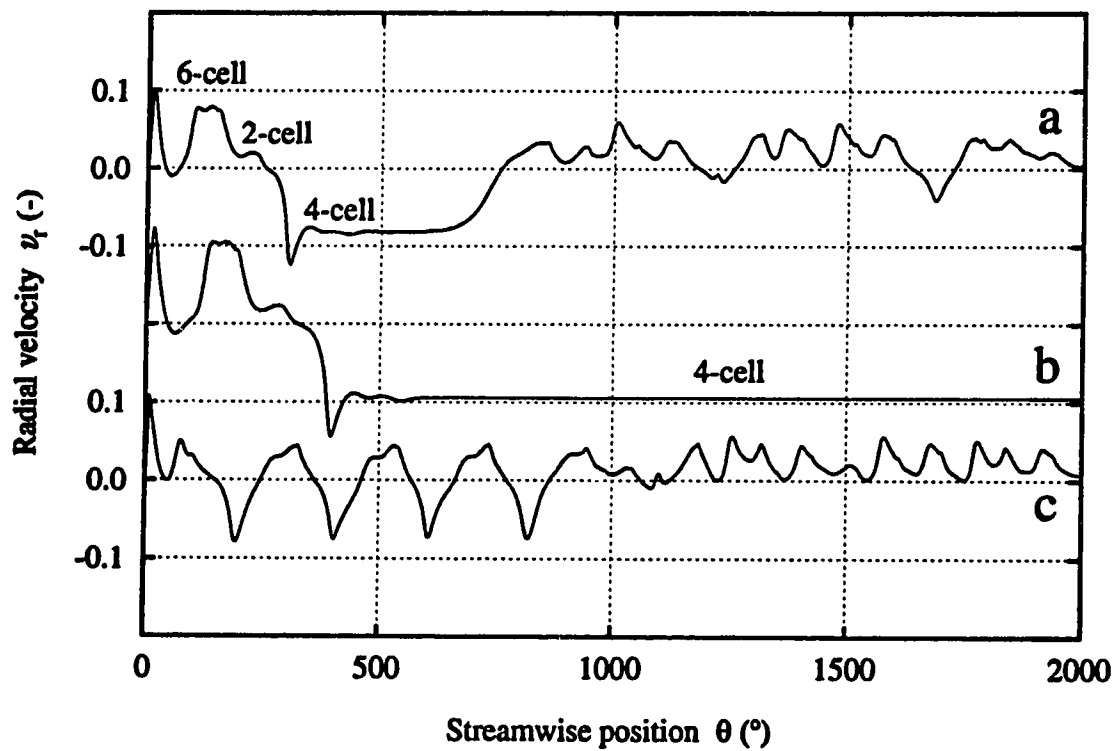
Figure 5.38: Calculated flow development diagrams of the radial velocity at
$x = 0.4$, $z = 0.0$, showing the flow development to $\theta = 2000°$
at $Dn = 500$; $R_c = 15.1$. a: no disturbances, full domain; b:
no disturbances, reflectional symmetry imposed at $z = 0$; c: flow
disturbed at $\theta = 5°$, $z = 0.06$, full domain.

5.8 Summary

Detailed experiments and numerical simulations of steady developing flow up to a Dean number of 600 (Re = 2335) were reported. Flow visualization and LDA measurements were used in the experiments. The simulations are based on the parabolized steady Navier-Stokes equations.

At Dean numbers between 131 and 300 a single pair of Dean vortices develops near the centre of the outer wall as the result of the primary centrifugal instability. This 4-cell flow state is unstable with respect to asymmetric disturbances and breaks down into either a stable 2-cell flow state or spatial oscillations between 2-cell and 4-cell states. These results are consistent with Winters' study of fully developed flows in this geometry (1987). Because the model did not include time dependence, the real flow could develop temporal or spatio-temporal oscillations.

Above a Dean number of 400 a 6-cell pattern is observed early in the flow development. A first small pair of Dean vortices splits and two new vortices are formed in between, resulting in two pairs of Dean vortices. These two vortex pairs are also the result of the primary centrifugal instability. The 6-cell flow breaks down symmetrically into a 2-cell state. This process is very similar to that observed experimentally by Sugiyama et al. (1988) in a curved duct with aspect ratio 2. Based on the similarity with the Görtler problem, it is suggested that the transition to 6-cell flow is the result of a decreasing spanwise wavelength of the Dean vortices with increasing flowrate.

At Dean numbers between 300 and 400 the flow changes gradually from a 4-cell development to a 6-cell development. Because in this region both the symmetric 4-cell and 6-cell states have relatively low growth rates, the flow development is dominated by asymmetric modes. The numerical simulation is very grid sensitive,

probably due to differences in random asymmetric disturbances, created by round-off errors, and grid characteristics.

The experimental flow development at Dean numbers of 272, 326, 375 and 453 was investigated in detail. The simulations are in good agreement with the flow visualization. At $Dn = 453$ also spanwise and radial profiles of the streamwise and spanwise velocity were measured. These velocity profiles are in very good agreement with the simulation. The parabolized Navier-Stokes equations capture the physics of the flow very well.

Numerical stability analyses of 4-cell and 6-cell flows were performed by imposing symmetry around the centre plane at $z = 0$ and by perturbing the inlet asymmetrically. It was shown that the 4-cell flow is unstable with respect to asymmetric disturbances, in agreement with Winters' calculations, and that the 6-cell flow is unconditionally unstable.

Chapter 6

Time Dependent Flow

Phenomena

In the previous chapter, experiments and simulations of developing steady flow were presented. Without perturbing the flow, steady flow development was observed up to a Dean number of about 500. The flow develops very differently when a pin is inserted along the horizontal centre line, $z = 0$, at 5° from the inlet of the curved section. At Dean numbers above 170 the pin induces flow oscillations in the form of traveling waves, which are the focus of this chapter. This traveling wave state in a curved square duct has not been reported before. The frequency of the oscillations increases with increasing flow rate and above $Dn = 260$ the flow becomes very unstable and difficult to analyse. Both flow visualization and LDA measurements of streamwise and spanwise velocity fluctuations were used in the investigation of the traveling wave state. In order to characterize the structure of the traveling wave state, forcing was used to excite a single frequency mode.

First, experimental results will be presented and the effects of the pin and the forcing will be discussed. Then, the structure of the fully developed traveling wave

state at a Dean number of 220 will be described in detail. Experimental results are compared to three-dimensional time dependent and elliptic numerical simulations using the CFD package FLOW3D.

The traveling waves observed here in a curved duct of square cross section are similar to twisting vortices in a curved channel (e.g. Finlay *et al.*, 1988; Ligrani *et al.*, 1992; Le Cunff and Bottaro, 1993) and the sinuous mode of wavy Görtler vortices (e.g. Swearingen and Blackwelder, 1987; Liu and Domaradzki, 1993). The traveling waves also show similarities with oscillations in a two-dimensional wake. An instability mechanism is proposed, based on these similarities.

6.1 Traveling Wave Experiments

The traveling wave state was induced by inserting a pin at $\theta = 5°$. The pin was inserted through the outer wall along the horizontal centre line, $z = 0$. Pin sizes of 33, 29, 27, 26 and 25 gauge were used with diameters of 0.2, 0.33, 0.41, 0.46 and 0.5 mm, respectively. The correct alignment of the pin is essential. By bending the pin slightly, the alignment can be adjusted by rotating the pin. When the pin is aligned correctly, the flow develops symmetrically; beyond the onset of the traveling wave the secondary flow is characterized by two oscillating Dean vortices. If the pin is aligned incorrectly, the oscillating 4-cell state either breaks down into a 2-cell flow, or does not form at all.

Side view visualization of a typical traveling wave, at $Dn = 220$, is shown in figure 6.1. Continuous dye injection was used. The photographs were taken at different moments in time and an attempt was made to match successive images. In this case the time dependence starts around $\theta = 140°$. The oscillations of the flow are quite irregular. If the dye pattern is observed carefully, wave packets that

Streamwise position θ (°)
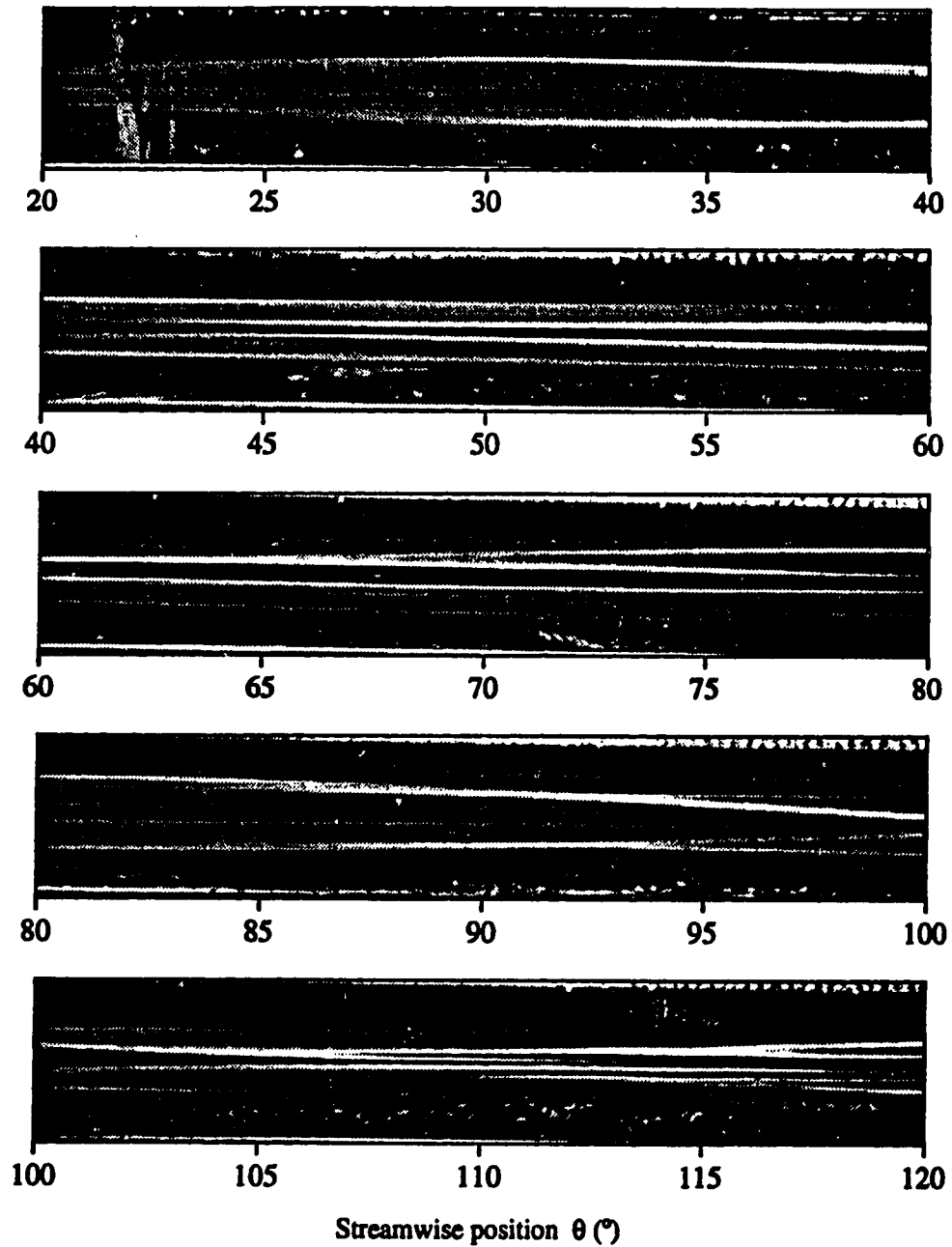
Figure 6.1a: Sideview flow visualization of a developing traveling wave without
forcing at Dn = 220 and with a 29 gauge pin. Dye was injected
continuously.

Streamwise position θ (°)
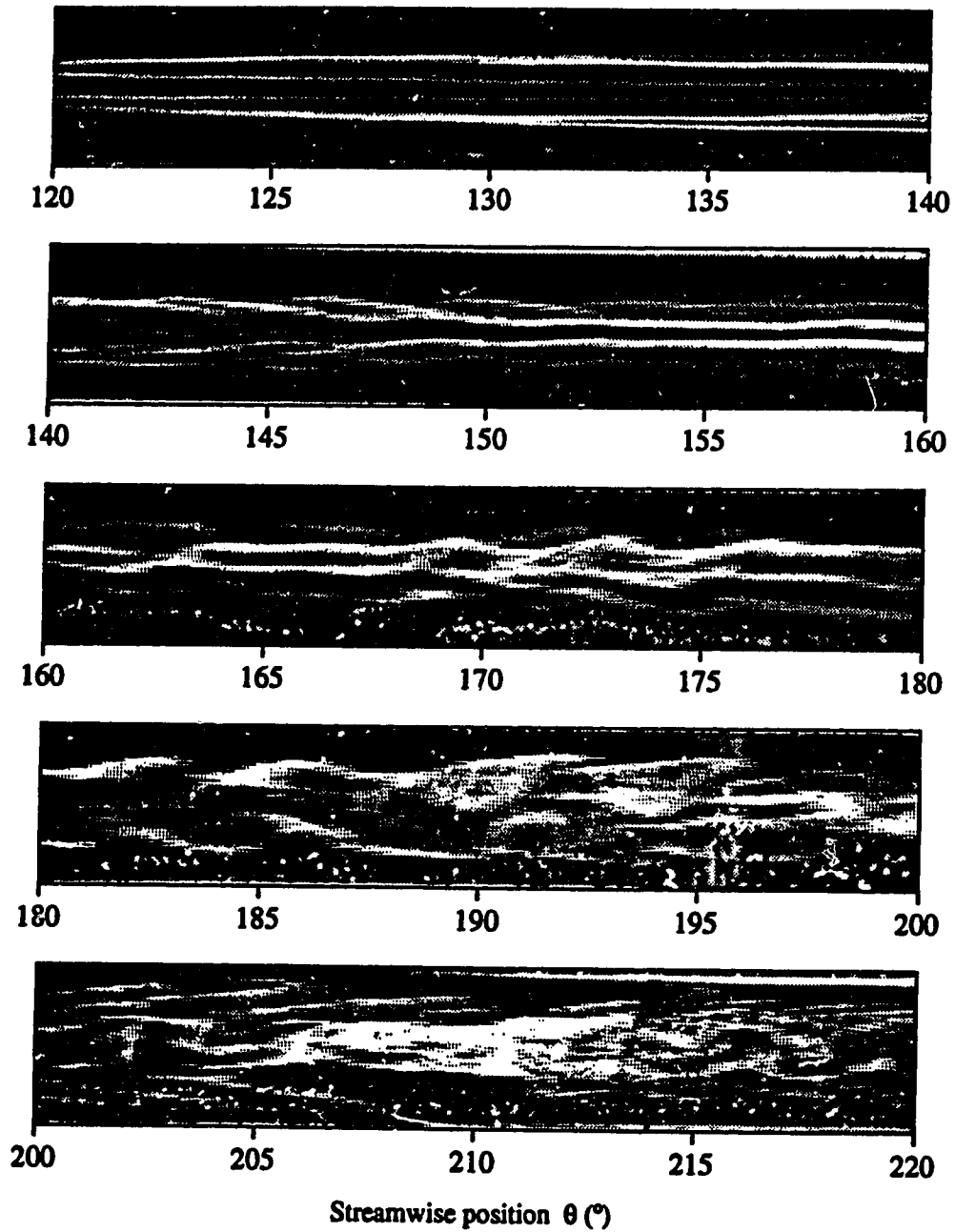
Figure 6.1b: See previous page for caption.

travel through the flow can be distinguished. One such a wave packet is shown in figure 6.1b between $\theta = 170°$ and $\theta = 175°$. In a moving reference frame, the dye pattern changes very slowly while it is convected downstream.

The time series of cross section visualizations in figure 6.2 shows that the two Dean vortices are oscillating while the large Ekman vortices remain relatively quiescent. A characteristic feature of the wavy flow is the oscillating inflow region between two Dean vortices, clearly visible in figure 6.2. The stagnation point near the centre of the outer wall does not move. The Dean vortices oscillate both in radial and in spanwise direction. The vortex centres seem to perform an almost circular motion with the upper Dean vortex rotating counter clockwise and the lower Dean vortex rotating in clockwise direction.

As was pointed out in section 5.3, the dye pattern in the photographs does not necessarily represent the secondary flow field. Because the dye moves at a different speed than the wave, the dye pattern will change with streamwise position, even if the flow field is fully developed or streamwise periodic. It is therefore possible that the flow in fig.re 6.1 has reached a streamwise periodic state, even though the dye pattern is no periodic.

The traveling wave state seems to consist of a series of wave bursts, or packets that grow and blend together as they travel downstream. The existence of these wave packets suggests that the flow is convectively unstable. In a convectively unstable system, a small disturbance of the flow only affects the flow field in the downstream direction, whereas in an absolutely unstable system a small disturbance eventually affects the whole flow field. These concepts are illustrated in figure 6.3. Good reviews of convective and absolute instability in fluid systems are given by Monkewitz (1990) and Huerre and Monkewitz (1990). A convectively unstable system is sometimes called 'noise driven', because small random disturbances, amplified as they are
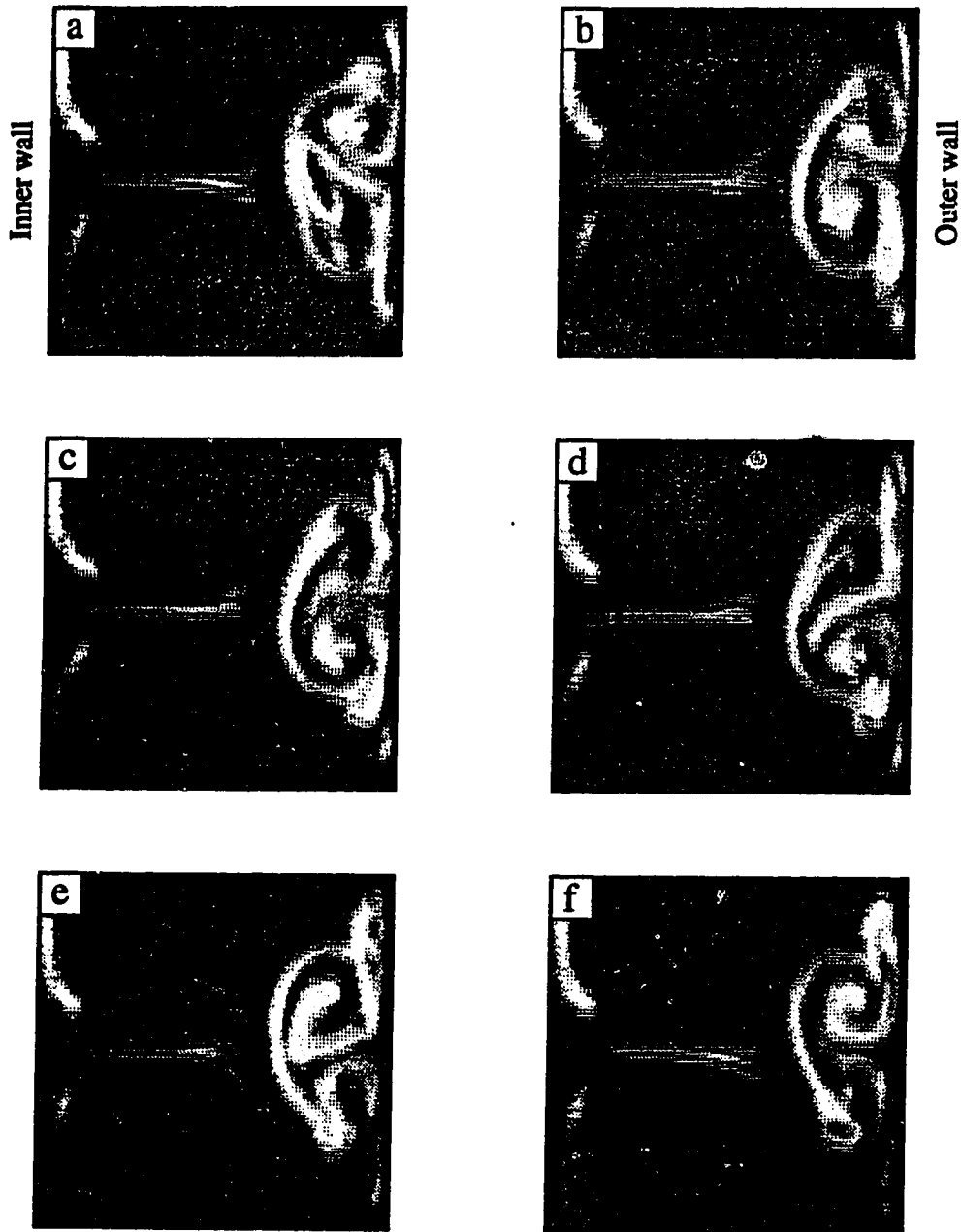
Figure 6.2: Cross section flow visualization showing oscillations at $Dn = 220$ and $\theta = 200°$ with a 29 gauge pin and forcing of 0.82 V^2 at 6.7 Hz.
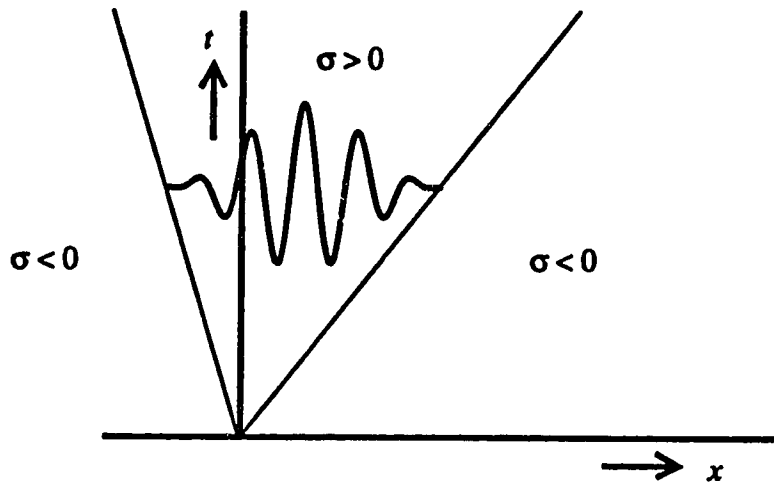
a: absolutely unstable flow
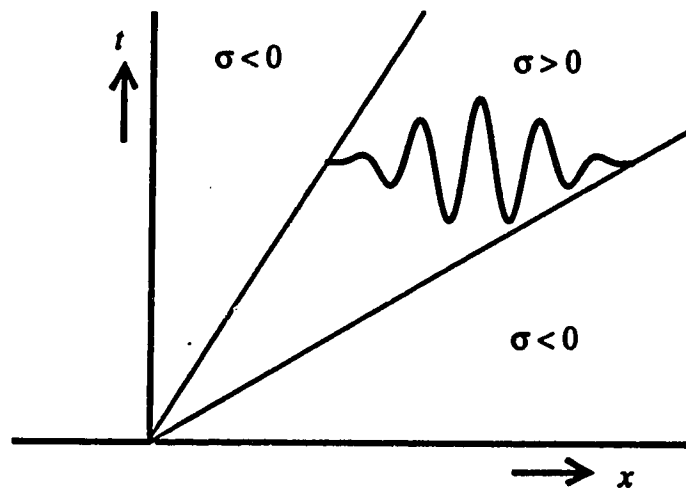
b: convectively unstable flow

Figure 6.3:   Time-space plots illustrating the evolution of a small disturbance
at $x = 0$, $t = 0$ for absolutely and convectively unstable flow. σ is
the amplitude growth rate.

convected downstream, determine the state of these systems. Naturally occurring disturbances are irregular and composed of many spectral components. The modes that are excited by these disturbances are selectively amplified in the flow direction at growth rates that are determined by the physics of the flow. In the curved duct small disturbances seem to be created by the pin that is inserted near the inlet. The role of the pin will be discussed in more detail in section 6.2.

The qualitative features discussed so far are quantified next using detailed velocity measurements. Frequency analysis of the streamwise velocity fluctuations is used to determine which modes are present. Velocity fluctuations were usually measured at 61 positions along a spanwise line at $x = 0.27$ from $z = -0.24$ to $z = 0.24$ ($\pm$ 3 mm from the centre line). Strong velocity fluctuations are found in this region. The frequency spectrum for a Dean number of 220 and $\theta = 180°$, averaged over the 61 positions, is shown in figure 6.4. At each position a sample of 1024 streamwise velocity values was taken at a rate of 100 Hz. The spectrum has a broad maximum around 7 Hz, indicating that at the specified conditions the 7 Hz mode has the fastest growth rate. Other modes in the 4-9 Hz range are present at very similar energy levels and have a significant effect on the flow. Only 35% of the total energy is found in 1.56 Hz wide bands around 7 Hz and its harmonics. The broad band character of the frequency spectrum confirms the convective instability of the flow.

The area under a frequency spectrum is equal to the variance, or mean square of the fluctuating velocity component $(\overline{v_f^2})$, and is a measure of the power of the velocity fluctuations. Therefore, the units of the energy that is shown in the frequency spectrum are determined by the units of the quantity that was measured, in this case velocity expressed in mm/s. One of the tools that will be used to identify the flow structure is the amplitude distribution, which is a plot of the velocity variance
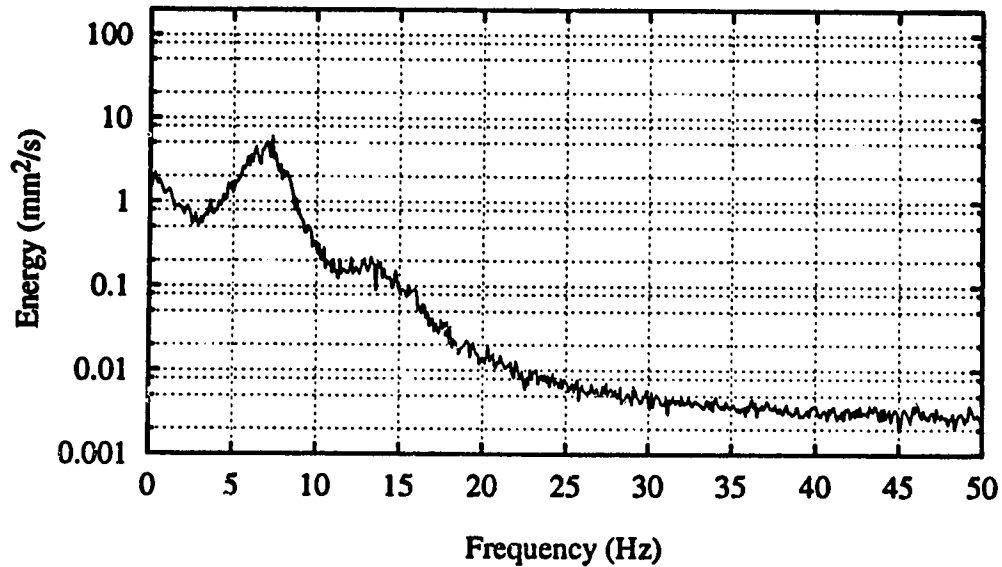
Figure 6.4:   Averaged frequency spectrum of streamwise velocity without forcing
at $Dn = 220$, $\theta = 180°$, $x = 0.27$ and with a 25 gauge pin.
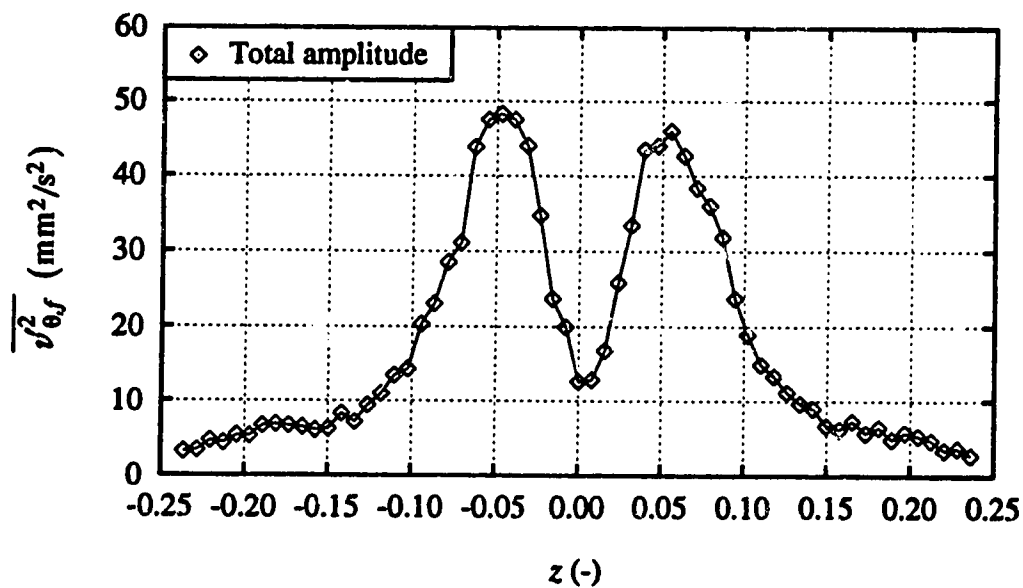
Figure 6.5:   Amplitude distribution of streamwise velocity without forcing at
$Dn = 220$, $\theta = 180°$, $x = 0.27$ and with a 25 gauge pin.

as a function of the spanwise position. The variance will often be called amplitude, and is related to the square of the actual amplitude of the velocity fluctuations. The amplitude distribution of the unforced system at $Dn = 200$ and $\theta = 180°$ is given in figure 6.5. The area under the amplitude distribution will be used as a measure of the total wave power.

One of the objectives of this study is to characterize the structure of the wavy flow. It is therefore necessary to study a single mode, rather than a combination of modes in a wide range of frequencies. Because the flow is very sensitive to upstream disturbances, a selected mode can be given advantage over other modes by introducing a periodic disturbance that is much larger than the disturbances created by random noise. This periodic disturbance was created by slightly compressing the tygon hose that leads the water to the stilling chamber (figures 3.1 and 3.4). The velocity fluctuations that are caused by the forcing are very small compared to the velocity fluctuations that are the result of the traveling wave. Depending on the forcing frequency and the forcing intensity, the excited mode can become the dominating mode, even if this is not the mode with the fastest growth rate. Both in the unforced and the forced system the development of traveling waves is the result of small disturbances in the flow. There is no essential difference between the two, except for the nature of the disturbances. The effect of the forcing will be discussed in section 6.3.

The peristaltic pump that was used for compressing the hose has an output signal in volts that is a measure of the torque delivered by the pump. This signal was sampled simultaneously with the velocity signal. The variance of the forcing signal is a measure of the forcing power. Although there is no direct correlation between this measure of the forcing power and the energy put into the system, this forcing power does provide a relative measure of the magnitude of the forcing and

will be used as such.

The average frequency spectrum with forcing at 6.82 Hz and otherwise identical conditions as figure 6.4 is shown in figure 6.6. The energy of the mode corresponding to the forcing frequency is much higher than the energy of any other mode. The harmonics are the result of the structure of the flow, as will be explained in section 6.5.2. The energy of other modes is much lower than in the unforced system. This suppression is the result of non-linear interactions between different modes. In figure 6.6, 95% of the total energy is concentrated in 1.56 Hz wide bands around the forcing frequency and its harmonics. The total wave power does not change significantly as a result of the forcing. The forcing merely causes a shift of energy from a wide range of modes to a single mode. A forcing frequency of 6.82 Hz is close to the fastest growing mode. It will be shown in section 6.3.4 that anywhere in the 3-10 Hz range the wave can lock in to the forcing frequency.

Amplitude distributions of the forced system are shown in figure 6.7. The amplitude of a frequency component was calculated by integrating the frequency spectrum over a 1.56 Hz wide band, centred around that frequency. The area under the amplitude distribution of a frequency component is a measure of the power of that component. The shape of the amplitude distributions will be discussed in detail in section 6.5.

Side view flow visualization of the forced system is shown in figure 6.8. Since the forcing favours a single mode, the dye pattern is much more regular than in the unforced system. No wave packets can be distinguished. Although the dye pattern changes continuously in the streamwise direction, over a small streamwise distance the pattern is shift-and-reflect symmetric. This means that the pattern is invariant over a reflection in the centre plane, combined with a spatial shift over half a streamwise wavelength. The shift-and-reflect symmetry is particularly evident
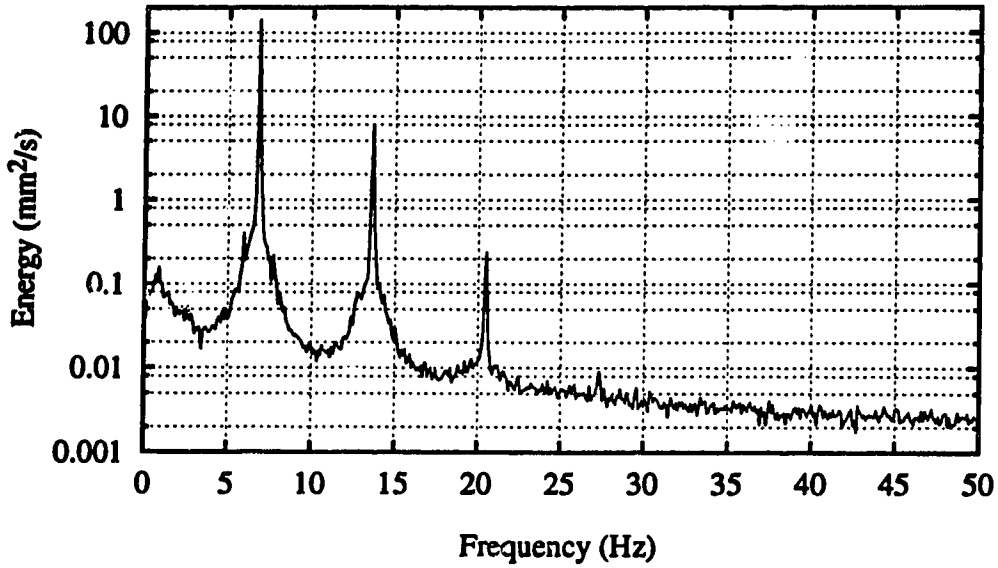
Figure 6.6:   Averaged frequency spectrum of streamwise velocity with forcing of
0.60 V^2 at 6.82 Hz. D_n = 220, θ = 180°, x = 0.27, 25 gauge pin.
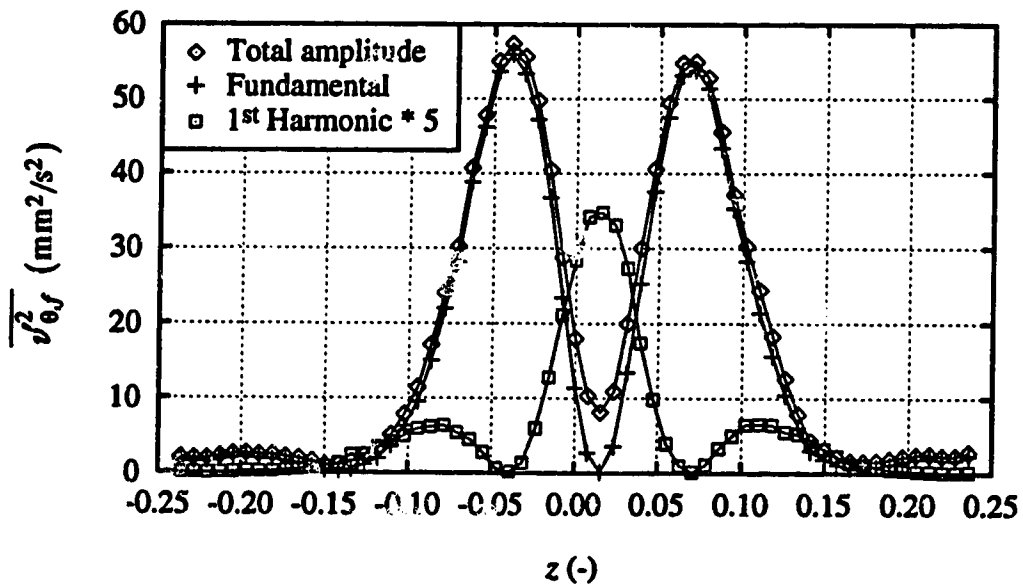
Figure 6.7:   Amplitude distributions of streamwise velocity with forcing of 0.60
V^2 at 6.82 Hz. Dn = 220, θ = 180°, x = 0.27, 25 gauge pin.

Streamwise position θ (°)
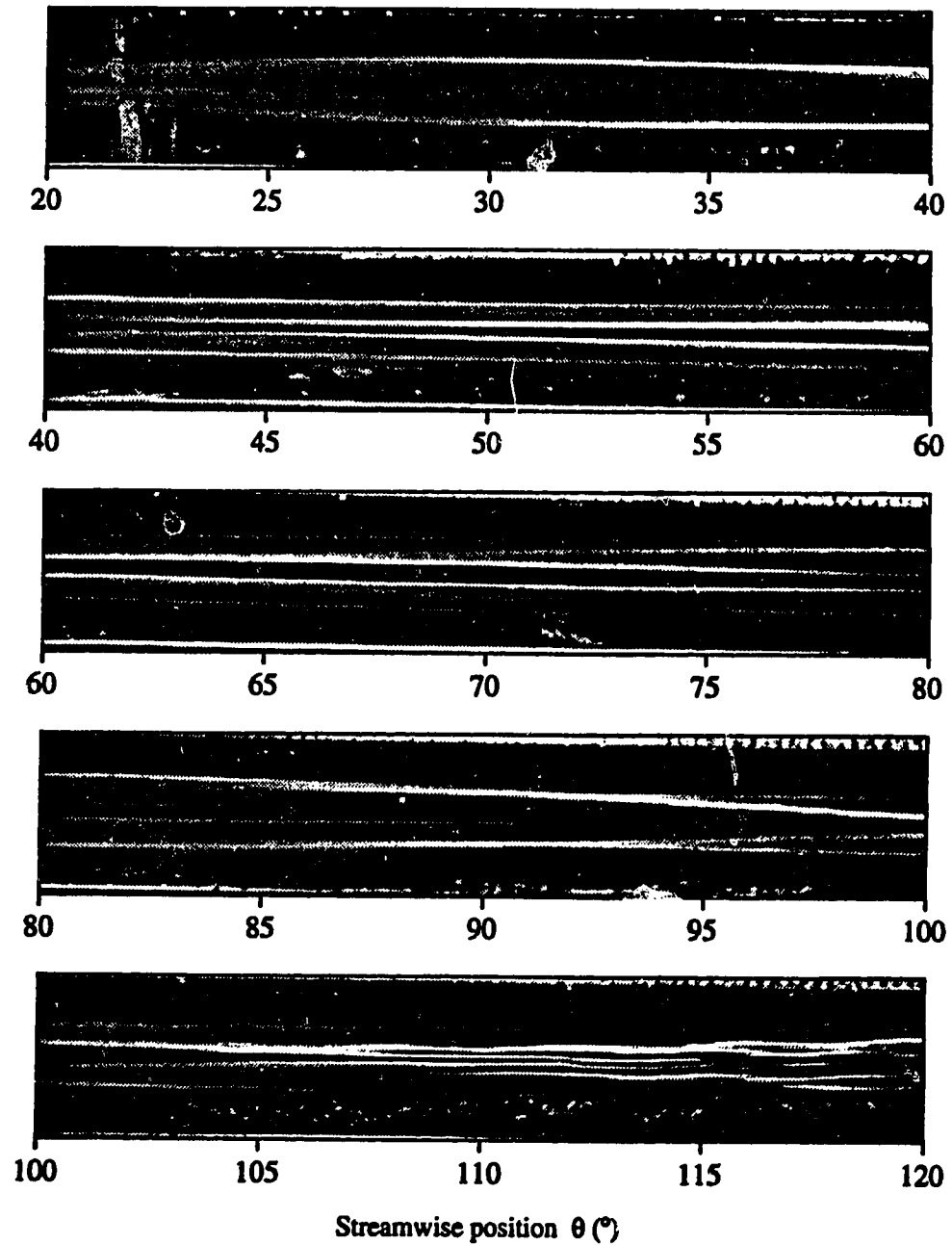
Figure 6.8a: Sideview flow visualization of a developing traveling wave with forcing of 1.08 V² at 6.6 Hz. $Dn = 220$, 29 gauge pin. Dye was injected continuously.

Streamwise position θ (°)
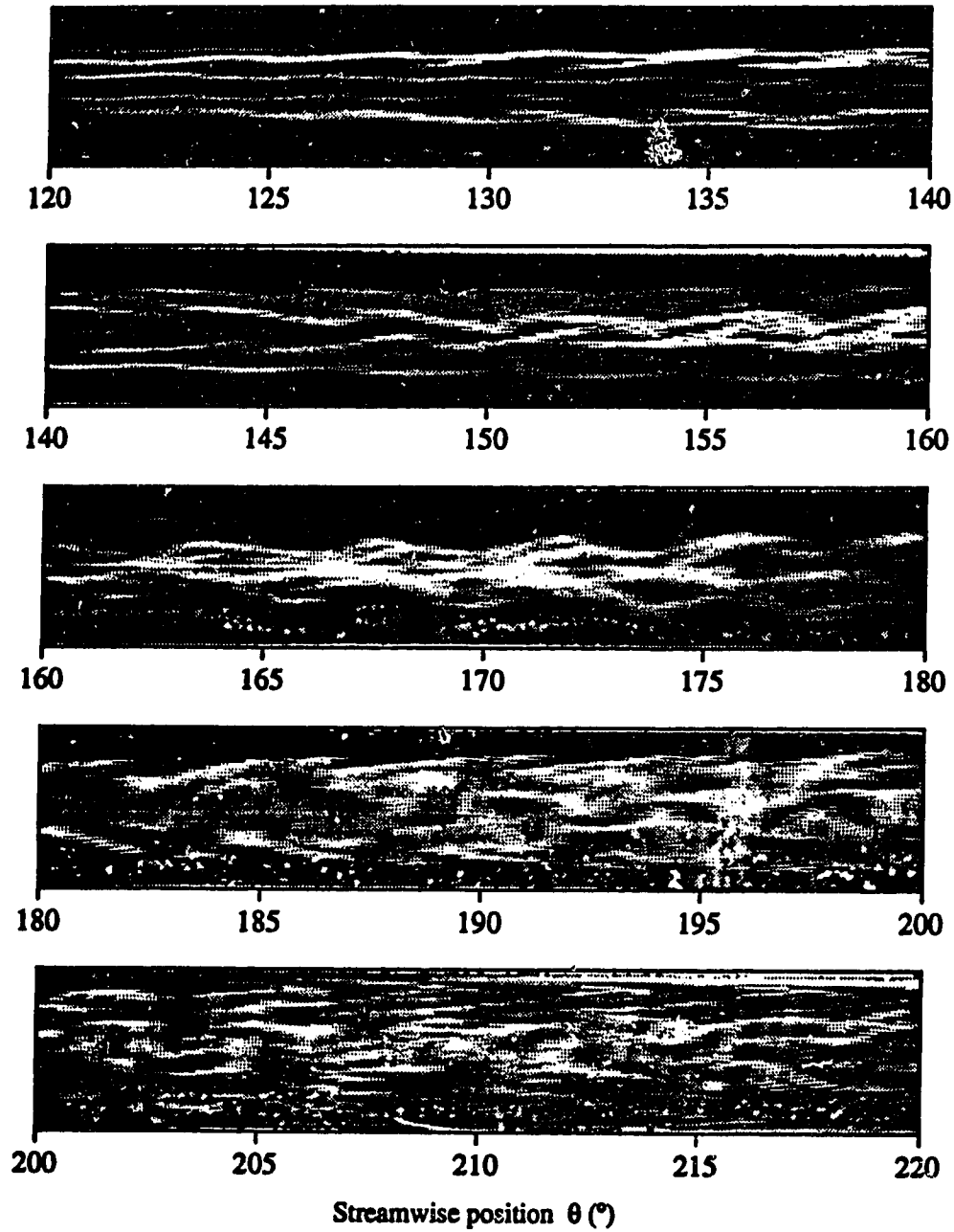
Figure 6.8b: See previous page for caption.

between $\theta = 160°$ and $\theta = 175°$.

The streamwise development of the oscillations is shown in figure 6.9. The flow appears to be steady and retains the reflective symmetry over the first 100°. Oscillations start to develop around $\theta = 120°$. The amplitude of these oscillations grows quickly between $\theta = 120°$ and $\theta = 160°$ after which the amplitude seems to have saturated.

The spatial development of the flow oscillations was quantified by measuring streamwise velocity fluctuation profiles at $x = 0.27$ and $-0.24 < z < 0.24$ for a series of streamwise positions. The power of different wave components is equal to the area under the corresponding amplitude distribution and has the same units as the amplitude (mm^2/s^2). The total wave power and the power of the fundamental and first and second harmonic components are plotted in figure 6.10. No direct comparison between figures 6.9 and 6.10 can be made, because different pin diameters were used. From $\theta = 80°$ to $\theta = 110°$, the wave power increases at a linear rate. Non-linearities start to dominate the wave development around $\theta = 120°$, at which point the wave power begins to saturate. After $\ell \approx 170°$ the wave power does not change much with streamwise position. In this region the time averaged flow field seems to be axially invariant, and this state is called the 'fully developed wave' state. The development length of the traveling wave is defined as the length needed to reach a fully developed traveling wave state.

Although the flow visualization is a good indication of the traveling wave character of the oscillating flow, a more rigorous method to show the existence of a traveling wave would be to take velocity measurements at two different streamwise positions simultaneously. In the case of a traveling wave the two signals will be out of phase by an amount corresponding to the time it takes the wave to travel between the two locations. The amplitude will not depend on the streamwise position. In
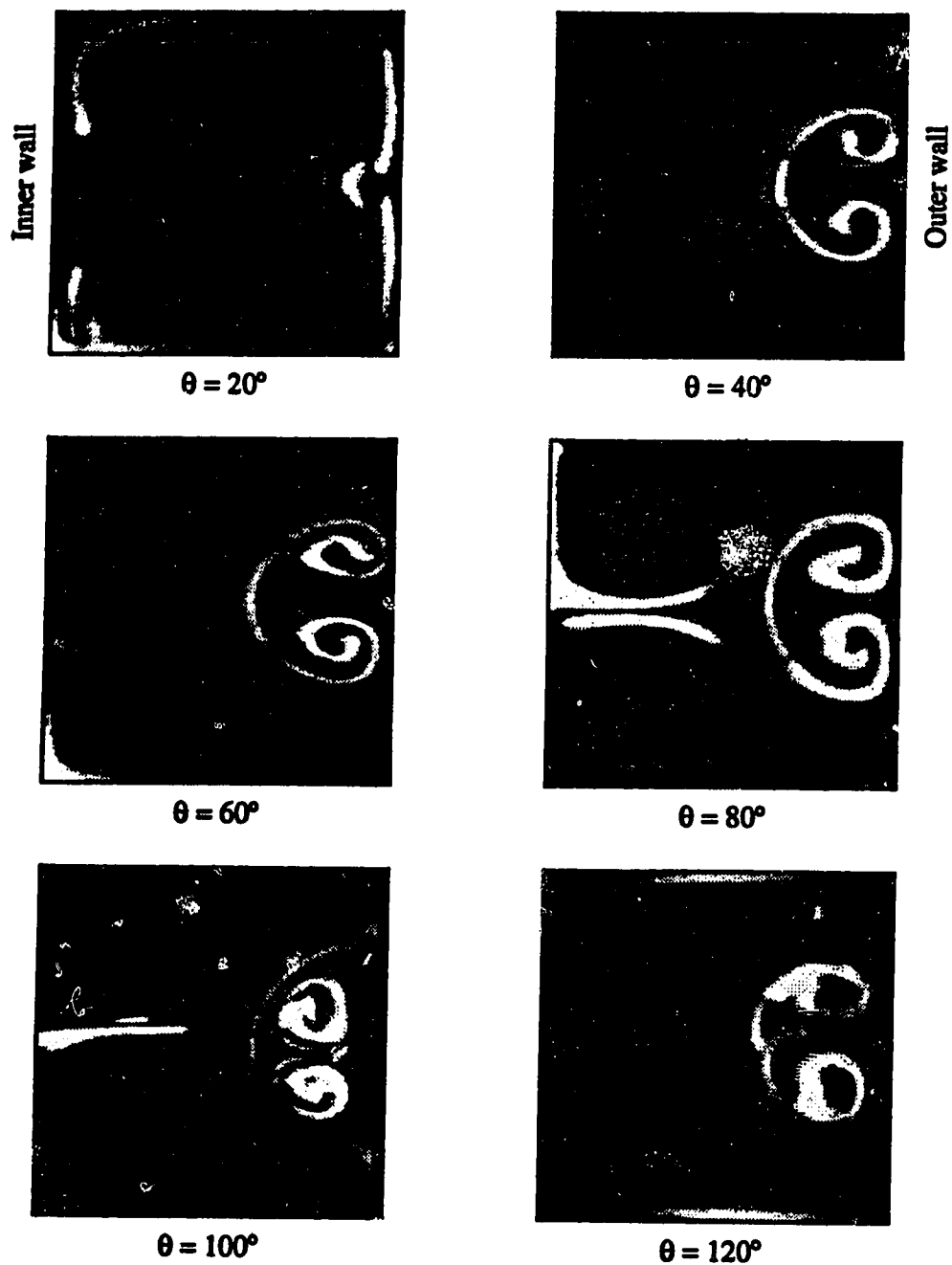
Figure 6.9a: Cross section flow visualization of the traveling wave development at $Dn = 220$ with a 29 gauge pin and forcing of 0.82 V^2 at 6.7 Hz.

θ = 140°   θ = 160°

θ = 180°   θ = 200°

θ = 220°   θ = 𝜅   ʳ
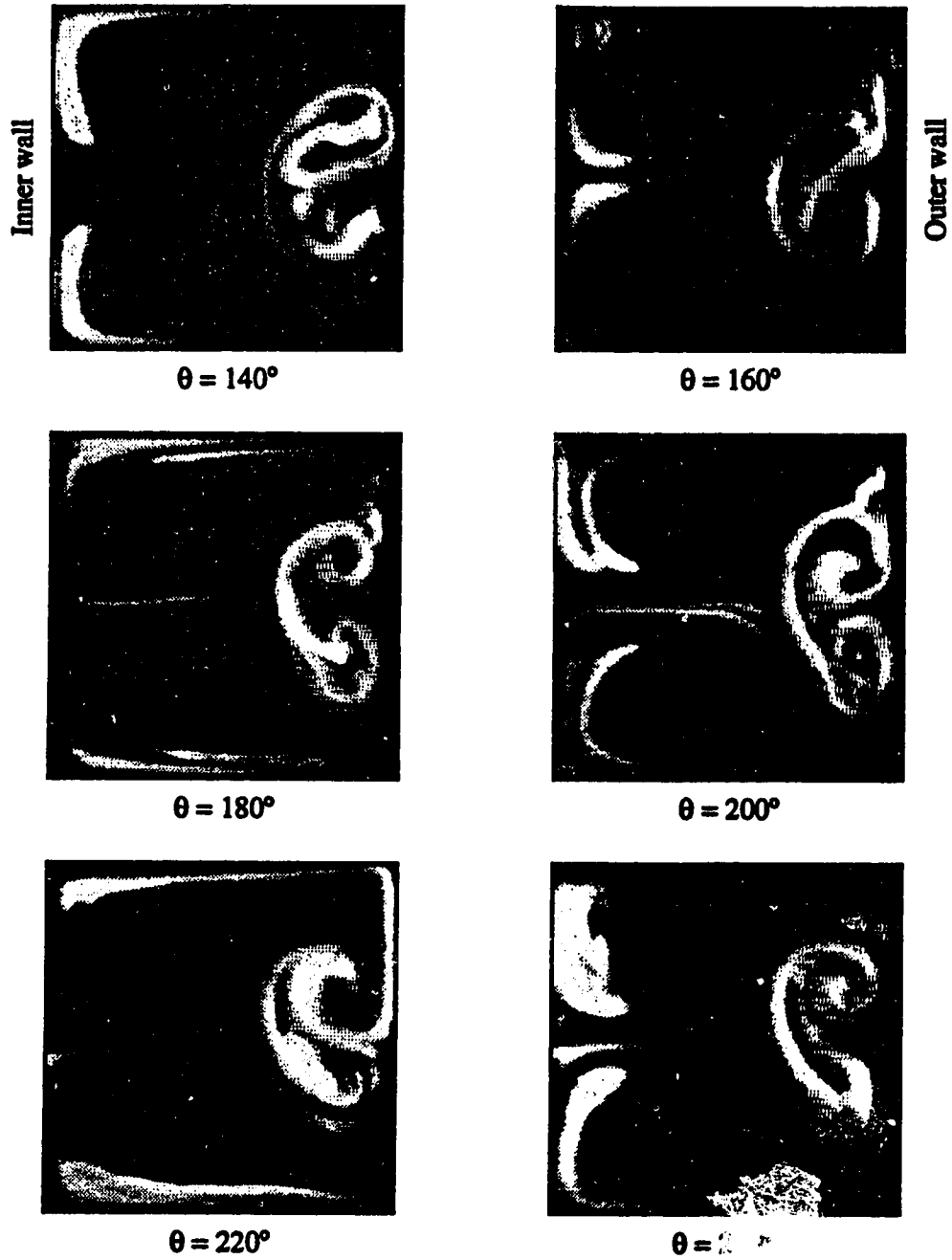
Figure 6.9b: See previous page for caption
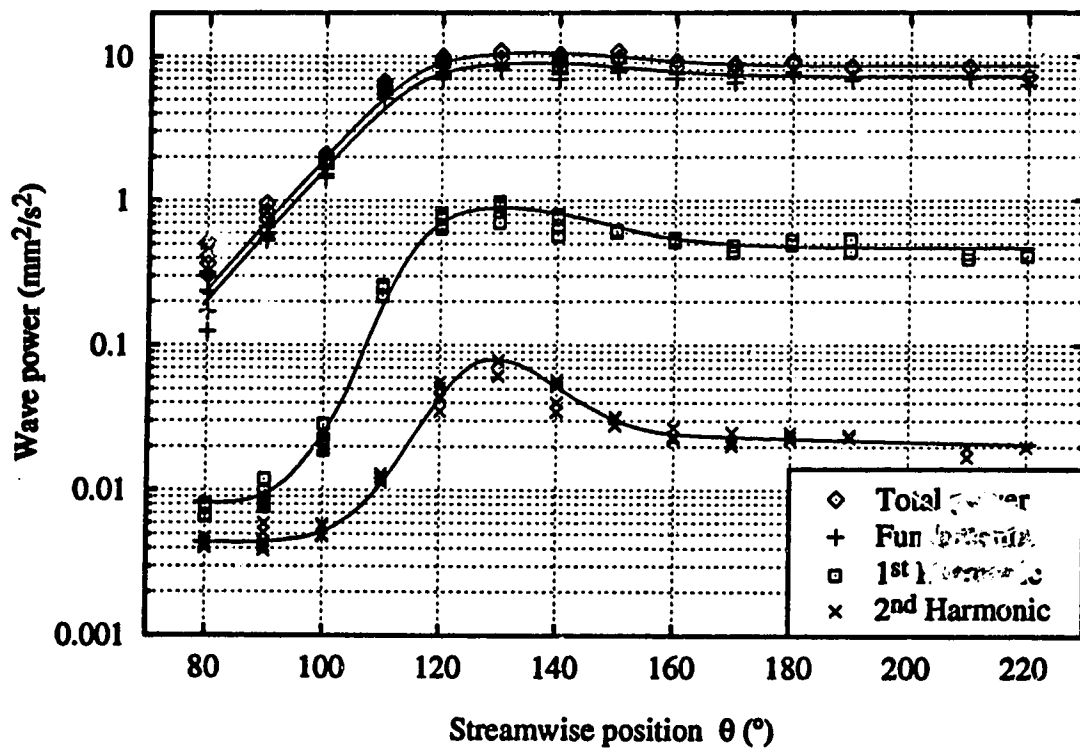
Figure 6.10 Spatial development of the streamwise velocity amplitude. $Dn =$ 220, $x = 0.27$, 25 gauge pin, average forcing of 0.975 V^2 at on average 6.71 Hz. 61 samples ($-0.24 < z < 0.24$) of 512 measurements sampled at 100 Hz.

the case of a standing wave the two signals will be in phase and the amplitude will be streamwise periodic. With the experimental setup used, it was not possible to sample the velocity at two positions simultaneously.

6.2 Role of the Pin in Inducing Time Dependence

The cross section flow visualization in figure 6.9 shows that the traveling wave develops from a steady 4-cell flow. Hence, in order to find a traveling wave state, first a steady 4-cell flow has to develop; then disturbances have to be created that destabilize the 4-cell flow. The pin plays an important role in both these processes. Bara (1992) showed that the pin reduces the streamwise length needed to reach a fully developed steady 4-cell state. It will be shown in this section that the pin also creates the disturbances that destabilize the steady 4-cell flow, leading to traveling waves. The development length of the traveling waves and the effect of the wake behind the pin are also discussed.

6.2.1 Destabilizing 4-Cell Flow

The traveling waves are the result of the destabilization of steady 4-cell flow. The fact that the oscillations only occur when a pin is inserted suggests that destabilizing disturbances are created by the pin. Forcing of the flow will be used to show that this is indeed the case.

The flow was forced by periodically compressing the hose to the stilling chamber. Compressing the hose causes a pressure pulse and possibly a flow rate change that affects the system globally. Because of the convective nature of the instability, the

wave can only lock in to the forcing if a localized disturbance is created as a result of this global pressure and flow rate fluctuation. Because disturbances travel at the speed of the traveling wave, the downstream effect of the forcing is only felt after a delay corresponding to the time it takes disturbances to ' $\mathcal{A}$: vn the system. By monitoring the downstream effect of a sudden change i târ ? using frequency, the streamwise position where the disturbances are created can be determined.

For this experiment the streamwise velocity at $\theta = 180°$ ($x = 0.27$, $z = 0.055$) was sampled during 82 seconds. After about 46 seconds the forcing frequency was changed from 6.8 Hz to 7.6 Hz. 4096 velocity measurements were collected at a rate of 50 Hz. The frequency of both the forcing signal and the measured velocity oscillations are shown in figure 6.11, with a detail in figure 6.12. There is a 6.97 s delay between the frequency change of the forcing signal and the frequency change of the measured v∙ 'y. This is the time it takes the disturbances that induce the flow oscillations from the point were they were created to a position at $\theta = 180°$. The pσ. 'ere the disturbr. ces are created can be found if the wave speed is known.

Each traveling wave mode has a characteristic speed that is constant throughout the system, or at least the fully developed wave region. If this was not the case, a fully developed wave state would not exist. Because the wave travels in the azimuthal direction, the wave speed must be expressed in degrees per time unit, rather than a distance per time uni⁺

An estimate of the wave speed was obtained by measuring the wave length, using flow visualization. The wave speed is found by multiplying the wavelength with the wave frequency, which is selected through the forcin, ᵡause the dye pattern keeps changing with streamwise position the wavelength of the oscillations can not be determined very accurately. A more accurate method for measuring wave speeds
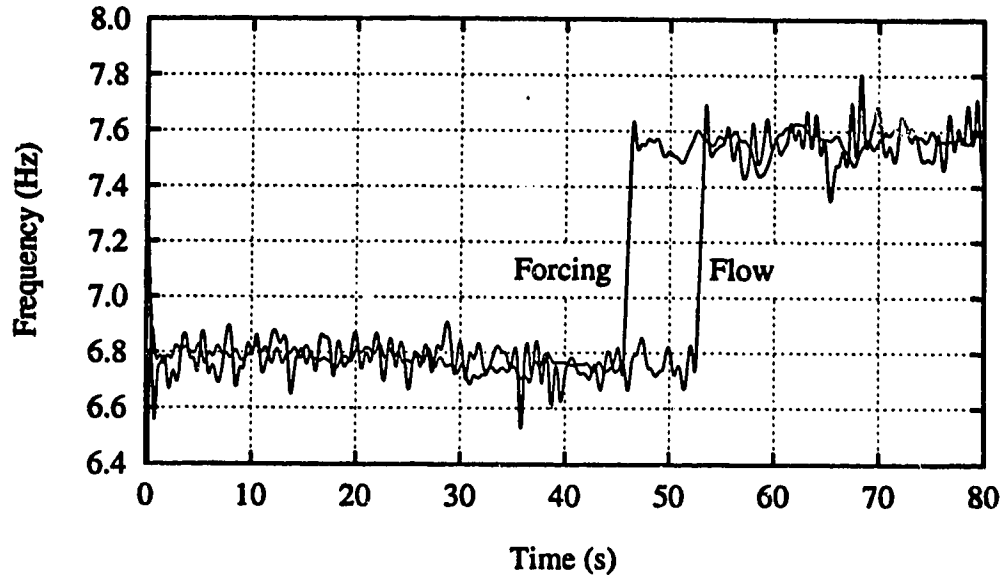
Figure 6.11: Response of streamwise velocity fluctuations to a step change in forcing frequency. $Dn = 220$, $\theta = 180°$, $x = 0.27$, $z = 0.055$, 25 gauge pin, forcing of 0.73 V^2, 4096 data points sampled at 50 Hz.
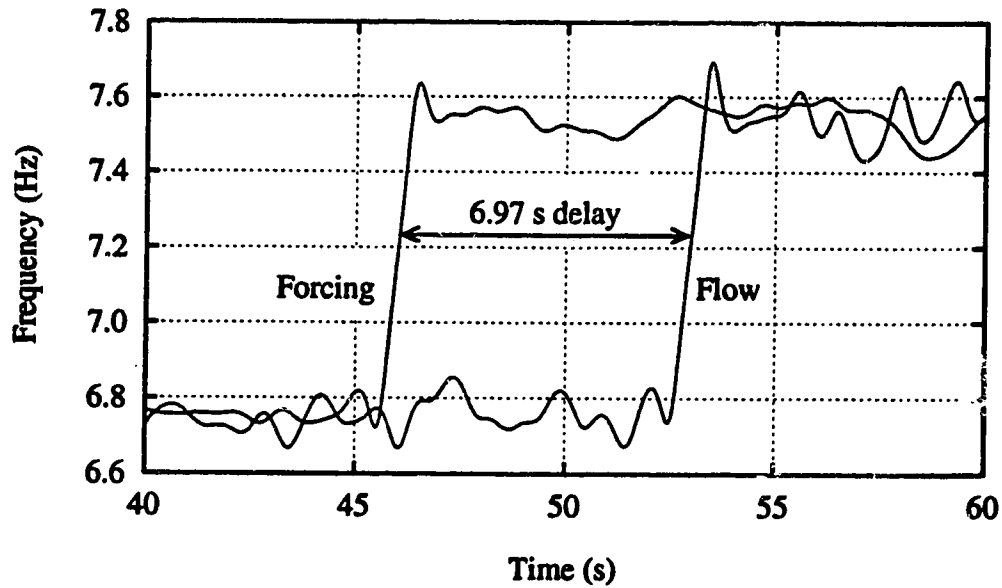
Figure 6.12: Detail of figure 6.11.

would be to measure the streamwise velocity at two different positions in the fully developed region of the traveling wave. The wave speed can then be found from the phase difference between the two signals and the distance between the two probes.

For the conditions of figure 6.12, the wave speed was estimated at $25.5°/s$ with an experimental error of about 5%. With the pin inserted at $5°$ from the inlet, the distance between the pin and the location at which the velocity is measured is $175°$. At a wave speed of $25.5°/s$, the wave travels $178° \pm 9°$ in 6.97 s, indicating that the disturbances were created somewhere between the inlet of the curved section and $11°$ from the inlet. In this section of the duct, the pin is the only source of localized disturbances. It seems likely that also in the unforced system the destabilizing disturbances are created by the pin.

6.2.2 Development Length of Traveling Waves

The development length of the traveling waves depends on the development of the steady 4-cell flow from which they develop, and on the presence of destabilizing disturbances. Matsson and Alfredsson (1993a) found that in a curved channel, twisting vortices develop simultaneously with the Dean vortices. This suggests that in a curved square duct the 4-cell flow does not have to be fully developed before the onset of traveling waves can take place.

Bara(1992) discovered that at Dean numbers between 131 and 150 the development length of steady 4-cell flow is reduced significantly by the pin. This is thought to be the result of the streamwise velocity profile induced by the pin. The pin reduces the streamwise velocity along the centre line, $z = 0$, thereby creating a streamwise velocity profile that promotes the development of a 4-cell state. Figure 6.13 shows the development length reduction at $Dn = 220$ using two
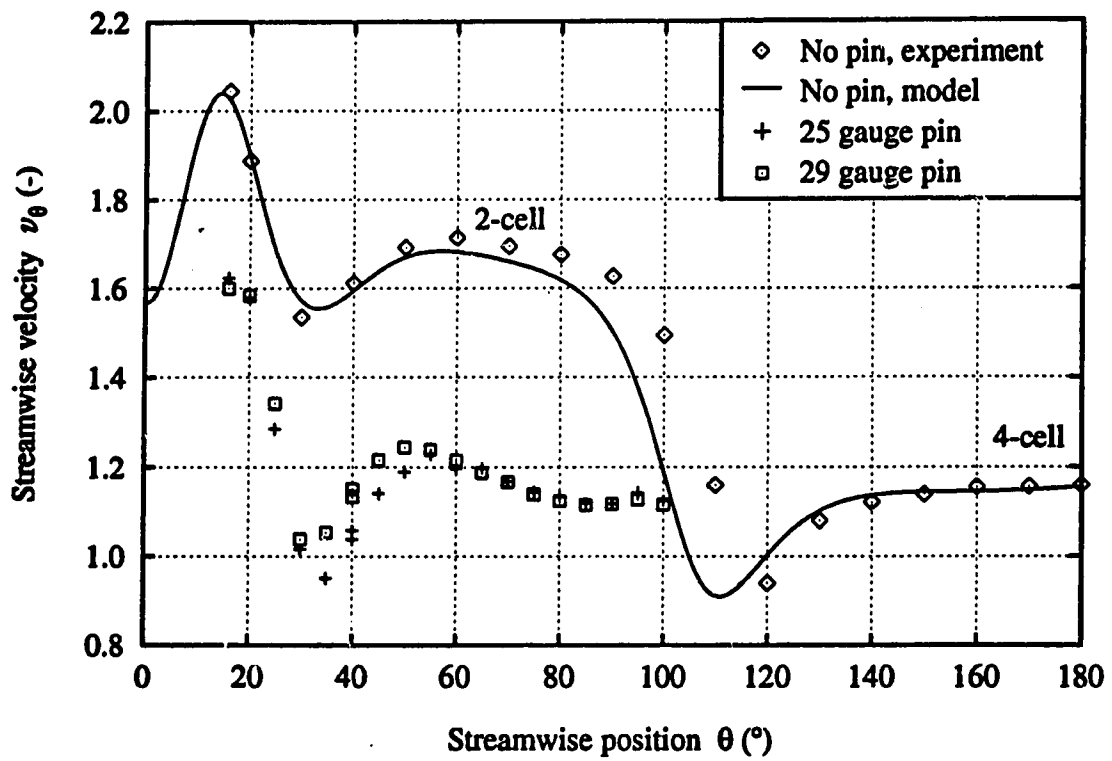
Figure 6.13: Development length of steady 4-cell flow without pin and with 25 and 29 gauge pins. $Dn = 220$, $x = 0.27$, $z = 0.0$.

different pin diameters. Although the different pins have different effects on the flow development, the development length for both pins is the same.

It was shown in section 6.2.1 that the pin also creates the disturbances that destabilize the 4-cell flow. Because of the combined effects of the pin, the traveling wave can be observed within the limited length of the apparatus.

Without inserting the pin no oscillations were observed within the first $270°$ for $170 < Dn < 260$ and one can only speculate about whether spontaneous oscillations would occur further downstream or not. There are two requirements for the development of traveling waves: a steady 4-cell state and disturbances that destabilize the 4-cell flow. Without the pin a 4-cell state will develop, although somewhat further downstream (figure 6.13). It seems likely that without the pin, random disturbances in the flow will grow and eventually destabilize the 4-cell flow, although this may take much longer. This suggests that in a longer apparatus traveling waves would form spontaneously. Some experimental evidence exists for these spontaneous oscillations: without inserting the pin, oscillations develop near the end of the duct for Dn around 600. Highly unstable flow and very fast oscillations make what seems like naturally occurring traveling waves very difficult to study.

6.2.3   Wake behind the Pin

It is well known that in wakes behind bluff bodies, self-sustained oscillations can be produced as a result of the local absolute instability of the flow (Chomaz *et al.*, 1988; Monkewitz, 1990; Oertel, 1990). The oscillations in the wake behind a circular cylinder are the result of a periodic vortex shedding at a distinct frequency. This phenomenon is called a von Kármán vortex street. Oscillations were observed in the wakes behind all pins used in this study. In order to make sure that the traveling

wave is a solution of curved duct flow, and not the result of wake oscillations, the onset and frequency of wake oscillation is compared with the traveling waves.

The wakes were observed using side view flow visualization with continuous dye injection. The wake behind a 25 gauge pin at $Dn = 220$ is shown in figure 6.14. No streamwise velocity fluctuations were detected in the wake with the laser Doppler anemometer. A stroboscope was used to determine the shedding frequency. A periodic pattern is visible for about 40° only, after which the dye is completely dispersed in the water. Because there is no continuous energy supply to the wake oscillations, the oscillations will decay by viscous dissipation. Schlichting (1979) reports that the vortex shedding behind a cylinder starts at $Re_{pin} = 50$ to 65, where Re_{pin} is the Reynolds number for the flow past a cylinder, defined as

$$Re_{pin} = \frac{v_\theta D_{pin}}{\nu} \tag{6.1}$$

where: v_θ = fluid velocity near the pin
          D_{pin} = pin diameter

In the curved duct the fluid velocity at the pin is not well defined, because the velocity varies with the position in the duct. The streamwise velocity profile at 5° from the inlet of the curved section, where the pin is inserted, is approximately fully developed straight duct flow so that the velocity at the pin varies from zero at the wall to $2.096 * \overline{v_\theta}$ in the centre. Assuming that the onset and shedding frequency of a wake is determined by the maximum velocity at the pin, $2.096 * \overline{v_\theta}$ is used to calculate Re_{pin}.

The flow rate at the onset of vortex shedding was determined for each of the five pin diameters. The results are plotted in figure 6.15 and are in good agreement with experimental results for flow past a cylinder. Vortex shedding is not essential
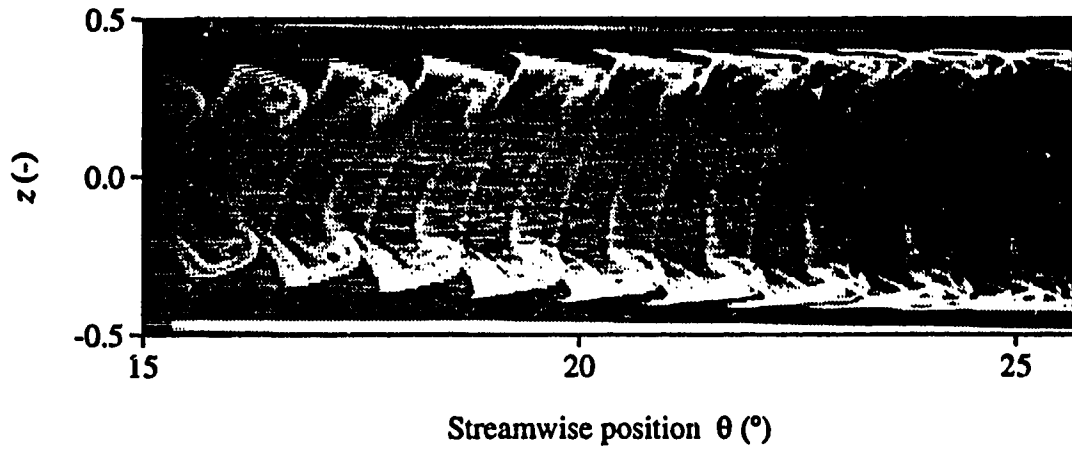
Figure 6.14:   Flow visualization of oscillations in the wake behind a 25 gauge pin
at $Dn = 220$. Wake frequency is 26.2 Hz.
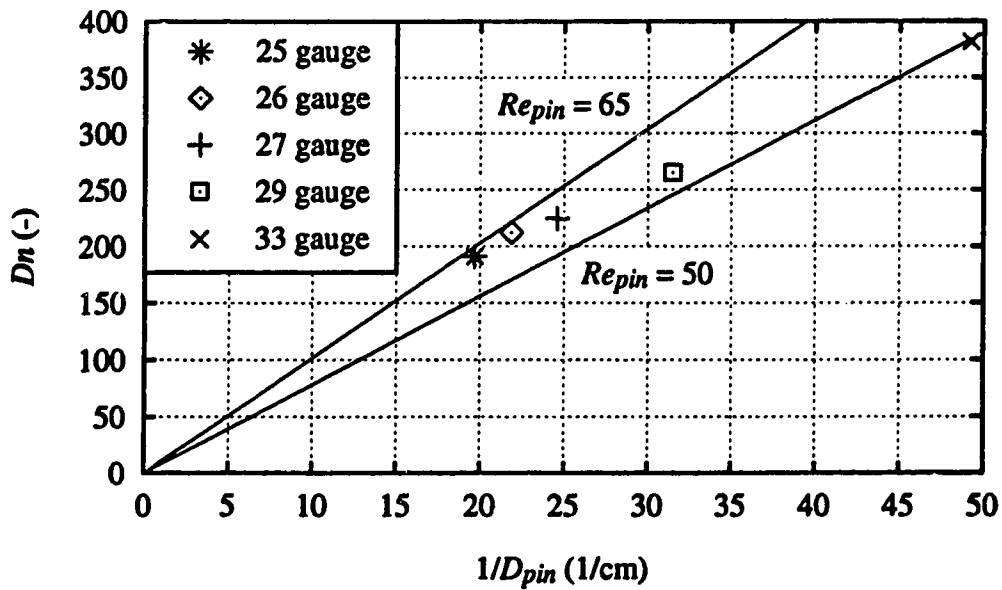
Figure 6.15:   Dean number at which the wake oscillations can first be observed
for various of pin diameters.

foi the existence of traveling waves, since for all pin diameters waves were observed below the onset of wake oscillations. This is especially evident for the 33 gauge pin. Onset of vortex shedding behind a 33 gauge pin takes place at $Dn =$ $)$, while traveling waves were induced by this pin at Dean number s betwee 18Γ and 250.

Schlichting (1979) presents a correlation between the dimensionless wake frequency or Strouhal number, $St = nD_{pin}/v_\theta$, and Re_{pin}, where n is the dimensional wake frequency. This correlation is reproduced in figure 6.16 in different dimensions. The dimensional wake frequency depends both on the pin diameter and the flow ra

In order to verify whether there is a relationship between the shedding frequency and the wave frequency, the dominant wave frequency was measured for a variety of pin diameters and flow rates. The maximum of the unforced frequency spectrum (see for example figure 6.4) was taken as the dominant frequency. Samples of 32768 velocity data were collected at a rate of 100 Hz and spectra were averaged over 31 blocks of 2048 points with 50% overlap. The results in figure 6.17 show that the wave frequency does not depend on the pin diameter. This confirms that the traveling wave is characteristic for curved duct flow and that the wave frequency is an inherent property of the wavy flow.

The predicted wake frequency and the measured wave frequency are plotted together in figure 6.18. Not only does the wake frequency depend on the pin diameter, but the wake frequency is also close to an order of magnitude higher than the wave frequency. The measured wake frequency for $Dn = 220$ and a 25 gauge pin of 26.2 Hz is close to the predicted frequency, considering the assumptions that were made in the calculations. The wake frequency of 26.2 Hz does not show up in the spectrum at these conditions (figure 6.4).

In summary, a comparison of the traveling wave with vortex shedding in the wake behind the pin shows that these two phenomena are not related.
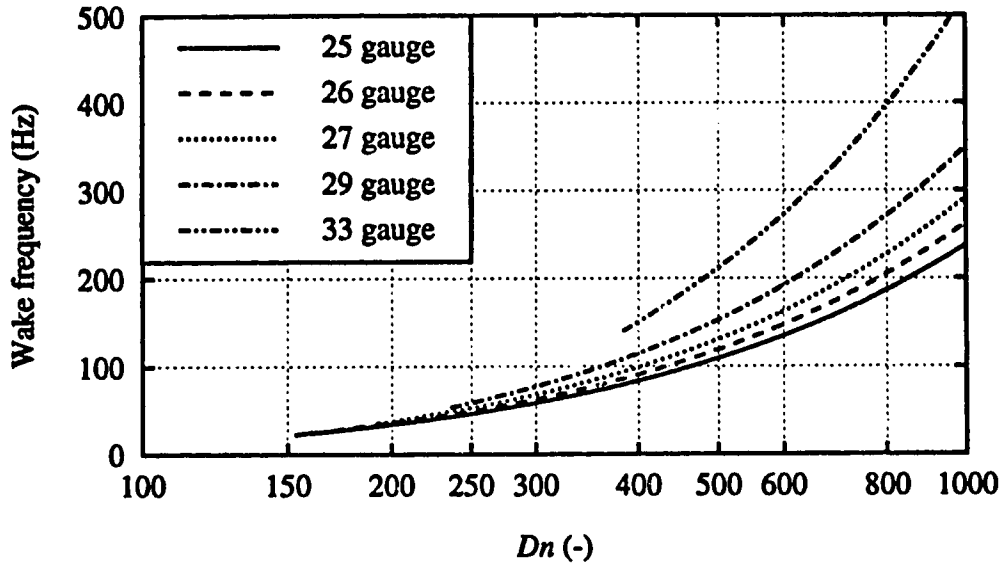
Figure 6.16:   Predicted frequency of the wake behind pins with various diameters
(from Schlichting, 1968).
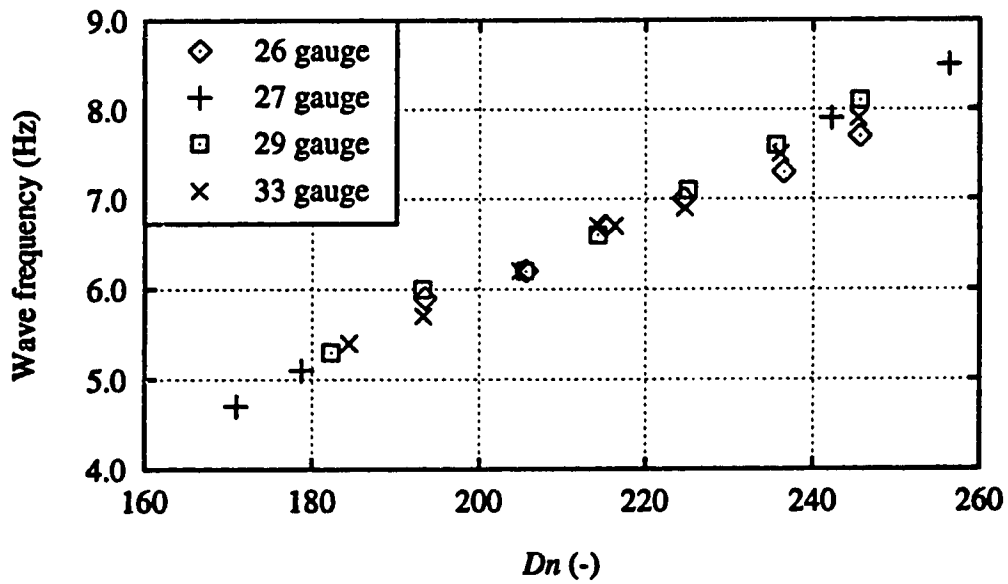
Figure 6.17: Dominant frequency of waves induced by pins with various diameters.
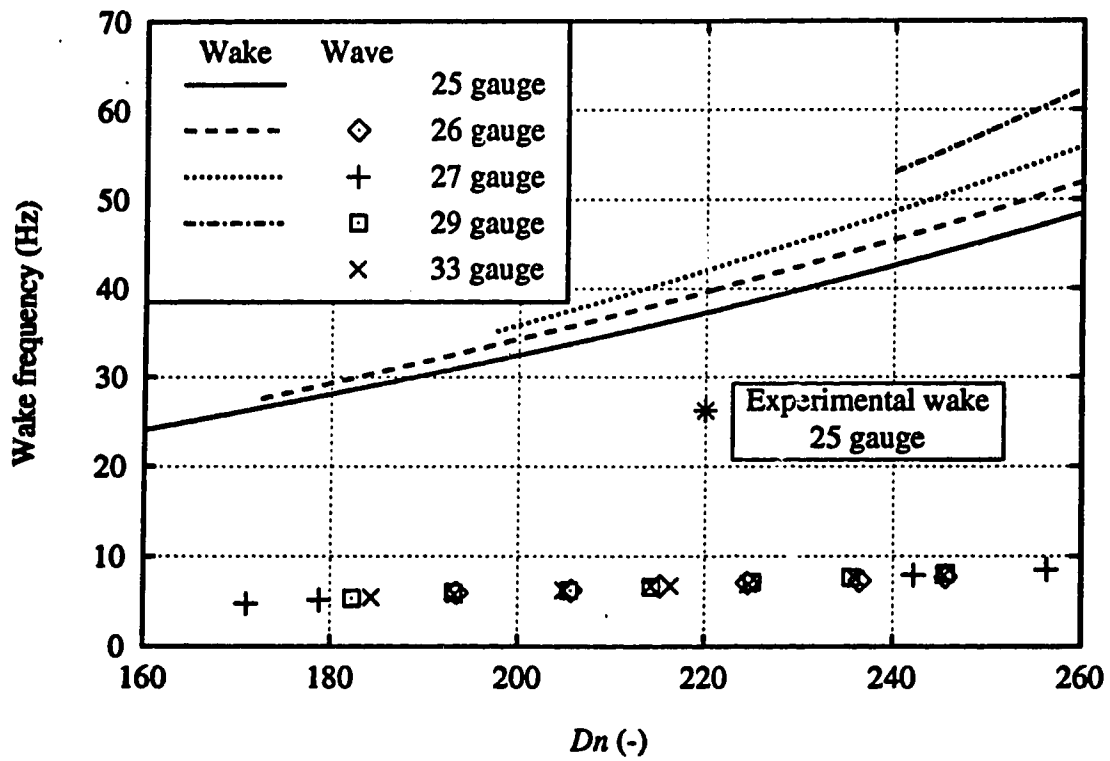
Figure 6.18: Predicted wake frequency and measured wave frequency.

6.3   Effect of Forcing on the Flow

Different methods can be used to introduce external perturbations into a flow system. Passive techniques use steady disturbances, such as trip wires, roughness elements and other objects (Schatz et al., 1991; Pouliquen et al., 1992). Active techniques are used to introduce disturbances at a selected frequency, and can have either a local or a global effect on the flow. Local forcing methods, such as moving flaps (Marasli et al., 1989; Schatz & Swinney, 1992), fluid bleed (Williams et al., 1992) or active heating elements (Gharib & Williams-Stuber, 1989) disturb the flow locally. Global techniques affects the entire flow field. Examples of global forcing methods are acoustic forcing (Sato & Kuriki, 1961) or flow rate fluctuations (Ho & Huang, 1982).

Forcing is generally used to select the nature and the intensity of the dominant disturbances in the flow, and to improve reproducibility. By forcing the flow, random disturbances which may vary from day to day do not play an important role in the often very sensitive transition processes. Active forcing can also be used as a phase reference, needed for phase-averaging velocity data.

The intensity of the imposed perturbations must be high enough to dominate the random disturbances in the system. On the other hand, large disturbances could alter the flow significantly. The forcing level must be a compromise between these two factors.

In this study the flow was forced by periodically compressing the hose that leads the water to the stilling chamber. Because of the incompressibility of water, this forcing method introduces a global pressure change and possibly a velocity fluctuation. It was shown in section 6.2.1 that as a result of the forcing a periodic disturbance is created locally by the pin. This disturbance destabilizes steady 4-cell

flow, leading to traveling waves.

The traveling wave state was characterized by measuring the velocity fluctuations that are the result of the traveling wave. Any additional velocity fluctuations caused by the forcing, could therefore affect the experimental results. In this section the magnitude of the velocity fluctuations induced by the forcing will be compared to the velocity fluctuations caused by the traveling wave. The effects that the forcing power and the forcing frequency have on the developing traveling waves will also be investigated.

6.3.1 Instability and Mode Interaction

The local linear stability of a flow field can be determined by evaluating the response to a localized disturbance. The flow is locally stable if the disturbance decays in any moving reference frame, otherwise the flow is locally unstable. If the disturbance grows, but is at the same time convected through the system in such a way that at any fixed location the response decays, the flow is locally convectively unstable. If the response grows at each location, the flow is absolutely unstable (figure 6.3). More details are given by Monkewitz (1990) and Huerre and Monkewitz (1990). Chomaz (1992) recently extended the concepts of convective and absolute instability to non-linear systems.

A flow field can have a region of absolute instability while at the same time other regions are convectively unstable or even stable. A good example is the wake behind bluff bodies (see for example Oertel, 1990). The region directly behind a bluff body is usually absolutely unstable, and the size of this region depends on the shape of the body and the flow rate. Experimentally, it is often very difficult to determine the local flow stability.

Chomaz *et al.* (1988) established the connection between local and global stability properties, using a Ginzburg-Landau model. A globally unstable system is characterized by a self-sustained, or global mode, which is intrinsic to the system. This global mode does not depend on the initial disturbances in the system. A region of absolute instability is essential for the development of a global mode. For example, vortex shedding in the wake behind a circular cylinder only takes place if the absolutely unstable region directly behind the cylinder is sufficiently large (Chomaz *et al.*, 1988; Maekawa *et al.*, 1992). The frequency spectrum of a global mode has sharp peaks at the fundamental frequency and possibly its harmonics.

Systems that are locally unstable, but globally stable, selectively amplify extrinsic noise, without developing a global mode. These systems are called noise driven and their state is strongly determined by random disturbances in the flow. Spectra are characterized by a broad band of frequencies, without a single dominating frequency. Deissler (1985; 1987; 1989) has studied the behaviour of noise driven systems extensively, using a Ginzburg-Landau model.

The observation of individual wave packets that are convected in the streamwise direction was used as an indication of the convective instability of curved duct flow at a Dean number of 220 (section 6.1). The convective nature of the flow was confirmed by the forcing frequency step response (figure 6.11). The broad band frequency spectrum of the unforced system (figure 6.6) is characteristic for a locally unstable, but globally stable system. However, the system does not necessarily have to be convectively unstable everywhere, in order to show this behaviour. Small regions of absolute instability could exist in a globally stable system.

Because the behaviour of globally stable systems is not much affected by small absolutely unstable regions, evidence for local absolute instability is difficult to obtain experimentally. The only experimental evidence of local absolute instability

is available for the region directly behind the pin. At those conditions where vortex shedding behind the pin takes place, the region behind the pin is absolutely unstable. It was shown in section 6.2.3 that this vortex shedding does not play a significant role in the development of traveling waves.

By forcing the flow, the traveling wave modes at the forcing frequency and its higher harmonics are excited. In the linear growth region all modes grow independently at their own linear growth rate, which is determined by the physics of the flow. In the non-linear region, interactions between modes can take place through the non-linear terms in the equation of motion. The nature of these interactions depends on the relative amplitudes of the modes. The presence of a single dominant mode tends to suppress the growth of low amplitude modes. This phenomenon has often been observed experimentally (e.g. Williams-Stuber & Gharib, 1990) and also numerically by Maekawa et al. (1992) in a plane wake. The reduction of noise in a forced system was also observed in this study. The averaged frequency spectra for the unforced and forced system at a Dean number of 220 and $\theta = 180°$ were shown in figures 6.4 and 6.6. In the forced system, the forcing frequency and its higher harmonics dominate the flow field. At the same time, the amplitude of other modes in the 0-15 Hz range is reduced by more than an order of magnitude as a result of the forcing. The forcing causes a shift of energy, while the total wave power remains unchanged.

Sato (1970) and Williams-Stuber and Gharib (1990) forced the convectively unstable wake of an airfoil at two different frequencies. When the amplitude of one of the frequencies is much higher than the other frequency, the weaker one is suppressed in the non-linear growth phase. If both modes are equally strong, new modes at frequencies that are combinations of the two forcing frequencies (e.g. $f_1 - f_2$, $f_1 + f_2$, $2f_1 - f_2$) are produced. This type of interaction was also observed

numerically by Karniadakis and Triantafyllou (1989) in the forced wake behind a circular cylinder. Flow past a cylinder exhibits a global mode and the interaction took place between the global mode and the forced mode.

6.3.2 Background Effect of Forcing

The effect that the forcing has on the flow rate was determined by measuring streamwise velocity fluctuations without inserting the pin. No traveling waves develop for Dean numbers between 170 and 260 when no pin is inserted. Therefore, all velocity fluctuations that are measured, apart from noise, are the result of the forcing.

If the forcing causes a fluctuation of the streamwise velocity, this fluctuation is expected to behave like a standing wave, because of the incompressibility of the fluid. The phase of standing wave oscillations is the same everywhere in the flow. Because there is a direct relation between the compressions of the hose and the velocity fluctuations, the phase difference between these two signals is not expected to depend on the forcing frequency or the flow rate. The standing wave character of the induced fluctuations was confirmed experimentally; figure 6.19 shows that the phase of the streamwise velocity fluctuations does not depend on the streamwise or spanwise position, forcing frequency, or flow rate.

In section 6.1, where the spatial development of the velocity amplitude was presented, the area underneath amplitude distributions was used as a measure of the wave power. The power of the velocity fluctuations induced by the forcing was measured in the same way. This makes it possible to compare the power of the traveling waves with the power of the fluctuations induced by the forcing.

Since most measurements of the traveling wave were taken at $\theta = 180°$ and
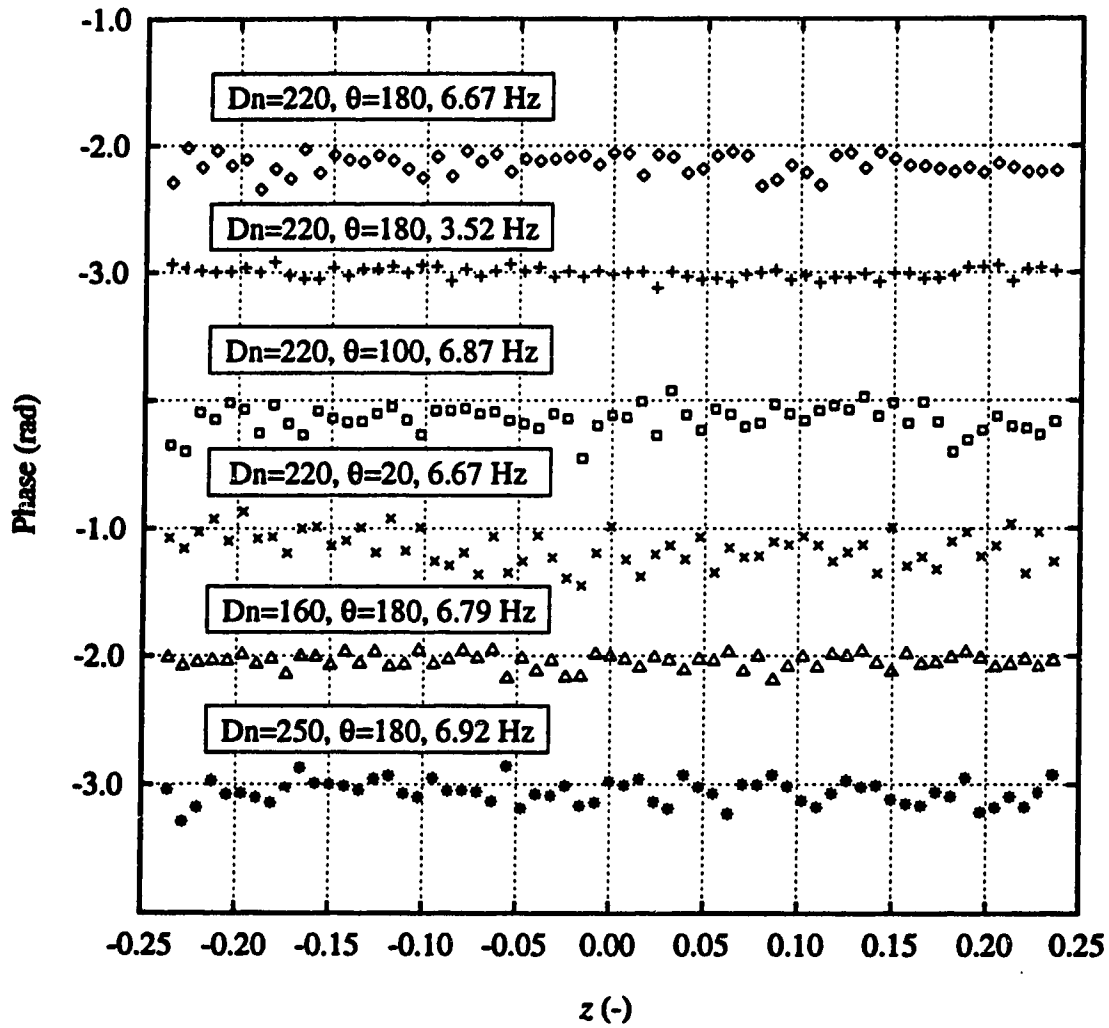
Figure 6.19:   Phase difference between the background fluctuations induced by
the forcing, and the forcing signal. $x = 0.27$, no pin, forcing power
around 1 V^2, samples of 512 measurements at a rate of 100 Hz.

$Dn = 220$, the background effect of the forcing was investigated most extensively for these parameter values. The fluctuation power was measured for three levels of forcing and for forcing frequencies between 1 and 12 Hz. For each set of parameters, the streamwise velocity was sampled at 61 positions along a spanwise line at $x = 0.27$ with z ranging from -0.24 to 0.24 ($\pm$ 3 mm from the centre line). Per position 512 velocity measurements were taken at a rate of 100 Hz. The frequency spectra of these velocity samples all show a single sharp peak at the forcing frequency. Two examples of averaged frequency spectra for forcing at 7 and 3.5 Hz are given in figures 6.20 and 6.21.

The fluctuation power was calculated in the familiar way, by integrating the spectrum in a 1.56 Hz wide band around the forcing frequency. The power of the streamwise velocity fluctuations at these four forcing conditions is shown in figure 6.22. The background noise of the unforced system was also measured, and the fluctuation power of the noise is shown in figure 6.22.

The background fluctuation power can be compared with the power of the traveling wave fluctuations in figure 6.10. The power of the fundamental component of the fully developed traveling wave, forced at 6.7 Hz, is around 7-8 $(mm/s)^2$. It will be shown in section 6.3.4 that the fully developed wave power strongly depends on the forcing frequency. At forcing levels of 2.6, 0.81 and 0.042 V^2, the background fluctuation power is 0.1, 0.04 and 0.016 $(mm/s)^2$ respectively, or 1.3, 0.53 and 0.21% of the wave power. Although it is very difficult to estimate the experimental error in the wave power, an additional error of around 1% that is introduced by the forcing was considered well within the acceptable range. It is only in the developing region of the traveling wave that the contribution of the forcing to the measured velocity fluctuations can become significant.

The background fluctuation power has a maximum around 3.5 Hz. This is most
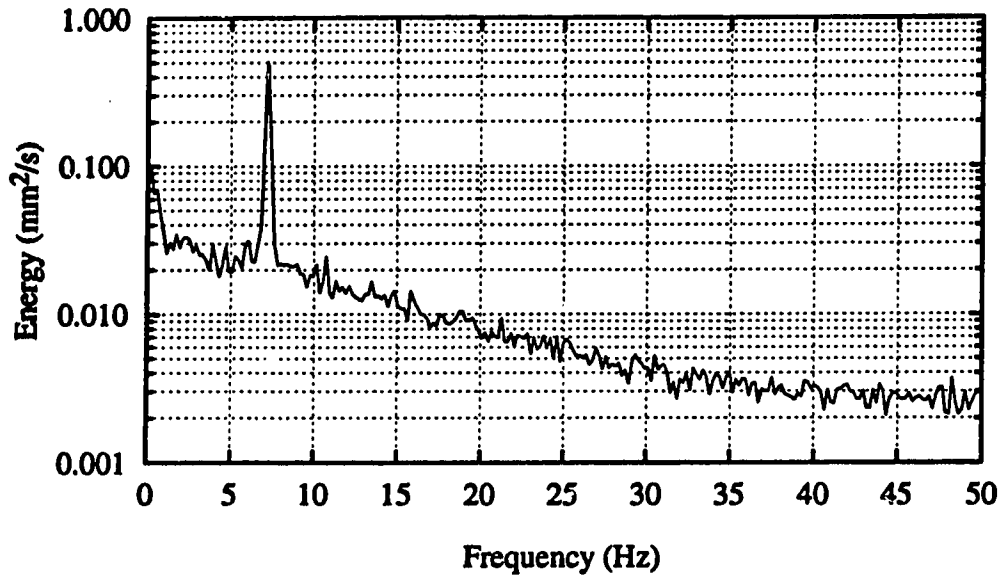
Figure 6.20: Frequency spectrum of velocity fluctuations induced by forcing at 7 Hz and a forcing power of 2.6 V^2. $Dn = 220$, $\theta = 180°$, $x = 0.27$.
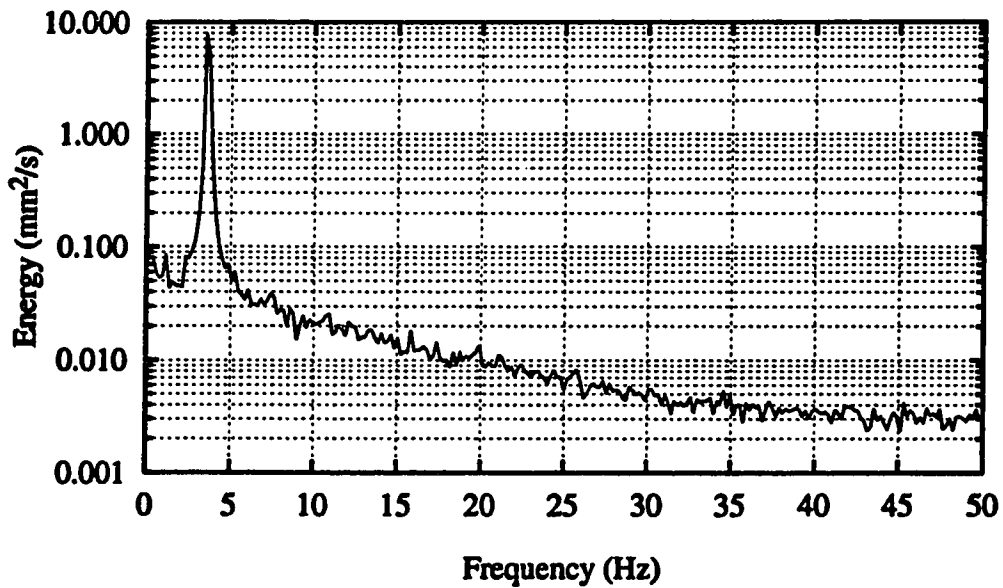
Figure 6.21: Frequency spectrum of velocity fluctuations induced by forcing at 3.5 Hz and a forcing power of 2.6 V^2. $Dn = 220$, $\theta = 180°$, $x = 0.27$.
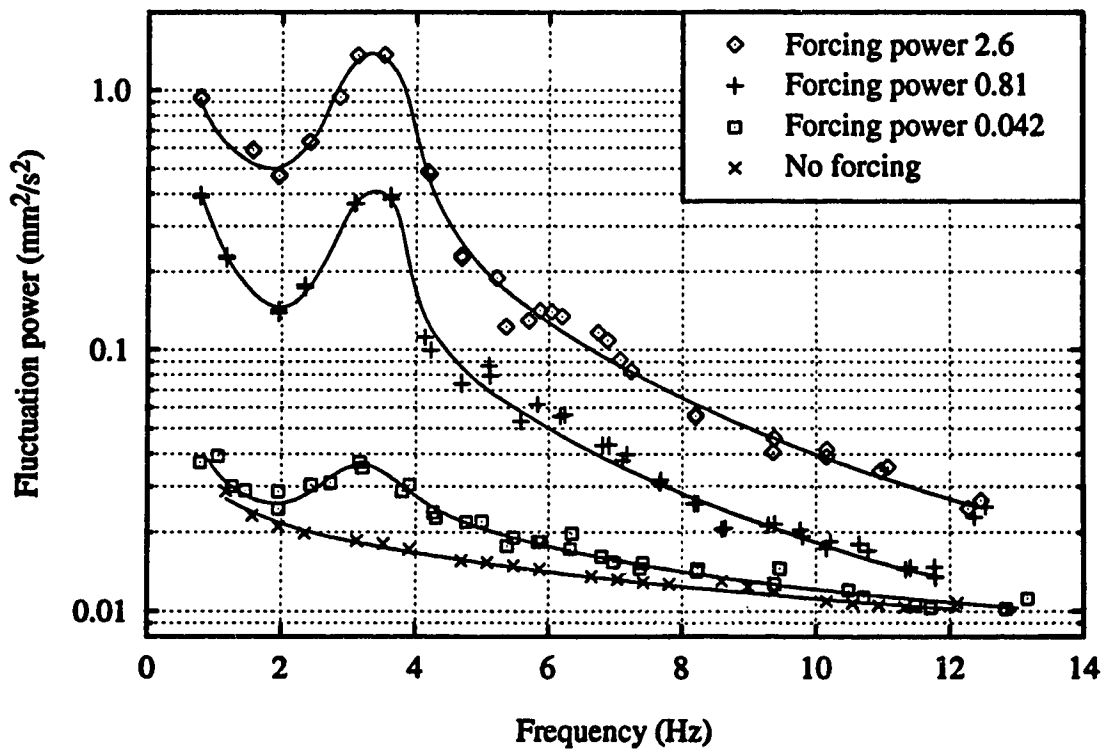
Figure 6.22: Background fluctuation power for different levels of forcing. $Dn = 220$, $\theta = 180°$, $x = 0.27$, no pin, 61 samples ($-0.24 < z < 0.24$) of 512 measurements sampled at 100 Hz.

likely the result of a resonance effect in the tygon hose that was compressed by the forcing pump. After the hose is compressed, it takes a short time before the hose returns to its original shape. At a forcing frequency of 3.5 Hz, the hose has just enough time to recover before the next roll of the forcing pump compresses the hose again.

The background effect of the forcing did not show any dependence on the flow rate and only a slight dependence on the streamwise position. The resonance effect at 3.5 Hz is also present at $\theta = 20°$, which demonstrates that this maximum in the streamwise velocity fluctuations is not the result of resonance in the secondary flow since at that position the secondary flow has only just started to developed.

6.3.3 Forcing Power

Frequency spectra of the fully developed wave for three levels of forcing are shown in figure 6.23. As the forcing power is increased, the peaks in the spectra become narrower, but the total wave power remains the same. This process is illustrated in figure 6.24, which shows the total power, the power of the fundamental and the power of the first harmonic as a function of the forcing frequency for a wave at $Dn = 220$ and a 25 gauge pin at $\theta = 180°$. The power of the fundamental component increases with increasing forcing power and reaches a constant value above a forcing level of around 1 V^2. The power of the first harmonic also reaches a constant value. The peaks in the spectra keep getting sharper with increasing forcing power, but this is not reflected in the amplitudes, since those are measured in a 1.56 Hz wide band. The wave is considered to be fully locked in to the forcing signal at forcing levels above 1 V^2.

Since the traveling wave state is the result of a selective amplification of flow disturbances, the development length of the traveling waves is expected to depend on
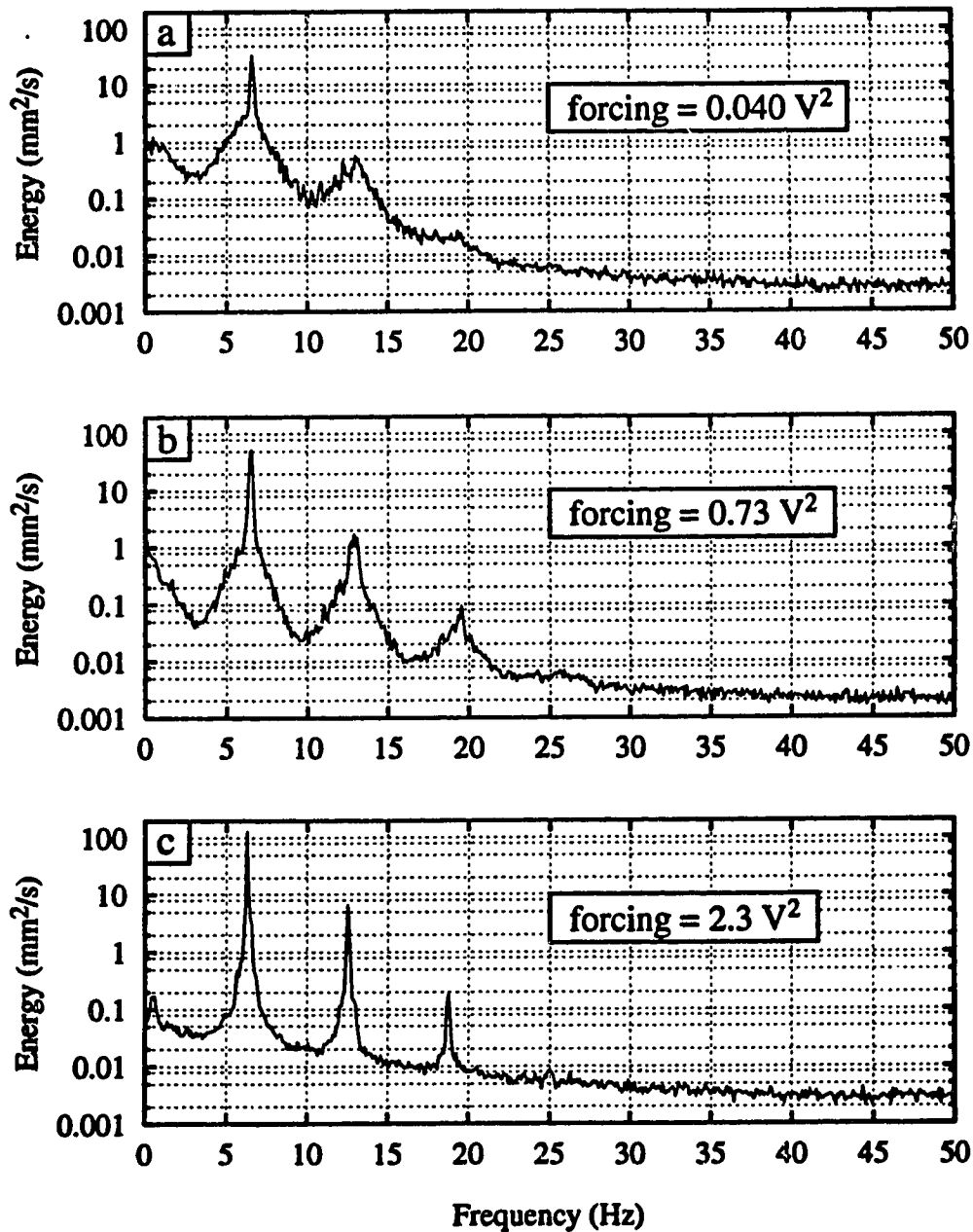
Figure 6.23: Measured averaged frequency spectra for increasing forcing power at
$Dn = 220$, $\theta = 180°$ and $x = 0.27$. 25 gauge pin, forcing frequency
around 6.5 Hz, 61 samples ($-0.24 < z < 0.24$) of 1024 measurements
sampled at 100 Hz.
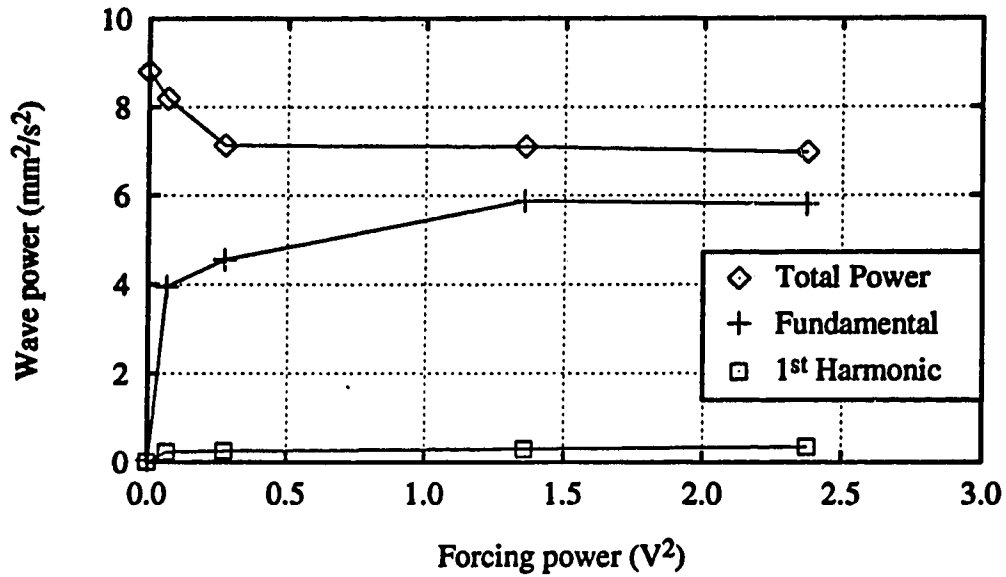
Figure 6.24: Wave power with increasing forcing power for 25 gauge pin at $Dn = 220$, $\theta = 180°$ and $x = 0.27$. Forcing frequency of 6.9 Hz.
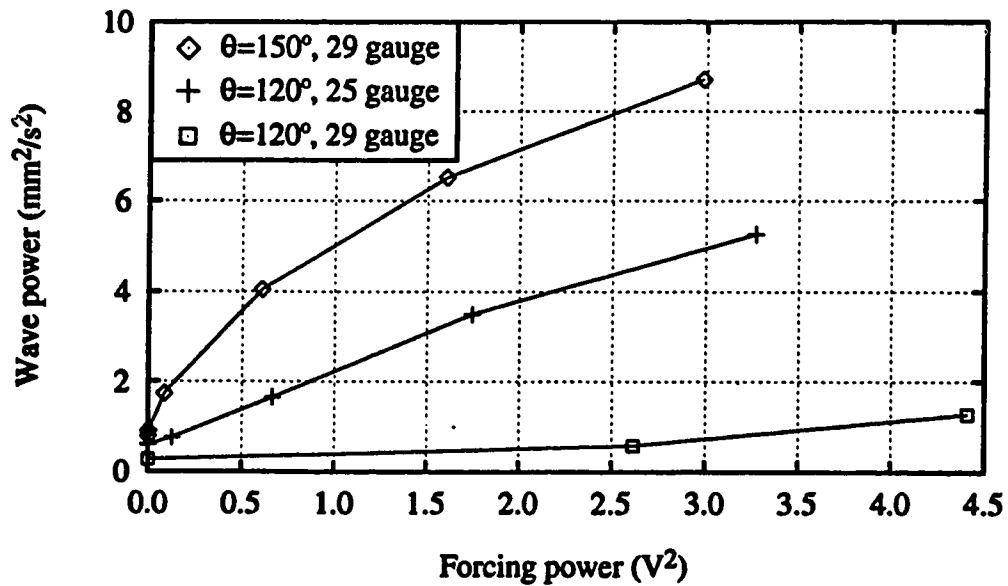
Figure 6.25: Total wave power with increasing forcing power in linear growth region. $Dn = 220$, $x = 0.27$, forcing frequency of 6.9 Hz.

the intensity of the forcing disturbances. These forcing disturbances in turn depend both on the pin diameter and the forcing power. Because the development length is hard to determine experimentally, the wave power in the linear growth phase is used as an indicator for the development length. Measurements were taken for three combinations of pin diameter and streamwise position. For each combination, the total wave power was measured at various forcing levels. The results are shown in figure 6.25.

At a fixed position, the wave power increases with increasing forcing power. Since in the linear growth region the wave power increases rapidly with streamwise position, this result indicates that at high forcing power the wave is further developed than at low forcing power. The experiments also show that at $\theta = 120°$ the traveling wave induced by a 29 gauge pin is less developed than the wave induced by a 25 gauge (thicker) pin, which creates larger disturbances. Both the forcing power and the pin diameter dependence of the development length demonstrate that the development length of the traveling waves is reduced when the intensity of the forcing disturbances is increased.

The forcing power dependence of the development length explains the higher total wave power at forcing levels below 0.3 V^2 in figure 6.24. At low forcing levels, the traveling wave may not have reached a fully developed state at $\theta = 180°$. It was shown in figure 6.10 that the wave power goes through a maximum before it reaches a steady value in the fully developed wave region. The high wave power that was found at low forcing levels likely corresponds to this region in the flow development.

The forcing level must be high enough to cause the wave to lock in to the forcing frequency but low enough to not disturb the flow too much. The wave is fully locked in to the forcing signal at forcing levels above 1 V^2 (figure 6.24). It was shown in section 6.3.2 that a forcing power of 2.6 V^2 causes a background fluctuation which is

1.3% of the wave power. This was considered to be an acceptable level. Hence, any forcing power between 1 V^2 and 2.6 V^2 causes the wake to lock in, without creating a significant background fluctuation.

6.3.4   Forcing Frequency

The traveling wave at a Dean number of 220 locks in to the forcing frequency if that frequency is between 4 and 9 Hz. This frequency range corresponds to the broad peak in the unforced frequency spectrum. Traveling wave modes in this region have a relatively large growth rate compared to other modes. In this section experimental results will be presented that show what happens when the forcing frequency is lower or higher than the natural frequency range of 4-9 Hz.

By forcing the flow at a certain frequency, not only the traveling wave mode at the forcing frequency is excited, but also modes at the harmonics of the forcing frequency. The relative growth rates of the excited frequencies determine which mode will become the dominant mode. In the non-linear region interactions between the dominant mode and other modes can take place.

The effect of the forcing frequency was determined for the traveling wave at a Dean number of 220, induced by a 25 gauge pin. Measurements were taken at $\theta = 180°$. The total wave power and the power at the fundamental and first harmonic frequencies were measured for forcing frequencies between 1 and 10 Hz. The forcing power was between 0.7 and 1.2 V^2. Considering the amount of data that had to be taken, the sample size was reduced to 256 measurements, taken at a rate of 100 Hz. This limits the frequency resolution to 0.4 Hz. The wave power as a function of the forcing frequency is shown in figure 6.26. The symbols indicate which component of the forcing frequency the flow is locked in to.

The results show that for a forcing frequency between 4 and 10 Hz the traveling wave locks in to the forcing frequency. At forcing frequencies between 2.5 and 4 Hz the traveling wave locks in to the first harmonic of the forcing. There is an overlap region between 3 and 4.5 Hz, where the wave locks in to either the forcing frequency, or the first harmonic. At forcing frequencies between 1 and 2.5 Hz, a new mode was observed with different characteristics than the dominant modes at higher forcing frequencies.

The frequency ranges where the wave locks in to the fundamental and first harmonic of the forcing are shown in figure 6.27. The line in figure 6.27 represents a wave frequency of 7 Hz and shows that the wave locks in to a frequency component close to 7 Hz. The 7 Hz mode corresponds to the maximum in the unforced frequency spectrum (figure 6.4) and is the mode with the highest growth rate.

The wave power at the fundamental forcing frequency as a function of the forcing frequency is shown in figure 6.28. There is no maximum of the fundamental wave power around 7 Hz. At forcing frequencies below 6.5 Hz the noise level of the amplitude distributions increases significantly and between 3 and 5 Hz the results are not very reproducible. Which frequency component the wave locks in to can be determined from the amplitude distributions of the different components. Sometimes the wave locks in to the forcing frequency, other times to the first harmonic of the forcing frequency; combinations of these two modes have also been observed. Two runs at 3-3.5 Hz locked in to the forcing frequency at very hig.. power. These two data points seem to continue the trend at forcing frequencies above 5.5 Hz. In the region where the forcing frequency and the first harmonic mode have equal growth rates, a competition between these two modes takes place. However, at a forcing frequency of 3 or 3.5 Hz, the first harmonic mode has a higher growth rate than the fundamental, and it is not clear what caused the wave to lock
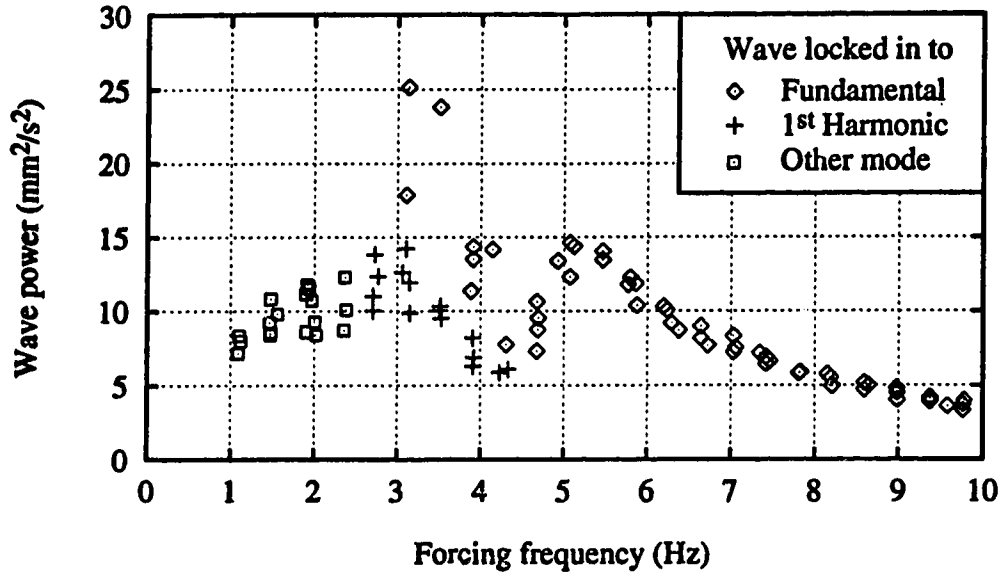
Figure 6.26: Total wave power as a function of the forcing frequency. $Dn = 220$, $\theta = 180°$, $x = 0.27$. Samples of 256 measurements at 100 Hz.
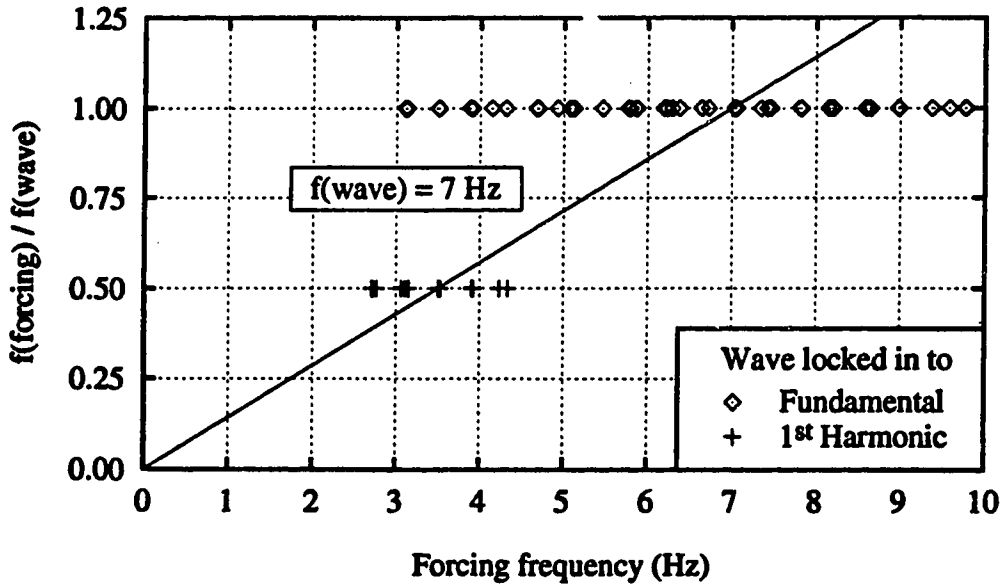
Figure 6.27: Ratio of forcing frequency and fundamental wave frequency, indicating frequency component that wave is locked in to.
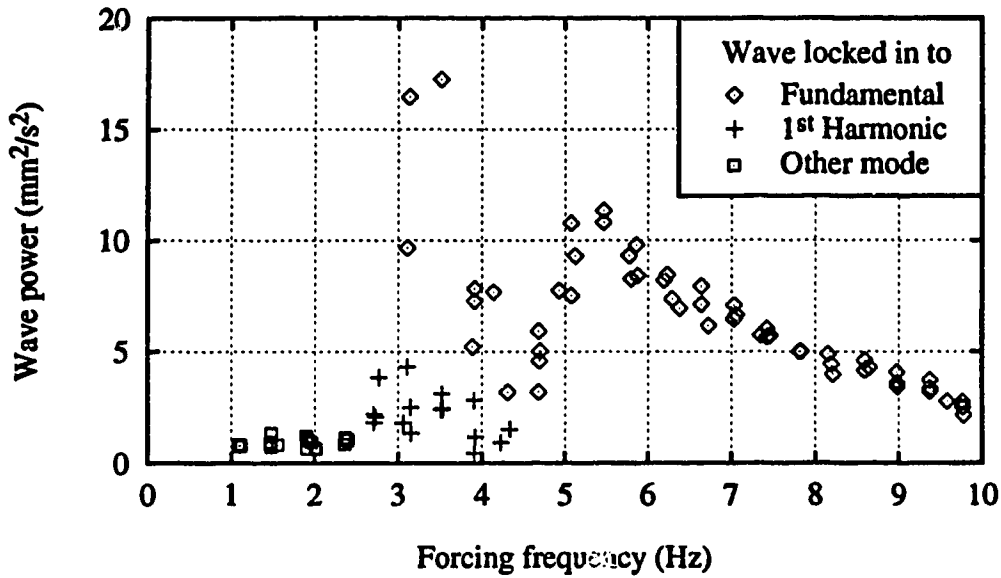
Figure 6.28: Wave power at fundamental frequency as a function of the forcing frequency. $Dn = 220$, $\theta = 180°$, $x = 0.27$.
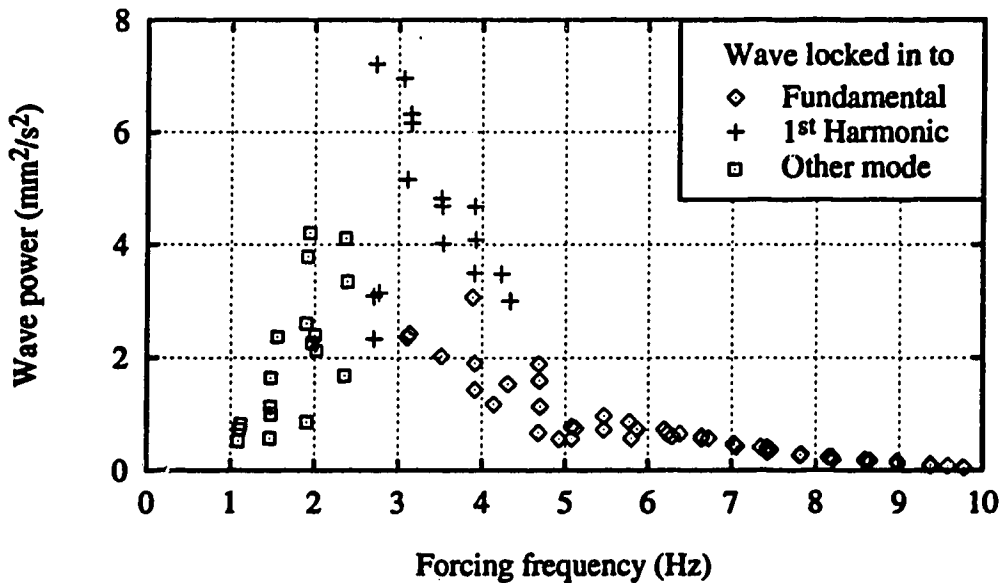
Figure 6.29: Wave power at first harmonic frequency as a function of the forcing frequency. $Dn = 220$, $\theta = 180°$, $x = 0.27$.

in to these low frequencies.

The wave power at the first harmonic of the forcing frequency as a function of the forcing power is shown in figure 6.29. The power has a maximum in the region where the wave locks in to the first harmonic of the forcing. At forcing frequencies between 2 and 4.5 Hz the growth rate of the first harmonic frequency (between 4 and 9 Hz) is higher than that of the fundamental.

The averaged frequency spectrum and amplitude distributions with forcing at 3.32 Hz are shown in figures 6.30 and 6.31. The traveling wave is locked in to the first harmonic of the forcing frequency, so that the fundamental wave frequency is 6.64 Hz. Comparison of the frequency spectra and amplitude distributions of this wave and the wave forced at 6.82 Hz shows that both modes are nearly identical.

The amplitude distributions for a wave forced at 6.82 Hz were shown in figure 6.7 and show great similarity with figure 6.31. For the wave forced at 3.32 Hz the first and third harmonics of the forcing correspond to the fundamental and first harmonic of the wave. Frequency spectra for both waves (figures 6.6 and 6.30) are also very similar. The frequency spectrum in figure 6.30 shows three peaks at 6.64, 13.4 and 20.0 Hz with decreasing power which are characteristic for a traveling wave with a fundamental frequency of 6.64 Hz. The peaks at the fundamental and second and fourth harmonics (3.32, 10.0 and 16.7 Hz) are an order of magnitude lower than neighbouring peaks. The total wave power with forcing at 3.32 and 6.82 Hz is respectively 8.27 and 8.35 $(mm/s)^2$.

At forcing frequencies below 2.5 Hz a new mode was observed. The averaged frequency spectrum and amplitude distributions with forcing at 2.39 Hz are shown in figures 6.32 and 6.33. The second harmonic of the forcing frequency, 7.17 Hz, is close to the fastest growing mode, but the spectrum does not show a peak at this frequency. The series of peaks at harmonics of the fundamental wave frequency,

Figure 6.30: Averaged frequency spectrum of streamwise velocity with forcing of 0.62 V^2 at 3.32 Hz. $Dn = 220$, $\theta = 180°$, $x = 0.27$, 25 gauge pin.

Figure 6.31: Amplitude distributions of streamwise velocity with forcing of 0.62 V^2 at 3.32 Hz. $Dn = 220$, $\theta = 180°$, $x = 0.27$, 25 gauge pin.

Figure 6.32: Averaged frequency spectrum of streamwise velocity with forcing of
0.62 V^2 at 2.39 Hz. $Dn = 220$, $\theta = 180°$, $x = 0.27$, 25 gauge pin.

Figure 6.33: Amplitude distributions of streamwise velocity with forcing of 0.62
V^2 at 2.39 Hz. $Dn = 220$, $\theta = 180°$, $x = 0.27$, 25 gauge pin.

which is characteristic for a traveling wave, is missing and none of the amplitude distributions has a maximum in the centre that identifies the first harmonic of the wave frequency (e.g. figure 6.7). The flow state excited by forcing at 2.39 Hz is fundamentally different from the traveling wave modes observed at forcing frequencies above 2.2 Hz.

The averaged frequency spectrum and amplitude distributions with forcing at 1.73 Hz are shown in figures 6.34 and 6.35. The spectrum has a peak at 7.03 Hz, corresponding to the third harmonic of the forcing frequency. However, just as in the previously discussed case with forcing at 2.39 Hz, the spectrum and amplitude distributions do not have the characteristics of the traveling wave modes that were observed at forcing frequencies between 4 and 10 Hz.

Since the forcing does not excite modes at subharmonics of the forcing frequency, forcing at frequencies above 10 Hz is not expected to have much effect on the flow. The averaged frequency spectrum and amplitude distribution with forcing at 13.66 Hz are shown in figures 6.36 and 6.37. The spectrum has no peak at the first subharmonic of 6.83 Hz and is very similar to the unforced frequency spectrum of figure 6.4.

In summary, forcing of the flow excites traveling wave modes at the forcing frequency and its harmonics. The dominant wave modes at forcing frequencies between 2.5 and 10 Hz have the same characteristics. In this range the wave locks in to the forcing frequency or its first harmonic, depending on which mode has the fastest growth rate. At forcing frequencies between 1 and 2.5 Hz a new mode with different characteristics was observed.
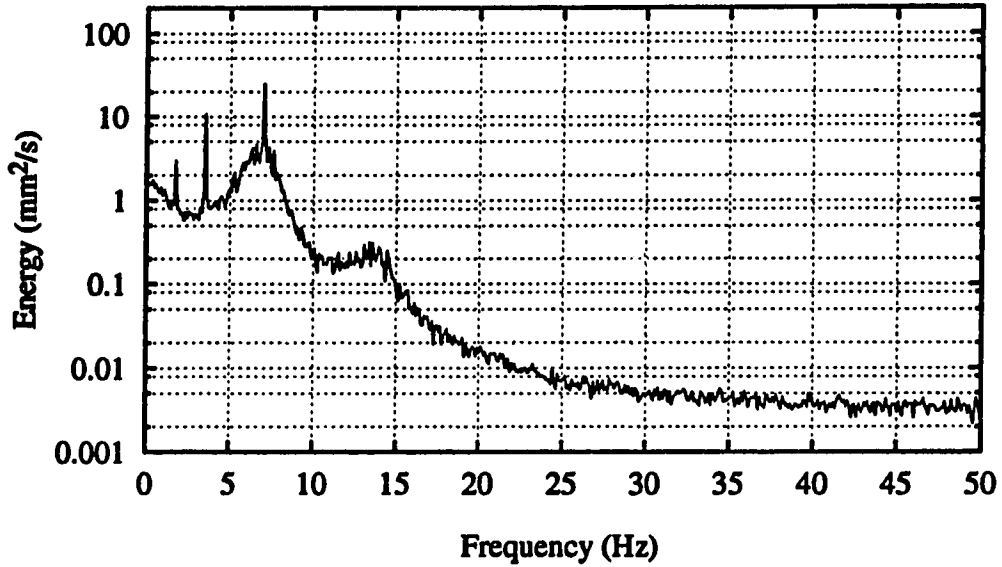
Figure 6.34: Averaged frequency spectrum of streamwise velocity with forcing of 0.59 V^2 at 1.73 Hz. $Dn = 220$, $\theta = 180°$, $x = 0.27$, 25 gauge pin.
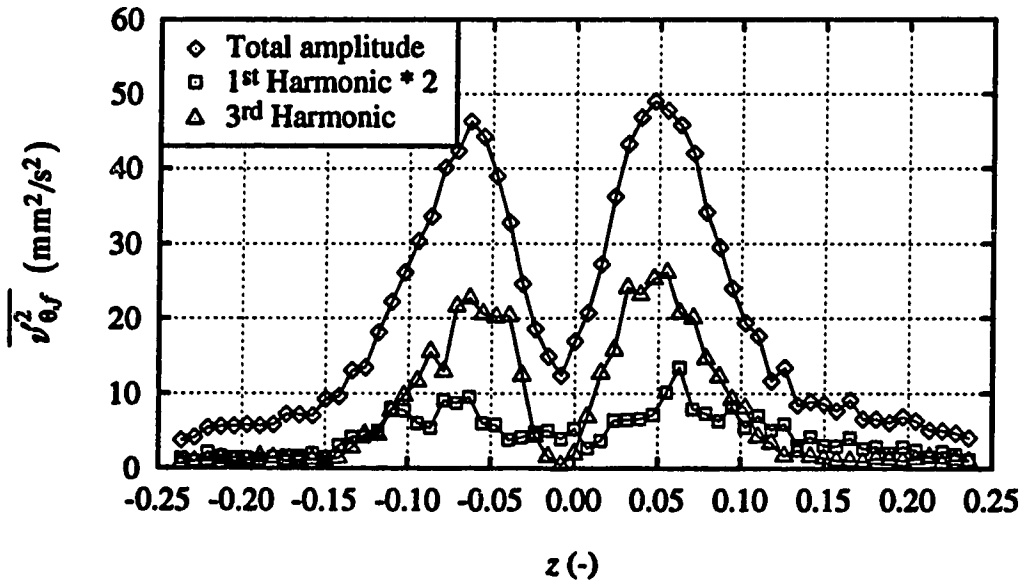
Figure 6.35: Amplitude distributions of streamwise velocity with forcing of 0.59 V^2 at 1.73 Hz. $Dn = 220$, $\theta = 180°$, $x = 0.27$, 25 gauge pin.
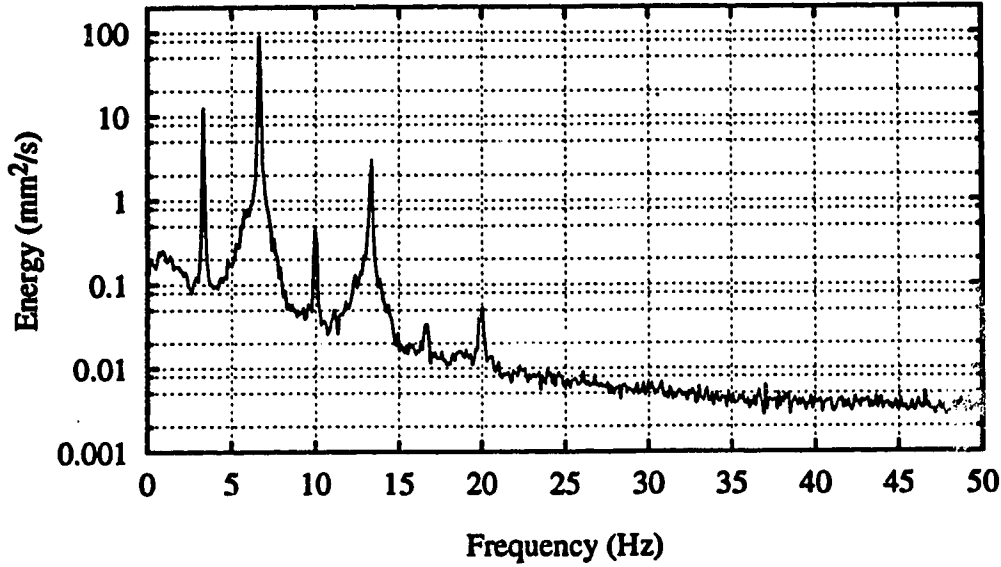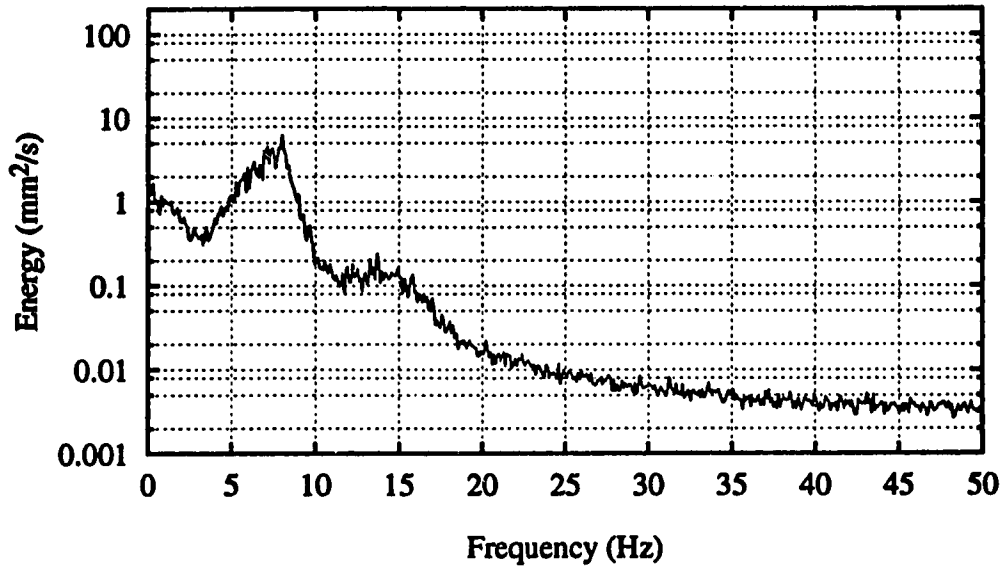
Figure 6.36: Averaged frequency spectrum of streamwise velocity with forcing of
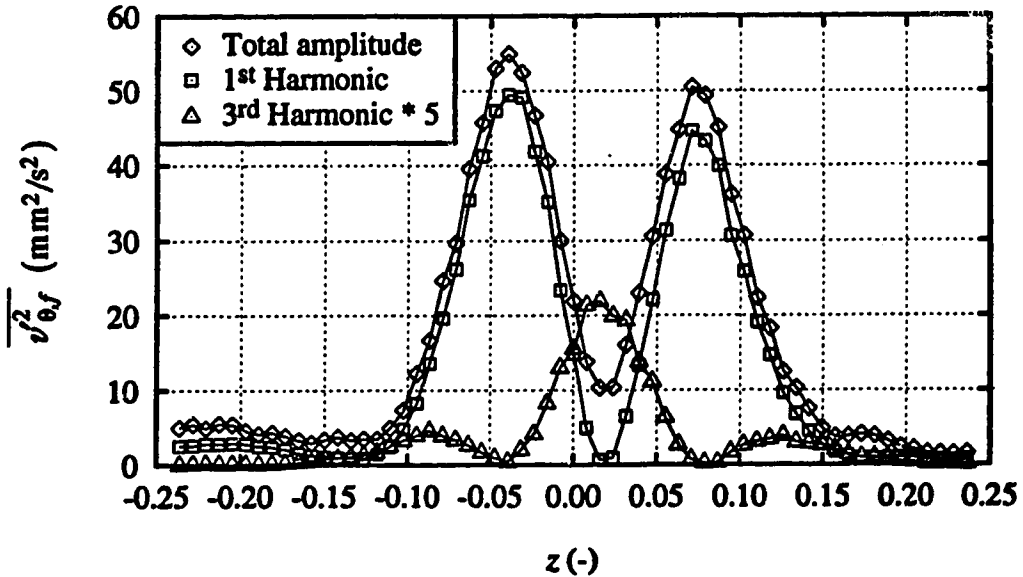0.41 V^2 at 13.66 Hz. $Dn = 220$, $\theta = 180°$, $x = 0.27$, 25 gauge pin.
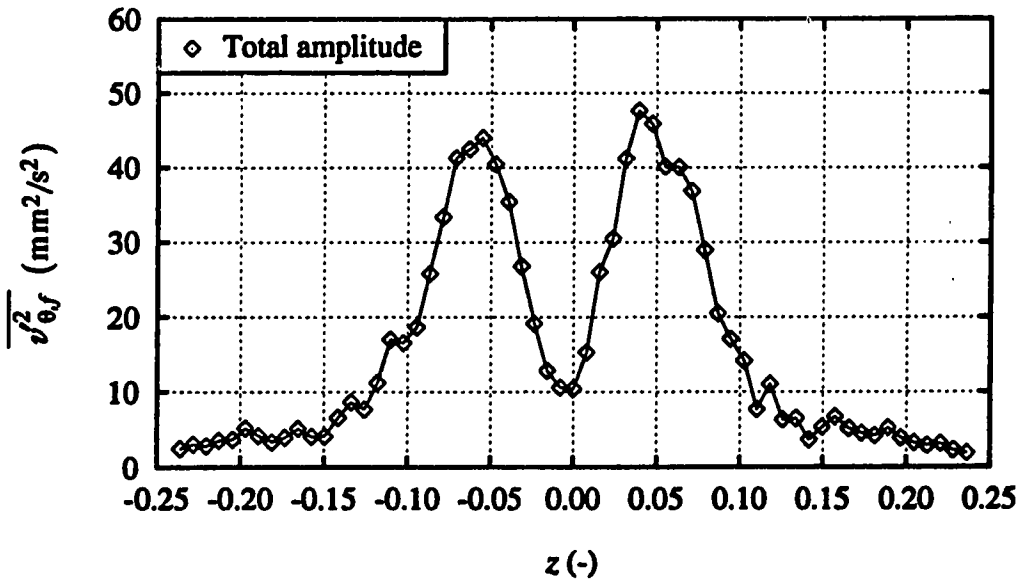
Figure 6.37: Amplitude distribution of streamwise velocity with forcing of 0.41
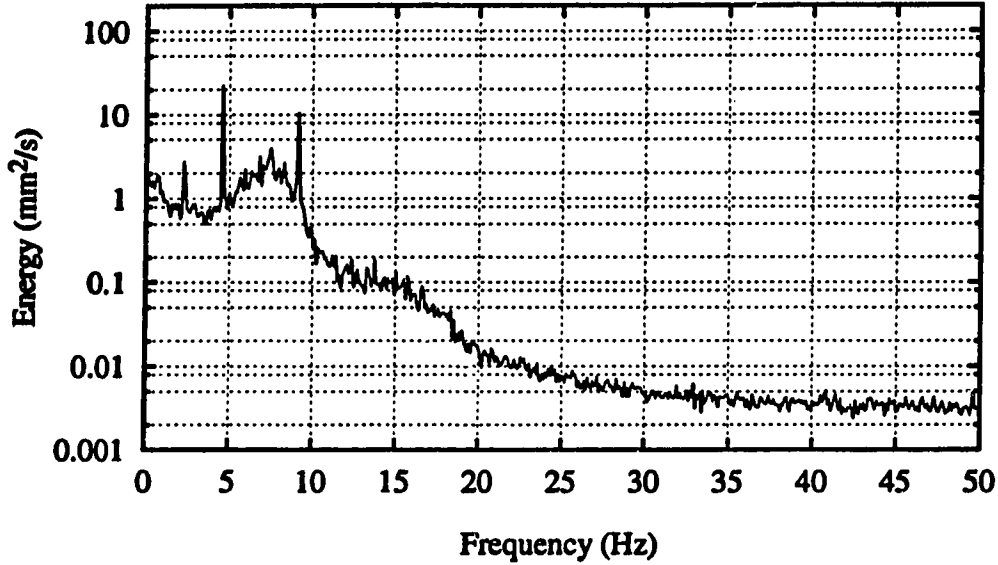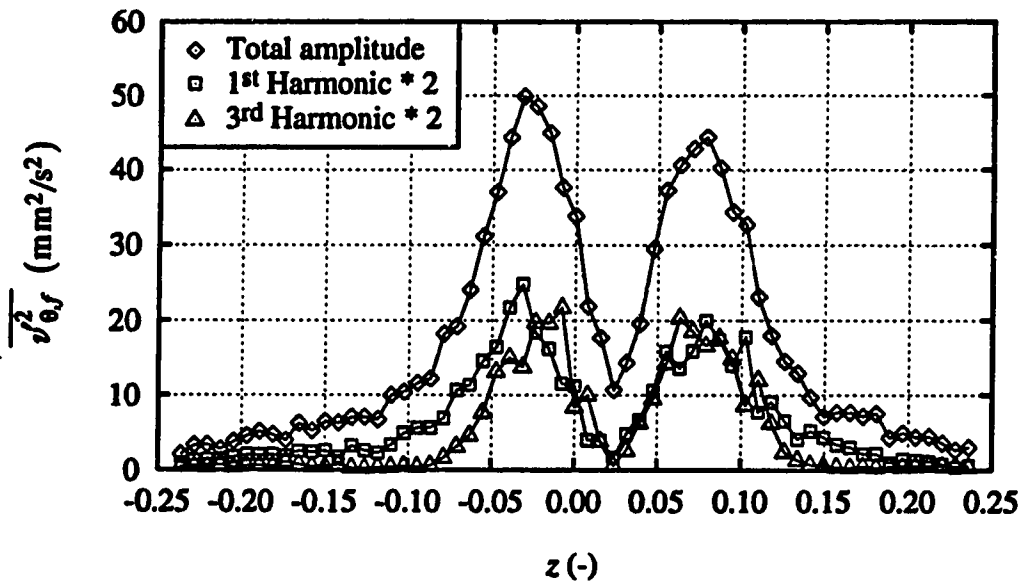V^2 at 13.66 Hz. $Dn = 220$, $\theta = 180°$, $x = 0.27$, 25 gauge pin.

6.4 Direct Numerical Simulations

Three-dimensional and time dependent simulations of the fully developed traveling wave state at a Dean number of 220 were performed using the commercial CFD package FLOW3D. First the simulation strategy will be discussed, followed by the geometry and the solution method. In the next section the simulation results will be compared to the experiments.

In an early attempt to model the traveling wave flow, the geometry of the experimental apparatus, including the straight inlet section, was modeled using inlet and outlet boundary conditions. Oscillating modes were induced by forcing the flow periodically at the inlet of the curved section, but no significant oscillations of the Dean vortices were observed. In a second attempt a curved section with fully developed 4-cell flow at the inlet was modeled. This time, oscillating Dean vortices were observed, but the oscillations slowly died out in the streamwise direction. Further grid refinement could have produced growing oscillating modes, but this was not possible within the available 256 Mega bytes of computer memory.

Because of the very fine grid resolution that is necessary to resolve the traveling wave state, the streamwise extent of the computational domain had to be reduced significantly. This was obtained by imposing periodic boundary conditions in the streamwise direction. The flow was driven by a mean pressure gradient.

The steady 4-cell flow from which the traveling waves develop is unstable with respect to asymmetric perturbations. In a simulation with periodic boundary conditions, a continuous feedback exists between the outlet and the inlet of the computational domain. Because of this feedback, asymmetries that are caused by round-off errors are amplified and eventually cause the breakdown of steady 4-cell flow. The development of asymmetries can be prevented by imposing symmetry

around the centre plane at $z = 0$. This does indeed stabilize stable 4-cell flow, but also makes the development of traveling waves impossible, since the traveling wave state is not symmetric around $z = 0$. It is clear that the traveling wave state can only be modeled in a streamwise periodic simulation if steady 4-cell flow is stabilized without eliminating the development of traveling wave modes.

It will be demonstrated in the next section that the fully developed traveling wave state has shift-and-reflect symmetry. This means that the flow field is invariant over a streamwise translation of half a wavelength, combined with a reflection in the centre plane, $z = 0$. The symmetry properties of the flow will be discussed in detail in section 6.5.2. Because of the shift-and-reflect symmetry of the traveling waves, this symmetry property can be imposed in the simulations, without affecting the development of oscillating modes. The shift-and-reflect symmetry condition also stabilizes steady 4-cell flow, because the asymmetric breakdown process of the 4-cell flow is not shift-and-reflect symmetric.

The most efficient implementation of shift-and reflect symmetry would be to model half a streamwise wavelength and impose a reflect condition between the outlet and the inlet. This is currently not possible in FLOW3D, which only allows periodic boundary conditions. Therefore, one full wavelength was modelled and the shift-and-reflect symmetry was implemented through user-defined Fortran routines. At each iteration the velocity field of the cross section in the middle of the computational domain was made equal to the reflected velocity field at the inlet.

The dimensions of the geometry are given in table 6.1. The spanwise and radial dimensions correspond to the dimensions of the experimental apparatus. A streamwise wavelength of 3.8° was used, which is close to the experimentally observed wavelength with forcing at 6.6 Hz (see figure 6.8). Three different grids were used: a coarse 32x22x100 grid (grid 1), an intermediate 46x32x128 grid (grid 2) and

a fine 58x40x160 grid (grid 3). The cells are uniformly distributed in the streamwise direction. In the spanwise and radial directions geometric compression was used. This increased the grid resolution near the centre of the outer wall, where the flow oscillations are most prominent. Both in the spanwise and in the radial direction, the ratio between the largest and the smallest grid dimension is equal to 4. A cross section of grid 3 is shown in figure 6.38.

Direction	Min. (m)	Max. (m)	grid 1	grid 2	grid 3
spanwise	-0.00635	0.00635	32	46	58
radial	0.18561	0.19831	22	32	40
streamwise	0.0	0.012731	100	128	160

Table 6.1: Geometry and grid dimensions.

FLOW3D solves the fully elliptic, three-dimensional, time dependent Navier-Stokes equation, using a control volume approach. Hybrid differencing was used to model the convective terms of the transport equations. Block Stone's method was used to solve the linearized difference equations for the velocity components in the inner iteration. The SIMPLEC algorithm (Patankar, 1980; Van Doormal & Raithby, 1984) was used for the pressure coupling of the outer iteration with under-relaxation factors for the velocity components of 0.8. The time stepping procedure used Crank-Nicolson differencing. Each time step was considered to be converged when the residual mass flow over the entire domain was less than 10^{-6}. User-defined Fortran was used extensively to monitor and analyse the flow. Simulations were carried out on IBM RS/6000 model 560 computers with 256 and 512 Mb.

The simulations with grids 1 and 2 were started from a steady 4-cell solution.

The streamwise velocity field of the steady 4-cell flow was perturbed by at most 10% of the local streamwise velocity. This perturbation preserved the shift-and-reflect symmetry. A transient simulation followed the temporal development of the perturbed state. Time steps of 0.01, 0.005 and 0.0025 seconds were used. After about 5 seconds of real time, the total wave power reached a constant value, indicating a state of fully developed traveling waves.

The simulations with grid 3 were started from the fully developed wave state from grid 2, that was interpolated to fit the finer grid 3. A fully developed traveling wave state was reached after 8 seconds of real time. This simulation took 235 Mb of RAM and the CPU time for one time step of 0.0025 s was about 52 minutes. The total simulation time for g 'd 3 was nearly 4 months.

The frequency of the traveling wave simulation with grid 3 is 6.45 Hz, which is very close to the 6.6 Hz of the experiment that the wave length for the simulation was based on (figure 6.8).

In the next section the simulation results will be compared to the experiments. The simulations will also be used to analyse the flow structure and the instability mechanism that causes the traveling waves.
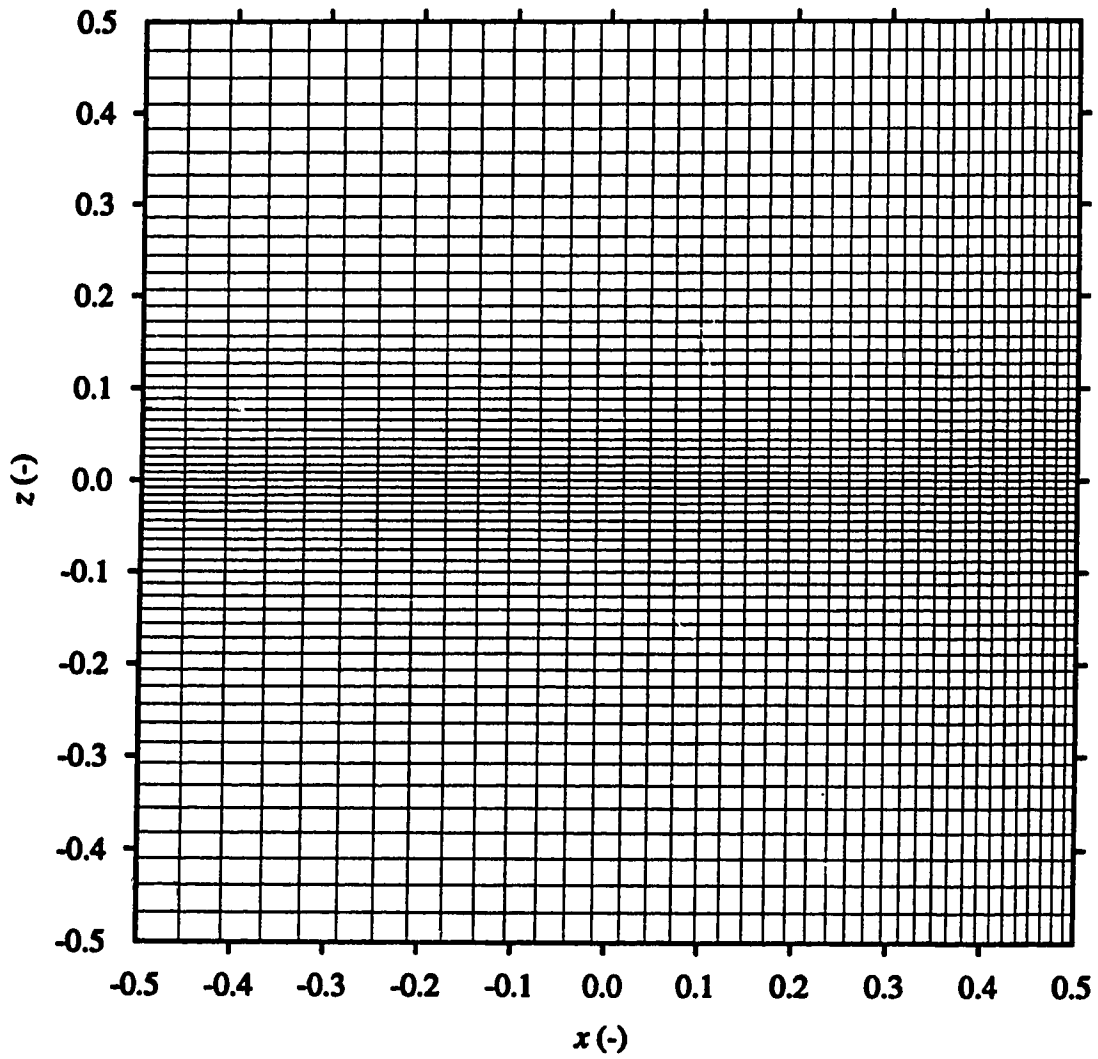
Figure 6.38: Cross section of grid 3 (58x40x160).

6.5   Flow Structure

One of the main objectives of this study of traveling waves in a curved square duct is to characterize the structure of the wavy flow. Experimentally, this was done by measuring amplitude and phase distributions. Numerical simulations provide further insight into the flow structure, in particular the vorticity field. The traveling waves show great similarity with twisting vortices in a curved channel, sinuous Görtler vortices and a two-dimensional wake. Symmetry considerations play an important role in the analysis of the flow structure. The experimental and numerical investigation focused on the fully developed traveling wave state at a Dean number of 220. All simulation results in this section were calculated with grid 3.

6.5.1   Amplitude and Phase Distributions

A velocity signal can be represented in the frequency domain as a sum of cosine functions, each with their own amplitude and phase. Since velocity signals in the forced system contain only a few frequency components, amplitude and phase information is a very efficient method to describe the fluctuating velocity field. The streamwise velocity fluctuations are strongest near the inflow region, and fluctuation characteristics change much more quickly in the spanwise direction than in the radial direction. Therefore, velocity fluctuations were only measured along a spanwise line at $x = 0.27$. Amplitude and phase distributions show how the amplitude and phase of a certain frequency component vary with the spanwise position along this line.

The amplitude of the total velocity fluctuations is equal to the area under the frequency spectrum, or the variance of the time series. The area in a 1.56 Hz wide band of the frequency spectrum was used as the amplitude of individual components.

The phase of the velocity fluctuations is only meaningful if it is defined relative

to a phase reference. The forcing pump signal, which is a measure of the torque delivered by the pump, was used as a phase reference. The advantage of this method is that the pump phase is constant throughout the flow field (see figure 6.19). Thus, any observed phase changes can be attributed to the velocity signal. However, measured phase distributions were fairly noisy. Internal phase referencing was also used, by calculating the phase difference between different frequency components of the same velocity signal. These phase differences are only meaningful between the fundamental frequency and its harmonics. Internal phase referencing produced much more reproducible results.

Velocity fluctuations were measured at a Dean number of 220 and $\theta = 180°$. At this position and Dean number the traveling wave has reached a fully developed state (figure 6.10). Typical amplitude and phase distributions of the streamwise velocity are shown in figure 6.39. The streamwise velocity was sampled at 61 positions along a spanwise line at $x = 0.27$, approximately through the centres of the Dean vortices. The forcing pump signal was sampled simultaneously. Measured amplitude distributions are usually slightly asymmetric, probably as the result of small disturbances in the flow. No systematic asymmetries were observed. The amplitude of the fundamental frequency reaches zero in the centre of the duct, with maxima on both sides of the horizontal centre line. The first harmonic has a maximum in the centre and goes to zero around $z = \pm0.05$ with secondary maxima around $z = \pm0.1$. With 89% of the total power at the fundamental frequency, the amplitude of the total power follows the amplitude of the fundamental frequency closely.

The shift of power between the fundamental frequency and the first harmonic near the centre of the duct is illustrated in figures 6.39c-h. At $z = 0.008$, close to the centre line and at the minimum of the fundamental amplitude, the first harmonic dominates the signal (figure 6.39c-d). At $z = 0.024$ the fundamental
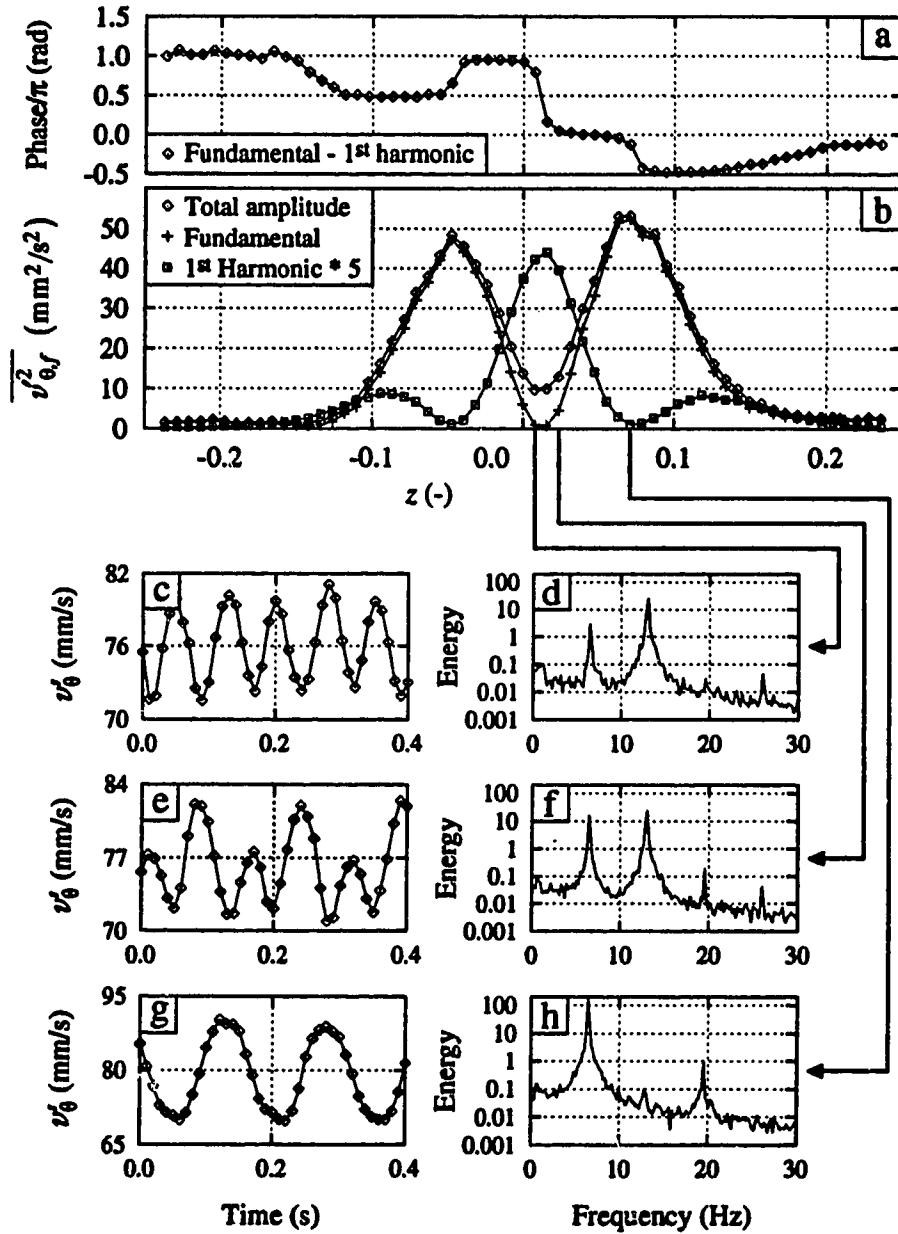
Figure 6.39: Streamwise velocity amplitude and phase distributions of fundamental and first harmonic (a-b). Time series and spectra illustrate the shift of power between the fundamental frequency and the first harmonic (c-h). $Dn = 220$, $\theta = 180°$, $x = 0.27$, 25 gauge pin, forcing of 1.82 V^2 at 6.5 Hz, 61 samples (-0.24 < z < 0.24) of 2048 measurements sampled at 100 Hz.

and the first harmonic are equally strong (figure 6.39e-f) and at $z = 0.071$, where the fundamental frequency is at its maximum, the signal is dominated by the fundamental (figure 6.39g-h). The time series on the other side of the centre line show the same trends. More detailed time series and frequency spectra at $z = 0.008$, 0.024, 0.039, 0.071 and 0.134 are shown in figures 6.40-6.49. A number of velocity profiles, simulated with FLOW3D, are shown in figure 6.50. The simulated profiles are in qualitative agreement with the experiments.

The phase jump at the centre line in figure 6.39a is associated with the fundamental frequency. This phase difference of 180° between the fundamental on both sides of the centre line is shown clearly in figure 6.50. Both this phase jump and the fact that the fundamental amplitude is zero in the centre will be explained in section 6.5.2, where the symmetry of the flow is discussed.

If a time series contains two or more frequency components, the shape of that time series depends on the phase differences between the components. Especially in the region where the fundamental and the first harmonic are equally powerful (figures 6.39e-f), the velocity signal depends strongly on the phase difference between these two components. It is shown in figure 6.39a that the phase difference between the fundamental and the first harmonic on either side of the centre line is 0 or π, both corresponding to the velocity signal shown in figure 6.39e.

Amplitude distributions of the streamwise velocity and distributions of the phase difference with the forcing signal are shown in figures 6.51-6.56 for the fundamental and first and second harmonics respectively. All phase differences are expressed as a fraction of the fundamental wavelength. Because of the arbitrary distance between the pin, where the forcing disturbances are created, and the position where the velocity is sampled, this phase difference is a relative quantity.

The phase differences with the forcing signal show a significant random
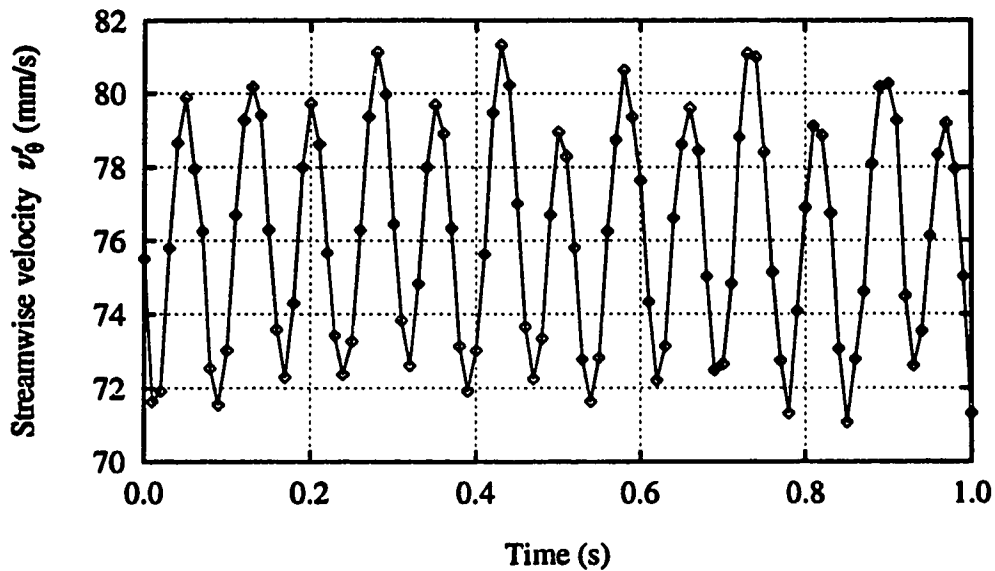
Figure 6.40: Part of streamwise velocity signal at $z = 0.008$ from data shown in figure 6.39.
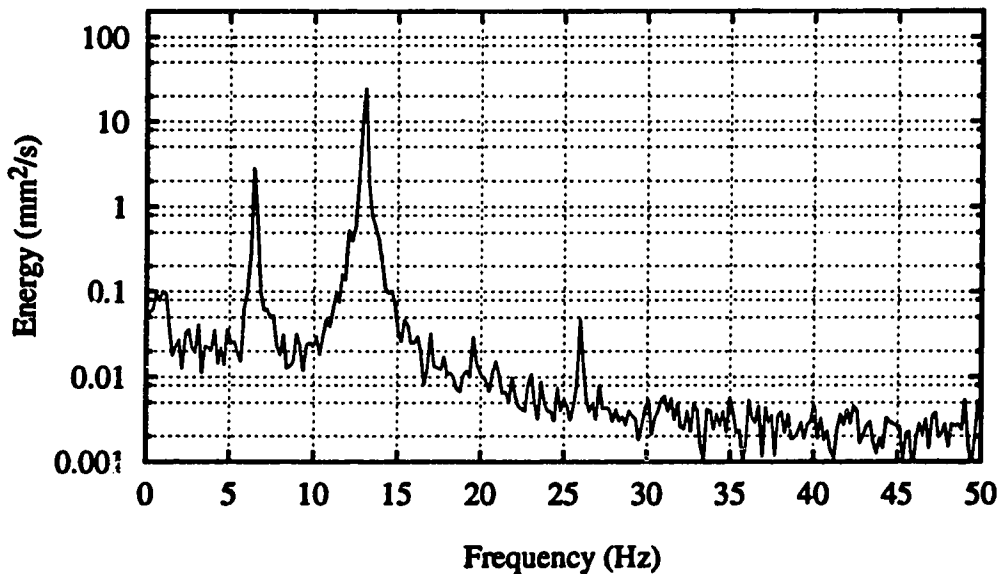
Figure 6.41: Frequency spectrum of time series shown in figure 6.40. Spectra were averaged over 7 blocks with 50% overlap.
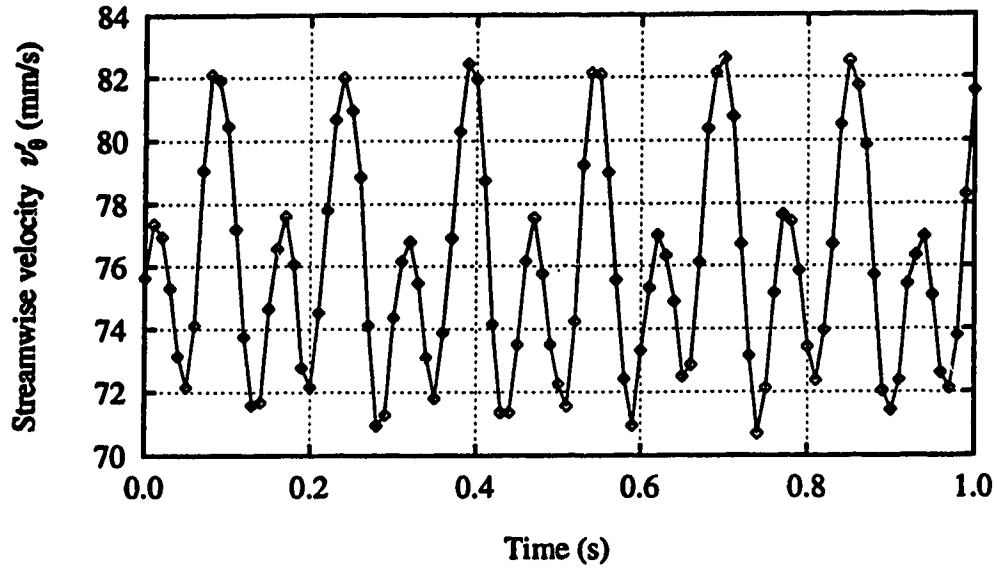
Figure 6.42:   Part of streamwise velocity signal at $z = 0.024$ from data shown in figure 6.39.
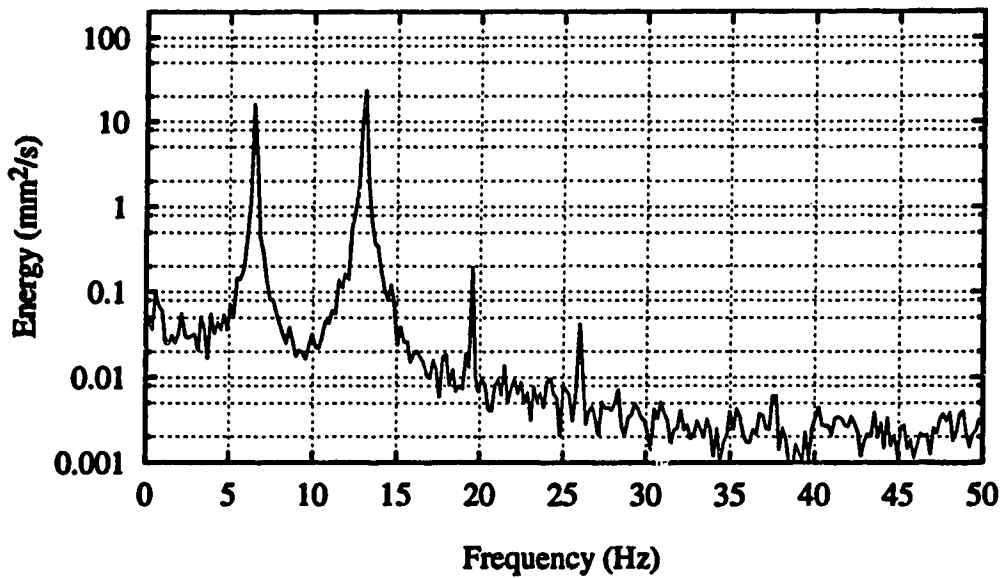
Figure 6.43:   Frequency spectrum of time series shown in figure 6.42. Spectra were averaged over 7 blocks with 50% overlap.
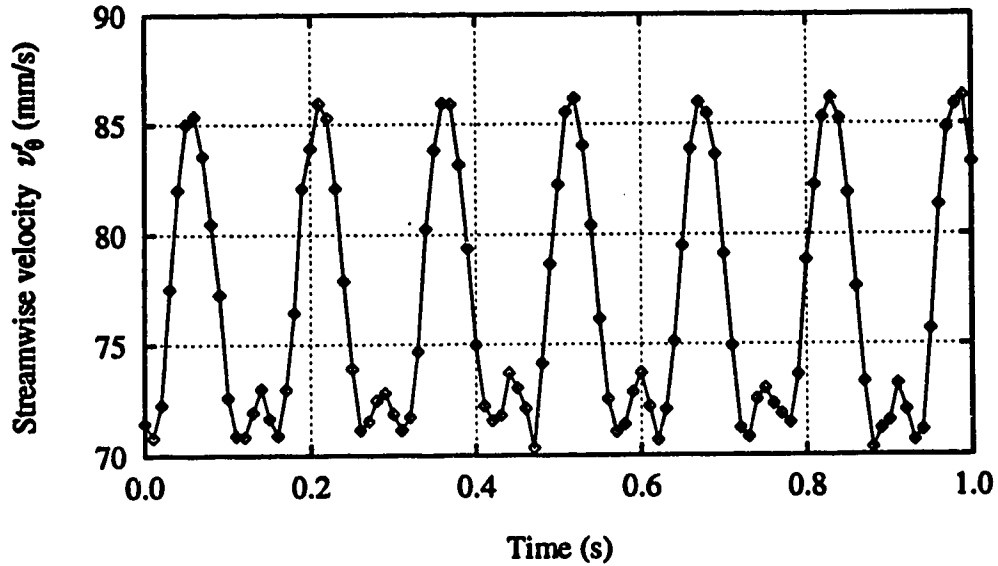
Figure 6.44: Part of streamwise velocity signal at $z = 0.039$ from data shown in figure 6.39.
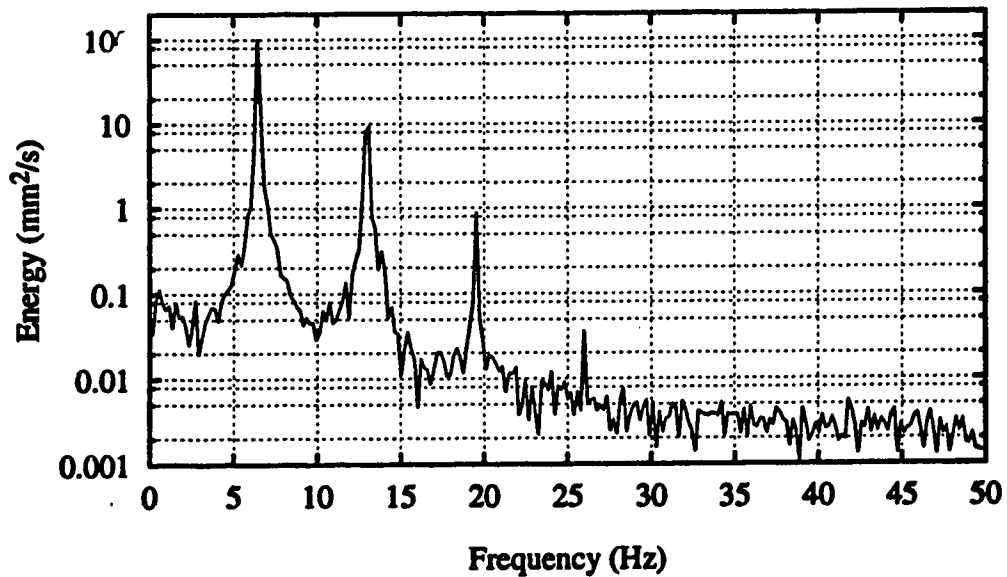
Figure 6.45: Frequency spectrum of time series shown in figure 6.44. Spectra were averaged over 7 blocks with 50% overlap.
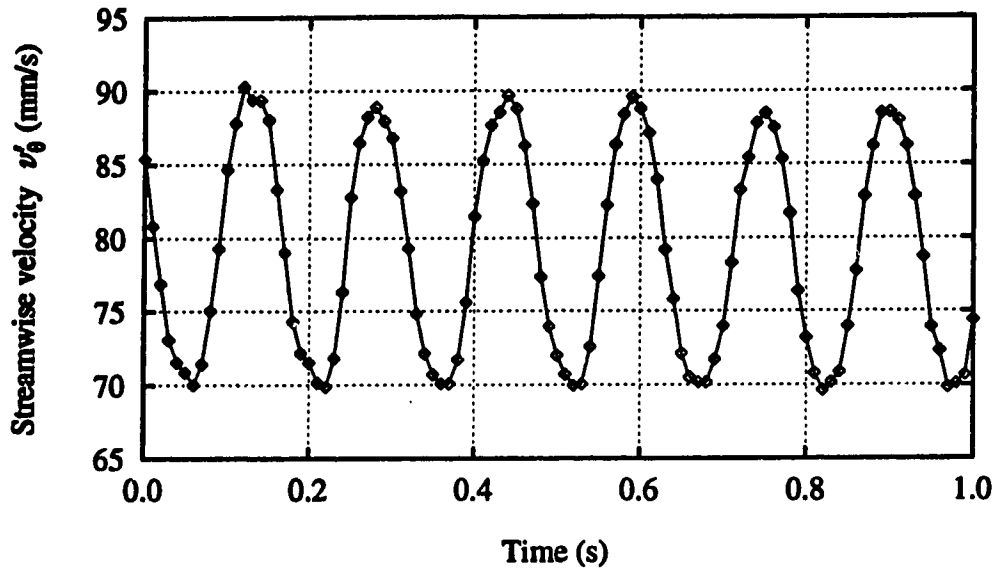
Figure 6.46: Part of streamwise velocity signal at $z = 0.071$ from data shown in figure 6.39.
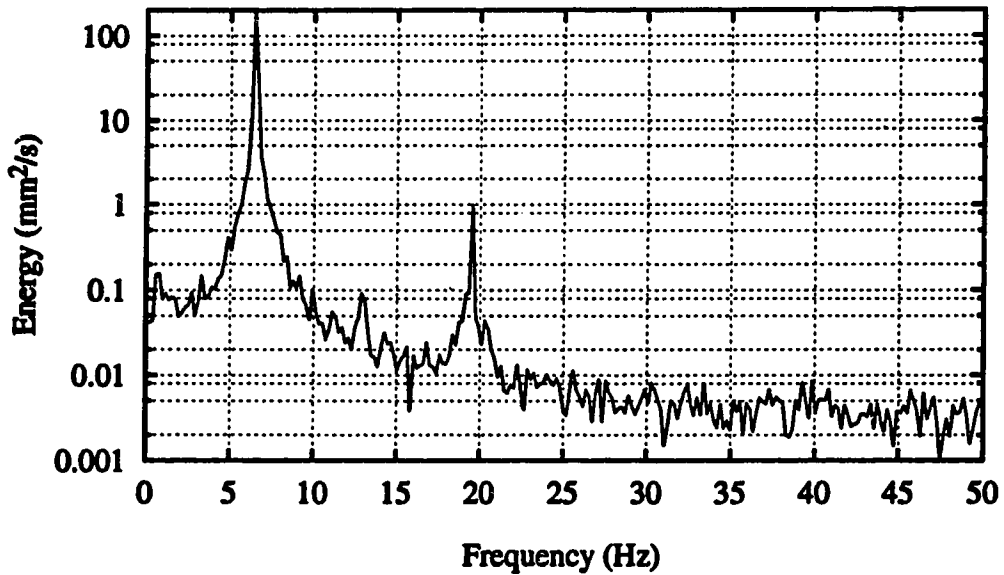
Figure 6.47: Frequency spectrum of time series shown in figure 6.46. Spectra were averaged over 7 blocks with 50% overlap.
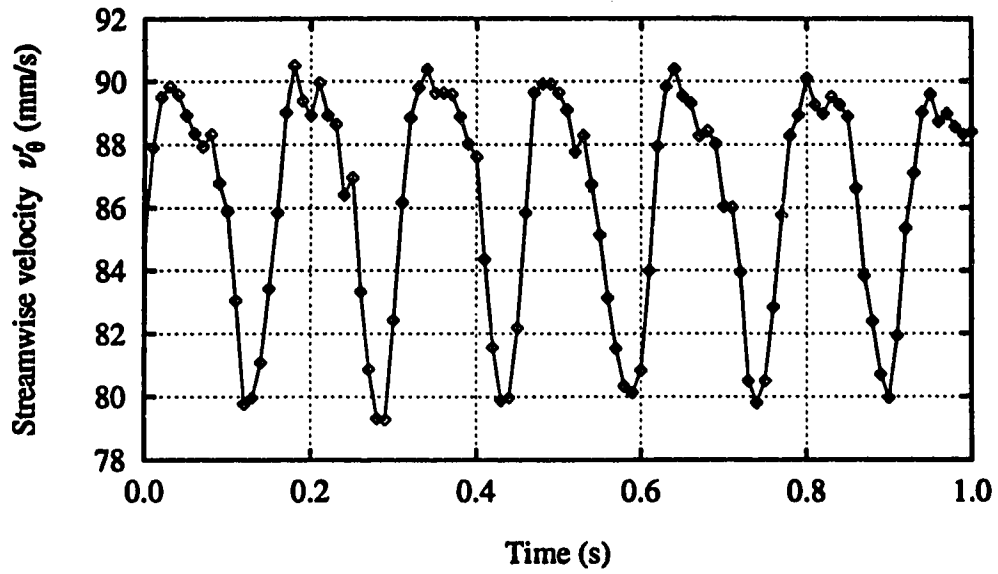
Figure 6.48:   Part of streamwise velocity signal at $z = 0.134$ from data shown in figure 6.39.
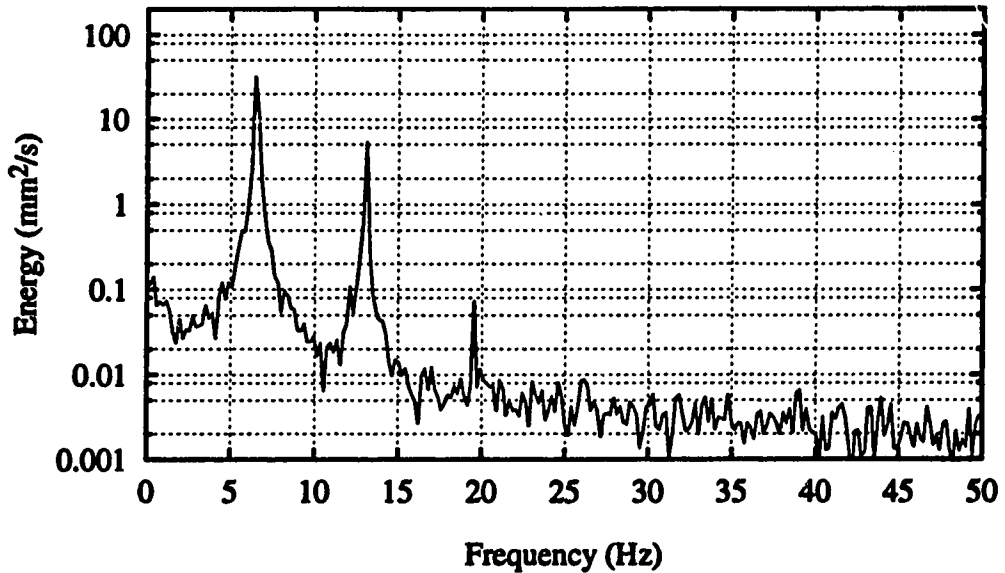
Figure 6.49:   Frequency spectrum of time series shown in figure 6.48.   Spectra were averaged over 7 blocks with 50% overlap.
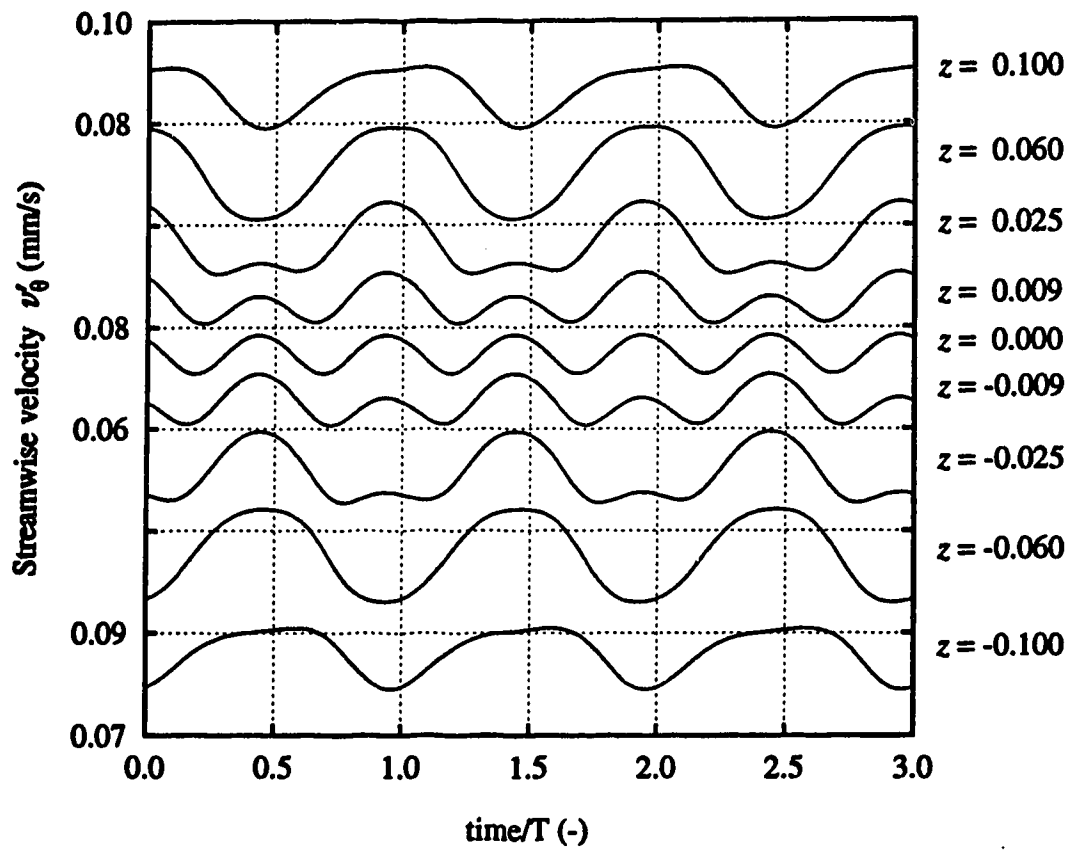
Figure 6.50: Streamwise profiles of the streamwise velocity at $x = 0.27$, from the
             FLOW3D simulation with grid 3.
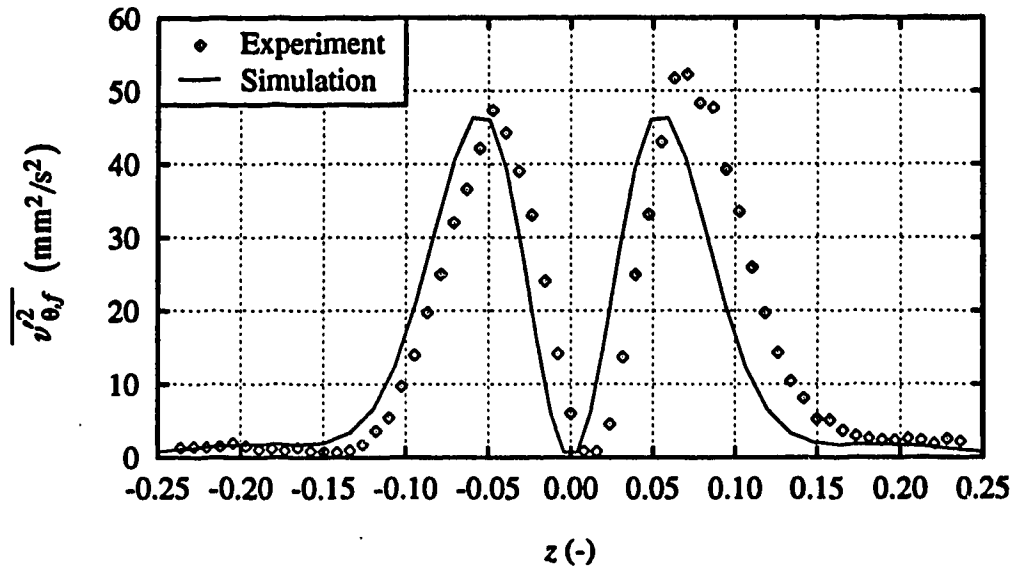
Figure 6.51: Streamwise velocity amplitude distribution of the fundamental component. Parameters as in figure 6.39.
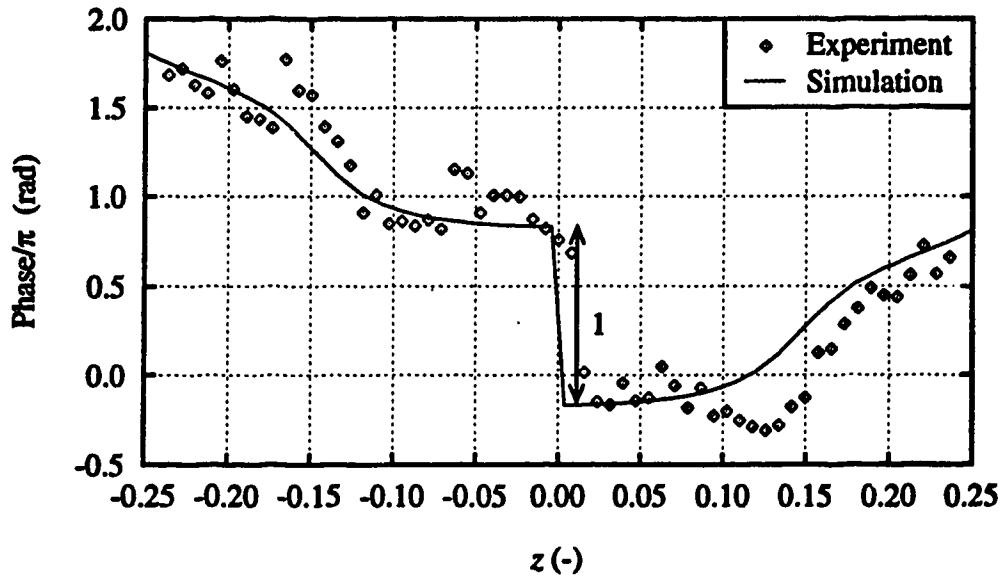
Figure 6.52: Streamwise velocity phase distribution of the fundamental component. Parameters as in figure 6.39.
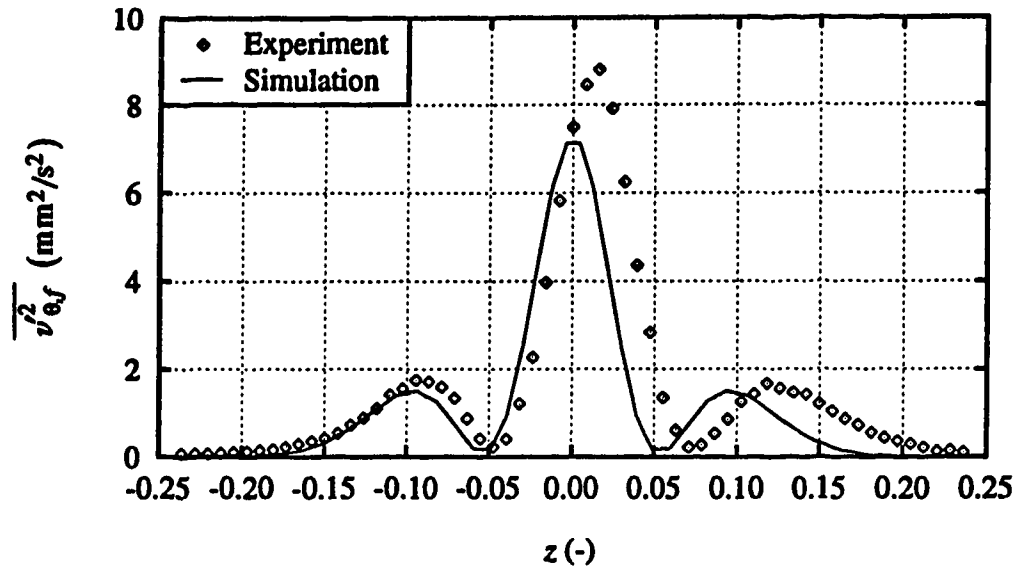
Figure 6.53: Streamwise velocity amplitude distribution of the first harmonic. Parameters as in figure 6.39.
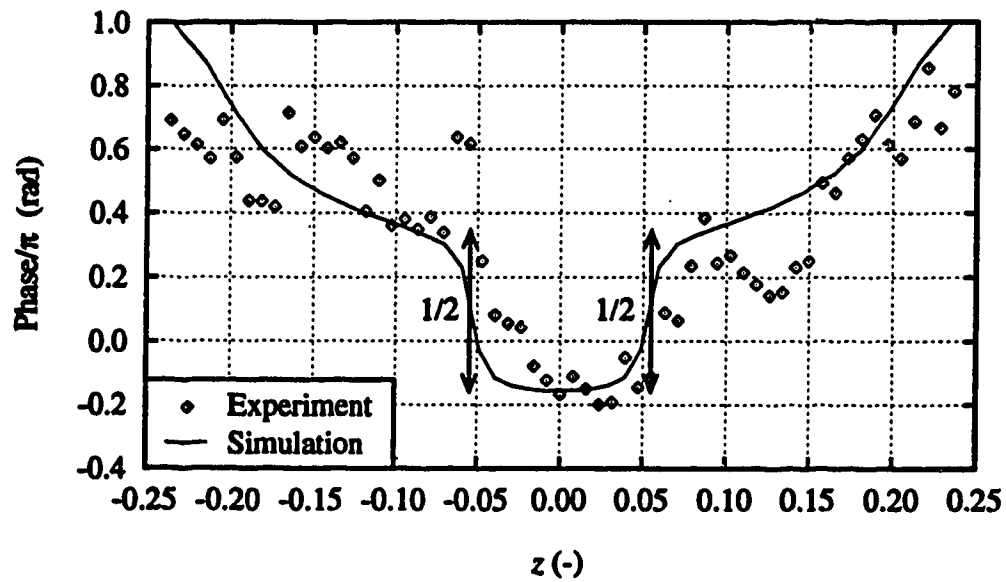
Figure 6.54: Streamwise velocity phase distribution of the first harmonic. Parameters as in figure 6.39.
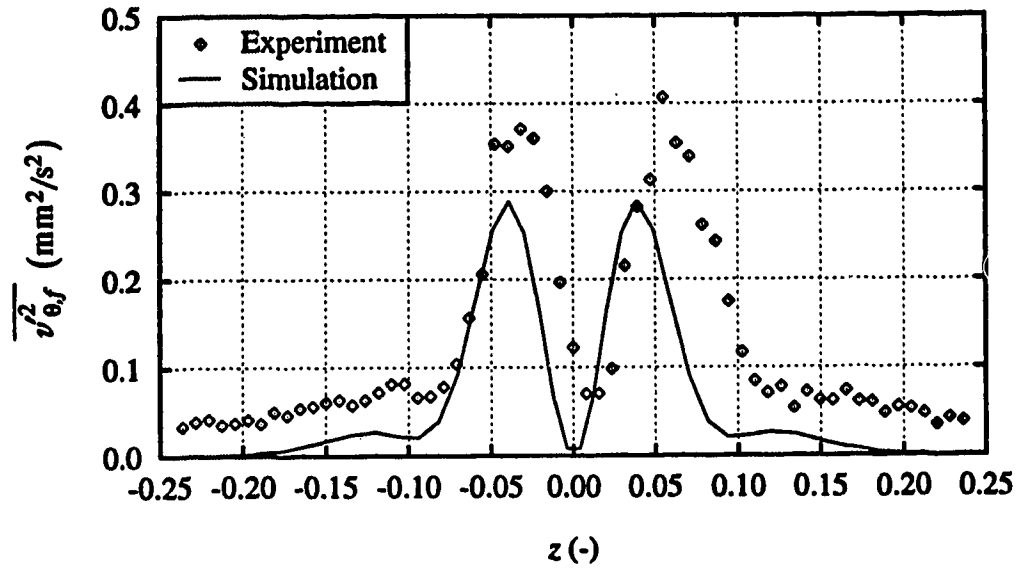
Figure 6.55:   Streamwise velocity amplitude distribution of the second harmonic. Parameters as in figure 6.39.

Figure 6.56:   Streamwise velocity phase distribution of the second harmonic. Parameters as in figure 6.39.

fluctuation which makes it difficult to detect phase jumps. The uncertainty in the phase is probably caused by the relatively large distance between the pin and the position where the phase is measured, in this case at $\theta = 180°$. The forcing pump determines the phase of the disturbance that is created near the inlet of the duct. It takes the disturbance about 50 wavelengths, or 7 seconds, to travel to the position where the velocity is measured. Hence, the velocity and forcing signals at any point in time are not directly related. Because of the delay, small fluctuations in the forcing frequency or flow rate cause large uncertainties in the phase difference between the forcing signal and the velocity measured at $\theta = 180°$.

There is a π phase jump of the fundamental component in the centre of the duct. The first harmonic has two phase jumps of $\frac{1}{2}\pi$ each at about $z = \pm 0.05$. Finally, the second harmonic has three phase jumps of $\frac{1}{3}\pi$ each: at the centre and at $z = \pm 0.1$. Some of these phase jumps, indicated in figures 6.52, 6.54 and 6.56, are not very distinct, but will become more clear when phase differences between different frequency components of the streamwise velocity are considered. All phase jumps occur where the amplitude is zero or nearly zero.

The solid lines in figures 6.51-6.56 are the results of the FLOW3D simulation with grid 3. The predicted phase distributions agree well with the experiments, especially with the uncertainty of the measured phase in mind. The amplitude distributions show the right trends, but are slightly lower than the experimental distributions. The experimental wave power and the wave power predicted by the two simulations are given in table 6.2. In the simulation, the wave power increases significantly with grid refinement and it is likely that the power will increase even more with further grid refinement. This has not been done due to the large amount of computer memory and CPU time needed for such a simulation. The power of the second harmonic is most sensitive to grid refinement and shows the largest difference

with the experimental results. A mechanism that explains this high grid sensitivity of the second harmonic will be presented in section 6.5.3.

The phase differences between different frequency components of the velocity are much better reproducible than phase differences with the forcing signal. Shown in figures 6.57-6.59 are the phase differences between the first three frequency components. These internal phase differences are absolute quantities. The phase jumps are much more distinct than before. Additional information is needed to determine which of the two velocity signals causes a phase jump. Since sudden phase jumps can only occur when the amplitude is zero, most phase jumps are easily identified. Only the second harmonic shows two gradual phase jumps. The simulated phase distributions are in good agreement with the experiments, especially in the lower half of the flow field. The asymmetries in the measured profiles cause some discrepancy between the measured and the calculated profiles in the upper half of the flow. The amplitude and phase distributions of the streamwise velocity are summarized in figure 6.60.

Amplitude distributions of the spanwise velocity are shown in figures 6.61-6.63. Just as for the streamwise velocity, amplitude plots are symmetric within experimental accuracy. The experimental and predicted wave power are compared in table 6.2. The simulation results are again very grid sensitive. At the finest grid, the predicted power of the first and second harmonics is higher than the experimental power. This is possibly due to an over filtering of the high frequency components by the frequency tracker. The phase difference between the fundamental and the first harmonic is shown in figure 6.64. The predicted phase distribution agrees well with the experiment. There are no phase jumps in the fundamental. The first harmonic has a $\frac{1}{2}\pi$ phase jump in the centre, where the amplitude is zero. Because of the low amplitude, there is a large uncertainty in the phase of the second harmonic.

	Experiment	grid 3	grid 2	grid 1
Streamwise velocity				
Total power	8.21	7.35	5.95	3.58
Fundamental	7.23	6.76	5.60	3.48
1st Harmonic	0.696	0.551	0.329	0.0971
2nd Harmonic	0.0387	0.0299	0.0127	0.00212
Spanwise velocity				
Total power	4.70	4.56	3.29	1.73
Fundamental	4.48	4.41	3.22	1.71
1st Harmonic	0.117	0.136	0.0705	0.0170
2nd Harmonic	0.00643	0.00931	0.00326	0.000536

Table 6.2: Experimental and simulated wave power (mm^2/s^2).
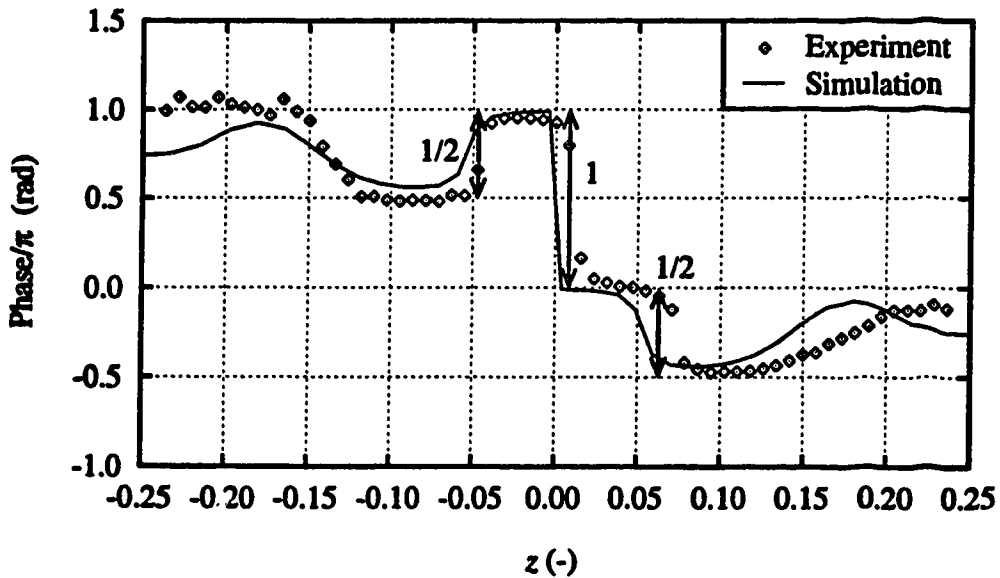
Figure 6.57: Phase difference between the fundamental and the first harmonic of the streamwise velocity. Parameters as in figure 6.39.
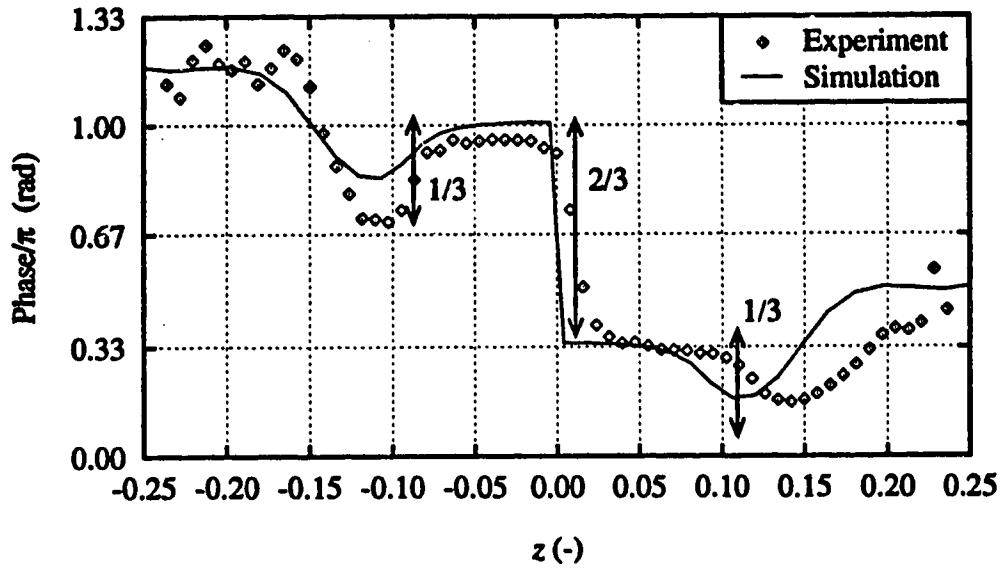
Figure 6.58: Phase difference between the fundamental and the second harmonic of the streamwise velocity. Parameters as in figure 6.39.
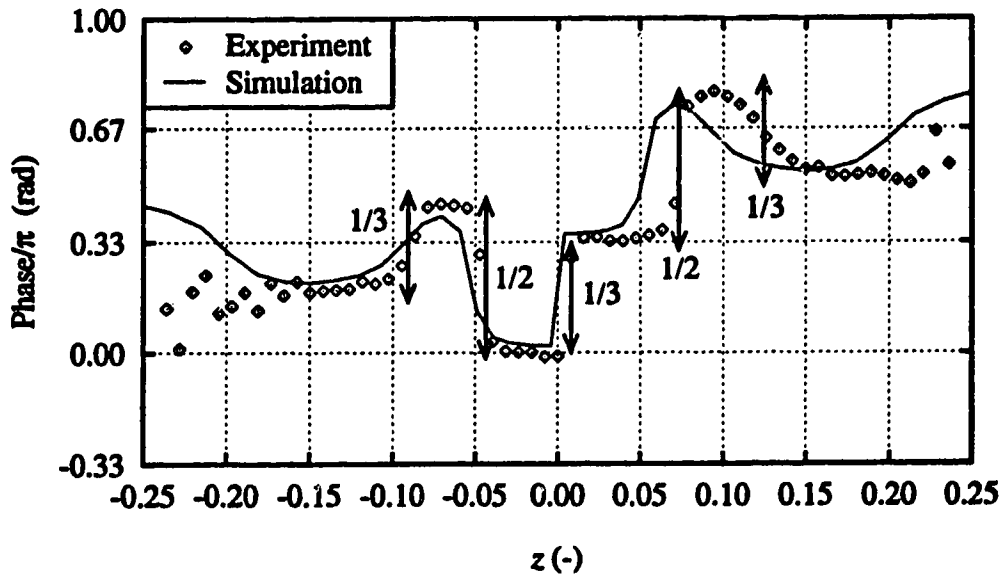
Figure 6.59: Phase difference between the first harmonic and the second harmonic of the streamwise velocity. Parameters as in figure 6.39.
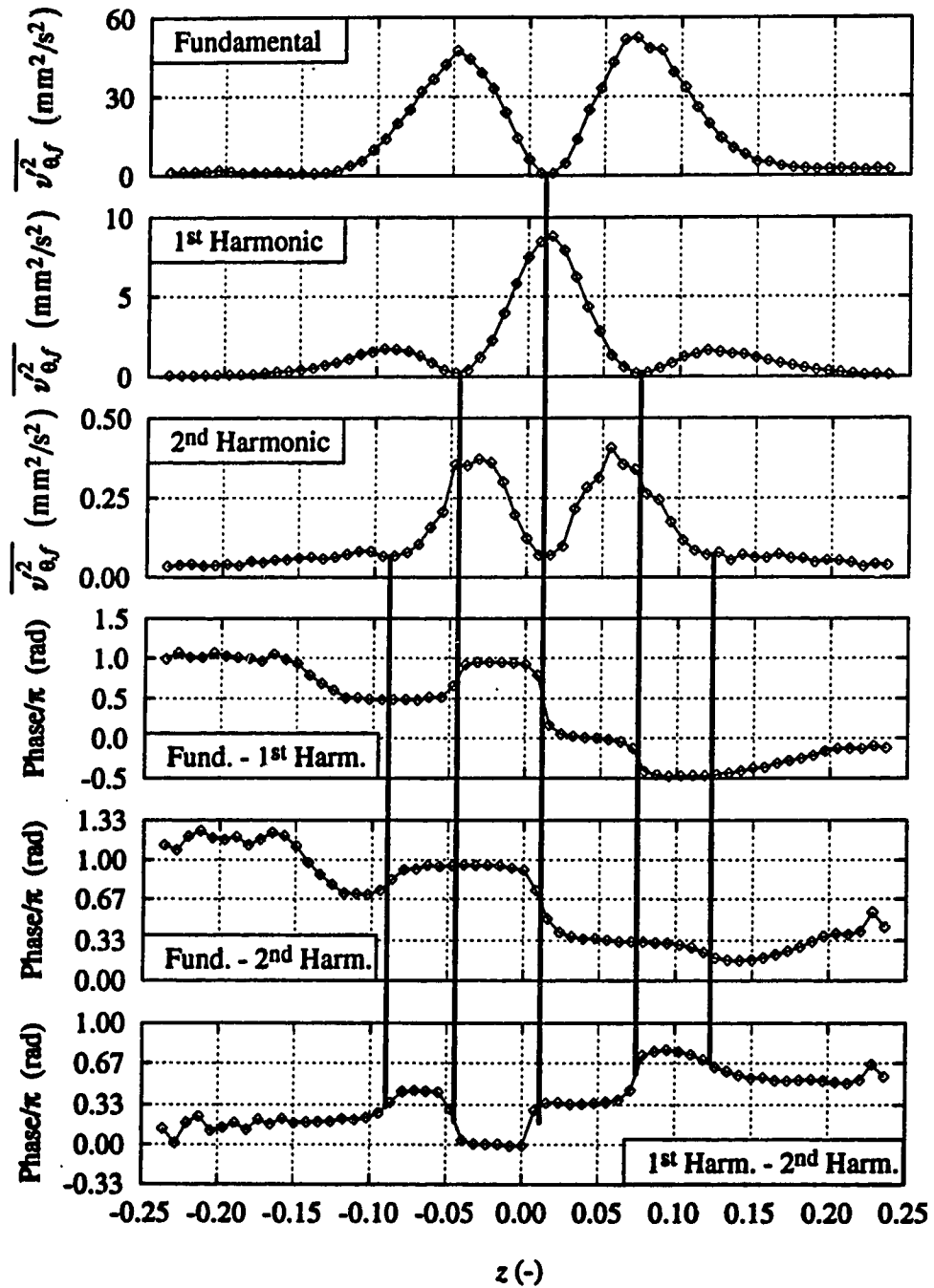
Figure 6.60: Summary of amplitude and phase distributions of the streamwise velocity. Solid vertical lines indicate phase jumps. Parameters as in figure 6.39.
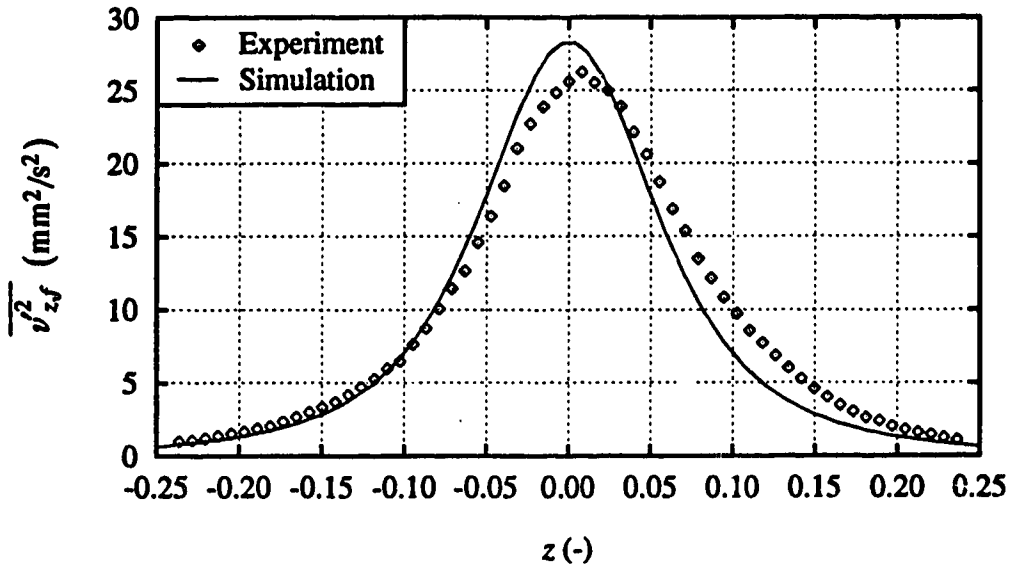
Figure 6.61: Spanwise velocity amplitude distribution of the fundamental component. Parameters as in figure 6.39.

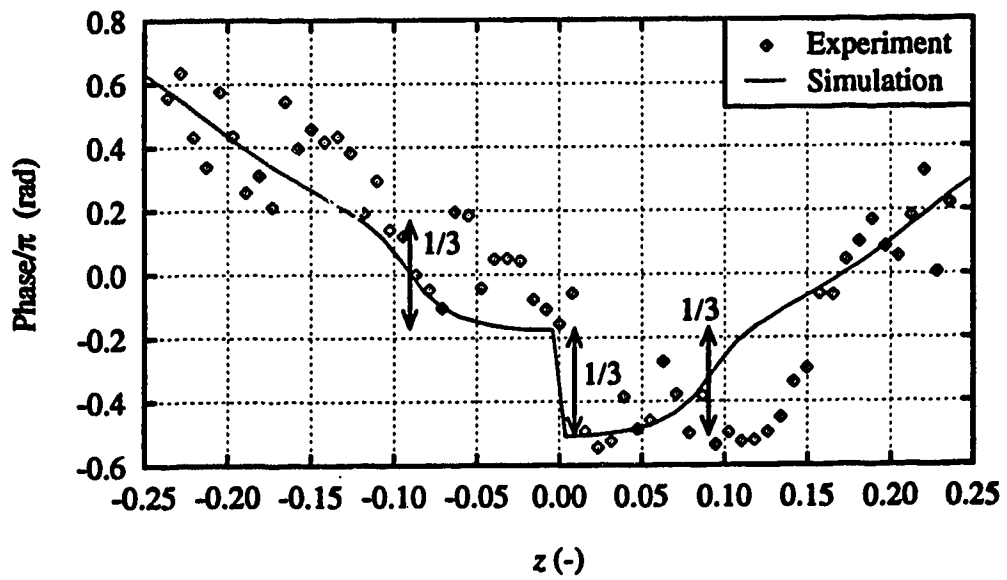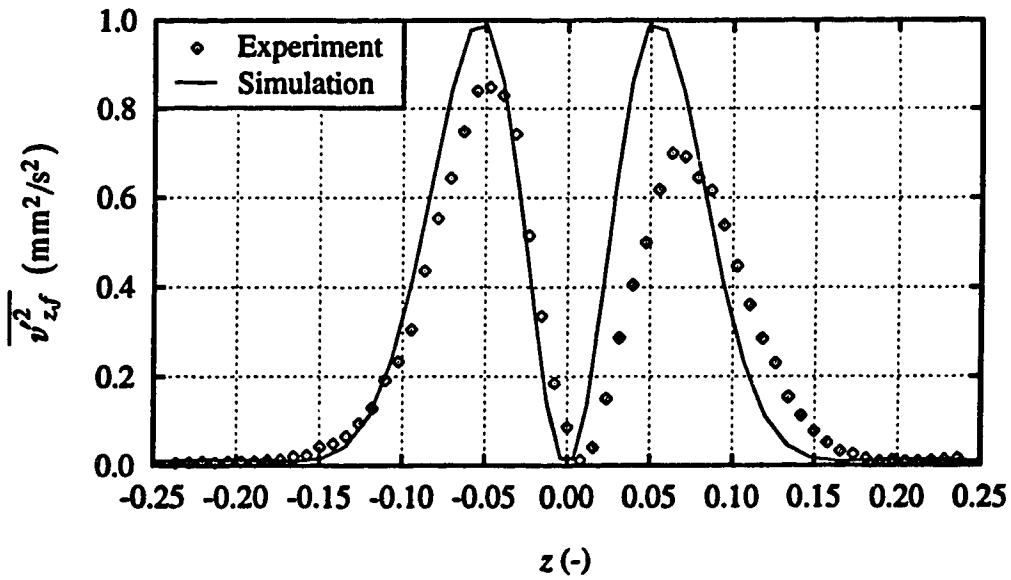Figure 6.62: Spanwise velocity amplitude distribution of the first harmonic. Parameters as in figure 6.39.
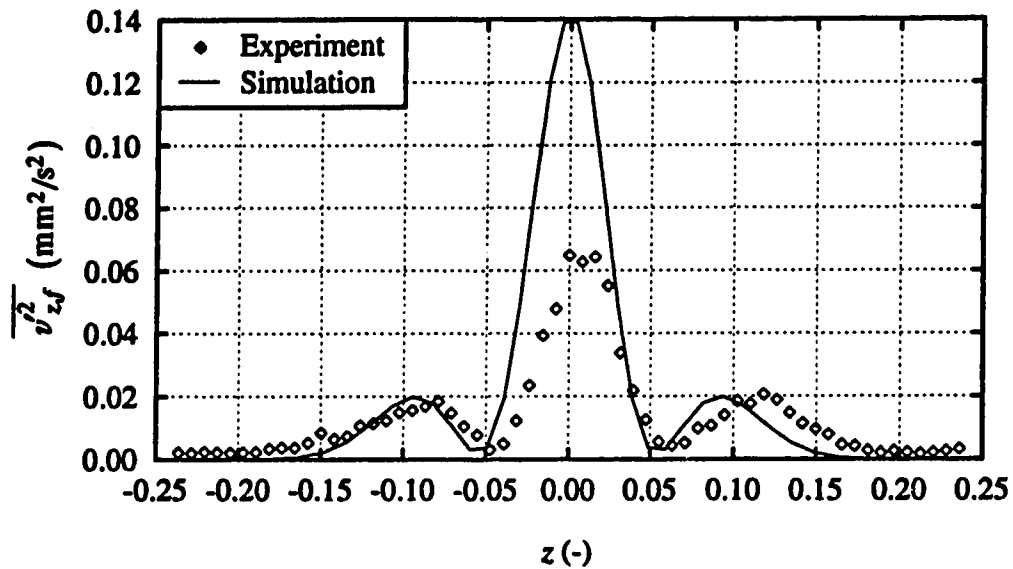
Figure 6.63:   Spanwise velocity amplitude distribution of the second harmonic.
Parameters as in figure 6.39.
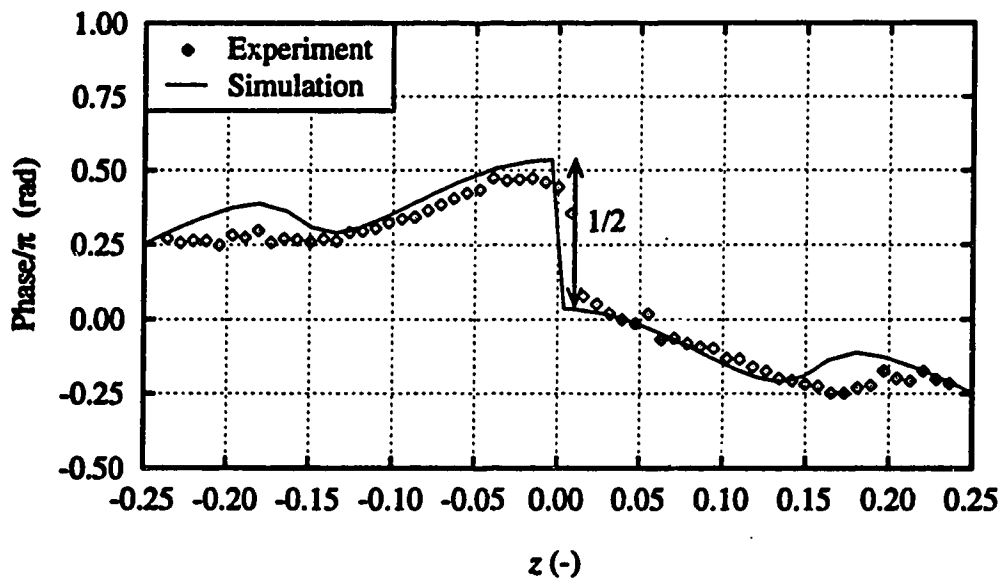
Figure 6.64:   Distribution of phase difference between the fundamental and first
harmonic of the spanwise velocity. Parameters as in figure 6.39.

6.5.2   Symmetry

Symmetry theory can be extremely useful in the analysis of flow phenomena. For example, knowing the symmetry of the apparatus, it is possible to determine a priori which types of solutions are possible, and how different solutions relate to each other.

The symmetry of the Dean problem will be compared to that of Taylor-Couette flow, which has been studied in great detail (e.g. Golubitsky & Stewart, 1986). The main difference between the two systems is that Dean flow is an open system, while Taylor-Couette flow is a closed system. Although this is a fundamental difference with far-reaching consequences, it will be shown that with certain restrictions most of the symmetry properties of Taylor-Couette flow also apply to the Dean problem.

The symmetries of a system are those transformations that leave that system apparently unchanged. The symmetries of the apparatus are considered first, since flow states can not have more symmetries than the apparatus. It is important to know the symmetries of the apparatus, because performing any of these symmetry transformations to a solution of the flow must lead to another valid solution, although not necessarily the same one. An excellent and very entertaining introduction to many of the symmetry concepts used here is given by Stewart and Golubitsky (1993).

Because the Dean problem is an open system with developing flow, the system has no rotational symmetry. However, an idealized system consisting of an infinitely long curved duct without entrance and exit regions, does have rotational symmetry, just like Taylor-Couette flow. An apparatus like this is obviously physically impossible because it closes into itself. Another symmetry of the real and idealized apparatus is reflect symmetry around the centre plane, $z = 0$. Finally, because the apparatus does not change with time, it possesses all possible time symmetries.

It was shown in section 5.2 that at low flow rates the flow develops into a fully developed 2-cell state. This flow state has the same symmetries as the entire apparatus: no symmetry has been broken. The transition to a fully developed 4-cell state does not break symmetry either; the fully developed 4-cell state also has the same symmetries as the apparatus.

When traveling waves develop from steady 4-cell flow, the time symmetry is broken by a Hopf bifurcation, leading to time periodic solutions. At the same time the rotational symmetry is broken. A Hopf bifurcation can lead either to standing wave or to traveling wave solutions. A traveling wave is characterized by mixed spatio-temporal symmetry; the flow field is invariant over a rotation, combined with a translation in time by a corresponding amount, which is determined by the wave speed.

It was shown in section 6.1 that at a Dean number of 220 the flow is developing over most of the length of the apparatus and seems to reach a fully developed state around $\theta = 180°$. Although the flow is periodic in time, it is not spatially periodic over the full length of the apparatus. Only the fully developed traveling wave state has mixed spatio-temporal symmetry. Because this spatio-temporal symmetry makes space and time interchangeable, the spatial structure of the flow in this region can be determined by investigating the time periodic flow field at an arbitrary position. The wave speed forms the connection between the spatial structure and the temporal structure of the flow. The temporal flow structure was represented by the amplitude and phase distributions in the previous section.

Since the apparatus has reflect symmetry in the centre plane ($z = 0$), reflection of the traveling wave in the centre plane must produce either the same solution or a different, but also valid, solution. There are two different periodic traveling wave solutions that meet this requirement: the sinuous mode and the varicose

mode. The varicose mode is symmetric in the centre plane. The sinuous mode is invariant under a reflection in the centre plane combined with a shift over half a fundamental wavelength. Because space and time are interchangeable, a spatial shift is equivalent to a temporal shift over a corresponding amount. This kind of symmetry is called shift-and-reflect symmetry (figure 6.65). It is clear from the flow visualization in section 6.1 that the flow field is not symmetric in the centre plane. The observed traveling wave state must therefore have shift-and-reflect symmetry. The measured and simulated amplitude and phase distributions confirm the shift-and-reflect symmetry of the flow.

Wavy vortex flow in the Taylor-Couette system also has shift-and-reflect symmetry. Because of the circular symmetry of the Taylor-Couette system, only discrete wavelengths that fit an integer number of times in the geometry are possible. In the Dean problem there is no such limitation of the possible wavelengths.

The amplitude distributions presented in the previous section are all symmetric around the centre line, $z = 0$. Because both the sinuous and the varicose modes of oscillations have symmetric amplitude distributions, phase information is needed to distinguish the two modes.

The streamwise velocity phase distributions of the fundamental, first harmonic and second harmonic have phase jumps at the centre of π, 0, and $\frac{1}{3}\pi$ respectively. Because the first harmonic is periodic over half a period of the fundamental, a zero phase jump of the first harmonic is equivalent to a π phase jump. Similarly, a phase jump of $\frac{1}{3}\pi$ in the second harmonic, which is periodic over 1/3 of the fundamental period, is equivalent to a π phase jump. Therefore, all phase distributions have a π phase jump in the centre, corresponding to a shift over half a fundamental wavelength. Apart from this phase jump, all phase distributions are symmetric around the centre line. The π phase jumps show that the flow is shift-and-reflect
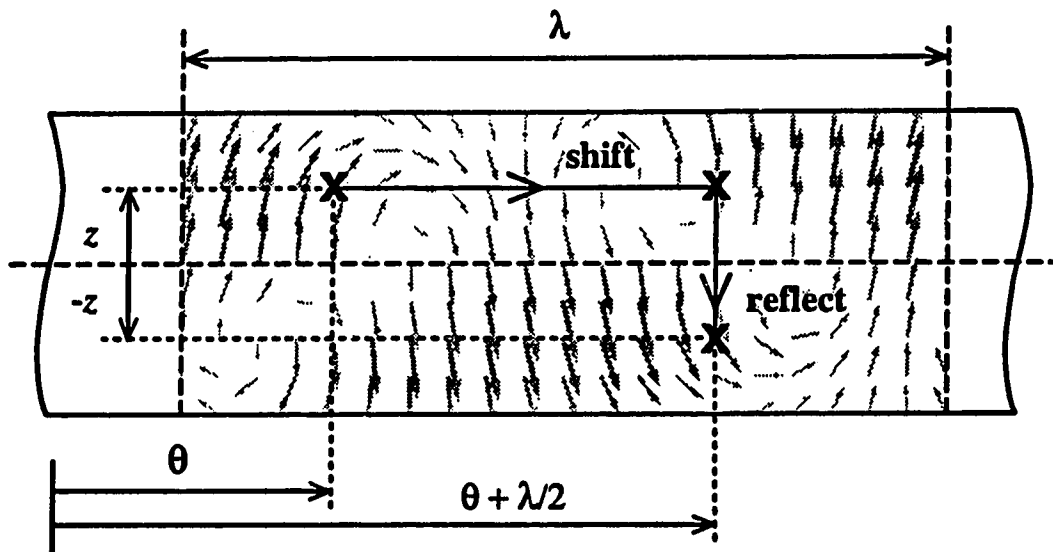
$$v_r(r, \theta, z, t) = v_r(r, \theta+\lambda/2, -z, t)$$

$$v_\theta(r, \theta, z, t) = v_\theta(r, \theta+\lambda/2, -z, t)$$

$$v_z(r, \theta, z, t) = -v_z(r, \theta+\lambda/2, -z, t)$$

Figure 6.65: Shift-and-reflect symmetry.

symmetric.

Amplitude and phase distributions of the developing traveling wave state have the exact same characteristics as fully developed traveling waves. Because the flow is not spatially periodic, the developing traveling wave flow is only shift-and-reflect symmetric with respect to a shift in time and not in space.

The fact that the amplitudes of the fundamental and the second harmonic at the centre line are zero, also follows directly from the shift-and-reflect symmetry: because the streamwise velocity at the centre line is unaffected by the reflection, the streamwise velocity profile in the centre is periodic over half a fundamental wavelength, and consequently has no fundamental and second harmonic components.

The shift-and-reflect symmetry is also confirmed by the amplitude and phase distributions of the spanwise velocity. Again the amplitude distributions are symmetric around the centre line. Because the spanwise velocity changes direction as a result of the reflection in the centre line, additional phase jumps of π, $\frac{1}{2}\pi$ and $\frac{1}{3}\pi$ are introduced to the fundamental, first harmonic and second harmonic respectively. If the measured phase jumps of 0, $\frac{1}{2}\pi$ and 0 are corrected for the effect of the reflection, all phase distributions have again a phase jump of π in the centre.

It was shown that in the fully developed region, the traveling wave phenomenon presented in this chapter, has shift-and-reflect symmetry, corresponding to the sinuous mode of oscillations. Symmetry theory was combined with information from flow visualization, and amplitude and phase distributions of the streamwise and spanwise velocity fluctuations.

6.5.3 Simulation Results

In section 6.5.1, simulated amplitude and phase distributions were compared with experimental distributions. The amplitude and phase distributions calculated with grid 3 are in good agreement with the experiments; the simulations capture the traveling wave phenomenon very well. Although the predicted amplitude distributions were quite grid sensitive, further grid refinement would probably only change the details of the simulated flow state. In this section more results of the simulation with grid 3 will be presented.

Cross section arrow plots over half a wavelength of the oscillations are given in figure 6.66. Because of the traveling wave character of the flow, these plots can either be interpreted as the temporal evolution at a fixed position, or the spatial variation at a fixed moment in time. The oscillation of the inflow region between the Dean vortices, which was observed in the flow visualization (figure 6.2), is clearly visible in these arrow plots. At the same time the Dean vortices oscillate in radial direction, as well as spanwise direction.

Contour plots of the streamwise vorticity are shown in figure 6.67. There are only four vortical structures in the flow: two Ekman vortices and two Dean vortices. The other streamwise vorticity is associated with shear layers along the walls. The strength of the Dean vortices doubles during the oscillations. The Dean vortices move away from the wall when they are weak and towards the wall when they are strong. Close examination of the streamwise vorticity shows that the vortices perform an approximately circular motion during the oscillations, very similar to that observed in the flow visualization (figure 6.2). The upper Dean vortex rotates counter clockwise, while the lower Dean vortices rotates clockwise, opposite to their sense of rotation. This circular motion gives the Dean vortices an approximately helical shape. Although a direct comparison with the experiment is not possible,
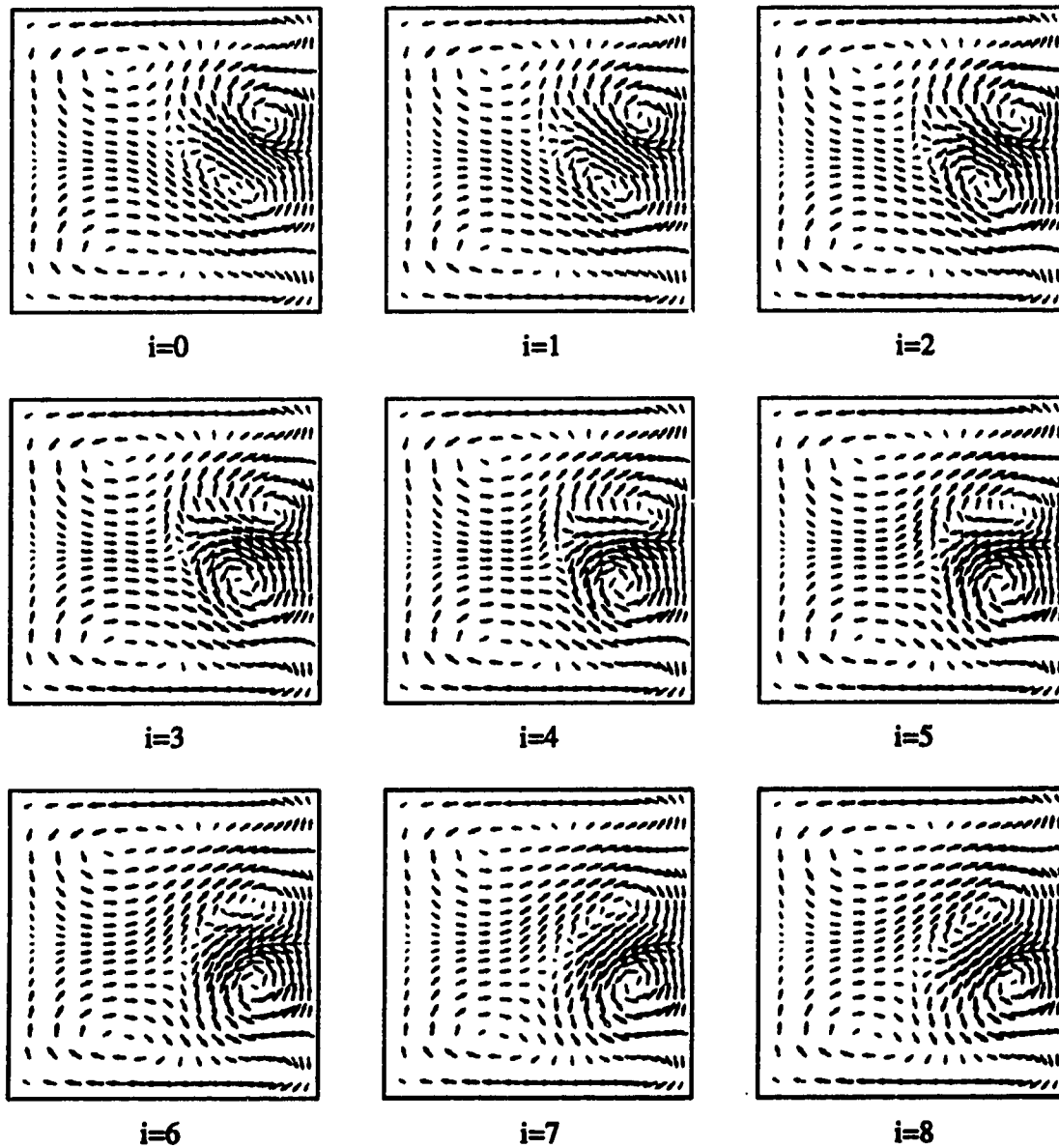
Figure 6.66:   Arrow plots of the secondary velocity for $t = T(i/16)$ or $\theta = \lambda(1 - i/16)$. $Dn = 220$, $\lambda = 3.8°$.
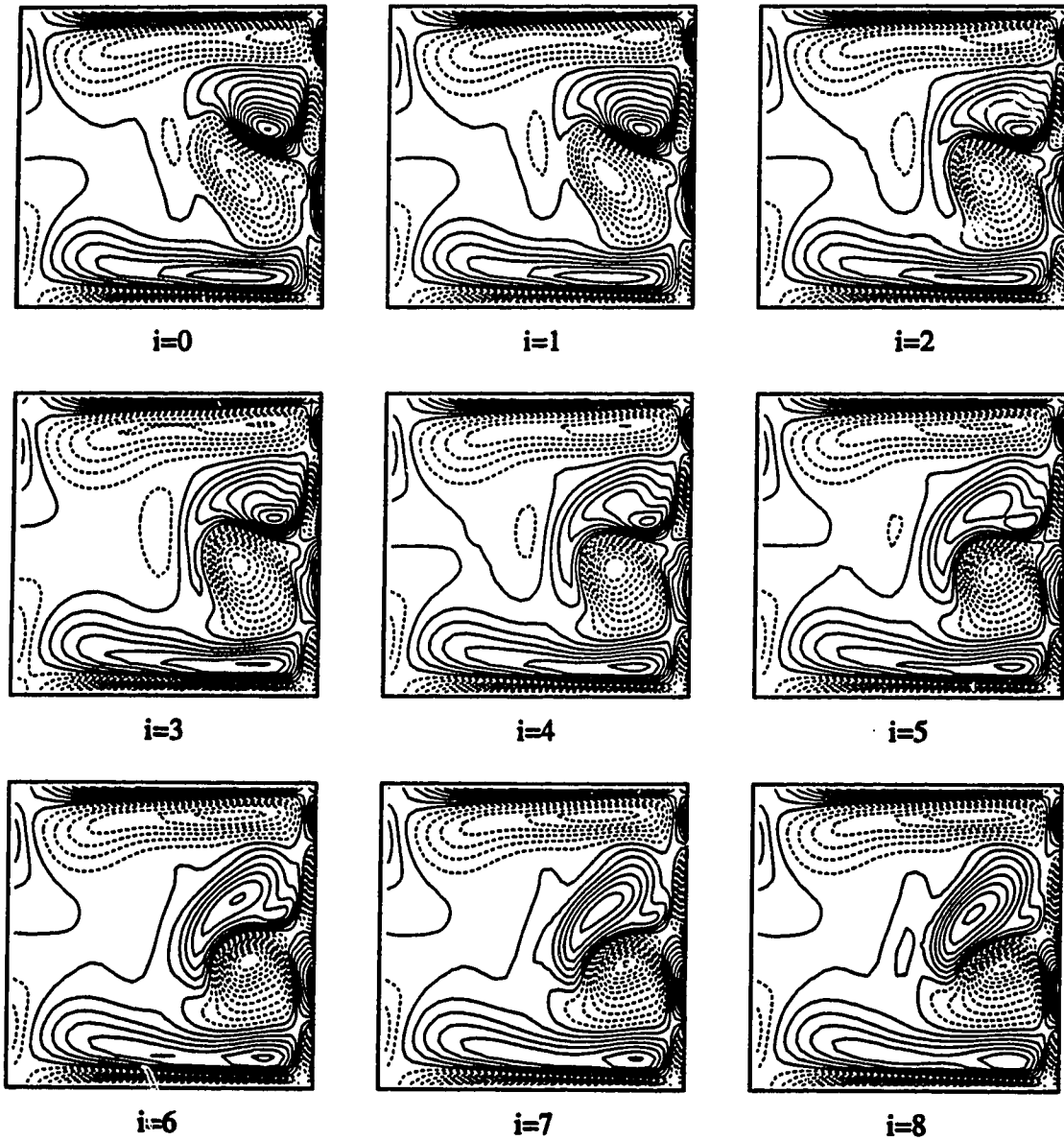
Figure 6.67: Streamwise vorticity plots in a (r,z)-plane for $t = T(i/16)$ or $\theta = \lambda(1 - i/16)$. Dn=220, λ=3.8°. Contour increments of 1.5 s^{-1}.

simulated streamwise vorticity and arrow plots show good qualitative agreement with the cross section flow visualization of figure 6.2.

Contour plots of all velocity and vorticity components in the cross section at one position are shown in figure 6.68. The streamwise velocity is more than an order of magnitude higher than the secondary velocities. There are regions with high radial vorticity on each side of the inflow region. This radial vorticity is associated with the spanwise inflectional profiles of the streamwise velocity. The radial vorticity near the top and the bottom walls is the result of the spanwise gradients of the streamwise velocity in those regions. In a similar way, the high spanwise vorticity near the outer wall is associated with the radial gradients of the streamwise velocity. By examining the velocity fields, no other vortical structures were observed than the two Ekman vortices and the two Dean vortices.

Difference velocities were defined as the velocity of the steady 4-cell flow, subtracted from the velocity field of the traveling wave state. The difference vorticity was defined in a similar way. Difference vorticity fields can give an idea of how vorticity is redistributed as a result of the traveling wave state. Contour plots of the velocities and difference velocities in a streamwise-spanwise plane at $x = 0.27$ are shown in figure 6.69. Vorticity and difference vorticity plots in that same (θ,z)-plane are given in figure 6.70. The maximum difference vorticity in the streamwise, radial and spanwise directions are 8.4, 33 and 6.1 s^{-1} respectively. The radial vorticity field is modified most strongly by the traveling wave instability.

A contour plot of the amplitude of the total streamwise velocity fluctuations is given in figure 6.71. There are two regions with high streamwise velocity oscillations, one on each side of the inflow region. Contours of the spanwise and radial gradients of the streamwise velocity are also shown in figure 6.71. The streamwise velocity gradients are very similar to the radial and spanwise vorticity (figures 6.68d and
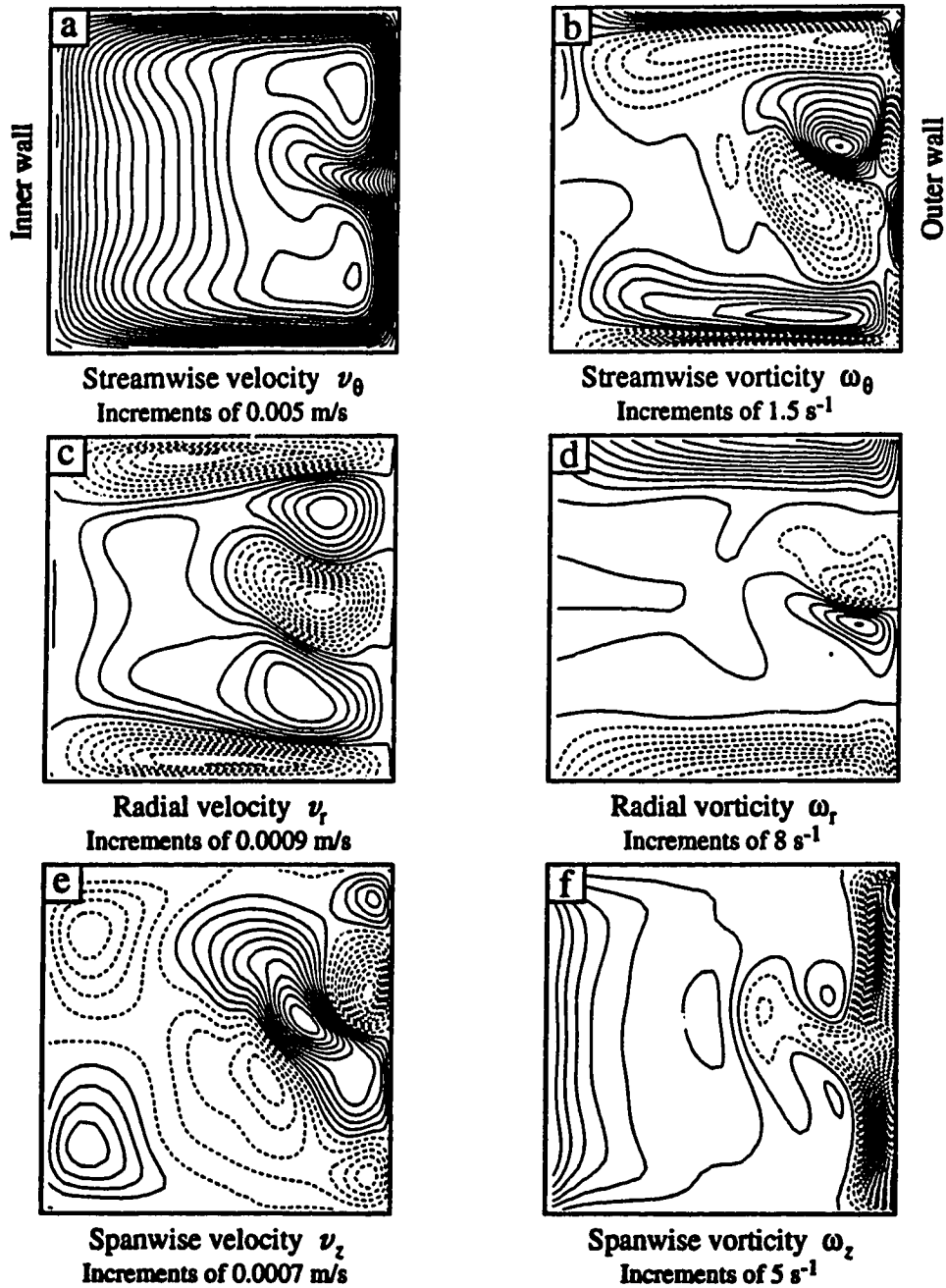
Figure 6.68: Velocity and vorticity contour plots in a (r,z)-plane. $Dn = 220$, $\lambda = 3.8°$. Contour increments as indicated.
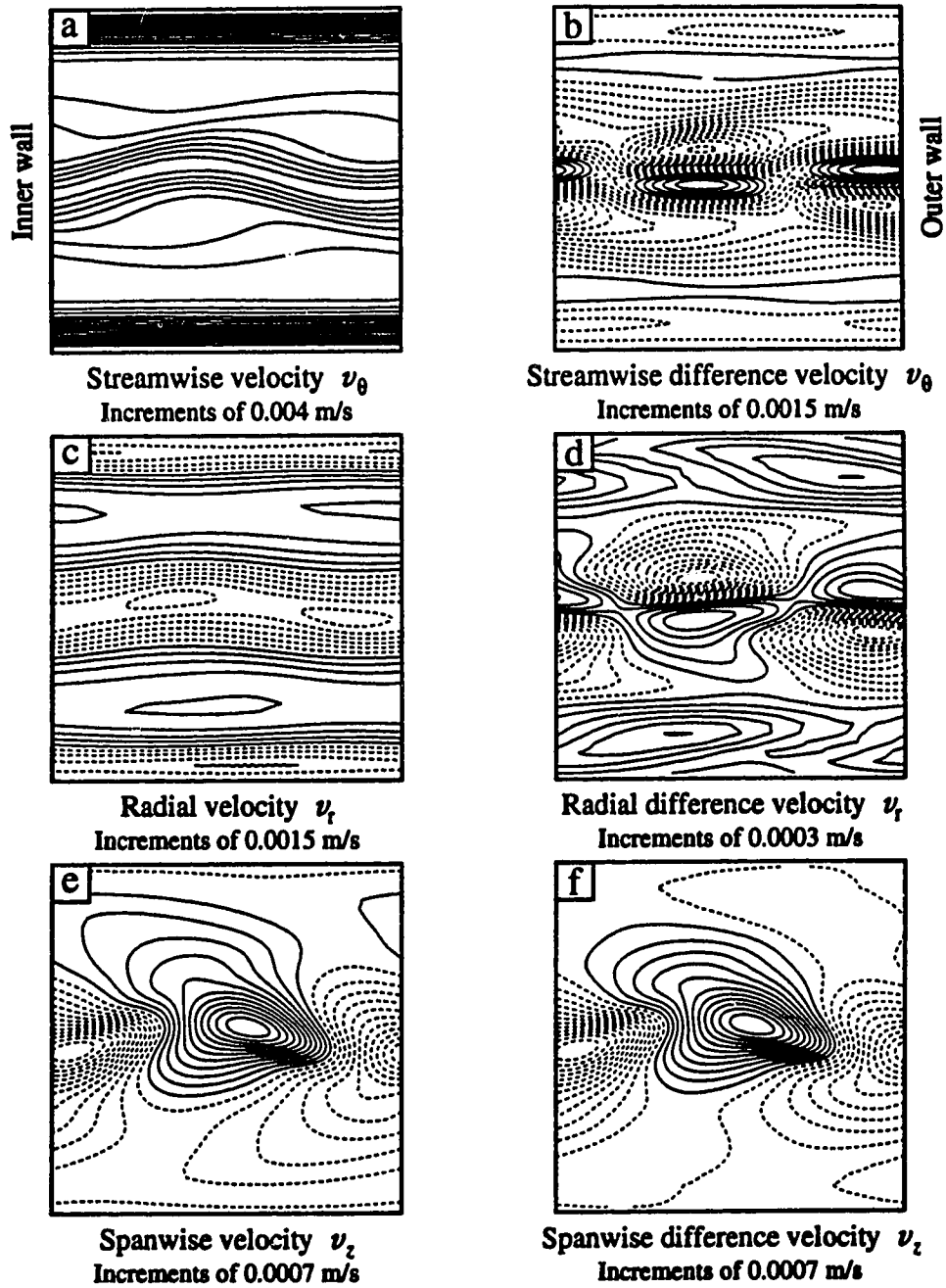
Figure 6.69:   Velocity and difference velocity contour plots in a (θ,z)-plane. $Dn = 220$, $\lambda = 3.8°$, $x = 0.27$. Contour increments as indicated.
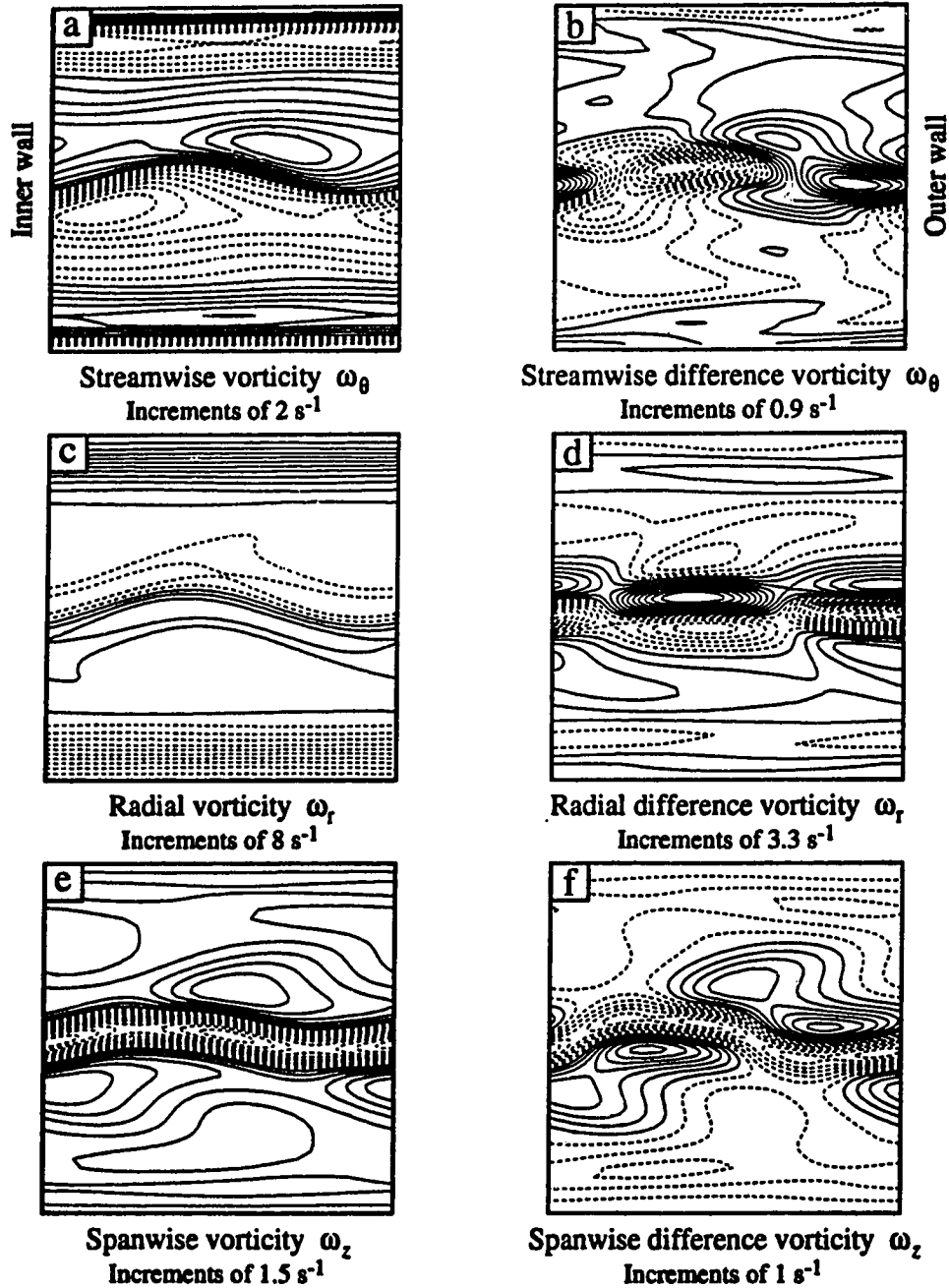
Figure 6.70: Vorticity and difference vorticity contour plots in a (θ,z)-plane. $Dn = 220$, $\lambda = 3.8°$, $x = 0.27$. Contour increments as indicated.
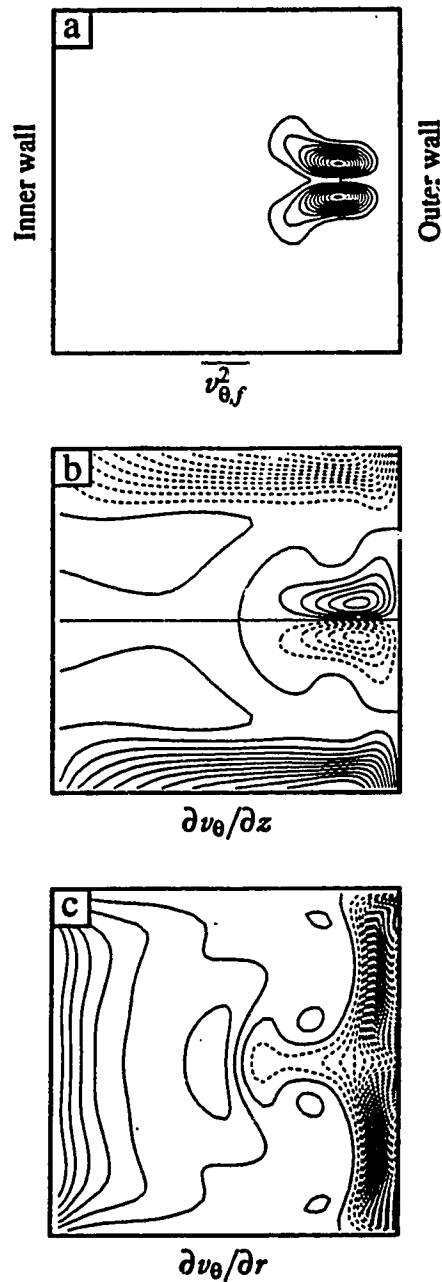
Figure 6.71: Amplitude of streamwise velocity fluctuations (a) and gradients of the streamwise velocity of steady 4-cell flow (b,c) in a (r,z)-plane. $Dn = 220$, $\lambda = 3.8°$.

6.68f) because gradients in the radial and spanwise velocities are relatively small. The regions with high streamwise velocity fluctuations correspond to high spanwise gradients of the streamwise velocity.

This correlation between high spanwise gradients of the streamwise velocity and high streamwise velocity fluctuations is easily explained by examining how the spanwise velocity profile varies with time. The spanwise profile of the streamwise velocity at $x = 0.27$ during steady 4-cell flow, simulated in FLOW3D, is shown in figure 6.72. The low velocity in the centre is due to the inflow region. Also shown are the spanwise profiles during the traveling wave state. The centre region with low streamwise velocity oscillates in spanwise direction, while the shape of this centre region remains almost unchanged.

A very simple model that explains the qualitative features of the measured amplitude and phase distributions is based on the assumption that the spanwise profile of the streamwise velocity does not change shape during the oscillations; the V-shaped centre region only oscillates in spanwise direction. The amplitude of the velocity fluctuations, induced by this oscillating profile, can be determined from the shape of the spanwise velocity profile. Fluctuations at the fundamental frequency are, as a first approximation, proportional to the spanwise derivative of this profile and to the distance over which this profile oscillates in spanwise direction (Δz). It can also be shown that the oscillations at the first harmonic frequency are, in first approximation, proportional to the second derivative of the spanwise velocity profile, and to $(\Delta z)^2$. The oscillations at the second harmonic are proportional to the third derivative of the velocity profile, and to $(\Delta z)^3$.

The first three derivatives of the spanwise velocity profile of the streamwise velocity are shown in figure 6.73. The shapes of the derivatives agree remarkably well with the amplitude distributions from section 6.5.1. The phase of the oscillations is

Figure 6.72: Simulated spanwise proüles of streamwise velocity in steady (a) and wavy (b) 4-cell flow. $Dn = 220$, $\lambda = 3\,5°$, $x = 0.27$.
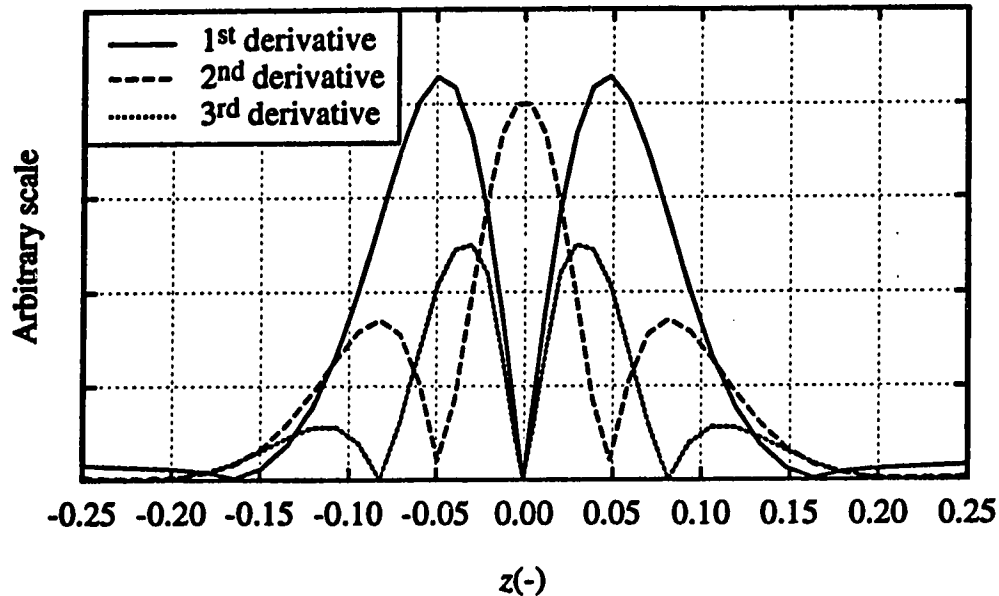
Figure 6.73: Derivatives of the spanwise profile of the streamwise velocity for steady 4-cell flow. $Dn = 220$, $\lambda = 3.8°$, $x = 0.27$.

related to the sign of the different derivatives. This simple model predicts phase jumps each time the amplitude is zero: in the centre for the fundamental, at $z = \pm 0.05$ for the first harmonic, and in the centre and at $z = \pm 0.08$ for the second harmonic. This is in qualitative agreement with the phase distributions in figures 6.52, 6.54 and 6.56.

This model also provides a possible explanation for the grid sensitivity of the wave power, summarized in table 6.2. The power of the second harmonic was most grid sensitive. The solutions with all three grids predict the spanwise oscillation of velocity profiles, which the simple model was based on. Although the simulations show qualitative agreement with the experiments, the spanwise distance Δz over which the velocity profiles oscillate increases with grid refinement. The simple model

predicts that the power of the fundamental, and first and second harmonic is in first approximation proportional to Δz, $(\Delta z)^2$ and $(\Delta z)^3$ respectively. Since the power of the second harmonic depends most strongly on Δz, this component is most grid sensitive.

Streamwise velocity fluctuations could also be the result of radial oscillations of the velocity profile. Radial profiles of the streamwise velocity during the traveling wave state are given in figure 6.74. The profile for steady 4-cell flow is also shown. The radial profile changes very little as a result of the traveling waves. Consequently, streamwise velocity fluctuations induced by radial oscillations are small compared to those induced by spanwise oscillations.

Spanwise profiles of the spanwise velocity are shown in figure 6.75. Profile shapes fluctuate strongly during the traveling wave state and velocity gradients are much higher than for steady 4-cell flow. There is no direct connection between the shape of the steady profile and the shapes of the profiles during the wavy flow. Therefore, the simple model that was used to explain the amplitude distributions of the streamwise velocity, can not be used here.

The time averaged spanwise profiles of the streamwise and spanwise velocity are shown in figure 6.76 and 6.77. The measured streamwise and spanwise velocity profiles agree very well with the simulation. The asymmetry of the measured spanwise velocity profile could be due to a slight misalignment of the LDA optics. Because streamwise velocities are much higher than spanwise velocities, alignment is critical, when measuring spanwise velocities.
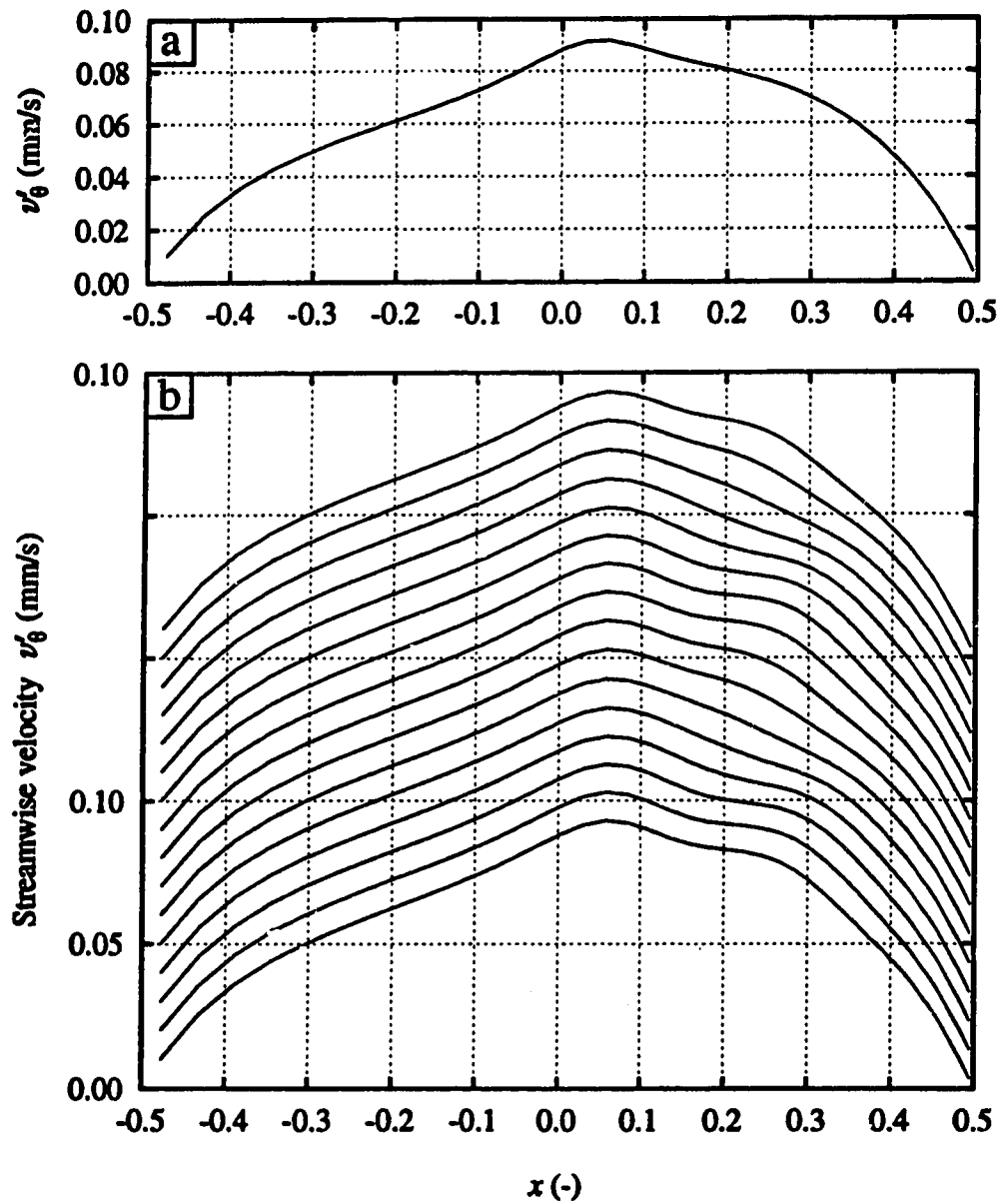
Figure 6.74: Simulated radial profiles of streamwise velocity in steady (a) and wavy (b) 4-cell flow. $Dn = 220$, $\lambda = 3.8°$, $z = 0.0$.
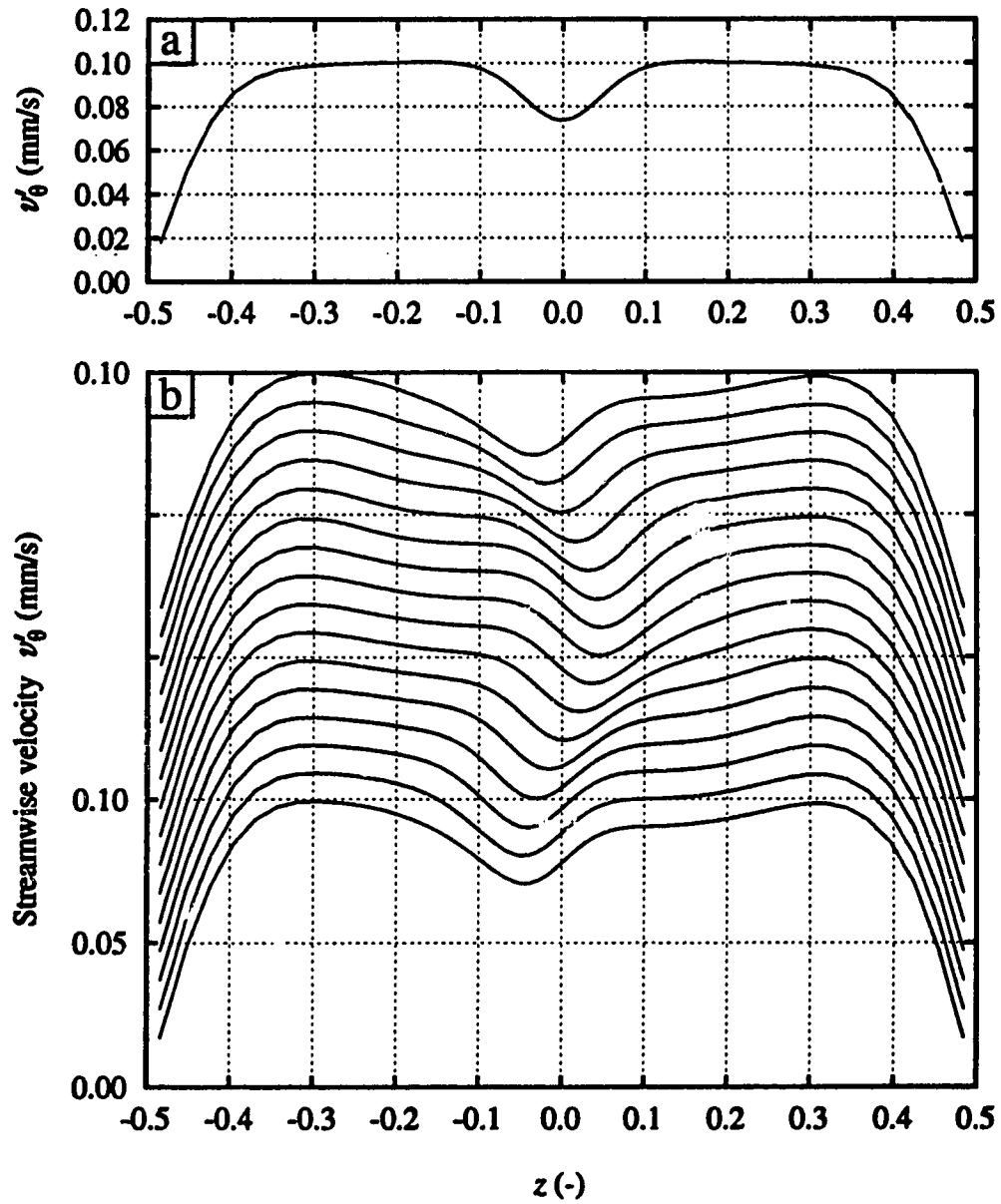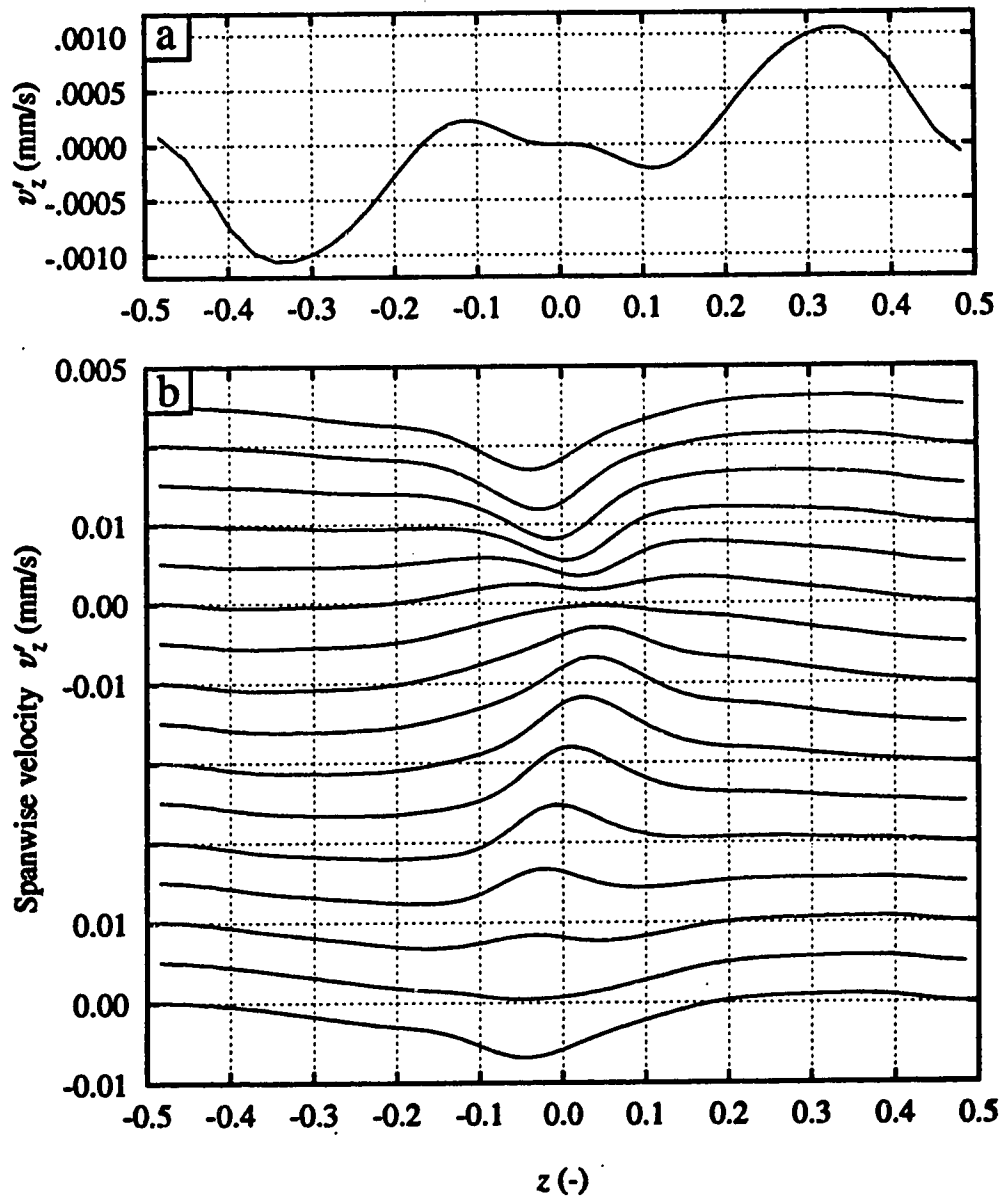
Figure 6.75: Simulated spanwise profiles of spanwise velocity in steady (a) and wavy (b) 4-cell flow. $Dn = 220$, $\lambda = 3.8°$, $x = 0.27$.
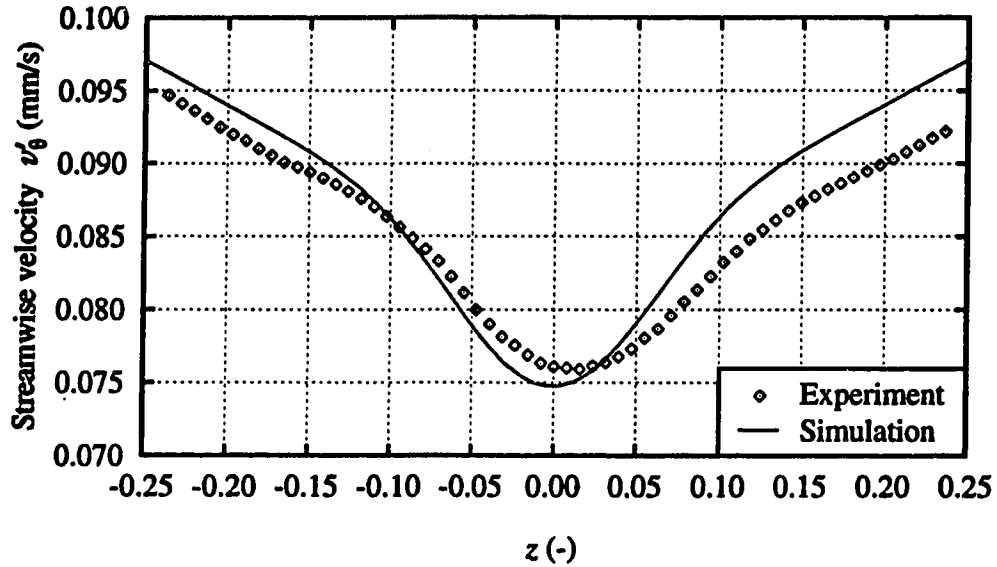
Figure 6.76: Average streamwise velocity of wavy 4-cell flow. $Dn = 220$, $\lambda = 3.8°$, $x = 0.27$.
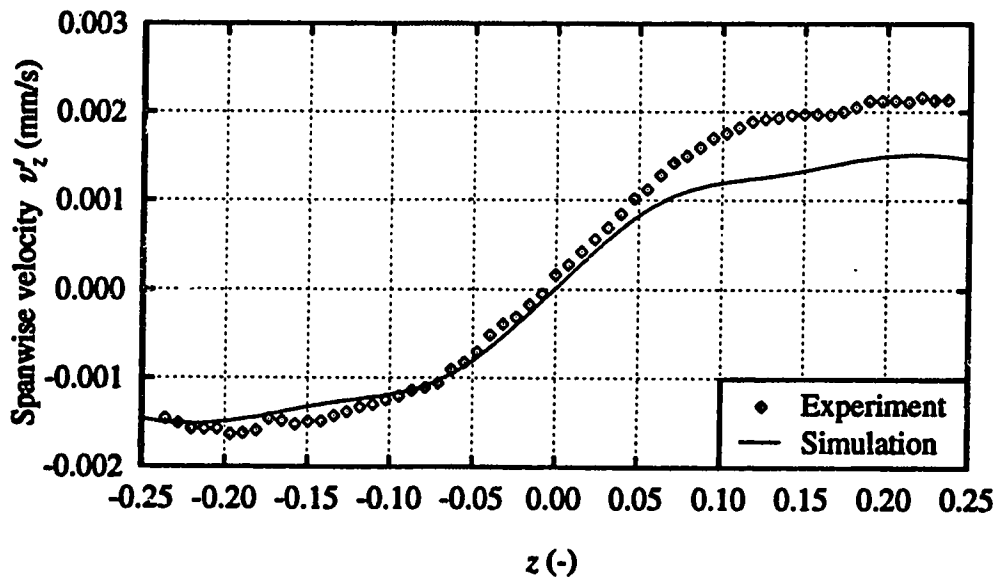
Figure 6.77: Average spanwise velocity of wavy 4-cell flow. $Dn = 220$, $\lambda = 3.8°$, $x = 0.27$.

6.5.4   Similarities with Other Systems

Curved geometries

The traveling waves in a curved square duct show great similarity with twisting waves in curved channel flow and the sinuous mode of wavy Görtler vortices. Twisting vortices in a curved channel were first observed experimentally by Kelleher *et al.* (1980) and later simulated by Finlay *et al.* (1987; 1988). Twisting vortices have streamwise wavelengths that are close to the spanwise wavelength. The undulating waves which were also observed in curved channel flow have much longer streamwise wavelengths. Finlay *et al.* found that the streamwise wavelength of twisting vortices in a curved channel with curvature ratio 39.6 is typically in the 2°-4° range and decreases with increasing flow rate. This compares well with the wavelength of 3.8° that was observed in this study for $Dn = 220$.

The arrow plots of secondary flow patterns of twisting waves in Finlay's figure 16 (Finlay *et al.*, 1988) are very similar to the ones in figure 6.66. In both cases the Dean vortices oscillate in radial and spanwise direction and fluctuate strongly in strength. The inflow region oscillates in spanwise direction, but the stagnation point near the outer wall does not move. Also Finlay's plots of the radial and spanwise velocity in the (r,z)-plane (Finlay *et al.*, 1987) are very similar to those in figures 6.68c and 6.68e.

Matsson and Alfredsson (1992; 1993a; 1993b) measured velocity fluctuations of twisting vortices in a curved channel with curvature ratio 29 and found the streamwise fluctuations to be strongest near the inflow regions. Contour plots of the streamwise velocity fluctuations associated with the twisting motion have a single maximum between two Dean vortices. However, because of the shift-and-reflect symmetry, a minimum in the velocity fluctuations is expected at the centre line.

Two separate maxima have indeed been observed at positions further upstream (Alfredsson, private communication).

Two modes of wavy Görtler vortices have been observed: the varicose mode, which is symmetric in a (r,θ)-plane between two Görtler vortices; and the sinuous mode, which has shift-and-reflect symmetry. Streamwise wavelengths of both modes are close to the spanwise wavelength. Swearingen and Blackwelder (1987) investigated experimentally the sinuous mode and found two regions with high streamwise oscillations, corresponding to high spanwise gradients of the streamwise velocity. The simulation results in figure 6.71 show a very similar correlation for wavy duct flow. Yu and Liu (1991) and Liu and Domaradzki (1993) found comparable results for simulated sinuous Görtler vortices.

Swearingen and Blackwelder (1987) measured velocity fluctuations at different spanwise locations, which show a phase jump of 180° in the fundamental across the inflow region and a strong first harmonic in the centre of the inflow region. These measurements show the same trends as the simulated profiles in figure 6.50, and confirm the shift-and-reflect symmetry. Swearingen and Blackwelder (1987) also measured spanwise profiles of the streamwise velocity and observed a spanwise oscillation of the low-speed inflow region, very much like the simulated profiles in figure 6.72.

Liu and Domaradzki simulated the transition to turbulence in Görtler flow. Their contour plots of all three velocity components in a (θ,z)-plane of the sinuous mode of wavy Görtler vortices (before the transition to turbulence) are very similar to the contour plots in figures 6.69a, 6.69c and 6.69e.

All the experimental and numerical work on wavy flows in the Dean and Görtler problem suggest that the wavy Dean vortices in a curved square duct, and twisting waves in a curved channel, and the sinuous mode of wavy Görtler vortices are all

different manifestations of the same phenomenon.

Andereck *et al.* (1983) reported twisted vortices in a Taylor-Couette system with co-rotating cylinders. Twisted Taylor vortices have a streamwise wavelength that is close to the spanwise wavelength. This is much shorter than the streamwise wavelength of the commonly observed wavy Taylor vortices. The pattern consists of a periodic rope-like structure, with flat inflow and outflow boundaries. Golubitsky and Stewart (1986) report that twisted Taylor vortices have reflect symmetry, and not shift-and-reflect symmetry, although that is not clear from the flow visualization (Andereck *et al.*, 1983). Twisted Taylor vortices therefore do not correspond to wavy curved duct flow.

Two-dimensional wakes

Little work has been done to reveal the structure of wavy vortex flows. For example, amplitude and phase distributions have never been measured before. However, those distributions are commonly used to describe oscillating flow phenomena in two-dimensional wakes. It turns out that the amplitude and phase distributions of wavy curved duct flow are very similar to those of sinuous oscillations in a wake.

Oscillations in wakes behind objects have been studied extensively, both experimentally and numerically. Two types of oscillations can develop in a wake: a varicose mode and a sinuous mode. The sinuous mode is more unstable and is observed most often. A wake can either develop a global mode, characterized by a single frequency, or be noise driven, leading to a broad band spectrum of frequencies. The existence of a global mode depends on the size of the absolutely unstable region in the wake, but in both cases the structure of the flow is identical.

The first detailed experimental investigation of oscillations in the wake behind

a flat plate was performed by Sato and Kuriki (1961), followed by many other experimental and numerical studies. Some studies focus on the structure of the oscillating flow, and the instability mechanism (Sato & Kuriki, 1961; Mattingly & Criminale, 1972), other studies focus more on mode interaction and the effect of forcing (Williams-Stuber & Gharib, 1990; Williams et al., 1992).

Amplitude and phase distributions of both streamwise and spanwise velocity fluctuations have been used by many researchers to characterize the flow (Sato & Kuriki, 1961; Sato, 1970; Mattingly & Criminale, 1972; Wygnanski et al., 1986; Gharib & Williams-Stuber, 1989; Marasli et al., 1989; Mansy & Williams, 1991; Marasli et al., 1991; Corke et al., 1992; Maekawa et al., 1992; Marasli et al., 1992; Williams et al., 1992). The amplitude and phase distributions of the sinuous mode are generally very similar to the distributions presented in section 6.5.1.

This similarity can be explained by looking at the shape of spanwise profiles of the streamwise velocity. In steady and wavy 4-cell curved duct flow, these profiles have a minimum near the centre, caused by the inflow of low-speed fluid from the outer wall. It was shown in section 6.5.3 that the qualitative features of the amplitude and phase distributions is described by a simple model, based on the spanwise oscillation of these V-shaped profiles. Spanwise profiles in a two-dimensional wake also have a V-shaped minimum, caused by the joining boundary layers behind the object. The sinuous mode of oscillations is characterized by a spanwise oscillation of the low-speed region, producing amplitude and phase distributions with the same qualitative features as those of wavy curved duct flow.

Von Kármán (1911; 1912) suggested that sinuous oscillations of a wake are the result of crosswise, staggered, and counter rotating vortices, now called a von Kármán vortex street. This vortex street is the result of a redistribution of the crosswise vorticity that is associated with the shear layers of the V-shaped

streamwise velocity profile. The crosswise vorticity layers first become wavy, and subsequently break up into separate crosswise vortices (Abernathy & Kronauer, 1962; Aref & Siggia, 1981). It was shown in figure 6.70 that the traveling wave state affects the radial vorticity distribution most strongly. The wavy radial vorticity field is similar to the crosswise vorticity in the early stage of sinuous oscillations in a wake (Abernathy & Kronauer, 1962). This wavy radial vorticity distribution is only present in the outer half of the curved duct, between $x = 0.2$ and $x = 0.5$.

Wygnanski et al. also simulated oscillations in a two-dimensional wake. The difference vorticity of the developing sinuous mode, before the formation of separate crosswise vortices (figure 30a of Wygnanski et al., 1986) is almost identical to the radial difference vorticity field in figure 6.70d.

In summary, a comparison was made between wavy curved duct flow and the early stage of developing sinuous oscillations in a two-dimensional wake; the velocity and vorticity fields at $x = 0.27$ in the curved duct are very similar to velocity and vorticity fields in a two-dimensional wake.

6.6   Instability Mechanism

No formal stability analysis of 4-cell flow in a curved square duct was performed in this study. However, stability analyses have been performed in other curved geometries, and also for two-dimensional wakes. These results will be used to propose an instability mechanism for the traveling waves in a curved square duct.

The instability mechanism for twisting waves in a curved channel was first studied by Finlay et al. (1988). They used an Orr-Sommerfeld analysis to calculate the stability of spanwise profiles of the streamwise velocity. Their results suggest that

twisting waves are the result of a shear instability. The inflection points of the spanwise profiles play an important role in this shear instability.

A similar analysis was used by Le Cunff and Bottaro (1993) to study the stability of both spanwise and radial velocity profiles. They also found the twisting waves to be the result of a shear instability of spanwise inflectional profiles. The sinuous mode is always more unstable than the varicose mode.

Swearingen and Blackwelder (1987) found a strong correlation between the regions of high velocity fluctuations and high spanwise shear for the sinuous mode of oscillating Görtler vortices. This would suggest that the sinuous mode is the result of unstable profiles in the spanwise direction. The FLOW3D simulation results in figure 6.71a-b show a similar correlation for wavy curved duct flow. The simple model, which was used in section 6.5.3 to explain the qualitative features of amplitude and phase distributions, forms a direct connection between high streamwise velocity fluctuations and high spanwise shear. Similar correlations between streamwise velocity fluctuations and spanwise inflectional profiles were found by Liu and Domaradzki (1993) and Matsson and Alfredsson (1993a).

The similarity between the velocity and vorticity fields of the traveling wave state and developing sinuous oscillations in a two-dimensional wake was discussed in section 6.5.4. The V-shaped streamwise velocity profile of a two-dimensional wake is also unstable to a shear instability. It is this shear instability that causes the redistribution of the crosswise vorticity that leads to a von Kármán vortex street.

The inflectional spanwise velocity profiles in 4-cell curved duct flow are very similar to those in curved channel flow, Görtler flow, and a two-dimensional wake. This similarity suggests that also in a curved square duct, the vortex oscillations are the result of a shear instability of spanwise inflectional profiles of the streamwise velocity. The proposed instability mechanism indicates that the 4-cell flow does

not directly lead to traveling waves. Instead, the 4-cell flow creates a streamwise velocity profile that is unstable to a secondary shear instability. It is this secondary instability that causes the transition to traveling waves.

6.7 Summary

Detailed experiments and numerical simulations of a traveling wave state in a curved duct of square cross section were reported. This new flow state has not been observed before. Flow visualization and LDA measurements were used in the experimental investigation. The commercial CFD package FLOW3D was used to simulate the fully developed traveling wave state.

The experiments suggest that the traveling waves are the result of a convective instability that destabilizes steady 4-cell flow. The waves were induced by inserting a pin along the horizontal centre line, $z = 0$, at $\theta = 5°$. The pin reduces the development length of the steady 4-cell state from which the traveling waves develop, and also creates the disturbances that destabilize steady 4-cell flow. Although the pin plays an important role in the development of the traveling waves, the traveling wave state is characteristic for curved duct flow. The wake behind the pin does not affect the traveling wave state.

The Dean vortices oscillate both in spanwise and in radial direction, while the large Ekman vortices remain almost steady. These oscillations develop from steady 4-cell flow, and the exact streamwise position where the oscillations start depends on the flow rate and the pin diameter. At a Dean number of 220 and a 25 gauge pin, a fully developed traveling wave state was reached at $\theta = 170°$.

The convective nature of the flow was demonstrated by the sideview flow visualization, which showed individual wave packets that are convected downstream

(figure 6.1). The state of a convectively unstable, or noise driven, system is determined by the selective amplification of flow disturbances. Because the random flow disturbances contain many different frequencies, the frequency spectrum of the velocity fluctuations has a broad maximum.

The flow was forced at a selected frequency by periodically compressing the hose that leads the water to the stilling chamber. A periodic disturbance is created by the pin as a result of the forcing. This disturbance is much larger than the random flow disturbances, causing the wave to lock in to the forcing frequency. The streamwise velocity fluctuations induced by the forcing are small compared to the velocity fluctuation that are the result of the traveling wave. At a Dean number of 220, the wave locks in to forcing frequencies between 4 and 9 Hz. Frequency spectra have sharp peaks at the forcing frequency and its harmonics. Between 2.5 and 4 hz, the flow locks in to the first harmonic of the forcing frequency.

Experimentally, the flow structure was determined by measuring amplitude and phase distributions at $x = 0.27$ and $-0.24 < z < 0.24$. Flow visualization and amplitude and phase distributions showed that the fully developed traveling wave state is shift-and-reflect symmetric; the flow field is invariant over a reflection in the centre plane, combined with a shift over half a fundamental wavelength. In the fully developed state, a shift in space corresponds to a shift in time.

The transient simulations in FLOW3D imposed periodic boundary conditions in the streamwise direction over one wavelength. Shift-and-reflect symmetry was imposed to stabilize the 4-cell flow that is unstable to asymmetric perturbations. Simulated arrow plots and streamwise vorticity plots in cross sections show qualitative agreement with the flow visualization. The simulations were also used to calculate velocity and vorticity contours in (r,z) and (θ,z)-planes.

The spanwise profiles of the streamwise velocity between $x = 0.2$ and $x = 0.5$

are strongly inflectional. This is a result of the inflow region, which takes low-speed fluid away from the outer wall. During the traveling wave state, the V-shaped centre region oscillates in spanwise direction, while its shape remains almost unchanged. The streamwise velocity fluctuations that are induced by this spanwise oscillation are much larger than those induced by radial oscillations. A simple model that is based on the assumption that spanwise profiles does not change shape while oscillating in spanwise direction, explains all qualitative features of the amplitude and phase distributions.

The structure of the traveling waves in a curved square duct is very similar to that of twisting vortices in a curved channel and sinuous oscillations of Görtler vortices. Finlay *et al.* (1988) performed a stability analysis of spanwise velocity profiles and suggested that twisting vortices are the result of a shear instability of spanwise inflectional velocity profiles. This was confirmed by Le Cunff and Bottaro (1993). The similarity between twisting vortices and wavy curved duct flow suggests that the traveling waves in a curved duct are also caused by a spanwise shear instability.

The velocity fluctuations at $x = 0.27$ are very similar to fluctuations in a sinuous two-dimensional wake. This is because the oscillations in a wake are also dominated by the spanwise oscillation of a V-shaped streamwise velocity profile. This produces amplitude and phase distributions with the same characteristics as those which were measured in the curved duct. The oscillations in a two-dimensional wake are the result of a spanwise shear instability, which supports the suggested instability mechanism for wavy curved duct flow.

Chapter 7

Conclusions and

Recommendations

Two new flow states in a curved duct of square cross section with a curvature ratio of 15.1 were investigated both experimentally and numerically: a 6-cell flow state, that was observed in steady developing flow at Dean numbers between 350 and 550; and a traveling wave state, that was induced by a pin at Dean numbers between 170 and 260. For both these flow states, the experiments are in very good agreement with the numerical simulations. This shows that 6-cell flow and traveling waves are characteristic for curved duct flow, and not artifacts of the experimental apparatus, or the numerical method.

The 6-cell flow state, consisting of two large Ekman vortices and two pairs of small Dean vortices, develops from the initial 2-cell flow at around 80° from the inlet of the curved section. The two Dean vortex pairs are the result of the same centrifugal instability that induces a single pair of Dean vortices at Dean numbers between 130 and 300. The 4-cell and 6-cell flow states are therefore different manifestations of the primary instability of this system. Based on the similarity

253

with the Görtler problem, it is suggested that the transition to 6-cell flow is the result of a decreasing spanwise wavelength of the Dean vortices with increasing flow rate.

The 8-cell flow state was not predicted by bifurcation studies of two-dimensional fully developed flows (Winters, 1987; Daskopoulos & Lenhoff, 1989). However, it seems likely that the 6-cell state corresponds to a fully developed solution of curved square duct flow. This 6-cell flow is unstable to arbitrary perturbations and therefore does not reach a fully developed state; the 6-cell flow breaks down spatially into a 2-cell flow state.

The traveling wave state, that was induced by inserting a pin along the symmetry line of the duct at $\theta = 5°$, is the result of a secondary instability of steady 4-cell flow. It was suggested th.. this secondary instability is a shear instability of spanwise inflectional profiles of the streamwise velocities. These inflectional profiles are created by the inflow region between the two Dean vortices, that transports fluid with low streamwise velocity away from the outer wall.

The existence of a fully developed traveling wave state is confirmed by the three-dimensional, time dependent simulations in FLOW3D with periodic boundary conditions in the streamwise direction. This traveling wave state is consistent with Winters' observation that no stable two-dimensional solutions exist above a Dean number of 131. In order to predict the onset of these traveling waves, a stability analysis of two-dimensional solutions to three-dimensional and time-dependent disturbances would have to be performed.

Numerical simulations based on the parabolized three-dimensional, time independent Navier-Stokes equations predict the development of spatial oscillations at Dean numbers between 131 and 230. During these oscillations, a 2-cell state develops into a 4-cell state, that subsequently breaks down asymmetrically into

another 2-cell state. FLOW3D simulations of two-dimensional, time dependent flows predict temporal oscillations that show a very similar pattern. These oscillations are very different from the oscillating Dean vortices that characterize the traveling wave state observed in the present set of experiments.

Although the spatial oscillations are a solution of the Navier-Stokes equations, they may not be physically realizable. An apparatus with a longer streamwise length is needed to verify the existence of spatially oscillating steady flows. Because of spatial constraints, this would either have to be a helical duct or a spiral shaped duct. In a helical duct, the reflect symmetry is broken, which could have a significant effect on the growth of asymmetric modes. Simulations by Liu and Masliyah (1993) of flow in helical pipes show that a small pitch does not change the development of the 2-cell flow significantly. However, they studied only the effect on the unconditionally stable 2-cell state, and not the 4-cell state. A spiral shaped duct does not break the reflect symmetry, but in this case the curvature ratio changes gradually. No simulations of a spiral duct have been performed, and the effect of the changing curvature ratio is not known.

In the existing apparatus, the traveling wave state could only be observed when a pin was inserted near the inlet of the curved section. An apparatus with longer streamwise length could also be used to determine whether the traveling wave state develops spontaneously (not induced by the pin) further downstream.

The experimental setup would be improved by a second LDA probe, allowing for simultaneous velocity measurements at two positions in the flow. By measuring the velocity at different streamwise positions in the fully developed region of the duct, but otherwise identical positions in the cross section, the wave speed can be determined from the phase difference between the two signals. In the present study, the wave speed was estimated from the flow visualization, but this does not give very

accurate results. Simultaneous velocity measurements can also be used to measure the growth rate of the oscillations in the region of developing flow. Because the flow is very sensitive to external disturbances, the repositioning of the apparatus, that is presently needed to measure the spatial growth ra: :s, can strongly affect the spatial development.

A final area of future study is based on experimental observations and numerical simulations of a varicose mode of oscillations in curved channel flow, Görtler flow, and a two-dimensional wake. In all these systems, the varicose mode is difficult to observe experimentally, because of its lower growth rate than the sinuous mode. However, since the two modes have different symmetry properties (the varicose mode has reflect symmetry, while the sinuous mode has shift-and-reflect symmetry), the possible existence of varicose oscillations in curved duct flow can be investigated numerically, by imposing reflect symmetry in the simulations.

References

ABERNATHY, F.H., & KRONAUER, R.E. 1962. The formation of vortex streets. *J. Fluid Mech.*, **13**, 1–20.

ADLER, M. 1934. Strömung in gekrümmten Rohren. *Z. Angew. Math. Mech.*, **14**, 257–275.

AGRAWAL, Y., TALBOT, L., & GONG, K. 1978. Laser anemometer study of flow development in curved circular pipes. *J. Fluid Mech.*, **85**, 497–518.

AIHARA, Y., & KOYAMA, H. 1981. Secondary instability of Görtler vortices: Formation of periodic three-dimensional coherent structure. *Trans. Japan Soc. Aeronaut. Space Sci.*, **24**(64), 78–94.

ANDERECK, C.D., DICKMAN, R., & SWINNEY, H.L. 1983. New flows in a circular Couette system with co-rotating cylinders. *Phys. Fluids*, **26**(6), 1395–1401.

AREF, H., & SIGGIA, E.D. 1981. Evolution and breakdown of a vortex street in two dimensions. *J. Fluid Mech.*, **109**, 435–463.

ARNAL, M.P., GOERING, D.J., & HUMPHREY, J.A.C. 1992. Unsteady laminar flow developing in a curved duct. *Int. J. Heat Fluid Flow*, **13**(4), 347–357.

AUSTIN, L.R., & SEADER, J.D. 1974. Entry region for steady viscous flow in coiled circular pipes. *AIChE J.*, **20**, 820–822.

BARA, B. 1991. *Experimental Investigation of Developing and Fully Developed Flow in a Curved Duct of Square Cross Section.* Ph.D. thesis, Department of Mechanical Engineering, University of Alberta.

BARA, B., NANDAKUMAR, K., & MASLIYAH, J.H. 1992. An experimental and numerical study of the Dean problem: Flow development towards two-dimensional multiple solutions. *J. Fluid Mech.*, **244**, 339–376.

BARUA, S.N. 1963. On secondary flow in stationary curved pipes. *Quart. J. Mech. Appl. Math.*, **16**, 61–77.

BELAIDI, A., JOHNSON, M.W., & HUMPHREY, J.A.C. 1992. Flow instability in a curved duct of rectangular cross section. *Trans. ASME, J. Fluids Eng.*, **114**, 585–592.

BELFORT, G., BREWSTER, M.E., & CHUNG, K.-Y. 1993. Curved channel membrane filtration. U.S. Patent No. 5,204,002.

BENJAMIN, T.B. 1978. Bifurcation phenomena in steady flows of a viscous fluid, I. Theory. *Proc. R. Soc. Lond A*, **359**, 1–26.

BERGER, S.A., TALBOT, L., & YAO, L.-S. 1983. Flow in Curved Pipes. *Annu. Rev. Fluid Mech.*, **15**, 461–512.

BIPPES, H. 1972. Experimentelle Untersuchung des laminar-turbulenten Umschlags an einer parallel angeströmten konkaven Wand. *Sitzungsber. Heidel. Akad. Wiss., Math.-naturwiss. Kl.*, **3**, 103–180. also NASA Techn. Mem. 75243 (1978).

BIPPES, H., & GÖRTLER, H. 1972. Dreidimensionale Störungen in der Grenzschicht an einer konkaven Wand. *Acta Mech.*, **14**, 251–267.

BLACKWELDER, R.F. 1983. Analogies between transitional and turbulent boundary layers. *Phys. Fluids*, **26**(10), 2807–2815.

BLAND, S.B., & FINLAY, W.H. 1991. Transitions toward turbulence in a curved channel. *Phys. Fluids A*, **3**(1), 106–114.

BOTTARO, A. 1993. On longitudinal vortices in curved channel flow. *J. Fluid Mech.*, **251**, 627–660.

BOTTARO, A., MATSSON, O.J.E., & ALFREDSSON, P.H. 1991. Numerical and experimental results for developing curved channel flow. *Phys. Fluids A*, **3**(6), 1473–1476.

BREWSTER, D.B., GROSBERG, P., & NISSAN, A.H. 1959. The stability of viscous flow between horizontal concentric cylinders. *Proc. R. Soc. Lond. A*, **251**, 76–91.

CAPRIHAN, A., & FUKUSHIMA, E. 1990. Flow measurement by NMR. *Phys. Rep.*, **198**(4), 195–235.

CHENG, K.C., & AKIYAMA, M. 1970. Laminar forced convection heat transfer in curved rectangular channels. *Int. J. Heat Mass Transfer*, **13**, 471–490.

CHENG, K.C., LIN, R.-C., & OU, J.-W. 1975. Graetz problem in curved square channels. *Trans. ASME, J. Heat Transfer*, **97**, 244–248.

CHENG, K.C., LIN, R.-C., & OU, J.-W. 1976. Fully developed flow in curved rectangular channels. *Trans. ASME, J. Fluids Eng.*, **98**, 41–48.

CHOMAZ, J.M. 1992. Absolute and convective instabilities in nonlinear systems. *Phys. Rev. Lett.*, **69**(13), 1931–1934.

CHOMAZ, J.M., HUERRE, P., & REDEKOPP, L.G. 1988. Bifurcations to local and global modes in spatially developing flows. *Phys. Rev. Lett.*, **60**(1), 25–28.

CHUNG, K.-Y., BELFORT, G., EDELSTEIN, W.A., & LI, X. 1993. Dean vortices in curved tube flow: 5. 3-D MRI and numerical analysis of the velocity field. *AIChE J.*, **39**(10), 1592–1602.

COLLINS, W.M., & DENNIS, S.C.R. 1975. The steady motion of a viscous fluid in a curved tube. *Quart. J. Mech. Appl. Math.*, **28**, 133–156.

CORKE, T.C., KRULL, J.D., & GHASSEMI, M. 1992. Three-dimensional-mode resonance in far wakes. *J. Fluid Mech.*, **239**, 99–132.

CUMING, H.G. 1952. The secondary flow in curved pipes. *Aeronaut. Res. Counc. Rep. Mem. No. 2880.*

CUNFF, C. LE, & ZEBIB, A. 1993. Linear stability of shear profiles and relation to the secondary instability of the Dean flow. *Phys. Fluids A*, **5**(9), 2161–2171.

DASKOPOULOS, P., & LENHOFF, A.M. 1989. Flow in curved ducts: bifurcation structure for stationary ducts. *J. Fluid Mech.*, **203**, 125–148.

DEAN, W.R. 1927. Note on the motion of fluid in a curved pipe. *Phil. Mag. Ser.* 7, **4**(20), 208–223.

DEAN, W.R. 1928a. Fluid motion in a curved channel. *Proc. R. Soc. Lond. A*, **121**, 402–420.

DEAN, W.R. 1928b. The stream-line motion of fluid in a curved pipe. *Phil. Mag. Ser.* 7, **5**(30), 673–695.

DEISSLER, R.J. 1985. Noise-sustained structure, intermittency, and the Ginzburg-Landau equation. *J. Stat. Phys.*, **40**(3/4), 371–395.

DEISSLER, R.J. 1987. Spatially growing waves, intermittency, and convective chaos in an open-flow system. *Physica*, **25D**, 233–260.

DEISSLER, R.J. 1989. External noise and the origin and dynamics of structure in convectively unstable systems. *J. Stat. Phys.*, **54**(5/6), 1459–1488.

DENNIS, S.C.R., & RILEY, N. 1991. On the fully developed flow in a curved pipe at large Dean number. *Proc. R. Soc. Lond. A*, **434**, 473–478.

DENNIS, S.R.C., & NG, M. 1982. Dual solutions for steady laminar flow through a curved tube. *Quart. J. Mech. Appl. Math.*, **35**, 305–324.

DRAIN, L.E. 1980. *The Laser Doppler Technique*. New York: J. Wiley.

ECKMANN, J.-P. 1981. Roads to turbulence in dissipative dynamical systems. *Rev. Modern Phys.*, **53**(4), 643–654.

EUSTICE, J. 1910. Flow of water in curved pipes. *Proc. R. Soc. Lond. A*, **84**, 107–118.

EUSTICE, J. 1911. Experiments on stream-line motion in curved ;·:··. *Proc. R. Soc. Lond.* .1, **85**, 119–131.

EUSTICE, J. 1925. Flow of fluids in curved passages. *Engineering*, No ː.ː, 604–605.

FINLAY, W.H. 1989. Perturbation expansion and weakly nonlinear analysis for two-dimensional vortices in curved or rotating channels. *Phys. Fluids A*, 1(5), 854–860.

FINLAY, W.H., & NANDAKUMAR, K. 1990. Onset of two-dimensional cellular flow in finite curved channels of large aspect ratio. *Phys. Fluids A*, 2(7), 1163–1174.

FINLAY, W.H., KELLER, J.B., & FERZIGER, J.H. 1987. Instability and transition in curved channel flow. *Rep. TF-30.* Dept. of Mech. Eng., Stanford University, CA.

FINLAY, W.H., KELLER, J.B., & FERZIGER, J.H. 1988. Instability and transition in curved channel flow. *J. Fluid Mech.*, 194, 417–456.

FINLAY, W.H., GUO, Y., & OLSEN, D. 1993. Inferring secondary flows from smoke or dye flow visualization: Two case studies. *Phys. Fluids A*, 5(11), 2689–2701.

FLORYAN, J.M. 1991. On the Görtler instability of boundary layers. *Prog. Aerosp. Sci.*, 28, 235–271.

FLORYAN, J.M., & SARIC, W.S. 1982. Stability of Görtler vortices in bo⸱⸱⸱⸱ry layers. *AIAA Journal*, 20(3), 316–324.

FLORYAN, J.M., & SARIC, W.S. 1984. Wavelength selection and growth of Görtler vortices. *AIAA Journal*, 22(11), 1529–1538.

GHARIB, M., & WILLIAMS-STUBER, K. 1989. Experiments on the forces wake of an airfoil. *J. Fluid Mech.*, 208, 225–255.

GHIA, K.N., & SORCHEY, J.S. 1977. Laminar incompressible viscous flow in curved ducts of regular cross-sections. *Trans. ASME, J. Fluids Eng.*, 99, 640–648.

GOLDSTEIN, R.J., & KREID, D.K. 1967. Measurement of laminar flow development in a square duct using a laser-Doppler flowmeter. *Trans. ASME, J. Appl. Mech.*, 34, 813–818.

GOLLUB, J.P., & BENSON, S.V. 1980. Many routes to turbulent convection. *J. Fluid Mech.*, 100, 449–470.

GOLUBITSKY, M., & STEWART, I. 1986. Symmetry and stability in Taylor-Couette flow. *SIAM J. Math. Anal.*, **17**(2), 249–288.

GÖRTLER, H. 1940. Über eine dreidimensionale Instabilität laminarer Grenzschichten an konkaven Wänden. *Nachr. Ges. Wiss. Göttingen, Math-. Phys. Kl., Fachgruppe I*, Neue Folge **2**, 1–26. also NASA Techn. Mem. 1375 (1954).

GÖRTLER, H. 1941. Instabilität laminarer Grenzschichten an konkaven Wänder gegenüber gewissen dreidimensionalen Störungen. *Z. Angew. Math. Mech.*, **21**, 250–252. also NASA Techn. Mem. 1375 (1954).

GUO, Y., & FINLAY, W.H. 1991. Splitting, merging and wavelength selection of vortices in curved and/or rotating channel flow due to Eckhaus instability. *J. Fluid Mech.*, **228**, 661–691.

GUO, Y., & FINLAY, W.H. 1994. Wavenumber selection and irregularity of spatially developing nonlinear Dean & Görtler vortices. *J. Fluid Mech.*, **264**, 1–40.

HALL, P. 1983. The linear development of Görtler vortices in growing boundary layers. *J. Fluid Mech.*, **130**, 41–58.

HAMAKIOTES, C.C., & BERGER, S.A. 1990. Periodic flow through curved tubes: the effect of the frequency parameter. *J. Fluid Mech.*, **210**, 353–370.

HÄMMERLIN, G. 1958. Die Stabilität der Strömung in einem gekrümmten Kanal. *Arch. Rational Mech. Anal.*, **1**, 212–224.

HANSON, S. 1973. Lroadening of the measured frequency spectrum in a differential laser anemometer due to interference plane gradients. *J. Phys. D: Appl. Phys.*, **6**, 164–171.

HARNETT, D.L. 1982. *Statistical Methods*. 3rd edn. Reading, MA: Addison-Wesley Pub. Co.

HILLE, P., VEHRENKAMP, R., & SCHULZ-DUBOIS, E.O. 1985. The development and structure of primary and secondary flow in a curved square duct. *J. Fluid Mech.*, **151**, 219–241.

HO, C.-M., & HUANG, L.-S. 1982. Subharmonics and vortex merging in mixing layers. *J. Fluid Mech.*, **119**, 443–473.

HUERRE, P., & MONKEWITZ, P.A. 1990. Local and global instabilities in spatially developing flows. *Annu. Rev. Fluid Mech.*, **22**, 473–537.

HUMPHREY, J.A.C. 1978. Numerical calculation of developing laminar flow in pipes of arbitrary curvature radius. *Can. J. Chem. Eng.*, 5⁺ .   -

HUMPHREY, J.A.C, TAYLOR, A.M.K., & WHITELAW, J.H. 1977 Laminar flow in a square duct of strong curvature. *J. Fluid Mech.*, **83**, 509–527.

HUMPHREY, J.A.C., IACOVIDES, H., & LAUNDER, B.E. 1985. Some numerical experiments on developing laminar flow in circular-sectioned bends. *J. Fluid Mech.*, **154**, 357–375.

ITO, A. 1980. The generation and breakdown of longitudinal vortices along a concave wall. *J. Japan Soc. Aeronaut. Space Sci.*, **28**(318), 327–333.

ITO, A. 1985. Breakdown structure of longitudinal vortices along a concave wall. *J. Japan Soc. Aeror . Space Sci.*, **33**(374), 166–173.

ITŌ, H. 1951. The   laminar flows through curved pipes of elliptic and rectangular cross-sec.   *Rep. Inst. High Speed Mech., Tōhoku Univ., Sendai, Japan*, **1**, 1–16.

ITŌ, H. 1959. Friction factors for turbulent flow in curved pipes. *Trans. ASME, J. Basic Eng.*, **81**, 123–134.

ITŌ, H. 1987. Flow in curved pipes. *JSME Int. J. II*, **30**(262), 543–552.

KAJISHIMA, T., MIYAKE, Y., & INABA, T. 1989. Numerical simulation of laminar flow in curved ducts of rectangular cross-section. *JSME Int. J. II*, **32**(4), 516–522.

KAO, H.C. 1992. Some aspects of bifurcation structure of laminar flow in curved ducts. *J. Fluid Mech.*, **243**, 519–539.

KÁRMÁN, TH. V. 1911. Über den Mechanismus des Widerstandes den ein bewegter Körper in einer Flüssigkeit erfährt. *Nachr. Ges. Wiss. Göttingen, Math-. Phys. Kl.*, 509–517.

KÁRMÁN, TH. V., & RUBACH, H. 1912. Über den Mechanismus des Flüssigkeits und Luftwiderstandes. *Phys. Z.*, 13(2), 49–59.

KARNIADAKIS, G.E., & TRIANTAFYLLOU, G.S. 1989. Frequency selection and asymptotic states in laminar wakes. *J. Fluid Mech.*, 199, 441–469.

KELLEHER, M.D., FLENTIE, D.L., & McKEE, R.J. 1980. An experimental study of the secondary flow in a curved rectangular channel. *Trans. ASME, J. Fluids Eng.*, 102, 92–96.

KLUWICK, A., & WOHLFAHRT, H. 1984. Entry flow in weakly curved ducts. *Ing. Archiv*, 54, 107–120.

KLUWICK, A., & WOHLFAHRT, H. 1986. Hot-wire-anemometer study of the entry flow in a curved duct. *J. Fluid Mech.*, 165, 335–353.

LEE, K., & LIU, J.T.C. 1992. On the growth of mushroomlike structures in nonlinear spatially developing Goertler vortex flow. *Phys. Fluids A*, 4(1), 95–103.

LIGRANI, P.M., & NIVER, R.D. 1988. Flow visualization of Dean vortices in a curved channel with 40 to 1 aspect ratio. *Phys. Fluids*, 31(12), 3605–3617.

LIGRANI, P.M., FINLAY, W.H., FIELDS, W.A., FUQUA, S.J., & SUBRAMANIAN, C.S. 1992. Features of wavy vortices in a curved channel from experimental and numerical studies. *Phys. Fluids A*, 4(4), 695–709.

LIU, S., & MASLIYAH, J.H. 1993. Axially invariant laminar flow in helical pipes with a finite pitch. *J. Fluid Mech.*, 251, 315–353.

LIU, S., AFACAN, A., NASR-EL-DIN, H.A., & MASLIYAH, J.H. 1994. An experimental study of pressure drop in helical pipes. *Proc. R. Soc. Lond. A*, 444, 307–316.

LIU, W., & DOMARADZKI, J.A. 1993. Direct numerical simulation of transition to turbulence in Görtler flow. *J. Fluid Mech.*, **246**, 267–299.

MAEKAWA, H., MANSOUR, N.N., & BUELL, J.C. 1992. Instability mode interactions in a spatially developing plane wake. *J. Fluid Mech.*, **235**, 223–254.

MANLAPAZ, R.L., & CHURCHILL, S.W. 1980. Fully developed laminar flow in a helically coiled tube of finite pitch. *Chem. Eng. Commun.*, **7**, 57–78.

MANLAPAZ, R.L., & CHURCHILL, S.W. 1981. Fully developed laminar convection from a helical coil. *Chem. Eng. Commun.*, **9**, 185–200.

MANSY, H., & WILLIAMS, D.R. 1991. Symmetry of interacting modes in a cylinder wake. *Phys. Fluids A*, **3**(9), 2047–2049.

MARASLI, B., CHAMPAGNE, F.H., & WYGNANSKI, I.J. 1989. Modal decomposition of velocity signals in a plane, turbulent wake. *J. Fluid Mech.*, **198**, 255–273.

MARASLI, B., CHAMPAGNE, F.H., & WYGNANSKI, I.J. 1991. On linear evolution of unstable disturbances in a plane turbulent wake. *Phys. Fluids A*, **3**(4), 665–674.

MARASLI, B., CHAMPAGNE, F.H., & WYGNANSKI, I. 1992. Effect of traveling waves on the growth of a plane turbulent wake. *J. Fluid Mech.*, **235**, 511–528.

MASLIYAH, J.H. 1980. On laminar flow in curved semicircular ducts. *J. Fluid Mech.*, **99**, 469–479.

MATSSON, O.J.E., & ALFREDSSON, P.H. 1990. Curvature- and rotation-induced instabilities in channel flow. *J. Fluid Mech.*, **210**, 537–563.

MATSSON, O.J.E., & ALFREDSSON, P.H. 1992. Experiments on instabilities in curved channel flow. *Phys. Fluids A*, **4**(8), 1666–1676.

MATSSON, O.J.E., & ALFREDSSON, P.H. 1993a. Secondary instability and breakdown to turbulence in curved channel flow. *Appl. Sci. Res.*, **51**, 9–14.

MATSSON, O.J.E., & ALFREDSSON, P.H. 1993b. The effect of spanwise system rotation on Dean vortices. Submitted to *J. Fluid Mech.* Also in O.J.E. Matsson, *Channel Flow Instabilities Induced by Curvature and Rotation.* Ph.D. thesis, Department of Mechanics, Royal Institute of Technology, Stockholm, Sweden (1993).

MATTINGLY, G.E., & CRIMINALE, W.O. 1972. The stability of an incompressible two-dimensional wake. *J. Fluid Mech.*, **51**, 233–272.

MAURER, J., & LIBCHABER, A. 1980. Effect of the Prandtl number on the onset of turbulence in liquid ^{4}He. *J. Phys. (Paris) Lett.*, **41**, L515–L518.

MIYAKE, Y., KAJISHIMA, T., & INABA, T. 1988. Numerical experiment of laminar flow in curved ducts of rectangular cross-section. *Pages 1192–1199 of:* SHAH, R.K., GANIĆ, E.N., & YANG, K.T. (eds), *Experimental Heat Transfer, Fluid Mechanics, and Thermodynamics: Proceedings of the First World Conference on Experimental Heat Transfer, Fluid Mechanics, and Thermodynamics.* Sept. 4-9, Dubrovnik, Yugoslavia.

MONKEWITZ, P.A. 1990. The role of absolute and convective instability in predicting the behavior of fluid systems. *Eur. J. Mech., B/Fluids*, **9**(5), 395–413.

MORI, Y., & NAKAYAMA, W. 1965. Study on forced convective heat transfer in curved pipes. Part 1. *Int. J. Heat Mass Transfer*, **8**, 67–82.

MORKOVIN, M.V. 1988. *Recent insights into instability and transition to turbulence in open-flow systems.* NASA CR-181693.

MULLIN, T. 1991. Finite-dimensional dynamics in Taylor-Couette flow. *IMA J. Appl. Math.*, **46**, 109–119.

NANDAKUMAR, K., & MASLIYAH, J.H. 1982. Bifurcation in steady laminar flow through curved tubes. *J. Fluid Mech.*, **119**, 475–490.

NANDAKUMAR, K., & MASLIYAH, J.H. 1986. Swirling flow and heat transfer in coiled and twisted pipes. *Pages 49–112 of:* MUJUMDAR, A.S., & MASHELKAR, R.A. (eds), *Advances in Transport Processes.* New Delhi: Wiley Eastern.

OERTEL, H. 1990. Wakes behind blunt bodies. *Annu. Rev. Fluid Mech.*, **22**, 539–564.

OHBA, K., TSUDA, N., & TAKAGI, K. 1986. A velocity fluctuation in developing laminar flow through a moderately curved U-bend of square cross-section. *Techn. Rep. Kansai Univ.*, no. **27**, 33–42.

OLSON, D.E., & SNYDER, B. 1985. The upstream scale of flow development in curved circular pipes. *J. Fluid Mech.*, **150**, 139–158.

PARK, D., & HUERRE, P. 1988. On the convective nature of the Görtler instability. *Bull. Am. Phys. Soc.*, **33**(11), 2252.

PATANKAR, S.V. 1980. *Numerical Heat Transfer and Fluid Flow*. Washington, DC: Hemisphere.

PATANKAR, S.V., PRATAP, V.S., & SPALDING, D.B. 1974. Prediction of laminar flow and heat transfer in helically coiled pipes. *J. Fluid Mech.*, **62**, 539–551.

PEERHOSSAINI, H. 1993. private communication.

PEERHOSSAINI, H., & WESFREID, J.E. 1988. On the inner structure of streamwise Görtler rolls. *Int. J. Heat Fluid Flow*, **9**(1), 12–18.

PETITJEANS, P. 1992. *Etude expérimentale des instabilités de couches limites sur des parois concaves: Instabilité de Görtler*. Ph.D. thesis, l'Université Paris VI.

PETITJEANS, P., WESFREID, J.E., DEPLANO, V., & VLAD, G. 1993. *Effect of curvature on the velocity profile and boundary layer in flow through a curved channel: Experimental, analytical and numerical study*. (in preparation).

PFISTER, G., BUZUG, TH., & ENGE, N. 1992. Characterization of experimental time series from Taylor-Couette flow. *Physica D*, **58**, 441–454.

POULIQUEN, O., CHOMAZ, J.M., HUERRE, P., & TABELING, P. 1992. Wave-number selection and phase solitons in spatially forced temporal mixing layers. *Phys. Rev. Lett.*, **68**(17), 2596–2599.

RAMSHANKAR, R., & SREENIVASAN, K.R. 1988. A paradox concerning the extended Stokes series solution for the pressure drop in coiled pipes. *Phys. Fluids*, **31**(6), 1339–1347.

RAYLEIGH, LORD. 1916. On the dynamics of revolving fluids. *Proc. R. Soc. Lond. A*, **93**, 148–154. also *Scientific Papers*, **6**, 447–453, Dover Publications (1964).

REID, W.H. 1958. On the stability of viscous flow in a curved channel. *Proc. R. Soc. Lond. A*, **244**, 186–198.

SANKAR, S.R., NANDAKUMAR, K., & MASLIYAH, J. H. 1988. Oscillatory flows in coiled square ducts. *Phys. Fluids*, **31**(6), 1348–1359.

SATO, H. 1970. An experimental study of non-linear interaction of velocity fluctuations in the transition region of a two-dimensional wake. *J. Fluid Mech.*, **44**, 741–765.

SATO, H., & KURIKI, K. 1961. The mechanism of transition in the wake of a thin flat plate placed parallel to a uniform flow. *J. Fluid Mech.*, **11**, 321–352.

SCHATZ, M.F., & SWINNEY, H.L. 1992. Secondary instability in plane channel flow with spatially periodic perturbations. *Phys. Rev. Lett.*, **69**(3), 434–437.

SCHATZ, M.F., TAGG, R.P., SWINNEY, H.L., FISCHER, P.F., & PATERA, A.T. 1991. Supercritical transition in plane channel flow with spatially periodic perturbations. *Phys. Rev. Lett.*, **66**(12), 1579–1582.

SCHENCK, H. 1979. *Theories of Engineering Experimentation.* 3rd edn. Washington DC: Hemisphere.

SCHLICHTING, H. 1979. *Boundary-Layer Theory.* 7th edn. New York: McGraw-Hill.

SHAH, R.K., & LONDON, A.L. 1978. *Laminar Flow Forced Convection in Ducts.* Advances in Heat Transfer. New York: Academic Press.

SHANTINI, W., & NANDAKUMAR, K. 1986. Bifurcation phenomena of generalized newtonian fluids in curved rectangular ducts. *J. Non-Newtonian Fluid Mech.*, **22**, 35–60.

SINGH, M.P. 1974. Entry flow in a curved pipe. *J. Fluid Mech.*, **65**, 517–539.

SMITH, F.T. 1976. Fluid flow into a curved pipe. *Proc. R. Soc. Lond. A*, **351**, 71–87.

SNYDER, B., & LOVELY, C. 1990. A computaional study of developing 2-D laminar flow in curved channels. *Phys. Fluids A*, **2**(10), 1808–1816.

SOH, W.Y. 1988. Developing fluid flow in a curved duct of square cross-section and its fully developed dual solutions. *J. Fluid Mech.*, **188**, 337–361.

SOH, W.Y., & BERGER, S.A. 1984. Laminar entrance flow in a curved pipe. *J. Fluid Mech.*, **148**, 109–135.

SPARROW, E.M. 1964. On the onset of flow instability in a curved channel of arbitrary height. *Z. Angew. Math. Phys.*, **15**, 638–642.

SREENIVASAN, K.R., & STRYKOWSKI, P.J. 1983. Stabilization effects in flow through helically coiled pipes. *Exp. Fluids*, **1**, 31–36.

STEWART, I., & GOLUBITSKY, M. 1993. *Fearful Symmetry: Is God a Geometer?* Penguin Books.

STEWARTSON, K., & SIMPSON, C.J. 1982. On a singularity initiating a boundary-layer collision. *Quart. J. Mech. Appl. Math.*, **35**, 1–16.

STEWARTSON, K., CEBECI, T., & CHANG, K.C. 1980. A boundary-layer collision in a curved duct. *Quart. J. Mech. Appl. Math.*, **33**, 59–75.

SUGIYAMA, S., HAYASHI, T., & YAMAZAKI, K. 1983. Flow characteristics in the curved rectangular channels. *Bull. JSME*, **26**, 964–969.

SUGIYAMA, S., AOI, T., YAMAMOTO, M., NARISAWA, N., & MIYAKE, Y. 1988. Measurements on developing laminar flow in a curved rectangular duct by means of LDV. *Pages 1185–1191 of:* SHAH, R.K., GANIĆ, E.N., & YANG, K.T. (eds), *Experimental Heat Transfer, Fluid Mechanics, and Thermodynamics: Proceedings of the First World Conference on Experimental Heat Transfer, Fluid Mechanics, and Thermodynamics.* Sept. 4-9, Dubrovnik, Yugoslavia.

SWEARINGEN, J.D., & BLACKWELDER, R.F. 1987. The growth and breakdown of streamwise vortices in the presence of a wall. *J. Fl· ! Mech.*, **182**, 255–290.

TALBOT, L., & WONG, S.J. 1982. A note on boundary-l: r collision in a curved pipe. *J. Fluid Mech.*, **122**, 505–510.

TAYLOR, A.M.K.P., WHITELAW, J.H.. & YIANNESKiS, M. 1982. Curved ducts with strong secondary motion: velocity measurements r leveloping laminar and turbulent flow. *Trans. ASME, .l. Fluids Eng.*, **104**   )–359.

TAYLOR, G.I. 1929. The criterion for turbulence in curveu pipes *Proc. R. Soc. Lond. A*, **124**, 243–249.

THANGAM, S , & HUR, N. 1990. Laminar secondary flows in curved rectangular ducts. *J. Fluid Mech.*, **217**, 421–440.

TSUDA, N., & OHBA, K. 1984. Laser Doppler measurement of developing laminar flow in a moderately curved U-bend of square cross-section. *Pages 1–15 of: Laser Doppler Velocimetry and Hot Wire/Film Anemometry, Proceedings of the Second Osaka Symposium on Flow Measuring-Techniques.* July 13, Osaka, Japan.

VAN DOORMAL, J.P., & RAITHBY, G.D. 1984. Enhancements of the SIMPLE method for predicting incompressible fluid flows. *Numer. Heat Transfer*, **7**, 147–163.

VAN DYKE, M. 1978. Extended Stokes series: laminar flow through a loosely coiled pipe. *J. Fluid Mech.*, **86**, 129–145.

WALOWIT, J., TSAO, S., & DIPRIMA, R. 1964. Stability of flow between arbitrarily spaced concentric cylindrical surfaces including the effect of a radial temperature gradient. *Trans. ASME, J. Appl. Mech.*, **31**, 585–593.

WEBSTER, D.R., & HUMPHREY, J.A.C. 1993. Experimental observations of flow instability in a helical coil. *Trans. ASME, J. Fluids Eng.*, **115**, 436–443.

WILLIAMS, D.R., MANSY, H., & AMATO, C. 1992. The response and symmetry properties of a cylinder wake subjected to localized surface excitation. *J. Fluid Mech.*, **234**, 71–96.

WILLIAMS, G.S., HUBBELL, C.W., & FINKELL, G.H. 1902. Experiments at Detroit, Michigan on the effect of curvature on the flow of water in pipes. *Trans. ASCE*, **47**, 1–196.

WILLIAMS-STUBER, K., & GHARIB, M. 1990. Transition from order to chaos in the wake of an airfoil. *J. Fluid Mech.*, **213**, 29–57.

WINTERS, K.H. 1987. A bifurcation study of laminar flow in a curved tube of rectangular cross-section. *J. Fluid Mech.*, **180**, 343–369.

WYGNANSKI, I., CHAMPAGNE, F., & MARASLI, B. 1986. On the large-scale structures in two-dimensional, small-deficit, turbulent wakes. *J. Fluid Mech.*, **168**, 31–71.

YANASE, S., GOTO, N., & YAMAMOTO, K. 1988. Stability of dual solutions of the flow in a curved circular tube. *J. Phys. Soc. Japan*, **57**(8), 2602–2604.

YANASE, S., YAMAMOTO, K., & YOSHIDA, T. 1994. Effect of curvature on dual solutions of flow through a curved circular tube. *Fluid Dyn. Res.*, **13**, 217–228.

YANG, Z.-H., & KELLER, H.B. 1986. Multiple laminar flows through curved pipes. *Appl. Num. M.*, **2**, 257–271.

YAO, L.-S., & BERGER, S.A. 1975. Entry flow in a curved pipe. *J. Fluid Mech.*, **67**, 177–196.

YAO, L.-S., & BERGER, S.A. 1988. The three-dimensional boundary layer in the entry region of curved pipes with finite curvature ratio. *Phys. Fluids*, **31**(3), 486–494.

YEE, G., CHILUKURI, R., & HUMPHREY, J.A.C. 1980. Developing flow and heat transfer in strongly curved ducts of rectangular cross section. *Trans. ASME, J. Heat Transfer*, **102**, 285–291.

YEUNG, W.S. 1980. Laminar boundary-layer flow near the entry of a curved cirlular pipe. *Trans. ASME, J. Appl. Mech.*, **47**, 697–702.

YU, X., & LIU, J.T.C. 1991. The secondary instability in Goertler flow. *Phys. Fluids A*, **3**(8), 1845–1847.